Machine Learning-Supported and Data-Driven Enhancements of Distributed Infrastructure Seismic Resilience

A dissertation submitted to the Civil and Natural Resources Engineering Department and Graduate Studies Office of the University of Canterbury in partial fulfilment of the requirements for the degree of Doctor of Philosophy.

Xavier Bellagamba, 2019

Abstract

This dissertation presents four research elements that aim to improve the seismic resilience of communities. Two of these elements are dedicated to directly improve the resilience of buried infrastructure networks (in particular, the water supply networks), whereas the two others are devoted to ground motion records analysis and immediate regional ground motion intensity estimation.

Utilizing pipe repair data collected following the 22 February 2011 Mw, the first research element introduces new empirical fragility functions for buried pipelines. These new functions integrate a quantifiable soil liquefaction susceptibility metric into their functional form. This enables the fragility assessment of water supply network assets in liquefaction-prone areas without having to estimate the liquefaction severity.

Complemented by additional datasets, the same pipe repair data is used in the second research element to infer the historical recovery of the water supply network, and to develop an optimization method to accelerate its post-earthquake functional recovery. The historical recovery inference provides both temporal and geographical insights on the efficiency of the inspection and repair operations. The optimization method is based on a mixed integer linear programming whose solution is approached using a genetic algorithm. Results show that the recovery was carried out efficiently but could have been optimized by using the proposed optimization method.

To enhance the immediate earthquake source identification and estimation of regional ground motion intensity, the third research element provides a framework to compare recorded ground motions at instrument stations with physics-based ground motion simulations from the Cybershake New Zealand v18.6 program. This framework is composed of two main parts based on machine learning algorithms: (1) an earthquake source discriminator based on a gradient boosting machine, and (2) a ground motion map generator based on a predictive generative network. Applied to the recent and complex 14 November 2016 Mw 7.8 Kaikōura earthquake, this method delivers immediate results that are superior to contemporary counterparts, and could provide valuable insights for precise source inversion.

The last research element proposes an automated quality classification of ground motion records. The method utilizes a neural network that non-linearly combines ground motion records quality metrics such as the shape of the Fourier spectrum or the several signal-to-noise ratios and is trained on manually classified data from two New Zealand regions. The automated method achieves a human-comparable classification quality and its effect on some intensity measures is thoroughly analyzed to ensure that it does not introduce any biases.

In aggregate, the work presented in this dissertation provides new methods that could benefit communities in the pursuit of seismic resilience and provide a solid incentive to foster the application of machine learning technique in the earthquake engineering research field.

Acknowledgements

This entire work would not have been possible without the help and support of many people. I would like to especially acknowledge my supervision committee, who guided my through this incredible journey and continuously shared their knowledge and wisdom with me. First and foremost, I would like to address very special thanks to Prof. Brendon A. Bradley, main supervisor, whose guidance, knowledge and constructive critics have helped me grow as a independent and self-confident researcher in the field of earthquake engineering and machine learning, for the level of trust he showed inviting me to present my work in front of worldwide-leading experts during QuakeCoRE Anuual meetings, and for allowing me to explore and develop some ideas presented in this dissertation. I would like to give my next but as important thanks to Dr. Liam M. Wotherspoon for providing very constructive critics and some essential conceptual improvements on my work, for enabling the dissemination of my work within the New Zealand earthquake engineering community by inviting me to speak during Resilience to Nature's Challenges (RNC) meetings on several occasions, as well as for attending and supporting my oral presentation at the 16th ECEE. I also address special thanks to Dr. Matthew W. Hughes for having shared with me his previous work on some of the data used in this dissertation, and also for introducing me to some knowledgeable key people. In addition to my supervision committee, I would like to greatly acknowledge my co-authors, whose contributions are essential to the achievement of the proposed objectives. Namely, I greatly thank Dr. Robin Lee for his expertise on ground motion record analysis, Dr. Daniel Lagrava for his expertise in code parallelization and optimization, and Dr. Varvara Vetrova for her expertise in machine learning. I also would like to acknowledge some additional people, whose minor but necessary contributions substantially improved my work. Namely, I would like to acknowledge Prof. Rachel Davidson and Dr. Sjoerd van Ballegooy for sharing their impression on my work on several occasions, Irmana Sampedro Garcia, Karn Snyder-Bishop, and Marcus Gibson for sharing their knowledge on the water supply network recovery following the 22 February 2011 Mw Christchurch earthquake, and Dr. Susie Meade, Ruth Hartshorn, Elizabeth Ackermann, and Danica Nel for their help in administrative matters. I also thank QuakeCoRE and RNC for their financial support.

From a more personal perspective, this work would not have been a fully positive experience without the people who were already and became close to my heart. These people are my colleagues from the university, with whom I shared time, experiences and moments in conferences, at university, or in front of a beer: Hoby Razafindrakoto, Seokho Jeong, Ashan Nazer, Reagan Chandramohan, Chris McGann, Sharmila Savarimuthu, Sung Bae, Claudio Schill, Jason Motha, Jonney Huang, Melody Zhu, Viktor Polak, Andrei Nguyen, Daniel Lagrava, Jagdish Vyas, Brandy Alger. Among my colleagues, I would like to thank in particular my PhD fellows, with whom I have shared office, moments of doubts, moments of joy, and a real passion for research: Chris de la Torre, Robin Lee, Ethan Thomson, Sarah Neil, Vahid Logman, Kevin Foster and Karim Tarbali. During my time in New Zealand, I was particularly grateful to form strong and long-lasting friendships with: Daniel Lagrava, Brendon and Brenda Bradley, Liam Wotherspoon, Michael and Jane Goreman, Guy Dubuis, Karim Tarbali, Ethan Thomson, Robin Lee, Jagdish Vyas, Vahid Logman, Robin Xie, Emilie, Bill and Ezra Bourdet, Kevin Foster, Chris de la Torre, Ribu Dhakal, Antonio and Maria Viselli, Eric Mouhica, Shannon Abeling, Franzisco Glavez, Stacy Walis. New Zealand being far away from my home country, Switzerland, I am also most grateful to my lifelong friends Benjamin Mayor, Benjamin Rohrer and his partner Ursina Suter, Romain Crettaz and his fiancée Laura Tibourcio, and Martin Héritier, as well as my cousin Caroline Pradurat and her husband Guillaume Berron who brought a bit of Switzerland to Christchurch. Very special thanks also go to my parents, Sylvie and Jean-Marc Bellagamba, and Anne-Catherine's parents, Danielle and Christian Berrut who made us feel at home during their stay in New Zealand. Finally, my most special thanks go to Anne-Catherine Berrut, my partner, who went through this entire adventure with me. The entire experience would not have been as pleasant without her as she supported me in the most difficult moments of doubts, helped me celebrate achievements, and above of all, provided me with her kindness and love.

Contents

List of Figures

This page is intentionally left blank

List of Tables

Chapter 1

Introduction

1.1 Motivation

This dissertation addresses two aspects of seismic community resilience, namely, the resilience of buried infrastructure networks, and the use and development of physics-based ground motion models. The paragraphs below provide the motivations that drove their respective development.

Buried horizontal infrastructure networks provide essential services required to sustain the well-being of modern societies. In particular, water supply systems provide water for personal and commercial consumption, and are required for fire protection and wastewater system operations. Massive service interruptions due to earthquakes have shown that incumbent costs due to population water deprivation, business interruption, and fire protection can be dramatically high. Significant recent historical examples of such losses are the 17 January 1994 Mw 6.7 Northridge earthquake (Rose et al., 1997; Tierney, 1997; Brookshire et al., 1997; Dahlhamer et al., 1999), the 22 February 2011 Mw 6.2 Christchurch earthquake (Stevenson et al., 2012; King et al., 2014), and the 14 November 2016 Mw 7.8 Kaikōura earthquake (Stevenson et al., 2017). Interruptions also tend to be longer for buried infrastructure than for surface systems, as the former are more difficult to access for inspections and repairs than the latter as observed during recoveries following the 22 February 2011 Mw 6.2 Christchurch earthquake (Giovinazzi et al., 2011; Eidinger and Tang, 2012) and the 14 November 2016 Mw 7.8 Kaikōura earthquake (Hughes *et al.*, 2017).

The 22 February 2011 Mw 6.2 Christchurch earthquake triggered the collection of a large amount of data in multiple domains such as ground motions (Bradley and Cubrinovski, 2011), geotechnical failures (Cubrinovski et al., 2011), building damage (Dizhur et al., 2011), infrastructure network performance (Giovinazzi et al., 2011), and economic losses (Stevenson et al., 2012), that were subsequently used to develop and validate loss models. In particular, the water supply damage data combined with geotechnical failure and ground motion data have been used to develop fragility functions (e.g. O'Rourke et al., 2014; Bagriacik *et al.*, 2018). However, immediately after the earthquake and during the recovery, little attention was dedicated to track the functional recovery, and few tools were available for managers to optimize service restoration.

As opposed to weather forecasting where data is abundant, empirical ground motion models are based on relatively little data. Furthermore, as the recent 14 November 2016 Mw 7.8 Kaikōura earthquake illustrates, it remains difficult to rapidly identify earthquake sources and provide accurate ground motion estimates following a major and complex event (Litchfield *et al.*, 2016; Hamling *et al.*, 2017; Bradley *et al.*, 2017c; Allstadt *et al.*, 2018). To improve the accuracy of ground motion intensity prediction, new physics-based ground motion models are developed. Results of these analyses are used to produce physics-based probabilistic seismic hazard analyses (Graves *et al.*, 2011; Iwaki *et al.*, 2016; Tarbali *et al.*, 2018a) or earthquake scenarios (Graves *et al.*, 2008; Akinci *et al.*, 2017; Smerzini & Pitilakis, 2018) that can be used to train emergency managers and prepare communities (e.g. AF8 project Orchiston *et al.*, 2018 and HayWired project Detweiler & Wein, 2018). Due to the numerous

sources of uncertainties (e.g. spatial distribution of the slip rate, deep ground tomography, velocity profile Duputel *et al.*, 2012; Minson *et al.*, 2013), the development of these models requires a particularly intense validation effort (Lee *et al.*, 2019). Nevertheless, these new models already provide well-calibrated data to more accurately assess damage to infrastructure and subsequently their residual functionality.

Both the assessment of infrastructure resilience and the utilization of ground motion data are data-intensive research domains. As machine learning emerges as a staple way to handle large amounts of data in various research fields (Miller *et al.*, 2018) and becomes increasingly relevant in earthquake engineering (Kong *et al.*, 2018), this dissertation contributes in four earthquake engineering-specific domains. Each individual contribution is detailed in Section 1.2.

1.2 Objectives

This dissertation has four main objectives described in the following subsections. Two of them are dedicated to directly improve the current understanding, assessment and optimization of buried infrastructure resilience, whereas the two others promote the adoption of machine learning techniques in engineering seismology by showing how they could improve and accelerate some processes.

1.2.1 Combined assessment of liquefaction and transient ground motion-induced pipeline damage

During an earthquake, buried pipelines are damaged by excessive ground strains induced by either transient or permanent ground deformations, the former being caused by wave propagation through the soil and the latter induced by co-seismic ground failures such as liquefaction or landslide. As relatively accurate ground motion intensity maps can be released moments after an event (Wald *et al.*, 2008; Allstadt *et al.*, 2018), a damage assessment considering transient ground deformations, which are summarized by peak intensities such as the peak ground acceleration or velocity, is relatively straightforward. However, due to the complex and often qualitative characterization of soils and slopes or lack of ground condition information (e.g. ground water surface depth or soil profile unknown or poorly characterized), the accuracy of current liquefaction and landslide models remains limited, and so are dependent, subsequent loss analyses (Maurer *et al.*, 2014). Post-earthquake assessments using satellite imagery or LiDAR information provide good substitutes for ground strain assessment, but are generally not available until a couple of days following the event (O'Rourke et al., 2014; Toprak et al., 2018).

By their size, their diversity, and the precision of information they contain, the datasets gathered following the 22 February 2011 Mw 6.2 Christchurch earthquake offer a unique opportunity to develop pipeline fragility functions that utilize quantifiable metrics of the soil combined with ground motion intensity and pipe information. This work examines the possibility of such an integration, provides comparisons with existing fragility functions, and proposes a method to validate such models.

1.2.2 Quantification and optimization of post-earthquake water supply recovery

Following major earthquakes, scientists and engineers try to recover as much data as possible to calibrate and validate the next generation of models. However, when it comes to infrastructure network functionality, this task becomes overwhelmingly complex as multiple key factors must be considered simultaneously. Among them, interdependencies between infrastructure systems play a critical role (Zorn and Shamseldin, 2016). Moreover, a real-time estimation of the functional loss is, for some buried infrastructure networks such as water supply, impossible as it can take several weeks to discover all earthquake-induced pipe failures (Giovinazzi et al., 2011; Eidinger and Tang, 2012; O'Rourke et al., 2014). Usually, damage data is gathered, rough outage impacts are estimated, and interviews of

key people from the recovery team are conducted to reveal potential improvements (Giovinazzi et al., 2011; Eidinger and Tang, 2012).

In order to enhance the current understanding of infrastructure network recovery and optimize it, finer details are required. The pipe damage data gathered following the 22 February 2011 Mw 6.2 Christchurch earthquake is combined with learnings from previous studies, interviews of key people, the power outage data, and the GIS dataset of the city buildings and network to reconstruct both temporally and geographically the recovery of the water supply system in that earthquake. Understanding how post-earthquake recoveries are carried out allows the development of optimization methods that account for interdependencies, available resources, as well as temporal and geographical changes in the network functionalities.

1.2.3 Near-real-time earthquake source identification and ground motion estimation via machine learning

In the case of major earthquakes (e.g. Mw $>$ 6.5), current source inversion methods are unable to identify rough finite-fault ruptures until hours following the events and assume a point-source (Allstadt *et al.*, 2018). As a first estimate, the point-source assumption may not be sufficient to produce a reliable regional ground motion estimate (Allstadt *et al.*, 2018). A precise source inversion process based on multiple data sources (e.g. ground motion instruments, geodetic data, satellite imagery, and observed surface fault traces) can be a long process that can last weeks (Litchfield *et al.*, 2016; Hamling *et al.*, 2017; Allstadt *et al.*, 2018). Yet, this step is crucial to estimate the regional ground motion intensity distribution and infer the expected losses on various systems and communities and to help emergency managers to make sound decisions. The recent 14 November 2016 Mw 7.8 Kaikōura earthquake has shown that a precise source inversion, and its subsequent ground motion estimation can take up to multiple weeks (Litchfield *et al.*, 2016; Hamling *et al.*, 2017; Bradley *et al.*, 2017c; Allstadt *et al.*, 2018).

To improve both the source identification and the first ground motion estimate, new perspectives must be adopted. Instead of trying to invert the earthquake source from ground motion recordings at instrument stations, the earthquake source can be inferred by comparing these recordings with an existing database of ground motion simulations. Regional ground motion intensities can then be estimated by recombining ground motion simulations. This kind of work is made possible by the recent advances in data-intensive machine learning algorithms that exploit non-linear features of the data in their predictions.

1.2.4 Automated quality classification of ground motion time series using a neural network

In many applications in earthquake engineering, ground motion time series of quality are required to develop or validate models. For example, designed to replace empirical ground motion models, physics-based ground motion models require extensive and expensive validation work (Lee *et al.*, 2019). In particular, waveforms and key intensity measures from real recordings are compared to their generated counterparts. These real waveforms must be carefully selected by analysts, who must pay attention to several quality metrics such as the signal-to-noise ratio, the shape of the Fourier amplitude spectrum, and the P-wave arrival time (Cauzzi & Clinton, 2013; Ancheta *et al.*, 2014; Van Houte *et al.*, 2016; Kishida *et al.*, 2017). As many thousands of ground motion records are necessary to validate a physics-based model at a country scale, the process can be dramatically time-consuming. Attempts to automate this process yielded relative poor performances when compared to a human processing (Dawood *et al.*, 2016; Kishida *et al.*, 2017).

Advances in statistical learning, and specifically neural network training, allow the non-linear combination of data features. Utilizing data previously classified for the purpose of validating physics-based ground motion models, this objective explores whether this technique could safely replace a

human analyst in order to accelerate the entire validation process.

1.3 Organization

This dissertation is composed of six chapters. Chapters 2 to 5 address the aforementioned four objectives, and Chapter 6 corresponds to the Conclusion. This section briefly outlines the context and structure of each chapter.

Chapter 2 presents a fragility model for buried pipelines that bypasses the need for liquefaction assessment. This model has been developed using the data collected following the 22 February 2011 Mw 6.2 Christchurch and 13 June 2011 Mw 6.0 earthquakes and relies on findings from independent previous findings. The new model is compared to other pipeline fragility models and is tested in a Monte Carlo simulation scheme against observed damage. Results show that the model yields globally good results, but tends to underestimate damage when severe lateral spreading is present.

Chapter 3 introduces an inference of the water supply network recovery following the 22 February 2011 Mw 6.2 Christchurch earthquake and a method to optimize future earthquake-induced outages based on a mixed-integer linear program (MILP). The solution of the MILP is approached using a genetic algorithm. The inference accounts for the dependency on power availability to operate the pump stations and tracks the water deprivation for community-based metrics (e.g. number of residential buildings or population). The recovery optimization is based on an iterative process that prioritizes inspection and repairs based on a statistical damage assessment and the discovered pipe failures, respectively. Compared to the inferred recovery, the optimization results show that application of such framework could improve the resilience of such infrastructure and ultimately of communities.

Chapter 4 proposes a machine learning-based framework to identify earthquake sources and generate regional ground motion maps in near-real-time. This framework is composed of an earthquake source discriminator designed with tree-based techniques, and a ground motion generator based on a predictive generative network. The method utilizes the CyberShake New Zealand v18.6 results as training dataset. Tested on the complex, multi-segmented 14 November 2016 Mw Kaikōura earthquake, this method delivers a relatively precise list of potential earthquake sources and a ground motion map that could have advantageously replaced the first Shakemap versions proposed within days of the earthquake.

Chapter 5 suggests a statistical learning method, a neural network combined with a principal component analysis, to accelerate the classification of ground motion records based on their quality. The training of the neural network utilizes quality metrics based on the signal-to-noise ratio and the Fourier spectra of pre-classified ground motion records from New Zealand small magnitude earthquakes. The results from the classifier are thoroughly validated by examining the distribution of intensity measures and the geospatial distribution of false positive and negative rates across regional instruments. The effects of statistically classified ground motion records are tested against the manually classified dataset on the physics-based ground motion model validation. These results indicate that the statistically classified dataset shows a marginal improvement in bias reduction, but a dramatic reduction in the time required to classify the data.

Chapter 6 summarizes the key findings and practical implications of the proposed research elements and their main limitations. Future possible extensions of this work are also discussed within this chapter.

This dissertation is composed of stand alone chapters that have been adapted from peer-reviewed journal articles. This may cause some repetitions and, occasionally, some notation inconsistencies between chapters. However, this format has the advantage of providing readers with all the information and context they require within each chapter, avoiding the conundrum of looking for references, figures or tables across the entire dissertation. Chapters 2 to 5 all possess a **Complementary material** section that contains the equivalent of the appendix or electronic supplement of each published paper.

1.4 References

Akinci, A, Aochi, H, Herrero, A, Pischiutta, M, & Karanikas, D. 2017. Physics-Based Broadband Ground-Motion Simulations for Probable Mw≥ 7.0 Earthquakes in the Marmara Sea Region (Turkey) Physics-Based Broadband Ground-Motion Simulations for Probable Mw≥ 7.0 Earthquakes. *Bulletin of the Seismological Society of America*, **107**(3), 1307–1323.

Allstadt, KE, Jibson, RW, Thompson, EM, Massey, CI, Wald, DJ, Godt, JW, & Rengers, FK. 2018. Improving near-real-time coseismic landslide models: Lessons learned from the 2016 Kaikōura, New Zealand, earthquake. *Bulletin of the Seismological Society of America*, **108**(3B), 1649–1664.

Ancheta, TD, Darragh, RB, Stewart, JP, Seyhan, E, Silva, WJ, Chiou, BS-J, Wooddell, KE, Graves, RW, Kottke, AR, Boore, DM, Kishida, T, & Donahue, J. 2014. NGA-West2 database. *Earthquake Spectra*, **30**(3), 989–1005.

Bagriacik, A, Davidson, RA, Bradley, BA, Hughes, MW, & Cubrinovski, M. 2018. Comparison of Statistical and Machine Learning Approaches to Modeling Earthquake Damage to Water Pipelines. *Soil Dynamics and Earthquake Engineering*, **112**, 76–88.

Bradley, BA, & Cubrinovski, M. 2011. Near-source strong ground motions observed in the 22 February 2011 Christchurch earthquake. *Seismological Research Letters*, **82**(6), 853–865.

Bradley, BA, Razafindrakoto, HNT, & Nazer, MA. 2017. Strong ground motion observations of engineering interest from the 14 November 2016 Mw7.8 Kaikoura, New Zealand earthquake. *Bulletin of the New Zealand Society for Earthquake Engineering*, **50**(2), 85–93.

Brookshire, DS, Chang, SE, Cochrane, H, Olson, R A, Rose, A, & Steenson, J. 1997. Direct and indirect economic losses from earthquake damage. *Earthquake Spectra*, **13**(4), 683–701.

Cauzzi, C, & Clinton, J. 2013. A high-and low-noise model for high-quality strong-motion accelerometer stations. *Earthquake Spectra*, **29**(1), 85–102.

Cubrinovski, M, Bradley, B, Wotherspoon, L, Green, R, Bray, J, Wood, C, Pender, M, Allen, J, Bradshaw, A, Rix, G, *et al.* 2011. Geotechnical aspects of the 22 February 2011 Christchurch earthquake. *Bulletin of the New Zealand Society for Earthquake Engineering*, **44**(4), 205–226.

Dahlhamer, JM, Tierney, KJ, & Webb, GR. 1999. *Predicting business financial losses in the 1989 Loma Prieta and 1994 Northridge Earthquakes: Implications for loss estimation research.* Tech. rept. Disaster Research Center, University of Delaware, Newark, DE.

Dawood, HM, Rodriguez-Marek, A, Bayless, J, Goulet, C, & Thompson, E. 2016. A flatfile for the KiK-net database processed using an automated protocol. *Earthquake Spectra*, **32**(2), 1281–1302.

Detweiler, ST, & Wein, AM. 2018. *The HayWired Earthquake Scenario — Engineering Implications*. Reston, VA, USA: U.S. Geological Survey and U.S. Department of the Interior. Chap. Chapter N: A New Model of Water-Network Resilience, with Application to the HayWired Scenario by Porter KA.

Dizhur, D, Ingham, J, Moon, L, Griffith, M, Schultz, A, Senaldi, I, Magenes, G, Dickie, J, Lissel, S, Centeno, J, *et al.* 2011. Performance of masonry buildings and churches in the 22 February 2011 Christchurch earthquake. *Bulletin of the New Zealand Society for Earthquake Engineering*, **44**(4), 279–296.

Duputel, Z, Rivera, L, Fukahata, Y, & Kanamori, H. 2012. Uncertainty estimations for seismic source inversions. *Geophysical Journal International*, **190**(2), 1243–1256.

Eidinger, J, & Tang, AK. 2012. *Christchurch, New Zealand Earthquake Sequence of Mw 7.1 September 04, 2010 Mw 6.3 February 22, 2011 Mw 6.0 June 13, 2011: Lifeline Performance*. Tech. rept. Technical Council on Lifeline Earthquake Engineering, Reston, VA.

Giovinazzi, S, Wilson, TM, Davis, C, Bristow, D, Gallagher, M, Schofield, A, Villemure, M, Eidinger, J, & Tang, A. 2011. Lifelines performance and management following the 22 February 2011 Christchurch earthquake, New Zealand: highlights of resilience. *Bulletin of the New Zealand Society for Earthquake Engineering*, **44**(4), 402–417.

Graves, R, Jordan, TH, Callaghan, S, Deelman, E, Field, E, Juve, G, Kesselman, C, Maechling, P, Mehta, G, Milner, K, *et al.* 2011. CyberShake: A physics-based seismic hazard model for southern California. *Pure and Applied Geophysics*, **168**(3-4), 367–381.

Graves, RW, Aagaard, BT, Hudnut, KW, Star, LM, Stewart, JP, & Jordan, TH. 2008. Broadband simulations for Mw 7.8 southern San Andreas earthquakes: Ground motion sensitivity to rupture speed. *Geophysical Research Letters*, **35**(22), L22302.

Hamling, IJ, Hreinsdóttir, S, Clark, K, Elliott, J, Liang, C, Fielding, E, Litchfield, N, Villamor, P, Wallace, L, Wright, TJ, *et al.* 2017. Complex multifault rupture during the 2016 M w 7.8 Kaikōura earthquake, New Zealand. *Science*, **356**(154), eaam7194.

Hughes, M, Nayyerloo, M, Bellagamba, X, Morris, J, Brabhaharan, P, Rooney, S, Hobbs, E, Wooley, K, & Hutchison, S. 2017. Impacts of the 14th November 2016 Kaikoura Earthquake on the Three Water Systems in Wellington, Marlborough and Kaikoura, New Zealand: Preliminary Observations. *Bulletin of the New Zealand Society for Earthquake Engineering*, **50**(2), 306–317.

Iwaki, A, Maeda, T, Morikawa, N, Miyake, H, & Fujiwara, H. 2016. Validation of the recipe for broadband ground-motion simulations of Japanese crustal earthquakes. *Bulletin of the Seismological Society of America*, **106**(5), 2214–2232.

King, A, Middleton, D, Brown, C, Johnston, D, & Johal, S. 2014. Insurance: its role in recovery from the 2010–2011 Canterbury earthquake sequence. *Earthquake Spectra*, **30**(1), 475–491.

Kishida, T, Di Giacinto, D, & Iaccarino, G. 2017. Comparison of Manual and Automated Ground Motion Processing for Small-to-Moderate-Magnitude Earthquakes in Japan. *Earthquake Spectra*, **33**(3), 875–894.

Kong, Q, Trugman, DT, Ross, ZE, Bianco, MJ, Meade, BJ, & Gerstoft, P. 2018. Machine Learning in Seismology: Turning Data into Insights. *Seismological Research Letters*.

Lee, RL, Bradley, BA, Stafford, P, Graves, RW, & Rodriguez-Marek, A. 2019. Hybrid broadband ground motion simulation validation of Canterbury, New Zealand. *TBD*, **TBD**(TBD), TBD.

Litchfield, NJ, Benson, A, Bischoff, A, Hatem, A, Barrier, A, Nicol, A, Wandres, A, Lukovic, B, Hall, B, Gasston, C, *et al.* 2016. 14th November 2016 Mw 7.8 Kaikoura earthquake. Preliminary surface fault displacement measurements, Version 2. *GNS Science*.

Maurer, BW, Green, RA, Cubrinovski, M, & Bradley, BA. 2014. Evaluation of the liquefaction potential index for assessing liquefaction hazard in Christchurch, New Zealand. *Journal of Geotechnical and Geoenvironmental Engineering*, **140**(7), 04014032.

Miller, TH, Gallidabino, MD, MacRae, JI, Hogstrand, C, Bury, NR, Barron, LP, Snape, JR, & Owen, SF. 2018. Machine learning for environmental toxicology: a call for integration and innovation. *Environmental Science and Technology*, **22**(52), 12953–12955.

Minson, SE, Simons, M, & Beck, JL. 2013. Bayesian inversion for finite fault earthquake source models I—Theory and algorithm. *Geophysical Journal International*, **194**(3), 1701–1726.

Orchiston, C, Mitchell, J, Wilson, T, Langridge, R, Davies, T, Bradley, BA, Johnston, D, Davies, A, Becker, J, & McKay, A. 2018. Project AF8: developing a coordinated, multi-agency response plan for a future great Alpine Fault earthquake. *New Zealand Journal of Geology and Geophysics*, 1–14.

O'Rourke, TD, Jeon, S-S, Toprak, S, Cubrinovski, M, Hughes, M, van Ballegooy, S, & Bouziou, D. 2014. Earthquake response of underground pipeline networks in Christchurch, NZ. *Earthquake Spectra*, **30**(1), 183–204.

Rose, A, Benavides, J, Chang, SE, Szczesniak, P, & Lim, D. 1997. The regional economic impact of an earthquake: Direct and indirect effects of electricity lifeline disruptions. *Journal of Regional Science*, **37**(3), 437–458.

Smerzini, C, & Pitilakis, K. 2018. Seismic risk assessment at urban scale from 3D physics-based numerical modeling: the case of Thessaloniki. *Bulletin of Earthquake Engineering*, **16**(7), 2609–2631.

Stevenson, J, Vargo, J, Seville, E, Kachali, H, McNaughton, A, & Powell, F. 2012. *The Recovery of Canterbury's Organisations: A comparative analysis of the 4 September 2010, 22 February and 13 June 2011 Earthquake*. Tech. rept. University of Canterbury. Civil and Natural Resources Engineering, Christchurch, New Zealand.

Stevenson, JR, Becker, J, Cradock-Henry, N, Johal, S, Johnston, D, Orchiston, C, & Seville, E. 2017. Economic and social reconnaissance: Kaikōura Earthquake 2016. *Bulletin of the New Zealand Society for Earthquake Engineering*, **50**(2), 346–355.

Tarbali, K, Bradley, BA, Huang, J, Lagrava, D, Motha, J, Bae, S, & Polak, V. 2018. Cybershake NZ v17.9: New Zealand simulation-based probabilistic seismic hazard analysis. *In: 16th European Conference on Earthquake Engineering*.

Tierney, KJ. 1997. Business impacts of the Northridge earthquake. *Journal of Contingencies and Crisis Management*, **5**(2), 87–97.

Toprak, S, Nacaroglu, E, Koc, AC, O'Rourke, TD, Hamada, M, Cubrinovski, M, & van Ballegooy, S. 2018. Comparison of horizontal ground displacements in Avonside area, Christchurch from air photo, LiDAR and satellite measurements regarding pipeline damage assessment. *Bulletin of Earthquake Engineering*, 1–18.

Van Houte, C, Bannister, S, Holden, C, Bourguignon, S, & McVerry, G. 2016. The New Zealand Strong Motion Database. *Bulletin of the New Zealand Society for Earthquake Engineering*, **50**(1).

Wald, DJ, Earle, PS, Allen, TI, Jaiswal, K, Porter, K, & Hearne, M. 2008. Development of the US Geological Survey's PAGER system (prompt assessment of global earthquakes for response). *In: Proceedings of the 14th world conference on earthquake engineering*.

Zorn, CR, & Shamseldin, AY. 2016. Quantifying directional dependencies from infrastructure restoration data. *Earthquake Spectra*, **32**(3), 1363–1381.

This page is intentionally left blank

Chapter 2

Development and validation of fragility functions for buried pipelines based on Canterbury earthquake sequence data

"One sees, from this Essay, that the theory of probabilities is basically just common sense reduced to calculus; it makes one appreciate with exactness that which accurate minds feel with a sort of instinct, often without being able to account for it."

Pierre-Simon de Laplace, 1814, Essai philosophique sur les probabilités

Adapted from: Bellagamba X, Bradley BA, Wotherspoon LM, and Hughes MW (in press). "Development and validation of fragility functions for buried pipelines based on Canterbury earthquake sequence data". *Earthquake Spectra.* DOI:10.1193/120917EQS253M

This chapter presents parametric fragility functions for buried pressurized water pipelines based on data collected following the 22 February and 13 June 2011 events in the Canterbury, New Zealand earthquake sequence. The fragility of buried pipelines is expressed as a repair rate and utilizes the peak ground velocity, pipe characteristics and soil liquefaction susceptibility expressed by the cyclic resistance ratio. The model explicitly takes into account both within-model uncertainty (the misfit to the data) as well as between-model uncertainty, based on unknown model parameters, such that for each unknown parameter the between-model uncertainty increases. The adopted framework enables a wide application of these fragility functions to analyse the seismic performance of pressurized water pipeline networks, irrespective of the available information on the analysed system. Utilized in a retrospective analysis via Monte-Carlo simulations, the proposed fragility functions yield good predictive results.

2.1 Introduction

Lifeline seismic performance is recognised as an important contributor to the resilience of modern societies. Following the 1994 Northridge earthquake, for example, the damaged water system in some areas of the city of Los Angeles could not be utilized by fire protection services to counter fires ignited by gas network failures (Borden, 1997). Davis (2014) estimates that the functionality of the water supply network of Los Angeles, CA was approximately 35% following this earthquake, reducing the total water delivery by a maximum of approximately 20%. To emphasise the economic importance of lifelines, Chang et al. (2002) estimated that a water supply outage in Memphis, Tennessee due to

a Mw 7.5 North Fault rupture would cost around USD 100M. Economic importance of lifelines is further emphasized by Tierney (1997); Rose et al. (1997); Brookshire et al. (1997); Dahlhamer et al. (1999); Stevenson et al. (2012, 2017).

The Mw 7.1 Darfield and the Mw 6.2 Christchurch earthquakes struck the Canterbury area in New Zealand on the 4th of September 2010 and 22nd of February 2011, respectively. They were notably followed by the Mw 6.0 13th of June and the Mw 5.8 23th of December 2011 earthquakes. This series of earthquakes is known as the Canterbury Earthquake Sequence (CES) and their seismological features and physical impacts have been extensively described by Gledhill et al. (2010); Cousins and McVerry (2010); Quigley et al. (2010); Bradley and Cubrinovski (2011); Wood et al. (2011). The February event, in particular, caused widespread liquefaction in the Christchurch urban area (Cubrinovski et al., 2011) and severely damaged the built environment (Palermo et al., 2011; Dizhur et al., 2011). Multiple civil infrastructure systems have also been studied. In particular, Giovinazzi et al. (2011); Eidinger and Tang (2012) investigated the performance and service restoration of the electric power distribution, the waste water and water supply networks. Cubrinovski et al. (2014) studied the effects of liquefaction on the waste water, water supply and road networks.

Following the CES, the liquefaction and lateral spreading that occurred in Christchurch was closely studied and several liquefaction-related damage maps were published. In a careful study of two sites during the 4 September 2010 and the 22 February 2011 earthquakes, Bowen et al. (2012) showed that '*rapid and complete liquefaction of susceptible layers is required to trigger lateral spreading*'. Based on the 56m LiDAR survey that took place after the 22 February 2011 earthquake, O'Rourke et al. (2014) developed the ground strains and angular distortion maps. To characterize liquefaction severity, van Ballegooy et al. (2014) introduced the liquefaction severity number (LSN), the integral of the calculated post-liquefaction volumetric reconsolidation strain over the depth. It was compared with the liquefaction potential index (LPI) (Iwasaki et al., 1984), the former showing a better between-event correlation across the CES than the latter. From the liquefaction observations following the 22 February 2011 earthquake, Cubrinovski et al. (2014) developed the liquefaction resistance index (LRI), which is a representation of the aggregated cyclic resistance ratio (CRR) of the top layers (up to 3.5m deep) of Christchurch soils using the simplified procedure for liquefaction evaluation proposed by Youd et al. (2001). Utilizing the Christchurch liquefaction database, van Ballegooy et al. (2015) compared different liquefaction triggering procedures coupled with several liquefaction severity metrics, showing that the use of different models could yield significantly different results. Toprak et al. (2018) assessed the influence of the ground strains and displacement estimates gathered from LiDAR 4m, LiDAR 56m, air photography and satellite imagery on pipe vulnerability assessment. Most of these datasets as well as the raw conical penetration test (CPT) data can be found on the New Zealand Geotechnical Database (NZGD) web portal: `https://www.nzgd.org.nz`.

From the aforementioned data collections, several fragility (probability of failure given a specific ground motion intensity) models have been developed based on the observed asset seismic vulnerability. For spatially-distributed systems, the vulnerability of an asset is generally expressed as a repair rate (number of repairs per unit of length). Cubrinovski et al. (2014) developed predictive repair rate functions for asbestos cement pipelines depending on the magnitude-weighted ($M_w = 7.5$) peak ground acceleration and LRI (discussed in a subsequent section) zone in which pipelines were buried. O'Rourke et al. (2014) and Bouziou and O'Rourke (2015); Bouziou and O'Rourke (2017) used angular distortion and horizontal ground strain to derive repair rate functions for several existing pipe materials in liquefied soils. To compare the results using horizontal ground strain and angular distortion with other intensity measures, O'Rourke et al. (2014) also used the geometric mean peak ground velocity (PGV) to estimate reported repair rate in non-liquefied soils. Toprak et al. (2017) proposed a relation between the repair rate and LSN. In addition to the PGV, other models (e.g. Isoyama et al., 2000) also incorporate categorical parameters dependent on the soil conditions and severity of observed liquefaction. Eidinger et al. (2001) and HAZUS (Federal Emergency Management Agency, 2003) both use a combination of PGV-based and permanent ground deformation (PGD)-based mod-

els to describe damage due to transient and permanent ground deformations. O'Rourke and Deyoe (2004) express the pipeline vulnerability given the ground strain induced by either the seismic wave propagation and the permanent ground deformation in a single regression.

In the context of seismic loss estimation of water supply networks, the aforementioned models can be used for a range of applications. Ground strain and PGD-based models are particularly useful to assess damage following an earthquake in regions subject to large permanent ground deformations. However, due to the difficulty in accurately predicting PGD and ground stains, these models also remain hard to apply within a predictive loss analysis. PGV-based fragility functions are easier to use in such cases. However, they are ignoring potential significant co-seismic PGD that may have occurred. Furthermore, PGV-based models that include a qualitative and local geologic parameter such as the type of deposit and the observed liquefaction severity makes their application to networks built in other regions difficult.

To address the aforementioned difficulty assessing predictive loss estimation in liquefaction-prone regions, the present study combines PGV with a quantitative soil parameter independent from the ground motion, CRR and utilizes some of the CES datasets, namely: the network dataset, the pipe repair report dataset, the simulated ground motion maps for each CES event and the estimated Christchurch soil liquefaction resistance index map. This parameter combination allows the assessment of networks subjected to transient ground motions and liquefaction-induced permanent ground deformations by proxy. The developed parametric repair rate functions are utilized in a Poisson distribution to express the fragility of the pipeline.

The next sections present the adopted datasets, the developed methodology and its numerical application details. Subsequently, the fitted functions and their uncertainties are presented and discussed. The proposed fragility functions are finally tested in a retrospective validation analysis via Monte-Carlo simulations (MCS).

2.2 Adopted datasets

2.2.1 Water supply network attributes

The Christchurch water supply network is owned and managed by the Christchurch City Council (CCC). CCC classifies its assets into four categories based on their functionality: (1) Trunk main: diameter greater than 300 mm, used for water transmission from main pump stations to large mains ; (2) Main: diameter between 80 to 300 mm, used to distribute water in residential and industrial areas ; (3) Submain: diameter between 15 to 80 mm, used to distribute water to a small group of buildings ; and (4) Crossover: diameter between 15 to 80 mm, connection between the mains and submains, relatively short. The water pressure within the network varies from 350 to 800 kPa. The network is 3246 kilometres long and contains 1612 kilometres of trunk main and main pipelines (49.9% of the network) and 1624 kilometres of submain and crossover pipelines (50.1% of the network). Note also that 192 kilometres (5.9% of the network) are located in the Port Hills area and situated in stiff soil. The network is mainly composed of high-density polyethylene (HDPE, 28.7%) and asbestos cement (AC, 26.2%) pipelines. Large portions of the network are also made of polyvinyl chloride (PVC, 14.4%) and medium-density polyethylene 80 (MDPE80, 14.0%) pipelines. The use of galvanized iron (GALV, 5.8%), cast iron (CI, 5.7%), concrete-lined steel (CLS, 1.6%), ductile iron (DI, 1.5%) and steel (STEEL, 1.0%) remains marginal. A negligible quantity of segments are built with other types of materials (1.0%). Note that the utilized dataset also contains other types of polyethylene pipes, namely PE100, MDPE100 and LDPE (low density polyethylene), which have been grouped under the category MDPE80 as their respective density does not qualify them as high density and their age of installation correspond to this type of pipes (Cubrinovski et al., 2014, Figure 3). Edkins et al. (2015) describe the fitting type of the most frequent pipe types (AC, HDPE, PVC and CI). It must also be noted that main pipes made of HDPE and MDPE80 are thermally welded, whereas submain pipes are joined with the help of a rubber gasket. Submain pipes represent 99% of HDPE

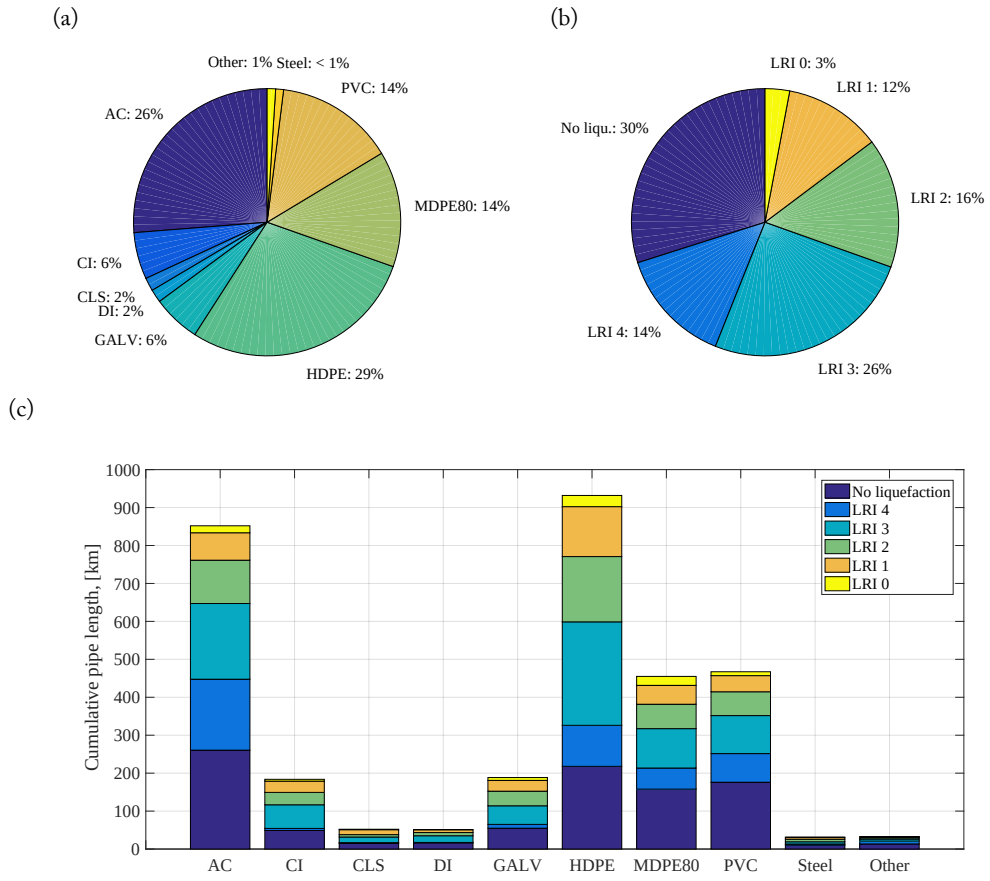

Figure 2.1: Composition of the Christchurch water supply network by: (a) construction material ; (b) LRI zone ; and (c) construction material and LRI zones

and MDPE80 pipelines. Figure 2.1 graphically summarises the pipe network composition and also subdivides each material based on the different LRI zones (introduced in a subsequent section). In Section 2.9.1, Figures 2.12 and 2.13 show the topology of the water supply network and Table 2.3 summarizes the pipeline attributes and their possible values.

2.2.2 Reported pipe repairs following the Canterbury earthquake sequence events

The pipe repair dataset was created and managed by the Stronger Christchurch Infrastructure Rebuild Team (SCIRT). A consistent data collection of executed repairs started after the 22 February 2011 Christchurch earthquake as mentioned by Cubrinovski et al. (2014, pp. 17-22). As a result, the majority of the repairs from the 4 September 2010 earthquake were not documented adequately and therefore, not considered in the analysis to follow.

The SCIRT repair dataset inventories all pipe repairs, regardless of their cause. Therefore, a screening is necessary to remove pipe repairs which were unlikely to have been earthquake-induced (i.e. repairs that have no or little effect on the global seismic system performance). Excluding the central business district areas cordoned off following the 22nd February 2011 (for safety reasons, access restriction was enforced for 15 months in the Christchurch Business District, see Chang et al. (2014) for more details), Giovinazzi et al. (2011) report that 95% of the buildings had recovered water access approximately one month following the February earthquake. Eidinger and Tang (2012) estimate that the repair period lasted approximately six weeks (i.e. that the repairs ended circa the 5th of April 2011). O'Rourke et al. (2014) defines the so-called transitional frequency of repairs period as a pe-

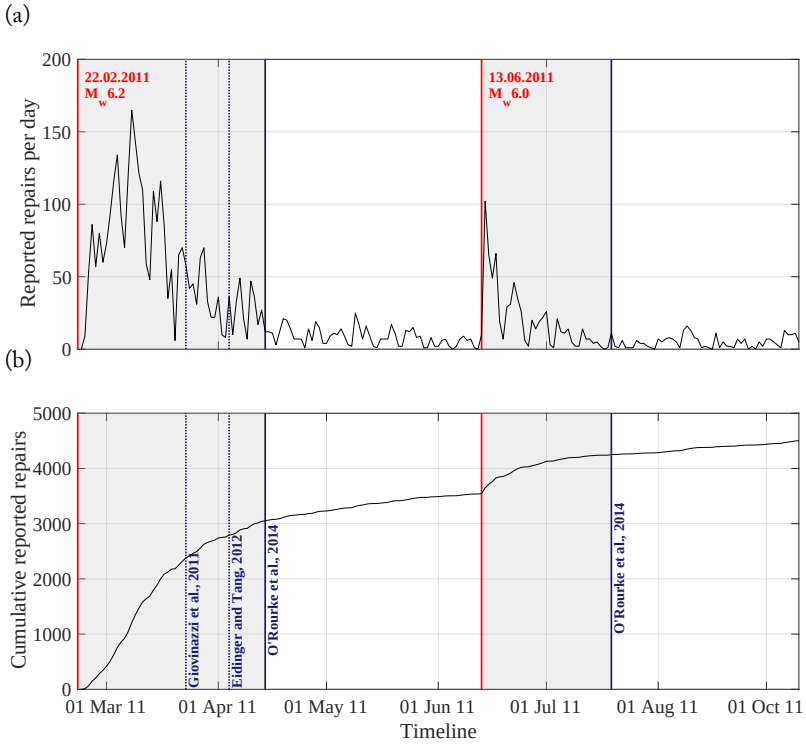

Figure 2.2: (a) Number of detected pipe repairs per day on the water supply network ; and (b) Cumulative number of detected pipe repairs. In both figures, red lines indicate the exact date of each major earthquake. Grey areas indicate the periods when pipe repairs are considered as a direct consequence of an earthquake, with the end of the effective repair period considered by prior studies, also explicitly noted.

riod during which the weekly repair rate of main pipelines is lower than the one observed during the emergency phase but still higher than the post-earthquake steady state frequency of repairs. O'Rourke et al. (2014) define the start of the former circa the 15th of April 2011 and circa the 21st July 2011 for the February and June earthquakes, respectively. In this analysis, repair periods proposed by O'Rourke et al. (2014) are selected to screen the earthquake-related pipe repairs. In total, 3039 pipe repairs are attributed to the February event and 732 to the June one. Changes in the pipe network materials and extent due to growth and repairs between the February and June earthquakes have been considered. Nonetheless, very few changes can be observed as the repairs were carried out following a *like-for-like* strategy as noted by Eidinger and Tang (2012, p. 170). The daily observed repair rate and cumulative number of repairs as well as the aforementioned key dates are given in Figure 2.2. The grey areas show the considered repair periods for each earthquake. In Section 2.9.1, Figure 2.16 shows the map of the spatial distribution of pipe repairs and Table 2.4 provides their attributes. Despite the accuracy and completeness of the pipe repair dataset, several limitations are worthy of note. First, when reported, the repaired pipe part (fitting, coupler or pipe hull) was not consistently described across the dataset due the non-uniform nomenclatures used by contractors. And second, pipe repairs were binarily recorded (i.e. failed or undamaged), making it impossible to classify repairs as either breaks or leaks. For these reasons, the developed functions express the fragility of pipelines as a whole (i.e. no discrimination between pipes, fittings and couplers are made) and do not provide a quantitative measure of the damaged pipe performance.

2.2.3 Ground motion intensity

For the purpose of correlating pipe damage with ground motion intensity, the geometric mean peak ground velocity (PGV) maps computed by Bradley (2014) for each considered event of the CES are adopted. These maps are based on PGV predictions on a dense uniformly-spaced grid, with each

grid point representing the predicted ground motion in the form of a log-normal distribution of PGV (defined by a median value and logarithmic standard deviation). The predicted distribution of PGV is based on a combination of an empirical ground motion model (Bradley, 2013) and recorded ground motions at strong motion stations, such that lower standard deviations in the prediction occur in the vicinity of strong motion stations. In Section 2.9.1, Figures 2.17 to 2.20 show the ground motion intensity and its lognormal standard deviation of the 22 February and 13 June 2011 events.

2.2.4 Soil liquefaction susceptibility

Previous observations and analyses (e.g. Eidinger et al., 2001; Cubrinovski et al., 2014; Bouziou and O'Rourke, 2015; Bouziou and O'Rourke, 2017) have identified higher repair rates in liquefaction-susceptible areas as a result of greater ground deformation for a given level of ground motion intensity. In the context of the CES, the LRI developed by Cubrinovski et al. (2014, pp. 13-14) summarizes the observed liquefaction-related land damage and the susceptibility of the ground to liquefy given the measured CRR of the different ground layers present in a particular area. In Christchurch, five LRI zones have been estimated for a shallow depth of the deposits. Each zone is defined by a range of CRR based on observed ground failures during the 22 February 2011 earthquake. Cubrinovski et al. (2014, Table 2) also provide an estimate of the CRR at the groundwater table depth for each zone (i.e. 0.065, 0.13, 0.195 and 0.26 for $LRI = 1$, $LRI = 2$, $LRI = 3$ and $LRI = 4$, respectively). Table 2.5 provides the CRR range for each zone as well as their associated ground settlement and lateral displacement amplitudes. In Section 2.9.1, Figure 2.21 presents the spatial extent of each zone.

To develop the subsequently-proposed model, a single value of CRR per LRI zone is used. The selection of this value is based on the assumed installation depth of the pipelines (between 0.75 and 1.5 meters, see Christchurch City Council (2014, pp. 25-29) for more details) and the estimated groundwater table depth at the time of the earthquakes. van Ballegooy et al. (2014, pp. 40-42) estimated the groundwater table to lie mostly between 0 and 2 metres deep. Hence, the CRR at the groundwater table depth is selected to represent the liquefaction susceptibility of the soil at pipeline installation depth. Further reference to the CRR in the development of fragility functions refers to the estimated CRR at the groundwater table depth. Note that as the value of CRR at the groundwater table depth for $LRI = 0$ is undefined by Cubrinovski et al. (2014), it is assumed to be 0.032. This value is chosen as the mid-point between an infinitely liquefaction-susceptible soil and the estimated CRR for $LRI = 1$ at the groundwater table depth.

2.3 Fragility function methodology

2.3.1 General framework

To create a widely applicable set of fragility functions for buried pipelines, the functions are built in a way such that they can be applied to pipelines for which some characteristics remain unknown. To achieve this goal, a parametric model is developed by combining the pipe segment, soil profile liquefaction susceptibility and ground motion intensity characteristics. Parameters considering the various dependencies have specific values if known and otherwise are random variables. Hence, the more parameters that are known, the smaller the between-model uncertainty is (discussed in a subsequent section). The next section details the development of the model and the subsequent section provides its numerical implementation.

2.3.2 Pipeline fragility model design

The pipeline fragility functions proposed in this study are developed as pipeline repair rate functions (i.e. number of reported pipe repairs per kilometre) assuming a Poisson distribution of repairs along pipelines as adopted in similar studies (e.g. O'Rourke and Ayala, 1993; Eidinger, 1998; Isoyama et al.,

2000; O'Rourke and Deyoe, 2004; O'Rourke et al., 2014; Bouziou and O'Rourke, 2015; Bouziou and O'Rourke, 2017). The specific functional form for the repair rate, λ, is given by Equation 2.1.

$$\ln(\lambda) = f_0(PGV) + \sum_{i=1}^{n} C_i(\underline{h_i}) + \epsilon \tag{2.1}$$

where $\ln(\lambda)$ is the natural logarithm of the repair rate, $f_0(PGV)$ is the so-called backbone function depending on PGV, $C_i(\underline{h_i})$ is the correction term corresponding to the i^{th} known model parameter which depends on the parameter vector $\underline{h_i}$. The number of known parameters is expressed by n and the uncertainty of the model by ϵ, a zero-centred normally distributed random variable.

The backbone function f_0 estimates the repair rate of a pipeline knowing only the PGV it experiences. This first estimate is then corrected by the terms C_i given the known parameters $\underline{h_i}$. The pipeline characteristics-related correction terms depend on the pipe material and pipe diameter. Pipe materials are also grouped within two performance categories: low or high observed seismic performance. This parameter is based on the observed repair rate residuals of each material and the backbone curve (i.e. how much does the residual diverges from the origin given its material). This extra grouping is useful to assess the effect of replacing vulnerable materials with a more robust material type or assess other networks having different pipe types, which seismic performances are qualitatively known but quantitatively not evaluated. This classification allows groupings of pipes that share similar seismic performance despite their material and joint types. On one side, as already expressed in (Eidinger et al., 2001, pp. 38–39) and Edkins et al. (2015), welded joints provide better seismic performance as they are less prone to being pulled apart than segmented pipelines (e.g. joined with rubber gasket). On the other side, the ductility of the pipe itself also influences the global performance of the pipe system as reported by (Eidinger et al., 2001, pp. 38–39), (Federal Emergency Management Agency, 2003, pp. 8.17–8.18) and (Cubrinovski et al., 2014, Figure 15). To correct the repair rate based on the soil liquefaction susceptibility, another correction term depending on CRR is created. This allows the soil liquefaction susceptibility to be described by a continuous variable, facilitating the use of the proposed functions on other networks. Hence, the backbone curve f_0 can be corrected by a maximum of four correction terms C_i depending on performance group (low or high), material, diameter and CRR. To account for the function misfit and unknown parameters, the uncertainty term ϵ is added to the corrected repair rate. The backbone function f_0 and the correction terms C_i are fitted on the observed repair rate or their difference with less develop model sharing the $n-1$ identical characteristics, respectively.

To ensure that the data points used to estimate the backbone function f_0 and the correction terms C_i are statistically valid, the screening criteria proposed by O'Rourke et al. (2014) is applied with the recommended values. Assuming a Poisson distribution, this criterion verifies that the pipe length used to compute the repair rate is long enough.

In order to minimize the model error, multiple functional forms, discussed subsequently, for the backbone function, f_0, in Equation 2.1 are tested via a K-Fold cross-validation process as described in (Friedman *et al.*, 2008, pp. 241-247). This method consists of splitting the dataset into K smaller subsets, which are subsequently used to estimate the error of each functional form fitted on the data belonging to the K-1 other subsets, and thus avoid over-fitting. The functional form with the smallest error is the model that is then chosen. In the present case, subsets are created with an approximately equal length of pipelines. Note that errors are estimated on the entire repair rate function set as detailed in Section 2.9.2.

As the created model is built by adding correction terms C_i to the backbone function f_0, it inherently contains two types of uncertainties: the within-model uncertainty due to the misfit of the parametric model to the empirical data, and the between-model uncertainty due to the additive feature of the model (i.e. the difference between levels of corrections of the backbone function f_0). The within-model uncertainty is computed as the standard deviation from the fitting residuals of C_i or f_0.

It is considered as a normally distributed random variable with zero mean as the curve fitting process aims to converge on this particular value.

The between-model uncertainty is estimated by computing the standard deviation of the residuals between the most detailed repair rate functions (i.e. depending on performance group, material, diameter and CRR) and the analyzed, less detailed function. Note that, by doing so, the between-model uncertainty of the most detailed repair rate functions is non-existent. To be considered valid, repair rate functions have to show a between-model residual mean close to zero (i.e. the most detailed functions must show both positive and negative residuals with the analysed one). The between-model uncertainty is also assumed to follow a normal distribution. It is subsequently demonstrated that the normal distribution for $\ln(\lambda)$ is an appropriate approximation. As both uncertainties are considered as independent normally distributed random variables with zero mean, the total uncertainty ϵ of a specific repair rate function can be sampled as a combination of two zero-centred normal distributions.

In addition, physics-based constraints are set to estimate the correction term functions C_i. First, according to the observations, a pipeline buried in soil with lower CRR (i.e. more susceptible to liquefaction) should experience, on average, more damage than a pipeline buried in soil having a higher CRR. Therefore, to remain physically consistent, the repair rate must increase with the reduction of CRR (i.e. the partial derivative of the correction term function C_i corresponding to the soil characteristic CRR must be negative with respect to CRR).

Furthermore, observations also show an increase in the mean repair rate with increasing ground motion intensity. To ensure that repair rate functions remain monotonically increasing for expected ground motion intensities, the partial derivative of the newly computed correction term C_n with respect to PGV must remain greater than the partial derivative of the repair rate function sharing the $n-1$ identical parameters. Details of the fragility function fitting process can be found in Section 2.9.2.

2.3.3 Implementation of the proposed framework

This section details the modelling choices and numerical implementation of the proposed framework. First, groupings of certain parameter values are justified. Then, functional forms of the backbone function f_0 and correction terms C_i are proposed. Finally, numerical values for the physics-based constraints and K-fold cross-validation are given.

As the sample length tends to be relatively small for some parameter combinations, certain values are grouped together to increase it. Based on the distribution of diameters and functionality of pipes (see Figure 2.14), diameters between 15-80 mm, 80-300 mm and 300-600 mm are grouped. Table 2.1 presents the performance grouping by materials as well as the materials referenced under the same label. This classification produces a distinct differentiation between the two performances as shown in Figure 2.3 (a). Note that, when no pipe characteristics are available (performance, material, and diameter), the term *generic* is used (i.e. the backbone curve describes the *generic* behaviour of a pipe). In addition, pipes situated in the $LRI = 4$ and *No observed liquefaction* zones are grouped together. Figure 2.3 (b) shows the empirical cumulative distribution of the residuals between the observed repair rates of the backbone function and the CRR-corrected function. It can be observed that the $LRI = 4$ curve is significantly below the *No observed liquefaction* curve. As the $LRI = 4$ zones are located exclusively on the western part of the city (see Figure 2.21), they experienced significantly smaller PGV (see Figures 2.17 to 2.20) and therefore smaller repair rates. As a result, they can reasonably be associated with the *No observed liquefaction* zones. Pipes in the Port Hills areas are considered for the development of CRR-independent functions, but excluded otherwise. Specific repair rates functions for the pipelines located in the Port Hills area are developed in Section 2.9.3. To perform the K-fold cross-validation on the backbone function f_0, three functional forms are tested: the linear function (Equation 2.2), the power function (Equation 2.3) and the 'corrected' power function (Equation 2.4).

$$f_0(PGV) = a \cdot PGV + b \tag{2.2}$$

Table 2.1: List of considered low and high performance materials. MDPE80 includes MDPE100, LDPE and PE100, and PVC includes UPVC and MPVC.

Observed seismic performance	Material name
Low (high repair rate)	AC
	CI
	CLS
	GALV
	Steel
High (low repair rate)	DI
	HDPE
	MDPE80
	PVC

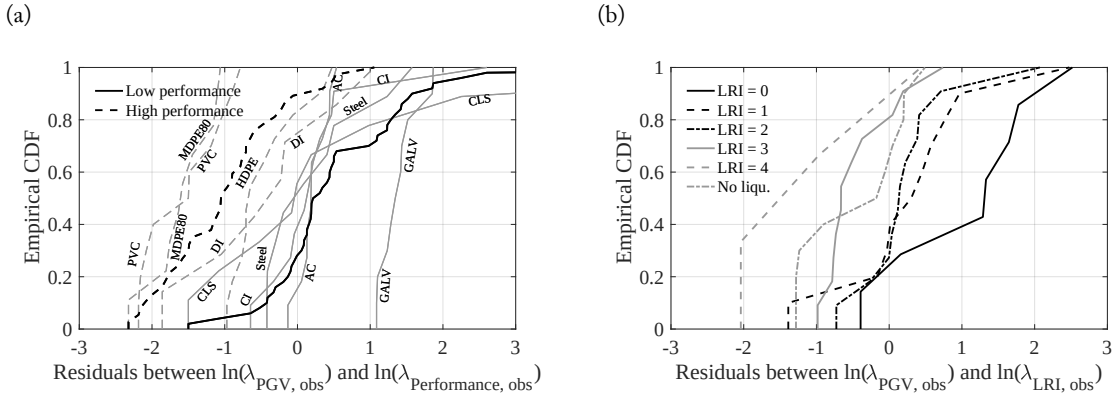

Figure 2.3: CDFs of the difference between the screened repair rate data from the backbone curve and from the classifications based on (a) observed seismic performance of pipe materials; and (b) LRI zones.

$$f_0(PGV) = a \cdot PGV^b \tag{2.3}$$

$$f_0(PGV) = a \cdot PGV^b + c \tag{2.4}$$

The functional forms utilized to fit the correction term functions C_i depending on the pipe (performance group, material and diameter) and the soil characteristics are the linear function (Equation 2.6) and the power function (Equation 2.5), respectively.

$$C_{Soil}(CRR) = a \cdot CRR^b + c \tag{2.5}$$

$$C_X(PGV) = a_X \cdot PGV + b_X \tag{2.6}$$

where X is either the performance group, the material or the diameter dependence.

The monotonically increasing behaviour of the repair rate functions is guaranteed for PGV inferior or smaller than 150 cm/s. Five folders are created to realize the K-fold cross-validation. It is also worth mentioning that, to reduce the effect of soil condition and ground motion spatial variability, the pipelines are discretized such that their maximum length does not exceed 50 m (the longest asset is longer than 2 km).

2.4 Repair rate fitting results

This section provides the results of the K-fold cross-validation and of the fitting process using the selected functional form for the backbone function f_0. The developed repair rate functions are plotted against the PGV and their uncertainties are discussed. The final form of the repair rate function is then explicitly given. Finally, some of the proposed functions are compared to existing ones, which also use PGV as ground motion intensity measure.

2.4.1 K-fold cross-validation and repair rate fitting results

K-Fold cross-validation errors for the linear, power and 'corrected' power models are 1.86, 1.85 and 1.76 respectively. The difference between the linear and power functions are insignificant. However, the score of the 'corrected' power model shows a clear 5.5 % model accuracy improvement. Hence, the 'corrected' power function is chosen over the linear and power ones to model the backbone function f_0. Due to the absence of individuals for some parameter combinations, numerous possible repair rate functions are not modelled (e.g. large diameter GALV). In addition, some functions are rejected as the sample length they are derived from is too small. Namely, all CLS, DI and Steel as well as the small diameter AC and PVC related functions are discarded. However, data from these discarded functions are integrated into their less developed form (e.g. small diameter PVC data is integrated into the PVC data and CLS data is included into low performance material data). It is recommended to replace the discarded functions by their associated less developed form (e.g. PVC D 0-80mm should be replaced by PVC and CLS-CRR should be replaced by Low performance-CRR). Further discussion is directed only toward the remaining valid 30 functions. It must also be observed that, in the case of HDPE and MDPE80 main pipelines (diameter greater than 80 mm), the developed functions should not be used as they are not deemed to represent the reality. In fact, these pipelines exhibit outstanding seismic performance during the two considered earthquakes: no damage was reported on this particular pipe type in regions suffering from extreme liquefaction and severe lateral spreading (i.e. in $LRI = 0$ zones), and almost no damage to the 170 km long LPG pipe network exclusively composed of MDPE welded pipelines was reported (Giovinazzi et al., 2011, Eidinger and Tang, 2012, p. 161 and pp. 210–215 and O'Rourke et al., 2014).

Figure 2.4 presents the fitted, CRR-independent repair rate functions. As expected and pictured in Figure 2.4 (a), pipelines made of low performance construction materials experience about a significant four times higher repair rate than pipelines made of high performance construction materials.

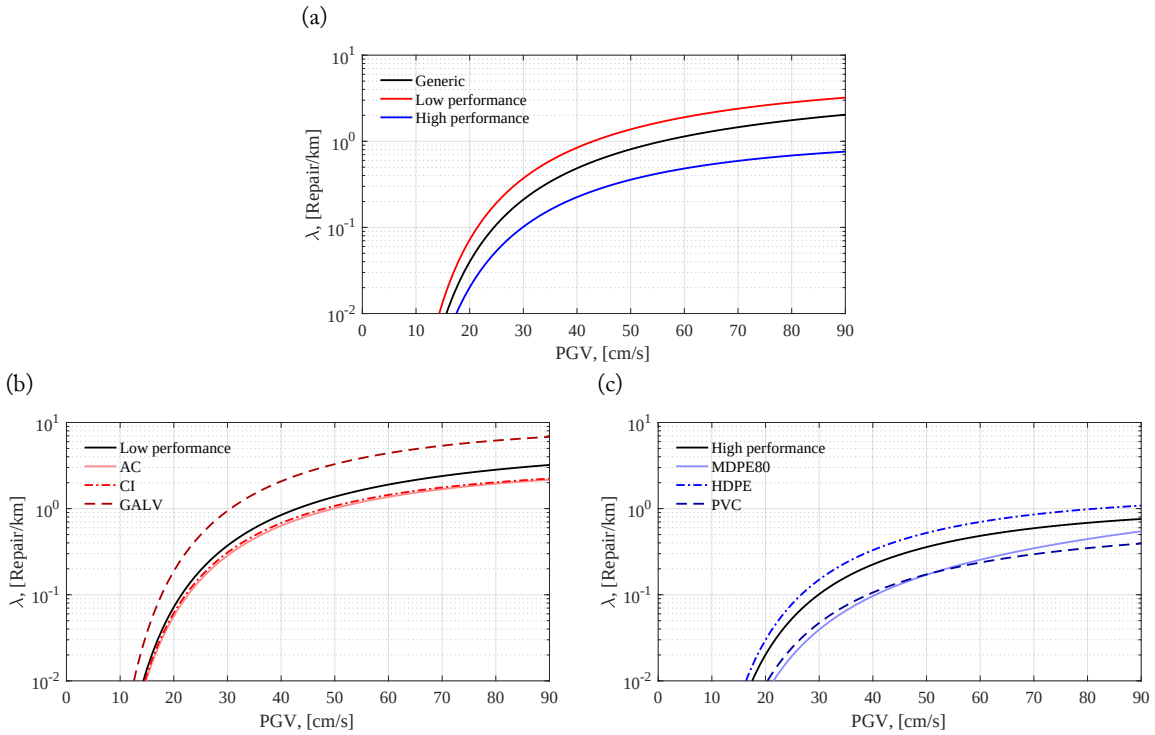

Figure 2.4: CRR-independent repair rates functions for (a) generic pipes (backbone function) and generic high and low performance pipes ; (b) pipes made of low performance materials ; (c) pipes made of high performance materials

Among the low performance construction materials present in Figure 2.4 (b), GALV is most vulnerable, whereas other materials have similar vulnerability curves. For construction materials classified as high performance in Figure 2.4 (c), PVC performs best, followed by MDPE80. HDPE pipelines have a higher repair rate. Due to the lack of data, diameter-dependent functions tend to show repair rates similar to their less developed forms and are therefore not graphically presented. Figure 2.5 presents CRR-dependent repair rate functions. For conciseness, the plotted functions represent only the three most basic CRR-dependent functions (namely, PGV - CRR, PGV - Low performance - CRR and PGV - High performance - CRR functions). Figure 2.5 (a) shows that for a given pipeline, regardless of its characteristics, the liquefaction susceptibility of the soil significantly contributes to its vulnerability. This trend is particularly pronounced when looking only at pipelines made of low performance construction material. However, the influence of the liquefaction susceptibility of the soil is less marked for pipelines made of high performance material. General trends related to material and diameter observed in Figure 2.4 remain valid for CRR-dependent functions. Quantile-quantile plot (QQ plot) is a graphical, statistical tool, that helps compare the empirical distribution (the data) with an assumed distribution (the hypothesis). A good alignment of the data along the identity line validates the original assumption that the lognormal distribution is appropriate for the repair rate. Figure 2.6 presents the QQ plots for both the within-model and between-model uncertainties of the PGV-CRR repair rate function shown in Figure 2.5 (a). This function is selected as it is fitted on a statistically-relevant number of points and has the maximum number of most developed forms (performance group, material, diameter and CRR-dependent functions). With the exception of the between-model uncertainty left tail in Figure 2.6 (b), both plots show that the normal distribution of $\ln(\lambda)$ is a reasonable assumption.

2.4.2 Repair rate uncertainty modelling

Figures 2.7 (a) and (b) present the within-model and between-model uncertainties, respectively, in terms of mean residual and its standard deviation for all valid repair rate functions. The within-model

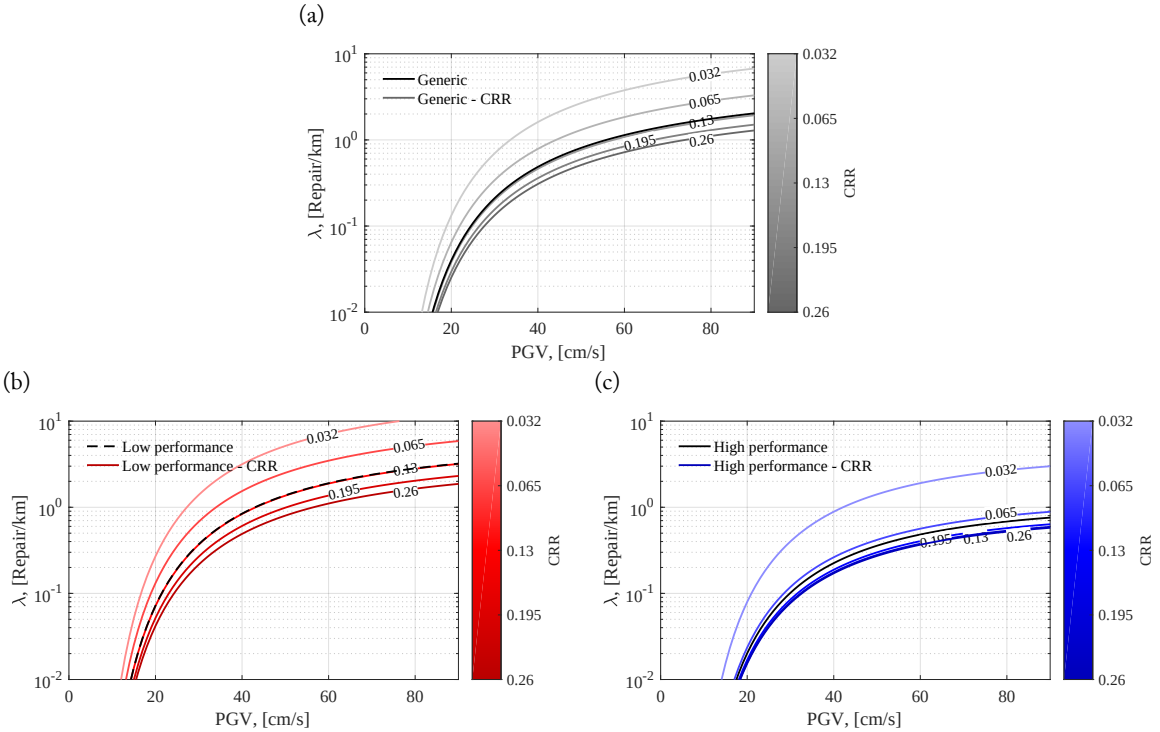

Figure 2.5: CRR-dependent repair rates functions for (a) generic pipes ; (b) generic low performance pipes ; and (c) generic high performance pipes. Colour intensity indicates the liquefaction susceptibility characterized by the CRR. CRR values presented correspond to the five LRI zones.

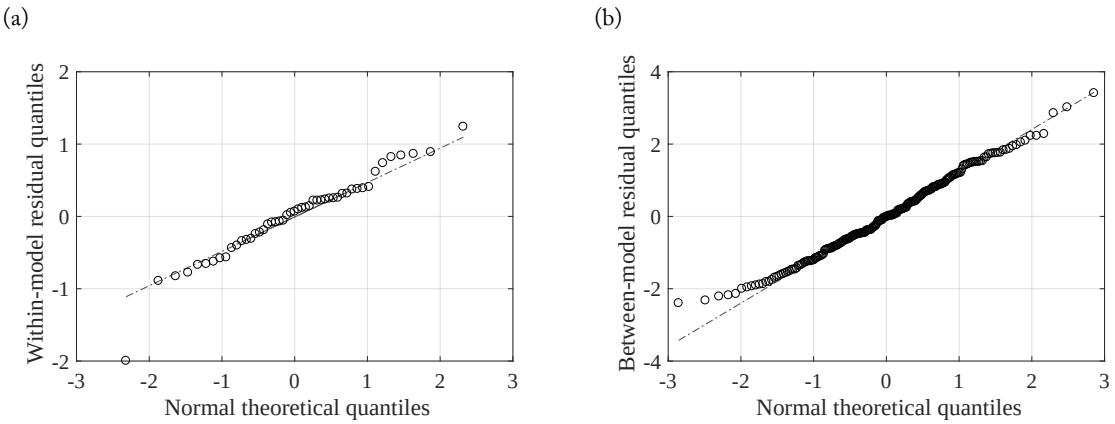

Figure 2.6: QQ plots of (a) the within-model ; and (b) the between-model uncertainties of the PGV-CRR repair rate function

uncertainty is expected to increase as the dataset size decreases. Hence, as the number of parameters increases, the data becomes scarcer and the within-model uncertainty increases. As their formulation is more complex (i.e based on two continuous variables, namely, the PGV and the CRR), the CRR-dependent functions tend to show a higher within-model uncertainty. Due to the almost exclusivity of material use for a certain functionality (which is directly linked to the diameter), diameter-dependent functions for these materials show almost no change in their within-model uncertainty.

The between-model uncertainty tends to decrease with the number of parameters (i.e. the analysed function becomes more similar to its most detailed form). For the PVC-dependent functions, the between-model uncertainty mean is significantly above zero (which means that the model tends to underestimate these repair rates). As the data from the removed small diameter PVC functions tend to show higher repair rates, their integration into the diameter-independent functions leads to this overestimate. Furthermore, data points from the PVC and CI fitted functions for the $LRI = 4$ zones have been manually excluded as they were showing equivalent repair rates as data points for the $LRI = 2$ zones, explaining both the positive value in within-model and between-model uncertainty for these two materials. As it can be observed in Figure 2.1, the amount of CI pipes in LRI = 4 zones is extremely low. Hence, a few observed pipe repairs in these areas yield a large repair rate. Albeit less marked, the same tendency can be observed for PVC. In addition to this factor, LRI = 4 zones are concentrated toward the West of the city (see Figure 2.21), and experienced only low PGV (see Figures 2.17 and 2.19). Hence, data points for LRI=4 are concentrated around low PGV values. Acknowledging that PVC pipes were among the most resistant during the CES (Eidinger and Tang, 2012, p. 166 and O'Rourke et al., 2014), the observed vulnerability in zones with $LRI < 4$ was relatively low for this range of PGV, leading to this inconsistency that have been manually removed. All numerical results from the fitting process and uncertainty estimation are gathered in Section 2.9.4.

2.4.3 Final form of the repair rate functions

Equations 2.7 and 2.8 give the fully-developed repair rate model for pipelines buried in soft soils (based on Equations 2.1-2.6 and related text). Table 2.6 provides the coefficient values for all repair rate functions included in this model.

$$\ln(\lambda) = \Big[a_0 PGV^{b_0} + c_0\Big] + \Big[a_1 PGV + b_1\Big] + \Big[a_2 \cdot PGV + b_2\Big] + \Big[a_3 \cdot PGV + b_3\Big] + \Big[a_4 CRR^{b_4} + c_4\Big] + \epsilon \tag{2.7}$$

$$\epsilon \sim \mathcal{N}\left(0, \sqrt{\sigma_W^2 + \sigma_B^2}\right) \tag{2.8}$$

where index 0 represent the backbone function of the model f_0, index 1 the performance group correction term, index 2 the material correction term, index 3 the diameter correction term, index 4 the CRR correction term and ϵ the normally distributed uncertainty term constituted of a within-model and a between-model standard deviations. A value of zero is assigned to every unknown pipeline or soil characteristic (e.g. absence of information regarding the precise type of material leads to assign 0.0 to all correction terms with index 2 and 3). For practical applications, Equation 2.7 can be rewritten as proposed in Equation 2.9.

$$\ln(\lambda) = (c_0 + b_1 + b_2 + b_3 + c_4) + (a_1 + a_2 + a_3) \cdot PGV + a_4 CRR^{b_4} + a_0 PGV^{b_0} + \epsilon \tag{2.9}$$

2.4.4 Comparison with existing pipe vulnerability functions

To compare the herein-presented functions the following models are selected: the brittle and ductile repair rate functions given by HAZUS (Federal Emergency Management Agency, 2003), the backbone function from the American Lifeline Alliance model (Eidinger et al., 2001) as well as the

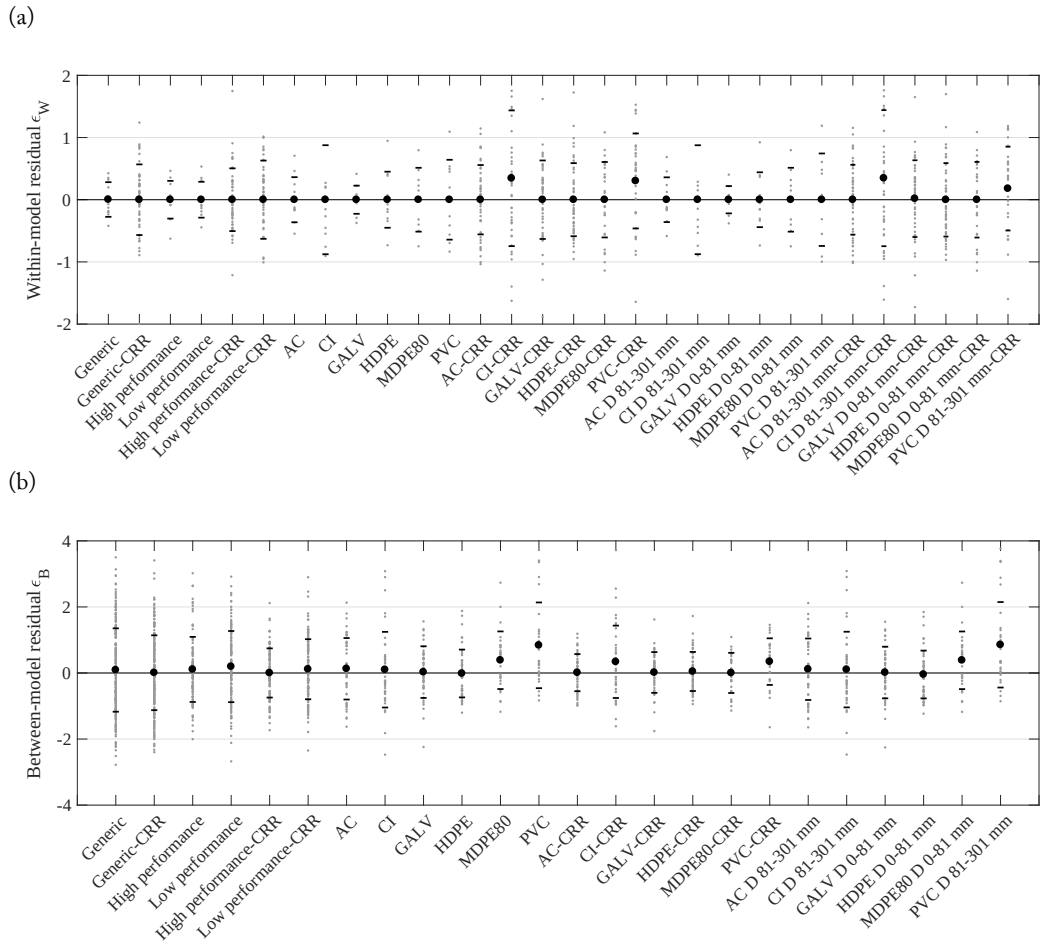

Figure 2.7: (a) Within-model uncertainty ; and (b) between-model uncertainty given in terms of mean and standard deviation of residuals for all developed repair rate functions. Note that some parameters are not explicitly listed in the labels (e.g. PGV for all functions except the backbone curve and performance grouping for material and diameter-dependent functions).

backbone function and its liquefaction-dependent forms from Isoyama et al. (2000). It should be noted that both the HAZUS (Federal Emergency Management Agency, 2003) and Eidinger et al. (2001) models propose PGD-dependent repair rate functions, which generally yields greater repair rates than their PGV-dependent counterparts for large PGD-prone areas. However, as the aim of the proposed model is to remove the liquefaction severity estimation from the seismic network analysis, only the PGV-dependent models are compared. Both models from HAZUS (Federal Emergency Management Agency, 2003) are the ones presented by O'Rourke and Ayala (1993) based on four US and two Mexican earthquakes. The brittle material model is assumed valid for AC, CI and RCC (reinforced cement concrete) pipelines, with the ductile material valid for DI, Steel and PVC. The Eidinger et al. (2001) repair rate function are based on a dataset where the CI construction material is most prevalent (38%). The Isoyama et al. (2000) backbone model expresses the repair rate of CI pipelines of diameters between 100 and 150 mm in alluvial soils, in which no liquefaction was observed. Coefficients for the liquefaction-dependent functions given by Isoyama et al. (2000) are provided for "No liquefaction", "Partial liquefaction" and "Total liquefaction". Existing functions are compared with the herein-presented backbone and performance grouping functions with low liquefaction susceptibility (i.e. equivalent to the CRR of $LRI = 4$ zones). Given the construction material used to develop the Isoyama et al. (2000) backbone function, the CRR-dependent low performance construction material repair rate is used for the liquefaction-dependent functions.

Figure 2.8 shows both the comparisons between the CRR-independent (a) and CRR-dependent functions (b). Figure 2.8 (a) shows that the proposed model yields similar results than the HAZUS (Federal Emergency Management Agency, 2003) model. However, both the Eidinger et al. (2001) and Isoyama et al. (2000) models return substantially lower repair rates. The same general trends can be observed for liquefaction susceptibility-dependent functions in Figure 2.8 (b): here also, the Isoyama et al. (2000) functions tend to underestimate the damage.

2.5 Retrospective analysis

To ensure that the presented fragility functions are reliable, they are tested in a retrospective analysis. This analysis is conducted via a Monte-Carlo simulation (MCS) process first at network level (i.e. using the entire network), and then at repair catchment level (i.e. for smaller portions of the network). The repair catchments are network portions, that were delineated by SCIRT during the Christchurch rebuild. Figure 2.15 presents the 94 repair catchments spatial distribution and their respective cumulative pipe length. The network level analysis allows to assess the predicting model performance of total number of pipe repairs, whereas the catchment level are used to assess the statistical validity of the model via a Pearson's residual analysis, as well as a geospatial comparison between the observed and simulated repair rates for both the February and June events.

2.5.1 Monte Carlo simulation method and results at network level

For the simulations, the maximum pipe length is set to 100 m. Longer pipelines are split into smaller segments of approximately equal size. PGV intensities are estimated on a rectangular grid of stations located at 500 meters and 100 meters from each other for the network level and catchment level analyses, respectively. A pipe segment is assumed to experience the same PGV as the nearest station to its centroid. For the network level analyses, two different MCS are performed. First, a conventional MCS is executed and second, to mimic reality, a threshold is applied on the maximum number of repairs a pipe can experience. The threshold is determined by the maximum repair rate observed on a 20+ meters long asset for each event, the minimum value of the threshold being 1. Based on observations, this threshold is set to 18 and 3 repairs on the same 100 meters long pipeline for the February and June event, respectively. This type of simulation is further referenced as a "capped" simulation. For the network level analyses, results are given in terms of mean, median, uncertainty and difference of number of repairs. For the catchment level analyses, results are given in terms of Pearson's

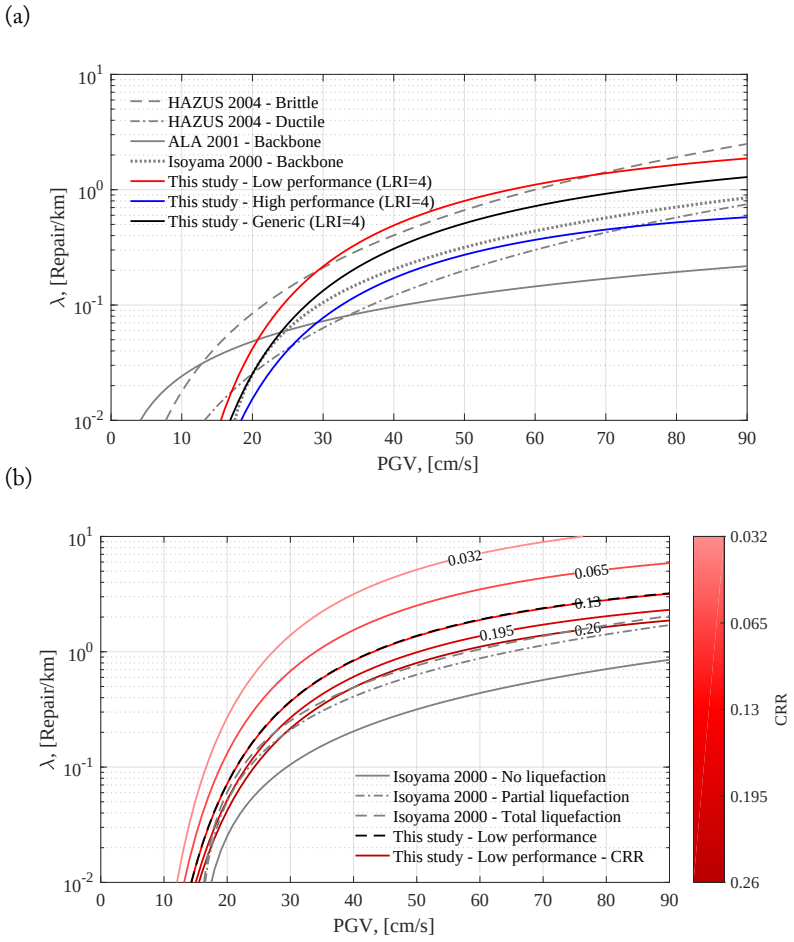

Figure 2.8: (a) Comparison between selected and proposed CRR-independent and performance grouping-dependent repair rate functions ; and (b) comparison between Isoyama et al. (2000) and the proposed CRR-dependent and brittle material repair rate function.

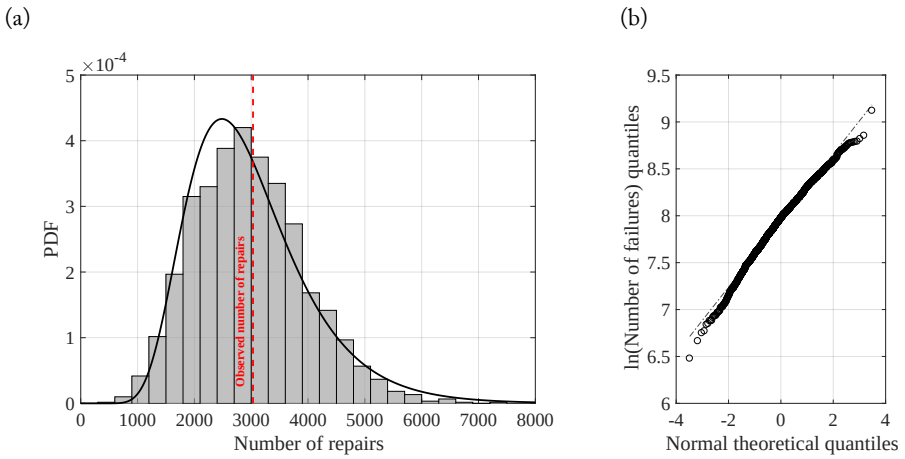

Figure 2.9: (a) Distribution of the simulated number of pipe repairs for the February earthquake ; and (b) QQ plot of the logarithmic simulated number of repairs for the February event

residuals of number of pipe repairs and graphically exposed in terms of median simulated repair rates to geospatially assess the model performance. For each analysed area (network and catchments), 2000 simulations are realized. Each MCS run consists of the following five steps:

1. Generate a spatially-correlated, multivariate random field to sample the ground motion residuals using the semi-variogram-based correlation model proposed by Jayaram & Baker (2009).
2. Compute PGV intensity at each station utilizing the simulated median and generated residuals
3. Evaluate the repair rate mean and standard deviation for each pipeline given the experienced ground motion intensity and the known characteristics of the repair rate model
4. Sample the repair rate for each pipeline
5. Simulate the number of repairs for each pipe segment.

In order to determine some of the result metrics, it is necessary to estimate the distribution of the number of pipe repairs. Figure 2.9 (a) presents the results at a network level for the 22 February 2011 event using the standard MCS scheme. The pipe repair number on the network is log-normally distributed, which is confirmed by the aspect of the logarithmic number of repairs QQ plot presented in Figure 2.9 (b). Therefore, further metrics are estimated assuming log-normally distributed number of pipe repairs. Table 2.2 presents the results for the four different network level analyses. The February simulations (standard and capped) show little difference and are relatively well-predicted. The June simulations (standard and capped) are relatively close from each other but tend to largely overpredict the number of pipe repairs. In this case, it is believed that the most vulnerable assets would have already failed during the February event, leading to a more resistant network. The maximum number of simulated repairs per pipe reduces the variance of the model for both the February and June event.

2.5.2 Pearson's residual analysis of observed vs. predicted repair rates

For all catchments and events, Pearson's residuals are computed following Equation 2.10 using the results' associated normal distribution.

$$r_{i,j}^{P} = \frac{y_{i,j} - \mu_{i,j}}{\sigma_{i,j}} \tag{2.10}$$

where $r_{i,j}^{P}$ is the Pearson's residual of catchment i for the event j, $y_{i,j}$ is the logarithmic observed number of repairs and $\mu_{i,j}$ and $\sigma_{i,j}$ are the associated mean and standard deviation of predicted number

Table 2.2: Number of pipe repair results at network level. Percentiles and deviations are expressed for the associated normal distribution of number of repairs.

Analysis	Mean	Median	Log. std dev.	Observation	Percentile	Deviation
February	2988	2895	0.337	3039	58%	$+0.14\sigma$
February (capped)	2971	2894	0.320	3039	59%	$+0.23\sigma$
June	1520	1403	0.446	732	8%	-1.40σ
June (capped)	1362	1279	0.400	732	9%	-1.34σ

of repairs. Pearson's residual analysis is a common technique to assess the statistical validity of a model by studying their dispersion and histogram shape. Figures 2.10 (a)-(d) show residuals plotted against median predicted number of repairs, catchment cumulative pipe length, estimated median PGV at the catchment centroid and logarithmic standard deviation of the PGV at the catchment centroid, respectively. Figure 2.10 (e)-(f) shows the distribution of the residuals for both events separately, whereas Figure 2.10 (g) exposes them together. Figure 2.10 (h) presents the observed number of repairs against the median predicted number of repairs. As it can be observed in the aforementioned figures, the model has a small negative bias and appears to be homoskedastic (i.e. residual value does not vary with the predicted median number of repairs). Apparently, none of the presented variables (cumulative pipe length, median PGV and its logarithmic standard deviation) tends to influence the model. In other words, no clear trend is observable while plotting Pearson's residuals against these variables. The three histograms show that the model is overdispersed (i.e. the predicted variability is smaller than the one observed in the dataset). It can be observed that the February and June residual histograms tend to balance themselves: The February one tends to be positive, whereas the June one is clearly negative. As the model is built on data from two distinct earthquakes at the same location, this can be interpreted as the between-event residuals being distributed around zero (note that more data would be required to strongly verify this assumption). Interestingly, the dispersion tends to be lower for the June event than for the February event. Figure 2.10 (h) shows that the difference between the observed and simulated median number of repairs tends to increase toward zero in the logarithmic space, but remains well distributed around the identity function for higher values.

2.5.3 Geospatial assessment of the repair rate model performance

Figure 2.11 presents the spatial distribution of the observed, simulated median and residual repair rates per considered event. The repair rate of a vast majority of catchments is well predicted for both events ($|\text{residual}| < 0.25$). It is noteworthy that, despite its smoother behaviour, the model captures the general trends relatively well. However, significant absolute errors can be noted between the observed and simulated repair rates. Great underprediction ($\text{residual} > 1$) occurs in areas that experienced extreme events such as the *Red Zone* (abandoned residential area due to infeasibility to rebuild) along the Avon River (north-eastern quadrant) due to severe lateral spreading and liquefaction (Cubrinovski et al., 2011), the Cashmere Hills (South of the city) due to landslides and rock falls and along the road to Sumner (South-East of the city) due to rockfalls and cliff collapse (Dellow et al., 2011). Great overprediction ($\text{residual} < -1$) occurs only in the Bromley area during the February earthquake. As no damage was reported following the earthquake and given that the size of these networks is slightly less than five kilometres, small absolute errors leads to large overestimates. Moderate under- and overpredictions ($0.25 < |\text{residual}| < 1$) can be explained by potential inaccuracy of the soil condition characterization, variability of the ground motion intensity, asset degradation status or different construction quality and standards that are not captured by the model.

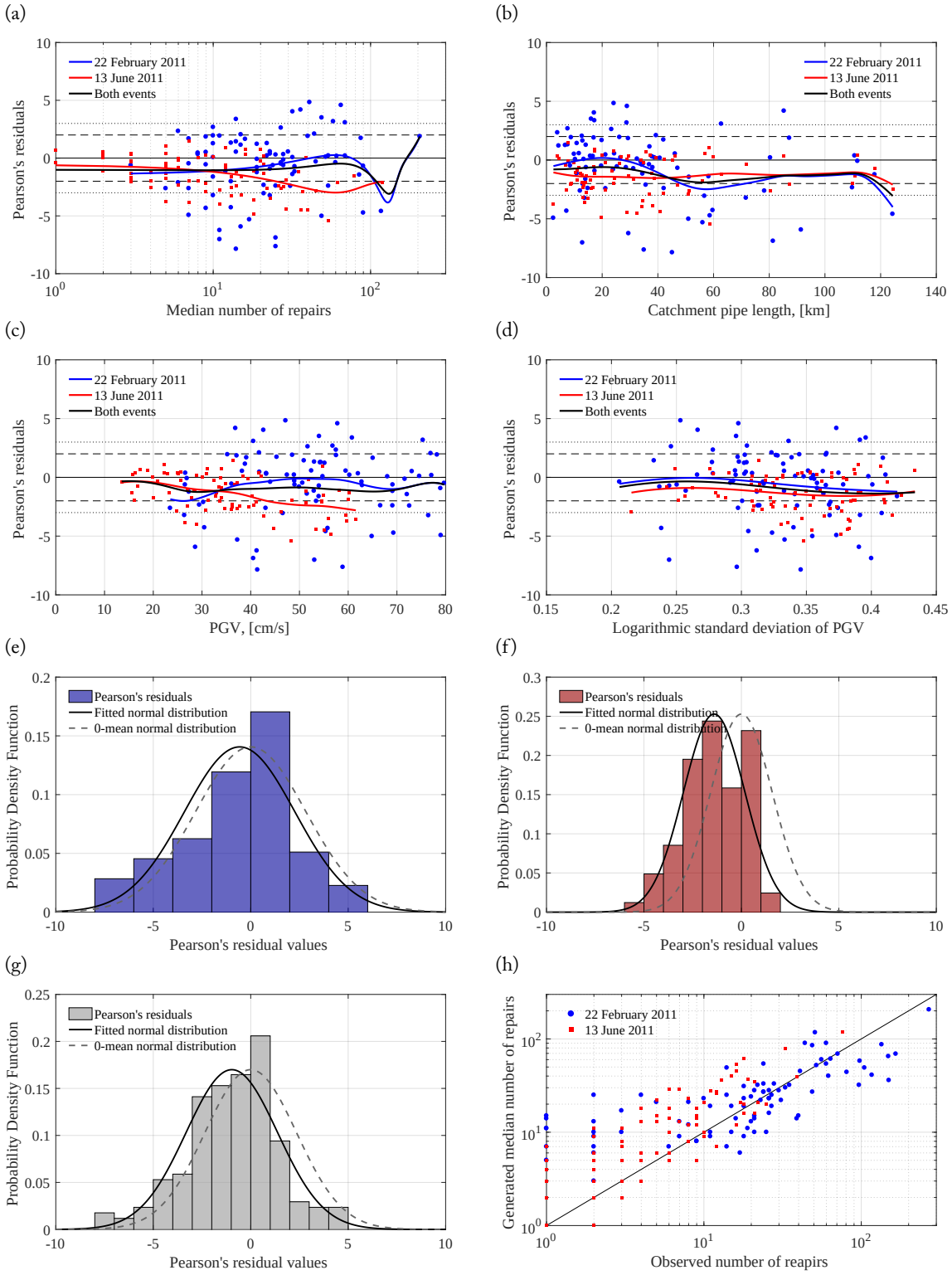

Figure 2.10: Pearson's residuals of both the 2011 February and June events against (a) median predicted repair rate ; (b) SCIRT catchment cumulative pipe length ; (c) simulated median PGV ; (d) logarithmic standard deviation of PGV ; Pearson's residual distribution for (e) the 2011 February event ; (f) the 2011 June event ; (e) both the 2011 February and June events ; and (g) observed number of repairs by median predicted number of repairs for each SCIRT catchments

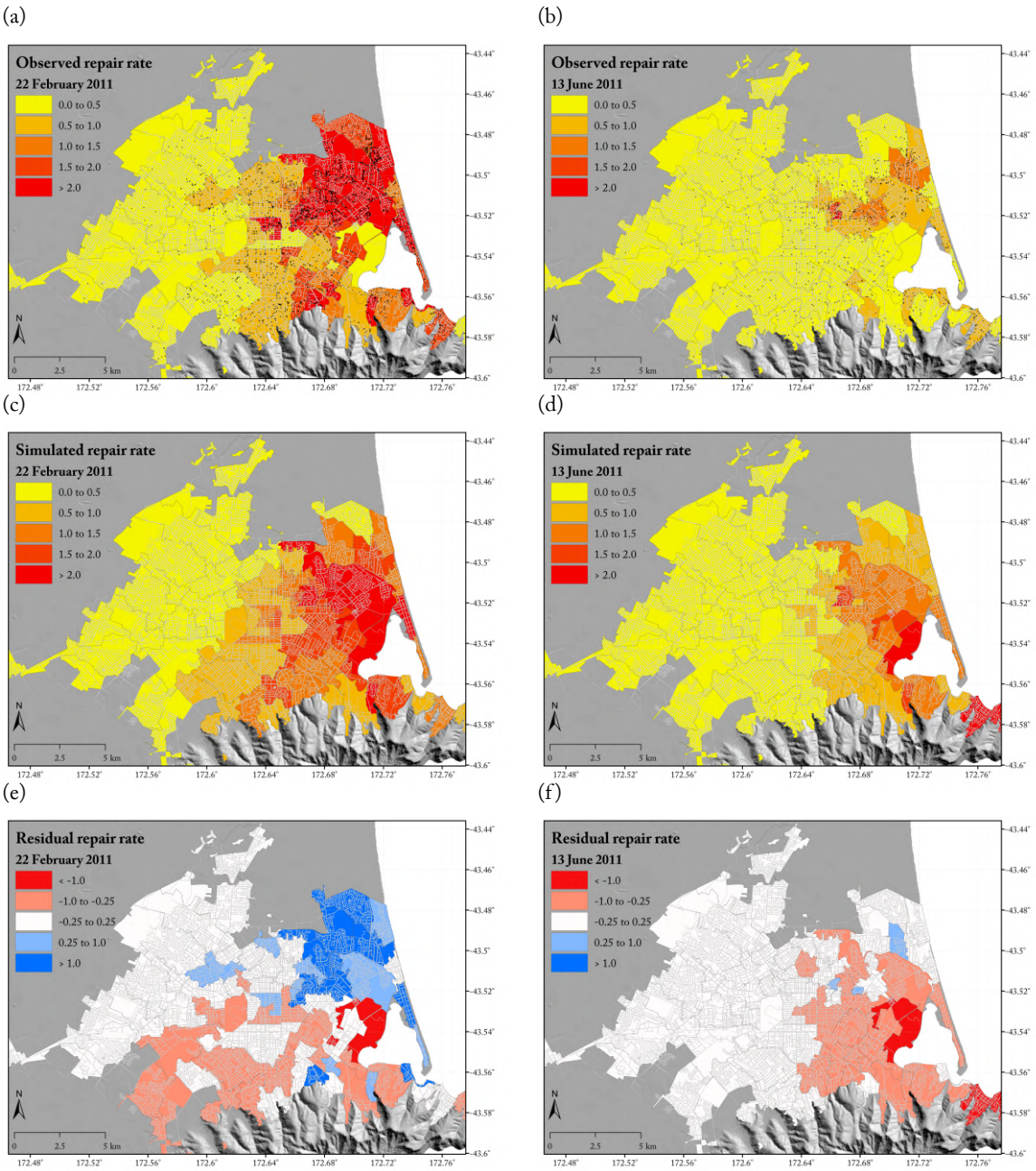

Figure 2.11: Maps of the (a)-(b) observed ; (c)-(d) simulated median ; and (e)-(f) residual repair rates for each SCIRT repair catchment. The left-hand side column gives the results for the 2011 February earthquake, whereas the right-hand side column provides them for the 2011 June earthquake.

2.6 Conclusion

This study presented a parametric, additive fragility function model for water-pressurized pipelines utilizing the data collected in Christchurch City after the 22 February and 13 June 2011 earthquakes. Among the available data, the selected parameters considered in the model are the PGV, the seismic pipe performance grouping, the pipe material and the pipe diameter, as well as the CRR to represent its liquefaction susceptibility. In order to take into account the misfit and the potentially unknown characteristics, the proposed model incorporates both the within-model and between-model uncertainties. It has been observed that soil liquefaction susceptibility significantly influences the experienced repair rate. Therefore, it is recommended that CRR-independent functions are applied only where soil characterization justifies it (i.e. where uncertainties are extremely high). For pipes in non-liquefiable soils, it is recommended that CRR-dependent functions are used with high CRR values (e.g. comparable to the value estimated for the *No observed liquefaction* zones in Christchurch). It must also be noted that, in the case of HDPE and MDPE80 pipes, the proposed results are valid for pipelines joined with a rubber gasket as thermally welded HDPE and MDPE80 pipes showed outstanding seismic performance during the studied earthquakes.

The retrospective analysis shows that the proposed model yields good estimates of the damage extent and location, when tested via MCS on the Christchurch repair catchment. However, some limitations of the model and its applicability are worth mentioning. First, the impact of extreme liquefaction and lateral spreading observed during the 22 February 2011 earthquake remains underestimated. Second, where PGV or liquefaction-induced strains are not the governing mode of pipe repairs (e.g. landslide or rockfall), the functions also underestimate damage. Furthermore, according to the June results, direct aftershock damage seems to be overestimated. Moreover, applications to other water supply networks should consider the potential changes in technology and construction quality, which often varies with the local standards and suppliers. One way to account for potential changes can be to use more primitive forms of the model, which will ultimately increase its uncertainty (e.g. seismic performance group and soil-dependent functions instead of material and soil-dependent functions). Finally, high level functions (e.g. the backbone function alone or the PGV-CRR repair rate function) remain governed by the most prevalent pipe type in their analysed data, leading to potential biases. These biases are nevertheless balanced by the explicit integration of the between-model uncertainty in the repair rate functions.

In order to reduce the influence of these limitations, additional data could be used to refine the model and reduce the data scarcity for some of the discarded functions. Moreover, if more observations from other events are gathered, these can be used to further validate the proposed model. Further efforts should also be devoted to study and compare the resistance of main against submain pipelines, as the proposed functions may not adequately represent the seismic performance in some instances. This could be achieved, for example, by combining data-derived insights with advanced physics-based modelling of pipe failure mechanisms. Finally, the developed methodology could be applied to other distributed infrastructure components such as fibre-optic cables, sewerage pipelines or underground power distribution lines, enabling a consistent assessment of the spatially-distributed infrastructure across liquefaction-prone regions.

2.7 Acknowledgements

The authors would like to acknowledge the two anonymous reviewers, whose comments significantly helped improve this study, as well as Mr Marcus Gibson, who provided precious insights on undocumented aspects of the utilized datasets. This project was supported by QuakeCoRE, a New Zealand Tertiary Education Commission-funded Centre and also the Royal Society of New Zealand Rutherford Discovery Fellowship. This is QuakeCoRE publication number 0237.

2.8 References

Borden, F., 1997. *The 1994 Northridge earthquake and the fires that followed*. Building and Fire Research Laboratory, National Institute of Standards and Technology.

Bouziou, D. and O'Rourke, T., 2015. Water Distribution System Response to the 22 February 2011 Christchurch Earthquake. In 6^{th} *International Conference on Earthquake Geotechnical Engineering*. Christchurch, New Zealand.

Bouziou, D. and O'Rourke, T., 2017. Response of the Christchurch water distribution system to the 22 February 2011 earthquake. *Soil Dynamics and Earthquake Engineering* **97**, 14–24.

Bowen, H., Jacka, M., van Ballegooy, S., Sinclair, T., and Cowan, H., 2012. Lateral spreading in the Canterbury earthquakes–Observations and empirical prediction methods. In *Proceedings, 15th World Conference on Earthquake Engineering*.

Bradley, B., 2013. A New Zealand-specific pseudospectral acceleration ground-motion prediction equation for active shallow crustal earthquakes based on foreign models. *Bulletin of the Seismological Society of America* **103**, 1801–1822.

Bradley, B., 2014. Site-specific and spatially-distributed ground-motion intensity estimation in the 2010–2011 Canterbury earthquakes. *Soil Dynamics and Earthquake Engineering* **61**, 83–91.

Bradley, B. and Cubrinovski, M., 2011. Near-source strong ground motions observed in the 22 February 2011 Christchurch earthquake. *Seismological Research Letters* **82**, 853–865.

Brookshire, D., Chang, S., Cochrane, H., Olson, R. A., Rose, A., and Steenson, J., 1997. Direct and indirect economic losses from earthquake damage. *Earthquake Spectra* **13**, 683–701.

Chang, S., Svekla, W., and Shinozuka, M., 2002. Linking infrastructure and urban economy: simulation of water-disruption impacts in earthquakes. *Environment and Planning B: Planning and Design* **29**, 281–301.

Chang, S., Taylor, J., Elwood, K., Seville, E., Brunsdon, D., and Gartner, M., 2014. Urban disaster recovery in Christchurch: the central business district cordon and other critical decisions. *Earthquake Spectra* **30**, 513–532.

Christchurch City Council, 2014. Christchurch City Council Infrastructure Design Standard - Part 7: Water supply.

Cousins, J. and McVerry, G., 2010. Overview of strong motion data from the Darfield earthquake. *Bulletin of the New Zealand Society for Earthquake Engineering* **43**, 222–227.

Cubrinovski, M., Bradley, B., Wotherspoon, L., Green, R., Bray, J., Wood, C., Pender, M., Allen, J., Bradshaw, A., Rix, G. et al., 2011. Geotechnical aspects of the 22 February 2011 Christchurch earthquake. *Bulletin of the New Zealand Society for Earthquake Engineering* **44**, 205–226.

Cubrinovski, M., Hughes, M., Bradley, B., Noonan, J., Hopkins, R., McNeill, S., and English, G., 2014. *Performance of horizontal infrastructure in Christchurch city through the 2010-2011 Canterbury earthquake sequence. Tech. rep.*, University of Canterbury. Civil and Natural Resources Engineering, Christchurch, New Zealand.

Dahlhamer, J., Tierney, K., and Webb, G., 1999. *Predicting business financial losses in the 1989 Loma Prieta and 1994 Northridge Earthquakes: Implications for loss estimation research. Tech. rep.*, Disaster Research Center, University of Delaware, Newark, DE.

Davis, C., 2014. Water system service categories, post-earthquake interaction, and restoration strategies. *Earthquake Spectra* **30**, 1487–1509.

Dellow, G., Yetton, M., Massey, C., Archibald, G., Barrell, D., Bell, D., Bruce, Z., Campbell, A., Davies, T., De Pascale, G. et al., 2011. Landslides caused by the 22 February 2011 Christchurch earthquake and management of landslide risk in the immediate aftermath. *Bulletin of the New Zealand Society for Earthquake Engineering* **44**, 227–238.

Dizhur, D., Ingham, J., Moon, L., Griffith, M., Schultz, A., Senaldi, I., Magenes, G., Dickie, J., Lissel, S., Centeno, J. et al., 2011. Performance of masonry buildings and churches in the 22 February 2011 Christchurch earthquake. *Bulletin of the New Zealand Society for Earthquake Engineering* **44**, 279–296.

Edkins, D., Orense, R., Henry, R., and Ingham, J., 2015. Signature failure modes of pipelines constructed of different materials when subjected to earthquakes. *Journal of Pipeline Systems Engineering and Practice* **7**, 04015014.

Eidinger, J., 1998. Water-Distribution System. In *The Loma Prieta, California, Earthquake of October 17, 1989—Lifelines*, pp. A63–A78. US Geological Survey.

Eidinger, J., Avila, E., Ballantyne, D., Cheng, L., der Kiureghian, A., Maison, B., O'Rourke, T., and Power, M., 2001. *Seismic Fragility Formulations for Water Systems: Part 1: Guidelines*. *Tech. rep.*, American Lifelines Alliance.

Eidinger, J. and Tang, A., 2012. *Christchurch, New Zealand Earthquake Sequence of Mw 7.1 September 04, 2010 Mw 6.3 February 22, 2011 Mw 6.0 June 13, 2011: Lifeline Performance*. *Tech. rep.*, Technical Council on Lifeline Earthquake Engineering, Reston, VA.

Federal Emergency Management Agency, 2003. *HAZUS-MH MR4 Technical Manual*. *Tech. rep.*, National Institute of Building Sciences, Washington DC.

Forsyth, P., Barrell, D., and Jongens, R., 2008. Geology of the Christchurch Area. Institute of Geological and Nuclear Sciences 1: 250,000 geological map 16, 1 sheet.

Friedman, J., Hastie, T., and Tibshirani, R., 2008. *The elements of statistical learning*, vol. 1. Springer series in statistics Springer, Berlin.

Giovinazzi, S., Wilson, T., Davis, C., Bristow, D., Gallagher, M., Schofield, A., Villemure, M., Eidinger, J., and Tang, A., 2011. Lifelines performance and management following the 22 February 2011 Christchurch earthquake, New Zealand: highlights of resilience. *Bulletin of the New Zealand Society for Earthquake Engineering* **44**, 402–417.

Gledhill, K., Fry, B., Ristau, J., Holden, C., and Reyners, M., 2010. The Darfield (Canterbury) earthquake of September 2010: preliminary seismological report. *Bulletin of the New Zealand Society for Earthquake Engineering* **43**, 215–221.

Isoyama, R., Ishida, E., Yune, K., and Shirozu, T., 2000. Seismic damage estimation procedure for water supply pipelines. In *12th World Conference Of Earthquake Engineering, New Zealand*.

Iwasaki, T., Arakawa, T., and Tokida, K.-I., 1984. Simplified procedures for assessing soil liquefaction during earthquakes. *International Journal of Soil Dynamics and Earthquake Engineering* **3**, 49–58.

Jayaram, N. and Baker, J., 2009. Correlation model for spatially distributed ground-motion intensities. *Earthquake Engineering & Structural Dynamics* **38**, 1687–1708.

O'Rourke, M. and Ayala, G., 1993. Pipeline damage due to wave propagation. *Journal of Geotechnical Engineering* **119**, 1490–1498.

O'Rourke, M. and Deyoe, E., 2004. Seismic damage to segmented buried pipe. *Earthquake Spectra* **20**, 1167–1183.

O'Rourke, T., Jeon, S.-S., Toprak, S., Cubrinovski, M., Hughes, M., van Ballegooy, S., and Bouziou, D., 2014. Earthquake response of underground pipeline networks in Christchurch, NZ. *Earthquake Spectra* **30**, 183–204.

Palermo, A., Wotherspoon, L., Wood, J., Chapman, H., Scott, A., Hogan, L., Kivell, A., Camnasio, E., Yashinsky, M., Bruneau, M. et al., 2011. Lessons learnt from 2011 Christchurch earthquakes: analysis and assessment of bridges. *Bulletin of the New Zealand Society for Earthquake Engineering* **44**, 319–333.

Quigley, M., van Dissen, R., Villamor, P., Litchfield, N., Barrell, D., Furlong, K., Stahl, T., Duffy, B., Bilderback, E., Noble, D., Townsend, D., Begg, J., Jongens, R., Ries, W., Claridge, J., Klahn, A., Mackenzie, H., Smith, A., Hornblow, S., Nicol, R., Cox, S., Langridge, R., and Pedley, K., 2010. Greendale Fault during the Mw 7.1 Darfield (Canterbury) earthquake, New Zealand: initial findings. *Bulletin of the New Zealand Society for Earthquake Engineering* **43**, 236–242.

Rose, A., Benavides, J., Chang, S., Szczesniak, P., and Lim, D., 1997. The regional economic impact of an earthquake: Direct and indirect effects of electricity lifeline disruptions. *Journal of Regional Science* **37**, 437–458.

Stevenson, J., Becker, J., Cradock-Henry, N., Johal, S., Johnston, D., Orchiston, C., and Seville, E., 2017. Economic and social reconnaissance: Kaikōura Earthquake 2016. *Bulletin of the New Zealand Society for Earthquake Engineering* **50**, 346–355.

Stevenson, J., Vargo, J., Seville, E., Kachali, H., McNaughton, A., and Powell, F., 2012. *The Recovery of Canterbury's Organisations: A comparative analysis of the 4 September 2010, 22 February and 13 June 2011 Earthquake*. *Tech. rep.*, University of Canterbury. Civil and Natural Resources Engineering, Christchurch, New Zealand.

Tierney, K., 1997. Business impacts of the Northridge earthquake. *Journal of Contingencies and Crisis Management* **5**, 87–97.

Toprak, S., Nacaroglu, E., Koc, A., O'Rourke, T., Hamada, M., Cubrinovski, M., and van Ballegooy, S., 2018. Comparison of horizontal ground displacements in Avonside area, Christchurch from air photo, LiDAR and satellite measurements regarding pipeline damage assessment. *Bulletin of Earthquake Engineering* pp. 1–18.

Toprak, S., Nacaroglu, E., Koc, A., van Ballegooy, S., Jacka, M., Torvelainen, E., and O'Rourke, T., 2017. Pipeline damage predictions in liquefaction zones using LSN. In *16th World Conference on Earthquake Engineering*. Santiago, Chile.

van Ballegooy, S., Cox, S., Thurlow, C., Rutter, H., Reynolds, T., Harrington, G., Fraser, J., and Smith, T., 2014. *Median water table elevation in Christchurch and surrounding area after the 4 September 2010 Darfield Earthquake: Version 2*. *Tech. rep.*, GNS Science Report, Lower Hutt, New Zealand.

van Ballegooy, S., Malan, P., Lacrosse, V., Jacka, M., Cubrinovski, M., Bray, J., O'Rourke, T., Crawford, S., and Cowan, H., 2014. Assessment of liquefaction-induced land damage for residential Christchurch. *Earthquake Spectra* **30**, 31–55.

van Ballegooy, S., Wentz, F., and Boulanger, R., 2015. Evaluation of CPT-based liquefaction procedures at regional scale. *Soil Dynamics and Earthquake Engineering* **79**, 315–334.

Wood, C., Cox, B. R., Wotherspoon, L., and Green, R., 2011. Dynamic site characterization of Christchurch strong motion stations. *Bulletin of the New Zealand Society for Earthquake Engineering* **44**, 195–204.

Youd, T., Idriss, I., CC, A., RD, A., Castro, I., Christian, G., JT, D., Finn, R., Hynes, L., Ishihara, M., Koester, K., Liao, J., Martin, W., GR, M., JK, M., Power, Y., Robertson, M., and Seed, P., 2001. Liquefaction resistance of soils: summary report from the 1996 NCEER and 1998 NCEER/NSF workshops on evaluation of liquefaction resistance of soils. *Journal of geotechnical and geoenvironmental engineering* **127**, 297–313.

2.9 Complementary material

2.9.1 Fragility function dataset maps and tables

Maps and tables of the Christchurch water supply network

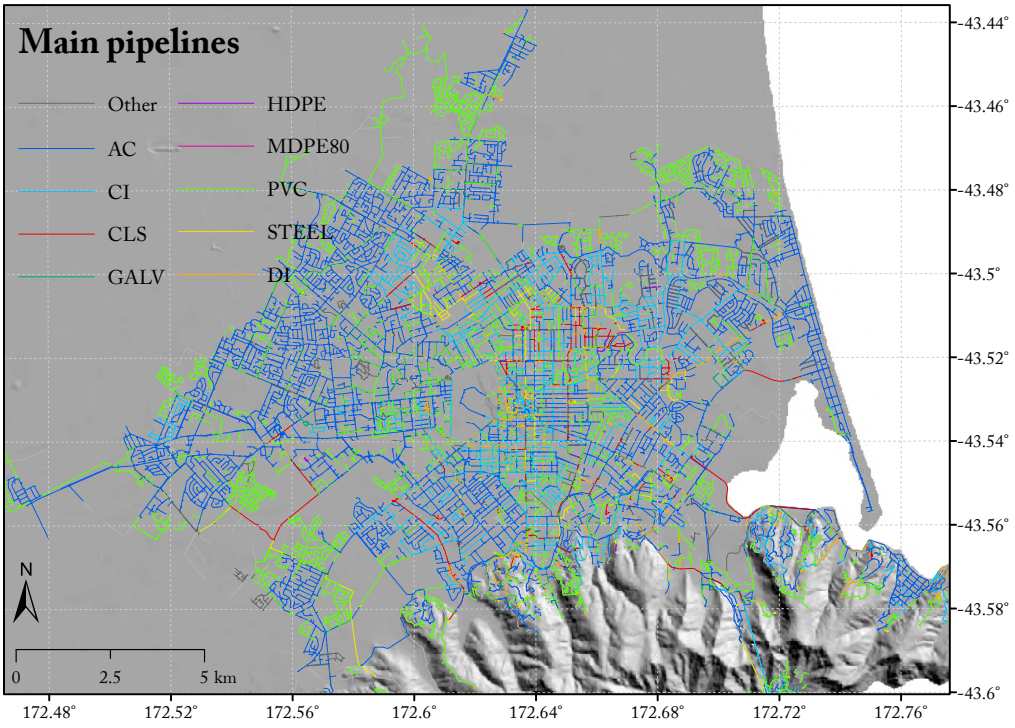

Figure 2.12: Map of the Christchurch water supply network showing the Trunk main and main pipelines. Colours indicate construction materials with the following acronyms: AC: asbestos cement, CI: cast iron, CLS: concrete-lined steel, DI: ductile iron, GALV: galvanized iron, HDPE: high-density polyethylene, MPDE80: medium-density polyethylene 80, PVC: polyvinyl chloride, STEEL: steel

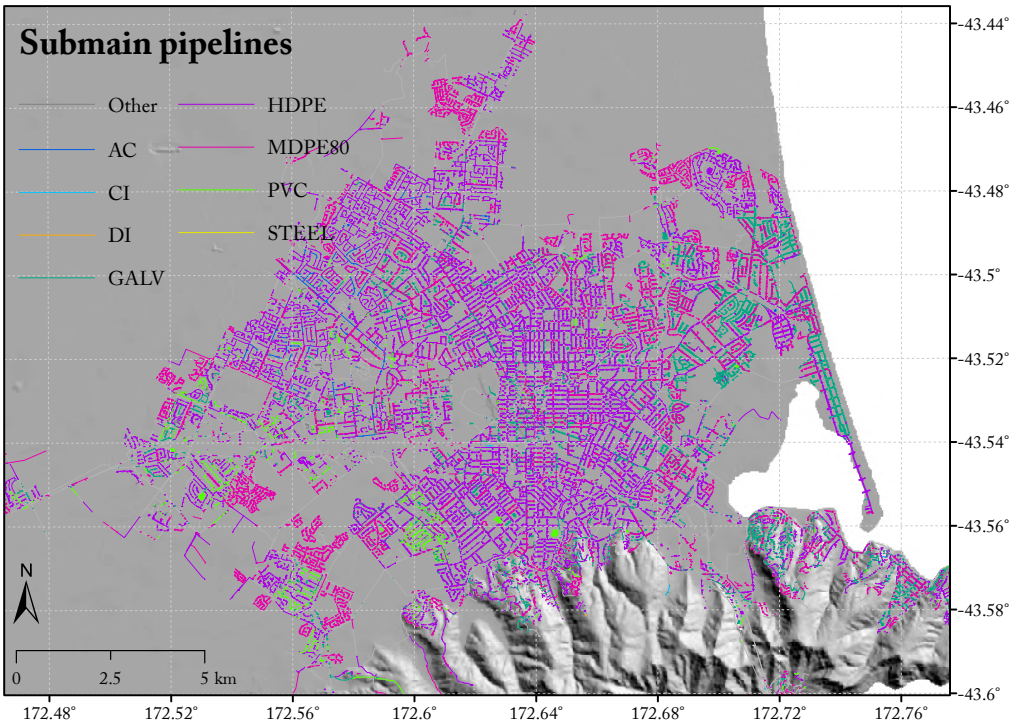

Figure 2.13: Map of the Christchurch water supply network showing the submain and crossover pipelines. Colours indicate construction materials with the following acronyms: AC: asbestos cement, CI: cast iron, CLS: concrete-lined steel, DI: ductile iron, GALV: galvanized iron, HDPE: high-density polyethylene, MPDE80: medium-density polyethylene 80, PVC: polyvinyl chloride, STEEL: steel

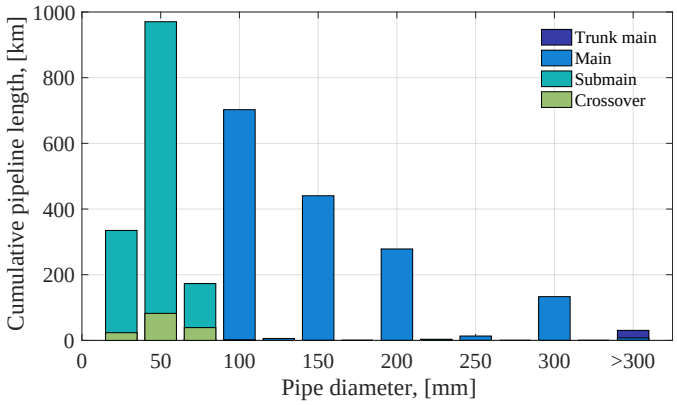

Figure 2.14: Distribution of pipe diameters in the Christchurch city network as a function of their typology

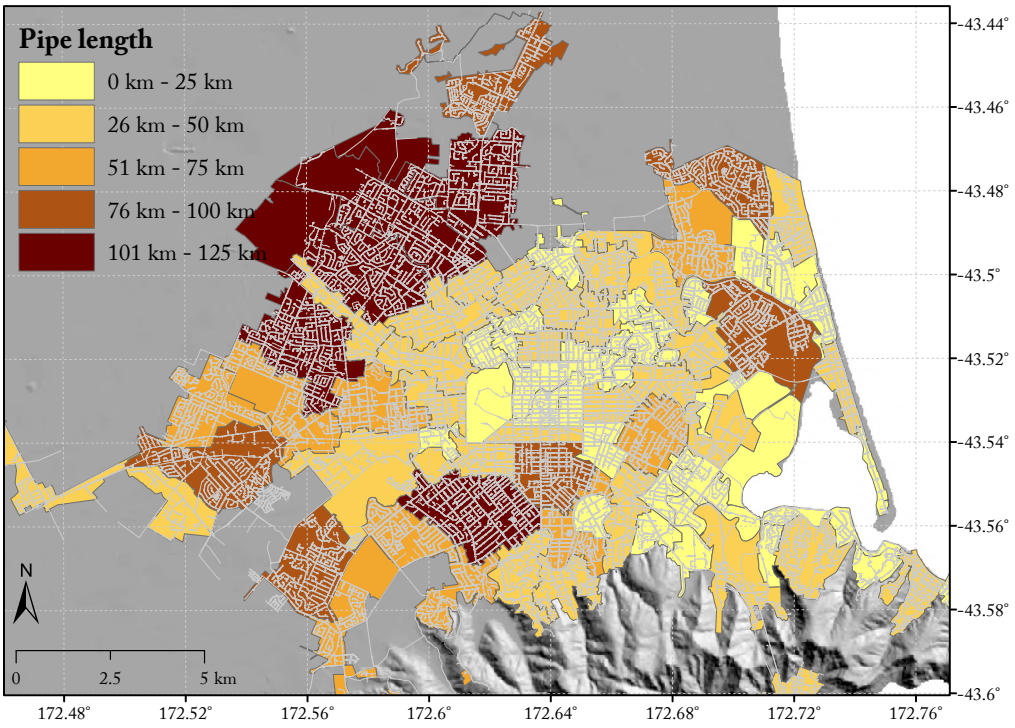

Figure 2.15: SCIRT repair catchment. Colours indicate the cumulative pipe length per SCIRT repair catchment.

Table 2.3: Pipe attributes in the Christchurch city water supply network dataset

Pipe attributes	Possible values
Location of the repair	Collection of point segments [Lat./Long.]
Pipe material	[AC; CI; CLS; DI; GALV; HDPE; MDPE80; PVC; STEEL; Other]
Pipe diameter	Millimeters
Pipe functionality	[Trunk main; Main; Submain; Crossover]
Pipe functional status	[In service; Decommissioned; Abandoned; Planed; Removed]
Year of construction	[YYYY]
Trench type	[Pre-1984, locally excavated backfill; Pre-1984, hill soils; Pre-1984, imported backfill; Pre-1984, estuary/reclaimed land; 1984 to 2000, AP40 backfill; Post-2005, AP20 backfill]
Date of decommission (if applicable)	[DDMMYYYY]
Unique key identifier given by the CCC	[Ws000000]

Table of the reported pipe repairs following the CES events

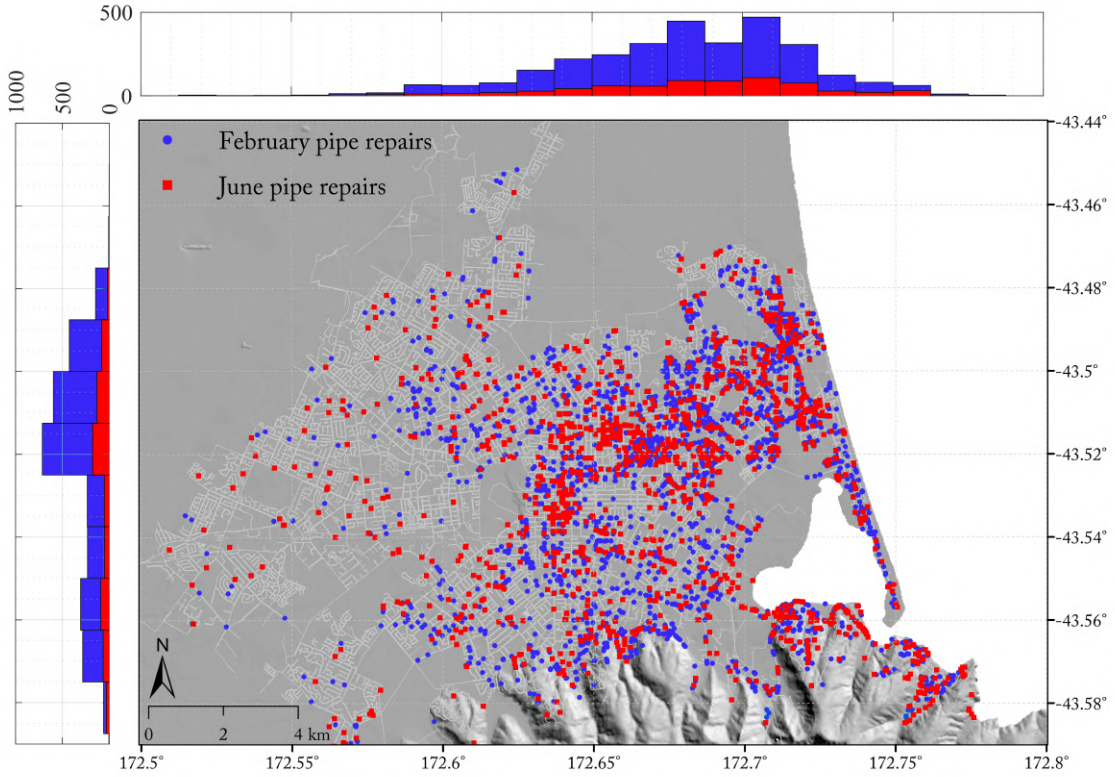

Figure 2.16: Map of the Christchurch water supply network and the pipe repairs induced by the 22 February and 13 June 2011 earthquakes. The histograms provide the number of reported pipe repairs per event as a function of the latitude and longitude.

Table 2.4: repair attributes contained in the dataset

repair attributes	Possible values
Unique key identifier of the pipe given by the CCC	[Ws000000]
Location of the repair	[Lat./Long.]
Date of repair detection	[DDMMYYYY]
Priority of repair	[Urgent 1 Day; 1 Day; 3 Days; 10 Days]
Type of repair	[Unknown; Fitting; Pipe]
Unique key identifier given by the SCIRT	[000000]

Maps of the estimated PGV intensity in Christchurch during the considered CES events

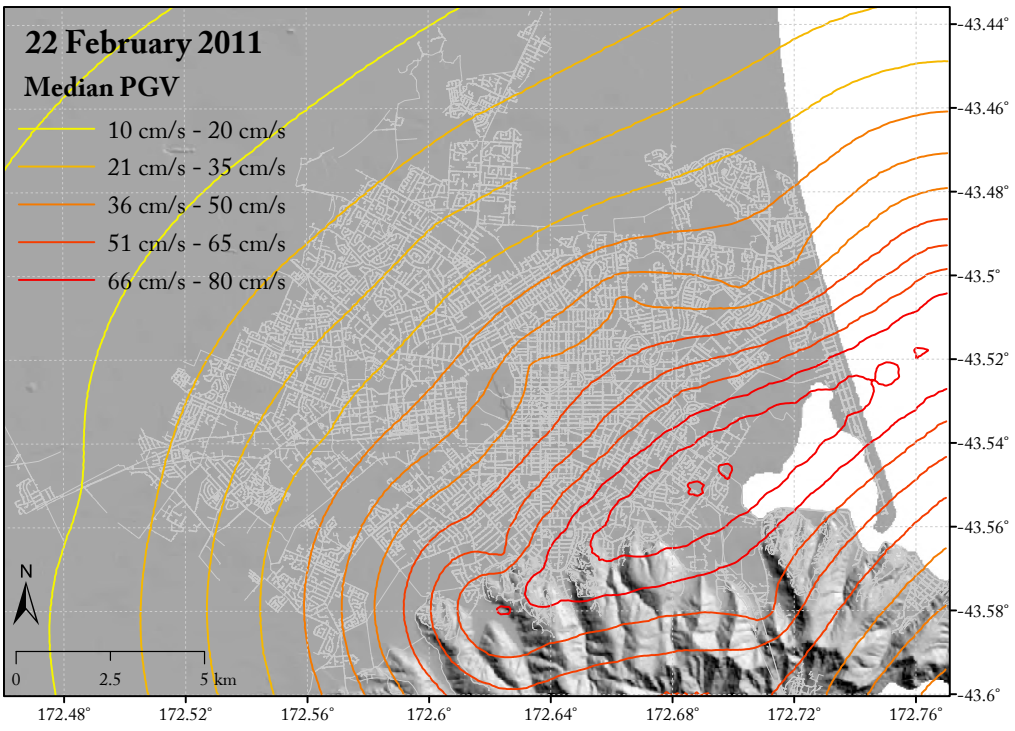

Figure 2.17: Geometric mean PGV of the 2011 February earthquake estimated by Bradley (2014)

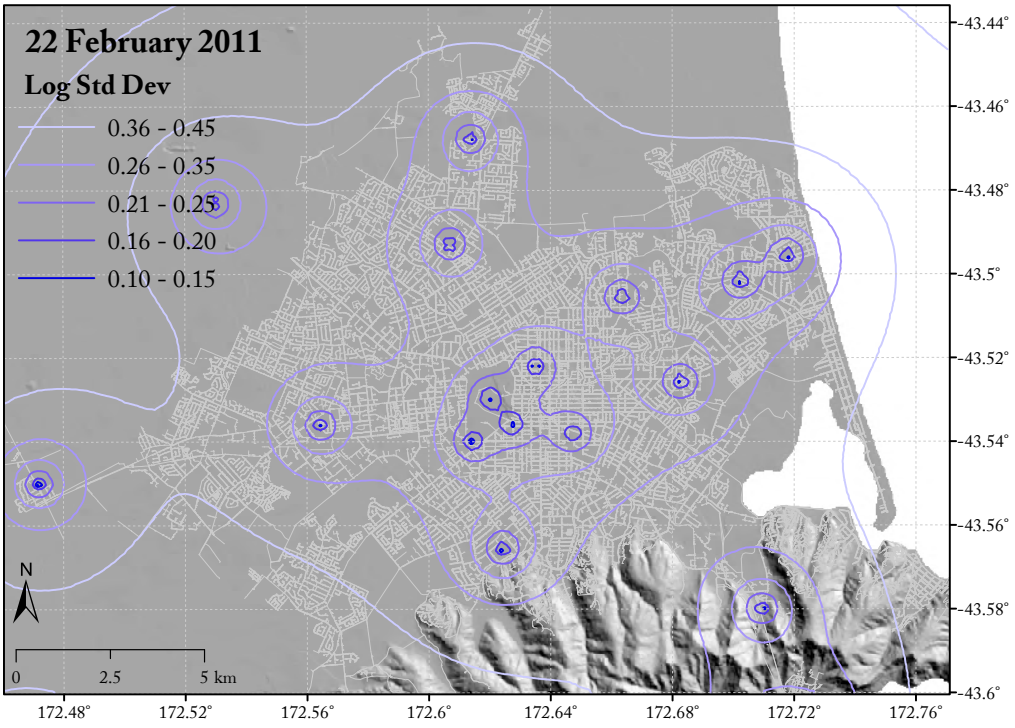

Figure 2.18: Logarithmic standard deviation PGV of the 2011 February earthquake estimated by Bradley (2014)

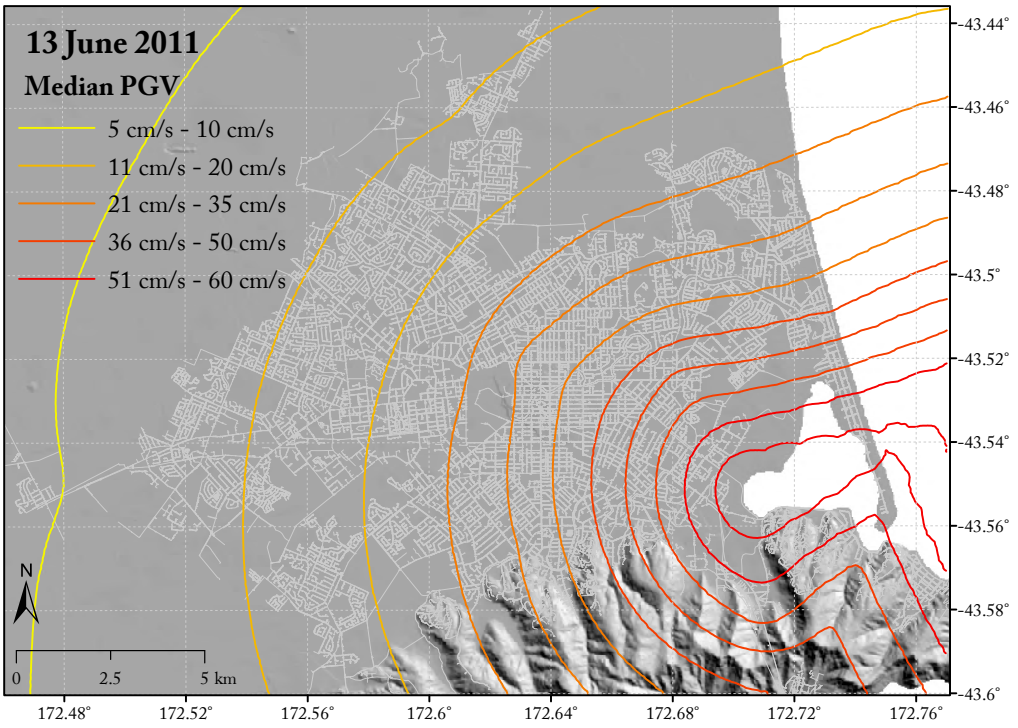

Figure 2.19: Geometric mean PGV of the 2011 June earthquake estimated by Bradley (2014)

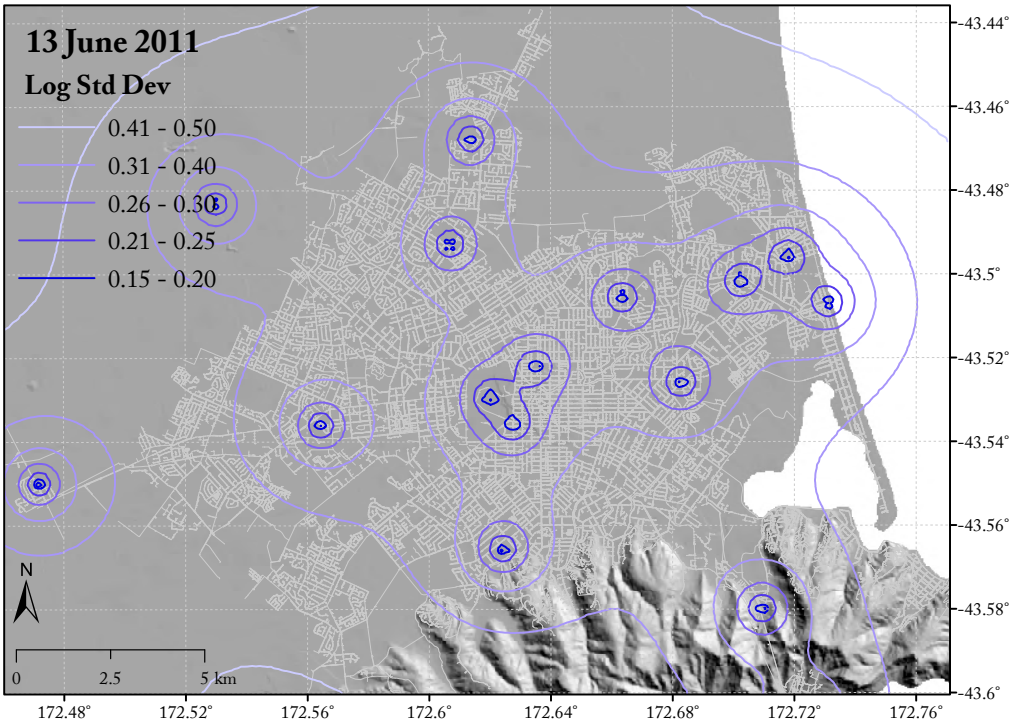

Figure 2.20: Logarithmic standard deviation PGV of the 2011 June earthquake estimated by Bradley (2014)

Maps and tables of the Christchurch soil liquefaction susceptibility

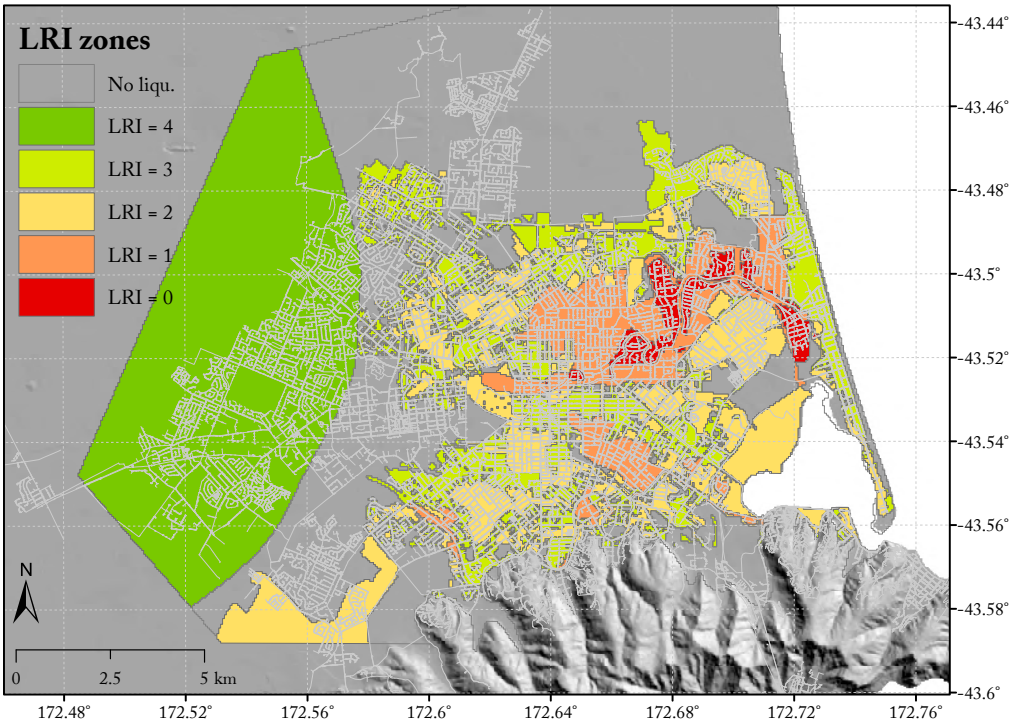

Figure 2.21: Christchurch LRI map estimated by Cubrinovski et al. (2014)

Table 2.5: LRI characteristics, defined by Cubrinovski et al. (2014, Table 2)

LRI [-]	Equivalent CRR [-]	Ground settlement [mm]	Lateral displacement [mm]	CRR at watertable depth [-]
0	<0.065	>500	>400	-
1	0.065 - 0.11	250 - 500	200 - 400	0.065
2	0.11 - 0.16	50 - 250	40 - 200	0.13
3	0.16 - 0.23	20 - 50	20 - 40	0.195
4	>0.23	<20	<20	0.26

2.9.2 Repair rate function development details

This section provides the details of the repair rate development. First, the K-fold cross-validation used to determine the best functional form of the backbone function f_0 is explained. Then, the fitting process of repair rate is detailed, and finally, the formal derivation of physics-based constraints are given.

K-fold cross-validation method used in the development of the pipeline repair rate functions

In order to minimize the model error, multiple functional forms are tested using the K-fold cross-validation method. This section briefly reviews the concept of the K-fold cross-validation and provides the details of the implementation of this method in the context of repair rate function development for spatially-spread objects. As detailed by Friedman *et al.* (2008, pp. 240-249), the K-fold cross-validation is a common method used to evaluate the performance of predictive models. The standard procedure for a K-fold cross-validation can be decomposed into four steps.

1. First, the potential functional forms $f(x)$ are carefully selected based on the observable trend in the data and indexed with the tuning parameter α.

2. In a second step, the dataset is subdivided into K subsets of approximately equal size. Classically, K is equal to five or ten.

3. Then, each selected functional form is evaluated using the subsequent procedure:

   (a) For each created subset $i \in [1, ..., K]$, the model is first trained with the data from all subsets except the i^{th} one.

   (b) The subset i is then utilized to estimate the error between the data y and the trained function $\hat{f}(x)$ using an appropriate loss function $L\left(y, \hat{f}(x)\right)$. Commonly adopted loss functions are the squared error or the absolute error functions presented in Equation 2.11.

$$L\left(y, \hat{f}(x)\right) = \begin{cases} \left(y - \hat{f}(x)\right)^2 \\ |y - \hat{f}(x)| \end{cases} \tag{2.11}$$

   (c) Finally, once all subsets have been used for validation, the average error of the model is estimated. Equation 2.12 given by Friedman *et al.* (2008, p. 242) formalizes the evaluation of a functional form $f(x)$ using K-Fold cross-validation.

$$CV(\hat{f}, \alpha) = \frac{1}{N} \sum_{i=1}^{N} L\left(y_i, \hat{f}^{-\kappa(i)}(x_i, \alpha)\right) \tag{2.12}$$

   where $\hat{f}$ is the evaluated functional form, α the tuning parameter indexing the evaluated functional forms $\hat{f}$, N the number of folders, $L(y, \hat{f}(x))$ the loss function measuring errors between the data y and $\hat{f}(x)$, y_i the target data from subset i, $\hat{f}^{-\kappa(i)}(x_i, \alpha)$ the evaluated functional form f with the i^{th} subset removed.

4. The functional form $f(x, \hat{\alpha})$, of which $\hat{\alpha}$ minimizes $CV(\hat{f}, \alpha)$, is picked to be trained with the entire dataset.

In the development of repair rates for spatially-spread objects, like pipelines, this procedure remains identical. However, because the sampling unit is the length of the analysed objects and not the objects themselves, the construction of the subsets is realized so that each of them has approximately the same pipe length rather than number of objects.

Details of the repair rate fitting process

The repair rate functions are derived following the subsequent five steps. First, the subset of interest is isolated from the pipe segment K-fold subset of interest corresponding to the analysed characteristics $\underline{h_i}$ (e.g. GALV pipelines with diameter between 1 and 150 mm experiencing a PGV between 40 cm/s and 50 cm/s). Second, the observed repair rates are computed for the subset of interest using Equation 2.13.

$$\lambda_{\underline{h}} = \frac{N_{\underline{h}}}{L_{\underline{h}}} \tag{2.13}$$

where $\underline{h}$ is the vector of analysed pipe and soil characteristics at a given PGV, $N_{\underline{h}}$ is the number of pipe repairs in the dataset corresponding to the parameters $\underline{h}$, and $L_{\underline{h}}$ is the total pipe length in the dataset corresponding the parameters $\underline{h}$. To ensure that the computed values are statistically significant (i.e. that the pipe length on which repairs are observed is sufficiently long), the screening criteria developed

by O'Rourke et al. (2014) is applied to each computed repair rate point λ. This criteria assumes a Poisson distribution repair occurrence as given in Equation 2.14.

$$L_{\underline{h}} \geq \frac{\left[\phi^{-1}(\beta_c)\right]^2}{\alpha^2 \cdot \lambda_{\underline{h}}} \tag{2.14}$$

where $\phi^{-1}()$ denotes the inverse probability density function of the standard normal distribution, β_c the confidence interval and α the percentage of observed number of repairs. The recommended values of $\beta_c = 90\%$ and $\alpha = 50\%$ (O'Rourke et al., 2014) are adopted in this study. Then, the pipe repair residuals between the fitted functions utilising $n-1$ parameters $\lambda_{fit,n-1}$ and observation depending on n parameters $\lambda_{obs,n}$ are computed. If the analysed function is not the backbone function f_0 (i.e. the number of model parameter n is zero), the residuals Δ_λ between the computed logarithmic repair rates and the ones from the function sharing the same $n-1$ characteristics are computed as presented in equation 2.15.

$$\Delta_\lambda = \ln\left(\lambda_{obs,n}\right) - \ln\left(\lambda_{fit,n-1}\right) \tag{2.15}$$

The backbone function f_0 and the correction terms C_i are evaluated by fitting the computed residuals Δ_λ.

Physics-based constraints applied to the repair rate fitting process

The CRR-dependent physics-based constraint discussed in Section 2.3 can be written as proposed in Equation 2.16.

$$\frac{\partial C_{Soil}(CRR)}{\partial CRR} \leq 0 \tag{2.16}$$

where $C_{Soil}(CRR)$ is the correction term for the soil depending on the CRR. The condition ensuring that the repair rates remain monotonously increasing with PGV can be written as proposed by Equation 2.17.

$$\frac{\partial\left[\ln(\lambda)\right]}{\partial PGV} = \frac{\partial\left[f_0(PGV) + \sum_{i=1}^{n-1} C_i(\underline{h_i}) + C_n(\underline{h_n})\right]}{\partial PGV} \geq 0 \tag{2.17}$$

where $C_i(\underline{h_i})$ is a known correction term i depending on $\underline{h_i}$ and $C_n(\underline{h_n})$ is the fitted correction term n. Hence, the newly fitted correction term C_n can be constrained as formulated in Equation 2.18.

$$\frac{\partial C_n(\underline{h_n})}{\partial PGV} \geq -\frac{\partial\left[f_0(PGV) + \sum_{i=1}^{n-1} C_i(\underline{h_i})\right]}{\partial PGV} \tag{2.18}$$

2.9.3 Repair rate functions for buried pipelines in the Christchurch Port Hills area

Introduction

The southern part of Christchurch is built on hills, which are referred as the Christchurch Port Hills (CPH). These hills are part of the Lyttleton Volcanic Group and are mainly composed of (1) '*basaltic to trachytic lava flows interbedded with breccia and tuff (Mvl)*', and (2) '*yellow-brown windblown silt on Banks Peninsula greater than 3m thick and commonly in multiple layers (mQe)*' (Forsyth *et al.*, 2008). During the 22 February and 13 June 2011 earthquakes, the network assets located in the CPH areas were subjected to ground repairs governed by landslides and rockfalls (Dellow et al., 2011). Hence CRR-dependent repair rate functions are not appropriate to assess the vulnerability of these assets. Therefore, in order to exploit the full potential of the data gathered during the restoration of the Christchurch water supply network following the CES and coherently assess its future losses, repair rate functions for pipelines located in the CPH areas are proposed. They are then used in the retrospective analysis presented in Section 2.5.

Christchurch Port Hills dataset

Water supply network attributes The considered network is a subset of the larger database presented in Section 2.2. Pipelines in this subset are selected given their altitude (above 15 meters) and location (in or near the CPH areas). The retained subset elements possess the same attributes as the other elements of the complete dataset (see Table 2.3). The CPH network is 192.3 km long, out of which 93.1 km (48.43%) are trunk main or main pipelines and 99.2 km (51.57%) are submain or crossover pipelines. It is mainly composed of AC, PVC and HDPE pipelines, corresponding to 38.27 km (19.9%), 35.93 km (18.7%) and 34.69 km (18.0%), respectively. Large portions of the network are also made of GALV and MDPE80 pipelines, which correspond to 24.84 km (12.9%) and 23.72 km (12.3%), respectively. The use of other materials such as CI (17.05 km, 8.9%), DI (6.07 km, 3.1%), Steel (4.47 km, 2.3%) and CLS (1.82 km, <1.0%) remains marginal. Note that 5.68 km (2.9%) of the network is made of non-classified material. Figure 2.22 presents both the trunk - main pipeline and the submain - crossover pipeline networks, on which the different colors indicate the construction material of the pipelines.

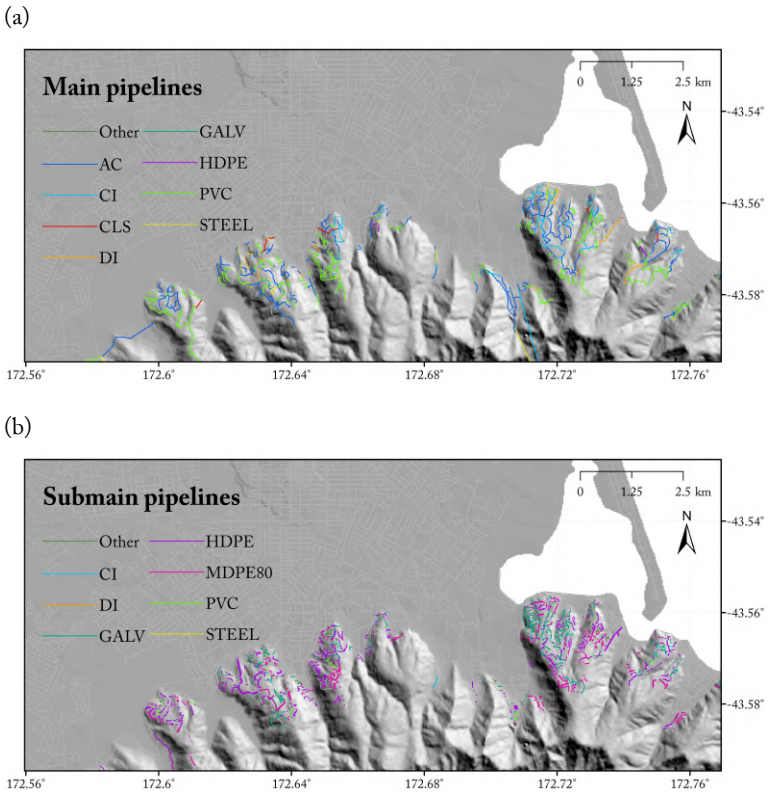

Figure 2.22: Maps of the Christchurch Port Hills water supply network. (a) trunk main and main pipe network ; and (b) submain and crossover pipe network. Colours indicate construction materials with the following acronyms: AC: asbestos cement, CI: cast iron, CLS: concrete-lined steel, DI: ductile iron, GALV: galvanized iron, HDPE: high-density polyethylene, MPDE80: medium-density polyethylene 80, PVC: polyvinyl chloride, STEEL: steel

Reported pipe repairs following the Canterbury earthquake sequence events Similarly to the CPH network dataset considered, the repair dataset is also a subset of the complete dataset used for the development of the fragility functions for pipelines in liquefiable soils. The reported number of repairs for the 22 February and 13 June 2011 earthquakes is 191 and 78, respectively. Figure 2.23 shows the reported pipe repairs for each considered event.

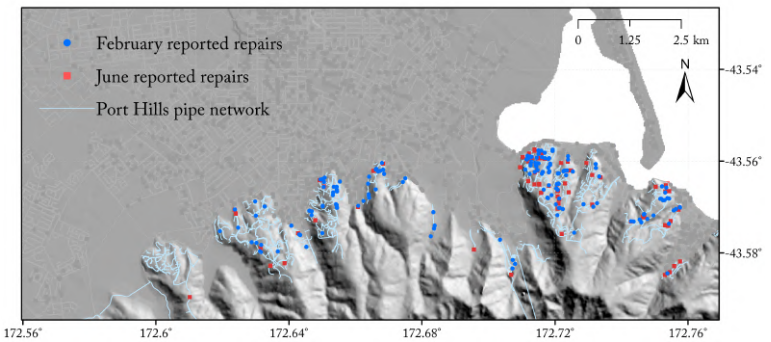

Figure 2.23: Map of the Christchurch Port Hills water supply network and the pipe repairs induced by the 22 February and 13 June 2011 events.

Methodology

The methodology used to derive the vulnerability functions for pipelines buried in the CPH soils is composed of the first and last steps of the methodology presented in Section 2.3. First, based on the backbone function f_0 evaluated in Section 2.4, the correction terms C_i are computed. Then, the uncertainty is computed following the procedure given in Subsection 2.3.2. As with the liquefaction-dependent functions presented in Subsection 2.3.2, the repair rate data is screened with the O'Rourke et al. (2014) criterion to ensure statistical significance of the results. However, no K-Fold cross-validation is performed. Although the procedures remain identical, some adjustments are necessary to achieve the development of repair rate functions for pipeline laying in the CPH soils. Namely, the considered characteristics and their number are modified. As the analysed subset represents only a fraction of the entire database, only three parameters are considered for the development of the new functions, in addition to the geometric mean PGV intensity: the CPH soil conditions, the performance group and the construction material.

All CPH-specific correction terms C_i are expressed as a PGV-dependent linear function given in Equation 2.6. The CPH-soil correction term C_{CPH} is fitted on the residuals between the observed repair rates considering the PGV as the only parameter and on the observed repair rates considering the PGV and the CPH soil condition as parameters. The performance grouping and material characteristics are treated as subsequent subsets of the CPH soil one only. The physics-based constraint, which enforces the function to be monotonously increasing is applied to this model with a threshold of 150 cm/s. Finally, the uncertainties are computed using the material-dependent functions as the most detailed repair rate functions as described in Section 2.3.2 (i.e. the between-model uncertainty of the CPH and material-dependent functions is zero).

Repair rate fitting results

Results from the development of the CPH-related repair rate functions are presented in two steps, similarly to Section 2.4. First, the repair rate functions are shown and then, their uncertainties are discussed. Figure 2.24 presents all CPH-related pipe repair rate functions. On Figure 2.24 (a), it can be observed that pipelines laying in the CPH soils are less vulnerable than the one laying in the Canterbury Plains Flatland. As in Section 2.4, low and high performance material pipes exhibit a significant difference in resistance. Note also that construction material-dependent functions presented in Figures 2.24 (b) and (c) are following the trends observed in Figures 2.4 (b) and (c) for CRR-dependent repair rate functions. Coefficient values for the CPH-related functions are presented in Section 2.9.4. Note that the CLS, DI and Steel related functions have not been developed as their counterpart for pipelines buried in soft soils are excluded.

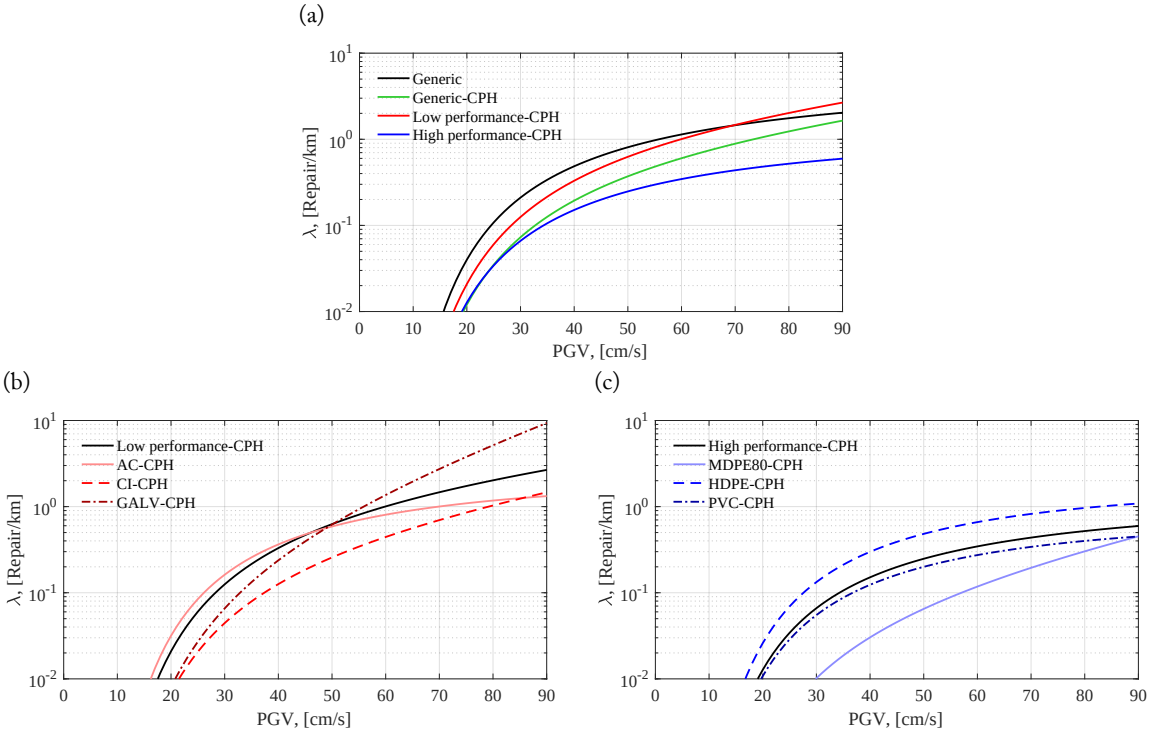

Figure 2.24: CPH-related repair rates functions for (a) generic pipes (backbone curve), generic low and high performance pipes ; (b) pipes made of low performance materials ; and (c) pipes made of high performance materials

Figure 2.25 presents both the between-model and within-model uncertainties of the CPH-related functions. As noted for the repair rate functions, similar trends are observed between the CPH-dependent and CRR-dependent uncertainties. However, in opposition to the function set developed for pipelines laying in soft soils, no function needs to be excluded as their residual means remain close to zero. These functions are utilized in the retrospective analysis presented in Section 2.5.

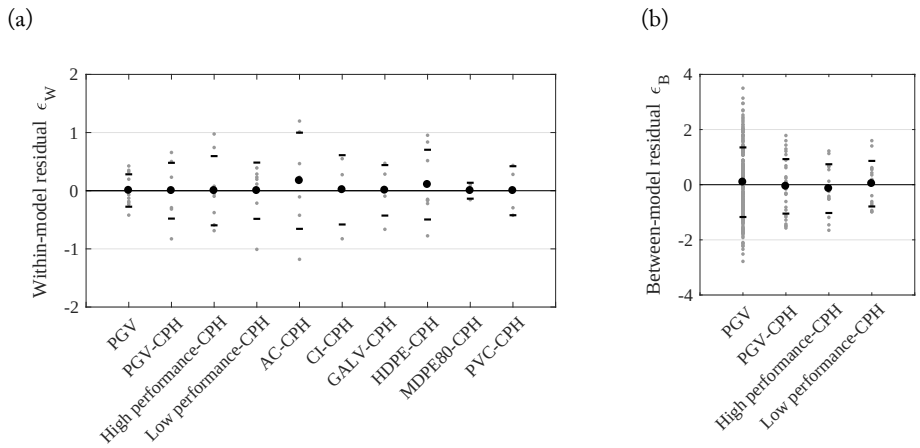

Figure 2.25: (a) Within-model uncertainty ; (b) Between-model uncertainty for CPH repair rate functions

The fully-developed Christchurch Port-Hill-specific repair rate model is given by Equations 2.19 and 2.20. Table 2.7 gives the coefficient values for the different repair rate functions included in this

model.

$$\ln(\lambda) = \Big[a_0 PGV^{b_0} + c_0\Big] + \Big[a_1 PGV + b_1\Big] + \Big[a_2 \cdot PGV + b_2\Big] + \Big[a_3 \cdot PGV + b_3\Big] + \epsilon \tag{2.19}$$

$$\epsilon \sim \mathcal{N}\left(0, \sqrt{\sigma_W^2 + \sigma_B^2}\right) \tag{2.20}$$

where index 0 represents the backbone function of the model f_0, index 1 the Christchurch Port Hill soil correction term, index 2 the performance grouping correction term, index 3 the construction material correction term and ϵ the normally distributed uncertainty term constituted of a within-model and a between-model standard deviations.

As a large number of repairs occurred in areas where landslides and rockfalls were the dominating ground repair mode, it is recommended to apply these functions to networks located in environments showing significant similarities (e.g. similar geologic formation, comparable slope and resembling hydrography).

2.9.4 Coefficient tables of buried pipeline repair rate functions

This section presents the model coefficients for the proposed repair rate functions computed using the methodology proposed in Sections 2.3 and 2.9.3 for pipelines buried in soft soils and Christchurch Port Hills soils, respectively.

Repair rate function coefficients for pipeline buried in soft soils

Table 2.6 provides the coefficient values for all repair rate functions included in this model. A value of zero is assigned to every unknown pipeline or soil characteristic.

Table 2.6: Repair rate function coefficient values and uncertainties for pipelines buried in soft soils

Function	PGV			Performance group		Material		Diameter		CRR			Uncertainty	
-	$a_0 \cdot PGV^{b_0} + c_0$			$a_1 \cdot PGV + b_1$		$a_2 \cdot PGV + b_2$		$a_3 \cdot PGV + b_3$		$a_4 \cdot CRR^{b_4} + c_4$			*Within*	*Between*
-	a_0	b_0	c_0	a_1	b_1	a_2	b_2	a_3	b_3	a_4	b_4	c_4	σ_W	σ_B
Backbone function	-75.1789	-0.9061	1.9981	0.0	0.0	0.0	0.0	0.0	0.0	0.0	0.0	0.0	0.2787	1.2620
Generic CRR	-75.1789	-0.9061	1.9981	0.0	0.0	0.0	0.0	0.0	0.0	0.7680	-0.3917	-1.7596	0.5681	1.1336
High performance	-75.1789	-0.9061	1.9981	-0.0043	-0.6031	0.0	0.0	0.0	0.0	0.0	0.0	0.0	0.3031	0.9856
Low performance	-75.1789	-0.9061	1.9981	-0.0019	0.6243	0.0	0.0	0.0	0.0	0.0	0.0	0.0	0.2884	1.0772
High performance CRR	-75.1789	-0.9061	1.9981	-0.0043	-0.6031	0.0	0.0	0.0	0.0	0.0033	-1.8135	-0.3100	0.5044	0.7446
Low performance CRR	-75.1789	-0.9061	1.9981	-0.0019	0.6243	0.0	0.0	0.0	0.0	2.8137	-0.1962	-4.2073	0.6291	0.9090
AC	-75.1789	-0.9061	1.9981	-0.0019	0.6243	-0.0021	-0.2050	0.0	0.0	0.0	0.0	0.0	0.3627	0.9305
GALV	-75.1789	-0.9061	1.9981	-0.0019	0.6243	-0.0030	1.0154	0.0	0.0	0.0	0.0	0.0	0.2264	0.7816
CI	-75.1789	-0.9061	1.9981	-0.0019	0.6243	-0.0030	-0.1010	0.0	0.0	0.0	0.0	0.0	0.8766	1.1454
PVC	-75.1789	-0.9061	1.9981	-0.0043	-0.6031	0.0019	-0.8225	0.0	0.0	0.0	0.0	0.0	0.6421	1.2977
MDPE	-75.1789	-0.9061	1.9981	-0.0043	-0.6031	0.0103	-1.2456	0.0	0.0	0.0	0.0	0.0	0.5133	0.8721
HDPE	-75.1789	-0.9061	1.9981	-0.0043	-0.6031	-0.0005	0.4039	0.0	0.0	0.0	0.0	0.0	0.4508	0.7233
AC CRR	-75.1789	-0.9061	1.9981	-0.0019	0.6243	-0.0021	-0.2050	0.0	0.0	99.9827	-0.0104	-102.0811	0.5576	0.5621
GALV CRR	-75.1789	-0.9061	1.9981	-0.0019	0.6243	-0.0030	1.0154	0.0	0.0	2.0873	-0.2074	-3.2429	0.6312	0.6166
CI CRR	-75.1789	-0.9061	1.9981	-0.0019	0.6243	-0.0030	-0.1010	0.0	0.0	44.7348	-0.0266	-47.5866	1.0913	1.0952
PVC CRR	-75.1789	-0.9061	1.9981	-0.0043	-0.6031	0.0019	-0.8225	0.0	0.0	0.0275	-1.4215	-0.7733	0.7638	0.7053
MDPE CRR	-75.1789	-0.9061	1.9981	-0.0043	-0.6031	0.0103	-1.2456	0.0	0.0	0.0076	-1.5810	-0.0980	0.6067	0.6079
HDPE CRR	-75.1789	-0.9061	1.9981	-0.0043	-0.6031	-0.0005	0.4039	0.0	0.0	0.0005	-2.2504	-0.2705	0.5874	0.5920
AC D80-300mm	-75.1789	-0.9061	1.9981	-0.0019	0.6243	-0.0021	-0.2050	-0.0004	0.0317	0.0	0.0	0.0	0.3600	0.9306
GALV D0-80mm	-75.1789	-0.9061	1.9981	-0.0019	0.6243	-0.0030	1.0154	0.0000	0.0126	0.0	0.0	0.0	0.2195	0.7816
CI D80-300mm	-75.1789	-0.9061	1.9981	-0.0019	0.6243	-0.0030	-0.1010	0.0000	-0.0039	0.0	0.0	0.0	0.8758	1.1454
PVC D80-300mm	-75.1789	-0.9061	1.9981	-0.0043	-0.6031	0.0019	-0.8225	-0.0024	0.1054	0.0	0.0	0.0	0.7436	1.2941
MDPE D0-80mm	-75.1789	-0.9061	1.9981	-0.0043	-0.6031	0.0103	-1.2456	-0.0001	0.0046	0.0	0.0	0.0	0.5136	0.8722
HDPE D0-80mm	-75.1789	-0.9061	1.9981	-0.0043	-0.6031	-0.0005	0.4039	0.0000	0.0305	0.0	0.0	0.0	0.4411	0.7233
AC D80-300mm CRR	-75.1789	-0.9061	1.9981	-0.0019	0.6243	-0.0021	-0.2050	0.0317	0.0317	93.8742	-0.0109	-95.9090	0.5614	0.0
GALV D0-80mm CRR	-75.1789	-0.9061	1.9981	-0.0019	0.6243	-0.0030	1.0154	0.0126	0.0126	6.6078	-0.0888	-7.9735	0.6171	0.0
CI D80-300mm CRR	-75.1789	-0.9061	1.9981	-0.0019	0.6243	-0.0030	-0.1010	-0.0039	-0.0039	36.7719	-0.0319	-39.6056	1.0940	0.0
PVC D80-300mm CRR	-75.1789	-0.9061	1.9981	-0.0043	-0.6031	0.0019	-0.8225	0.1054	0.1054	0.0135	-1.5967	-0.3887	0.6738	0.0
MDPE D0-80mm CRR	-75.1789	-0.9061	1.9981	-0.0043	-0.6031	0.0103	-1.2456	0.0046	0.0046	0.0077	-1.5760	-0.0990	0.6081	0.0
HDPE D0-80mm CRR	-75.1789	-0.9061	1.9981	-0.0043	-0.6031	-0.0005	0.4039	0.0305	0.0305	0.0005	-2.2806	-0.2748	0.5904	0.0

Repair rate function coefficients for pipeline buried in Christchurch Port Hills soils

Table 2.7 gives the coefficient values for the different repair rate functions included in this model. A value of zero is assigned to every unknown pipeline or soil characteristic.

Table 2.7: Repair rate function coefficient values and uncertainties for pipelines buried in Christchurch Port Hills soils

Function	PGV			CPH soil		Performance group		Material		Uncertainty	
-	$a_0 \cdot PGV^{b_0} + c_0$			$a_1 \cdot PGV + b_1$		$a_2 \cdot PGV + b_2$		$a_3 \cdot PGV + b_3$		*Within*	*Between*
-	a_0	b_0	c_0	a_1	b_1	a_2	b_2	a_3	b_3	σ_W	σ_B
Backbone function	-75.1789	-0.9061	1.9981	0.0	0.0	0.0	0.0	0.0	0.0	0.2787	1.2620
Generic CPH	-75.1789	-0.9061	1.9981	0.0141	-1.4703	0.0	0.0	0.0	0.0	0.4794	0.9882
High performance CPH	-75.1789	-0.9061	1.9981	0.0141	-1.4703	-0.0153	0.3484	0.0	0.0	0.5950	0.8839
Low performance CPH	-75.1789	-0.9061	1.9981	0.0141	-1.4703	-0.0010	0.5698	0.0	0.0	0.4837	0.8262
AC CPH	-75.1789	-0.9061	1.9981	0.0141	-1.4703	-0.0010	0.5698	-0.0160	0.7201	0.8268	0.0
GALV CPH	-75.1789	-0.9061	1.9981	0.0141	-1.4703	-0.0010	0.5698	0.0316	-1.5604	0.4340	0.0
CI CPH	-75.1789	-0.9061	1.9981	0.0141	-1.4703	-0.0010	0.5698	0.0073	-1.2467	0.5958	0.0
PVC CPH	-75.1789	-0.9061	1.9981	0.0141	-1.4703	-0.0153	0.3484	-0.0016	-0.1376	0.4213	0.0
MDPE CPH	-75.1789	-0.9061	1.9981	0.0141	-1.4703	-0.0153	0.3484	0.0266	-2.6439	0.1367	0.0
HDPE CPH	-75.1789	-0.9061	1.9981	0.0141	-1.4703	-0.0153	0.3484	-0.0016	0.7438	0.5994	0.0

This page is intentionally left blank

Chapter 3

A decision-support algorithm for post-earthquake water services recovery and its application to the 22 February 2011 Mw 6.2 Christchurch earthquake

"Experience without theory is blind, but theory without experience is mere intellectual play."

Immanuel Kant, 1781, Critique of Pure Reason

Adapted from: Bellagamba X, Bradley BA, Wotherspoon LM, and Lagrava WD (in press). "A decision-support algorithm for post-earthquake water services recovery and its application to the 22 February 2011 Mw 6.2 Christchurch earthquake". *Earthquake Spectra.* DOI:10.1193/052218EQS119M

As the cost of lifeline disruption rises with the size and complexity of urban communities, increasing efforts are put into enhancing infrastructure resilience to natural disasters. Aiming to improve the understanding of water supply network seismic resilience, this paper examines in detail the initial performance and restoration of the water supply network following the 22 February 2011 Mw 6.2 Christchurch, New Zealand, earthquake. In addition, a method to optimize the recovery of such systems is developed in two phases: the prioritization of pipe inspection and the prioritization of pipe repairs. The results inferred from observed pipe repairs suggest that the recovery was carried out efficiently, however, applying the proposed methodology would have substantially improved the recovery of the system with a 30% reduction in the number of buildings deprived of water in the first two days. Assumptions and limitations of the modelling are also discussed and practical solutions given to apply this framework in real-time for post earthquake restoration.

3.1 Introduction

In increasingly connected and complex societies, infrastructure resilience and post-disaster recovery is receiving growing attention from public and private sectors, such as RESILENS (Hynes et al., 2016) from the European Union, Resilience to Nature's Challenges (Fraser, 2017) from the New Zealand Government and 100 Resilient Cities (Choi, 2017) from the Rockfeller Foundation. Acute stresses on infrastructure caused by extreme events, such as earthquakes, are recognized as a major factor in socio-economic disruption as observed by Rose et al. (1997); Tierney (1997); Dahlhamer et al. (1999); Miles and Chang (2006); Hallegatte (2008) and Love (2011). In particular, disruptions in the water supply system can disable fire-fighting capabilities (Borden, 1997; Hughes et al., 2017); impede business and

farming productivity, including tourism attractiveness (Rose et al., 1997; Stevenson et al., 2012, 2017); and alter the daily life of the resident population (McReynolds and Simmons, 1995 ; Chung et al., 1996, pp. 301 - 333 ; Hughes et al., 2017).

The aftermath of the 22 February 2011 Mw 6.2 Christchurch earthquake and its geotechnical consequences provide a stark illustration of the importance of resilient infrastructure (Bradley and Cubrinovski, 2011; Cubrinovski et al., 2011; Bradley et al., 2014; Bouziou et al., 2015). King et al. (2014) estimated that the costs of public infrastructure rebuild would be NZD 6 billion or 3% of the New Zealand GDP. Previously technical literature has extensively described the damage to the road, gas, water supply, sewerage and electricity networks, which were severely impacted by liquefaction and lateral spreading (Giovinazzi et al., 2011 ; Eidinger and Tang, 2012, pp. 152–171 ; Cubrinovski et al., 2014, pp. 10–45 ; O'Rourke et al., 2014). In particular, Giovinazzi et al. (2011) reported that approximately 50% of Christchurch was without water access on the day of the event and that it took a month to restore 95% of water supply services. By tracking the number of detected pipe failures over time, O'Rourke et al. (2014) estimated that the system was nominally restored after 53 days following the event.

In order to reduce the impact of lifeline disruption due to widespread system damage impacting functionality, several inspection and repair scheduling algorithms have been developed while optimizing the use of available resources. In particular, linear programming (LP) or mixed-integer linear programming (MILP) algorithms have proven relatively efficient to accelerate recovery processes of different lifeline systems, e.g. Yao and Min (1998) for electricity networks and Feng and Wang (2003) for the road networks. Fang and Sansavini (2017) proposed an MILP-based model that optimizes restoration of network connectivity, while mitigating future losses by rebuilding infrastructure in less vulnerable areas. While the latter approach suits strategic rather than urban infrastructure due to the high asset density and the already-existing redundancy in urban systems (e.g. high-voltage transmission power lines or continental gas pipelines versus power distribution grid, sewerage or water supply networks), solving any of these approaches can become prohibitly computationally expensive for large systems with current resources. In such cases, the optimum can alternatively be obtained by using metaheuristic techniques. For example, Xu et al. (2007) propose a genetic algorithm (GA)-based scheduling recovery process (inspection, damage assessment and restoration) for a collection of power stations that minimizes the number of people disconnected from the network over time. Power lines are not considered in the analysis and the problem's constraints are given by the number of repair teams. Bocchini et al. (2013) also use a GA-based algorithm to produce Pareto-set optimal solutions that maximize the connection between vertices of a road network composed of several bridges.

Few studies have focused on improving or measuring the resilience of water supply networks. Among these, Tabucchi et al. (2010) propose a restoration process for the Los Angeles City water supply network. It prioritizes the inspection of pipes based on their distance to the epicentre and repair based on the distance from the closest water source (e.g. wells or reservoirs). The primary objective of this method is to minimize the number of people disconnected during the recovery period. In their study, the water flow is simulated, however only main pipelines are considered, and the community is modelled as demand nodes. Klise et al. (2017) propose a software to analyse the resilience of water supply networks, which accounts for the water flow, the capacity to produce fresh water and the demand from the community. However, the suggested recovery strategy does not consider the inspection and damage assessment processes (i.e. it assumes all pipe failure locations and their severity are known).

Despite the efforts made to develop accurate recovery models for water supply systems, several problems remain. First, as emphasized by Zorn and Shamseldin (2016), interdependencies between systems can play a crucial role in their respective functionality. This is particularly true for water supply systems, which are highly reliant on the functionality of the electric power network. Second, the detection of pipe failure can mobilize a non-negligible portion of the available human resources and take several weeks as noted by Hughes et al. (2017) in the context of the 14 November 2016

Mw 7.8 Kaikoura earthquake. Third, as new pipe failures are detected, repair priorities might evolve. Hence, a periodic re-assessment of the repair priorities is necessary to ensure the implementation of the optimal solution.

In this paper, the historical recovery of the Christchurch water supply following the 22 February 2011 event is inferred from reported pipe failures and a GA-based optimization method for post-earthquake recovery dedicated to water supply systems is proposed. The recovery is expressed utilizing city-scale metrics such as the number of impacted buildings, the population or the building utility (see Table 3.1) and explicitly accounts for the dependency on the functionality of the electric power network. The proposed optimization method operates on a periodic basis and minimizes a weighted combination of the population, the utility of buildings and the number of buildings disconnected from the water supply system. Finally, both the historical and optimized recoveries are compared.

3.2 Inferred recovery of the water supply network following the 22 February 2011 Mw 6.2 Christchurch earthquake

This section briefly describes the datasets used in the historical analysis, the assumptions and the results of the inferred co-seismic performance of the water supply network. The phrase '*inferred*' is used to indicate that quantitative metrics to describe network-level recovery were not directly catalogued, but are reconstructed through more granular, historical records of repairs combined with an understanding of the network topology and interviews with water supply network personnel. In addition, the inferred co-seismic performance is compared to a prediction considering the same assumptions, where pipe failures are generated through a Monte-Carlo simulation scheme. The Monte-Carlo simulations are used as a basis for optimization as detailed in Section 3.3. The historical recovery is then derived from reported pipe repairs and discussed with respect to the community.

3.2.1 Water supply network and community datasets

The Christchurch water supply network is composed of 3,246 kilometres of pipelines, out of which 1,612 kilometres are trunk main or main pipelines and 1,634 kilometres are submain or crossover pipelines. Cubrinovski et al. (2014, pp. 3–9) provide an accurate description of the pipe network in terms of topology, material composition and technology. The analysed network is supplied by 92 pump stations out of which 23 have a diesel generator allowing them to operate during long power outages. Most pump stations are located nearby a water supply source (bored wells or tanks). A few exceptions are located in low density residential suburbs in the Port Hills area.

The Christchurch community is described by three different datasets: (1) the land usage that provides the category of buildings (business, medical, school, residential, rural or critical) (M. Hughes, pers. comm.); (2) the building footprints that gives the location and geometry of each building (M. Hughes, pers. comm.); and (3) the census that provides an estimate of the population over meshblocks, areas delineated by the New Zealand authorities for this specific purpose (Statistics New Zealand, 2013a). To reduce the computational burden and avoid mis-assignment of population to buildings, building footprints of less than 20 square meters were removed, while building footprints more than 200 meters from a submain pipe were considered off-grid and also removed. The final building footprint dataset enclosing the usage information contains 209,442 buildings, of which 8,008 are business buildings, 2,239 school, childcare or university buildings, 355 hospitals or medical buildings and 55 critical buildings, with the remainder being essentially composed of residential, rural, cultural and recreational buildings. Based on the usage category, the Christchurch City Council assigns utility of buildings values to buildings as presented in Table 3.1. These values represent the importance of the building for the functioning of the community. As the acquired building dataset does not possess all presented categories, the distribution of utility value is slightly simplified: the label *High water user* is ignored, there is no utility value equal to 4 and a value of 5 is given to all medical buildings (i.e. to

Table 3.1: Christchurch City Council utility values (Irmana Garcia Sampedro, pers. comm.)

Utility value	Description	Categories
1	Very low	Rural ; Residential
2	Low	Commercial ; Industrial
3	Medium	School ; Childcare ; High water usage
4	High	Hospital without emergency facilities ; Rest home ; Emergency services ; Correction department facility ; General practitioner office
5	Very high	Lifeline facility ; Civil defence welfare center ; Hospital with emergency facilities

hospital without emergency facilities, rest homes and hospital with emergency facilities). To assign population to buildings, it is assumed that people can only occupy *Residential* and *Rural* buildings. As the 2011 population census was not carried out due to the 2010-2011 Canterbury earthquake sequence (Statistics New Zealand, 2013b), the population is estimated by a linear extrapolation from the two previous censuses realized in 2001 and 2006 by the Statistics New Zealand (2013a). The estimated population in 2011 in the considered buildings is approximately 351,500 people. The population was then assigned to each *Residential* and *Rural* building depending on the density of population over the inhabitable area of the meshblocks and the building footprint size. Figure 3.1 shows the different usage of the building footprints and the Christchurch water supply network.

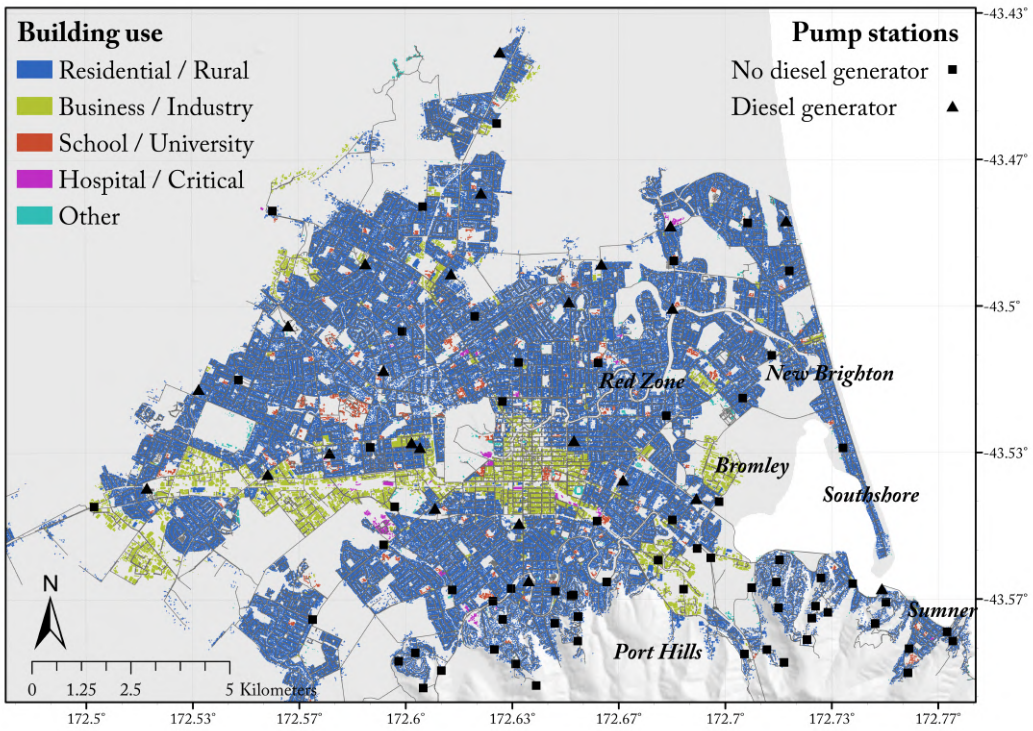

Figure 3.1: Map of the Christchurch building stock annotated according to building use, water supply pipe network and pump stations

3.2.2 Estimated initial performance and its modelling

The 22 February 2011 Mw 6.2 Christchurch earthquake caused 3,039 pipe failures (Eidinger and Tang, 2012, p. 159), mostly due to severe liquefaction and lateral spreading. Cubrinovski et al. (2014,

p. 19) discussed their geospatial distribution and O'Rourke et al. (2014) provide the observed daily repair rate and inferred the '*effective*' completion of the earthquake-related repairs on the 15th of April 2011, 53 days after the earthquake. Immediately after the earthquake, large portions of the city were also in areas with power outages (L. Dueñas-Osorio, pers. comm. ; Fenwick et al., 2011), disabling the majority of the pump stations. Access to power was the most important factor for the network in order to operate pump stations (K. Snyder-Bishop, pers. comm.).

Two neighbouring pump stations located in the Port Hills (South-East of the city; Figure 3.1) suffered from critical failures (one from cliff collapse, see Dellow et al. (2011) for more details, and the other from extensive structural damage) and have not been brought back to service (K. Snyder-Bishop, pers. comm.). To estimate the initial impact of pipe failures and disabled pump stations, several assumptions have been made. First, water flow is not explicitly considered for computational reasons as detailed in a subsequent section (i.e. the proposed work is based solely on pipe connectivity). However, given the relatively uniform geospatial distribution of the pump stations across the city, it is believed that this assumption has only a second order effect. Furthermore, the type and severity of pipe damage has not been adequately documented, such that individual pipe functionality cannot be inferred. Hence, this analysis monitors the *water delivery* as defined in Davis (2014). Second, a pipe is assumed to have lost its connection if at least one failure has occurred on all its potential routes from any source or on itself (as presented in Equation 3.1 below). Third, pump stations equipped with a diesel generator have been brought back to service within the first 24 hours of the earthquake as road access was not a major problem in Christchurch (Eidinger and Tang, 2012, pp. 248–265). Hence, diesel-powered pump stations were considered out of service only on the day of the event itself. Fourth, despite minor relocation of population and businesses (Stevenson et al., 2011; Chang et al., 2014), buildings are considered to require reconnection to the water supply (i.e. they are all considered as a demand node for water resources, irrespective of what their damage state was). Note that this assumption is consistent with the fact that government-provided temporary housing was unused and quickly closed down (Giovinazzi et al., 2012). Fifth, buildings are assumed to be connected to their closest submain and private connections from the submains to the buildings are not considered. Finally, as long as one undamaged pipeline route exists from a building to a pump station, the former is considered connected to the latter as expressed in Equation 3.1.

$$\begin{cases} \text{Connected}, & \text{if} \quad \min\limits_{1 \leq j \leq M_i} N_{fail,i,j} = 0 \\ \text{Disconnected}, & \text{otherwise} \end{cases} \tag{3.1}$$

where M_i is the number of potential routes from any source to building i and $N_{fail,i,j}$ is the number of pipe failures on existing route j of building i. Note that this equation is also valid to assess pipe connectivity status.

As subsequently discussed, to optimize the recovery process, pipe damage and building connectivity predictions are necessary. Damage prediction is evaluated for each individual pipe and uses the pipe fragility functions developed from Christchurch damage data by Bellagamba et al. (in press). These functions require, in addition to the pipe characteristics (length, material and diameter), the estimated peak ground velocity (PGV) and the liquefaction susceptibility of the soil expressed as its cyclic resistance ratio (CRR) at pipe installation depth. The PGV is probabilistically generated as a spatially correlated random field using the median and standard deviation of the PGV estimated by Bradley (2014) and the spatial correlation coefficient proposed by Jayaram & Baker (2009). The CRR is inferred from the liquefaction resistance index map compiled by Cubrinovski et al. (2014, pp. 13–15) as proposed by Bellagamba et al. (in press). Building connectivity is assessed following the procedure used to infer the inferred initial network performance. To achieve stable results, 2000 realizations from the Monte-Carlo scheme were executed and sufficient convergence was attained. Either inferred or predicted, the performance and recovery of the water supply network are expressed by means of community-oriented metrics at two levels of granularity - global and specialized. The

three global metrics measure the population, utility of buildings and number of buildings (all types) deprived of water. The specialized metrics quantify the business, medical (including hospitals and rest homes), school (including universities and childcare) and critical buildings deprived of water.

Figure 3.2(a) presents the results of the inferred co-seismic performance, whereas Figure 3.2(b) shows the results of the prediction. The difference between the reported (50% of the dwellings without water access immediately after the earthquake reported by Giovinazzi et al., 2011) and inferred number of buildings deprived of water indicates that not considering the water flow during a generalized power outage leads to a significant underestimate of the initial impact. However, because the power outage only lasted one day for most of the city (L. Dueñas-Osorio, pers. comm. ; Fenwick et al., 2011), it is expected that the map presented in Figure 3.2(a) approximately reflects the real state of the water outage by the end of day 1 following the earthquake.

The eastern suburbs of Christchurch (New Brighton, Southshore and Sumner; indicated in Figure 3.1) as well as the most severely liquefied areas (along the Avon River, also known as the *Red zone*; Figure 3.1) are the areas where most of the simulated outages take place. The former are indeed likely to suffer from an outage as they are topologically easily isolated and the latter are the most vulnerable to suffer from large permanent ground deformations (Cubrinovski et al., 2011), leading to extensive pipe damage. Some areas in the Port Hills (South of the city; Figure 3.1) might have been more impacted than what is shown in Figure 3.2(a) due to the pressure loss caused by altitude changes, which was not explicitly modelled as previously noted. Figure 3.2(b) presents the prediction results and illustrates important similarities with the inferred co-seismic initial impact: a significant portion of the buildings likely to lose their connection to the water supply network (i.e. probability of water outage $\geq$50%) are, according to the inferred co-seismic performance, disconnected from the water supply network. It must be noted that building connectivity is relatively well predicted, whereas pipe damage remain inaccurate. Further details such as the receiver operation characteristics (Fawcett, 2006) for both pipe damage and building connectivity, and the differences between the inferred and predicted analyzed metrics can be found in Figures 3.7 and 3.8, respectively.

3.2.3 Inferred water service recovery

Following the Christchurch earthquake, the recovery started quickly. Most suburbs recovered access to electricity on the day after the earthquake (L. Dueñas-Osorio, pers. comm. ; Fenwick et al., 2011). Pump stations were restored once electricity access was restored or when their diesel generator was turned on. Despite the existence of damage, and excluding the two suffering from critical failures, all pump stations were able to deliver some outflow (K. Snyder-Bishop, pers. comm.). Pipe failure detection was realized following a two-step iterative process. First, pump stations were required to deliver their maximal outflow and then, repair teams were in charge of detecting any major leakage from abnormal traces of water on the surface. This process started near the pump stations and, as repairs were executed, inspections were moved away from their original start point. A repair priority varying from 1-10 days was assigned to every detected pipe failure. It is worthy to note that only the dates of detections are known, not the actual dates of repairs completed as described in the pipe failure dataset. A peak of 300 repair teams has been noted by Eidinger and Tang (2012, p. 159). According to the Christchurch City Council estimations reported by Giovinazzi et al. (2011), the system had recovered approximately 95% of its serviceability a month following the earthquake. Eidinger and Tang (2012, p. 159) inferred the full recovery of the system 40 days after the earthquake (on the 5th of April), whereas O'Rourke et al. (2014) made a corresponding estimate of 53 days (on the 18th of April). Note finally that the results presented here do not consider the temporary bypasses and pumps as well as isolation capabilities of the water supply network that may have been put in place and use during the recovery to reduce the global disruption.

As the pipe repair dates are unknown, 100 realizations of the historical recovery are simulated. The delay between the discovery of a pipe failure and its repair is assumed following a discrete uniform

(a)

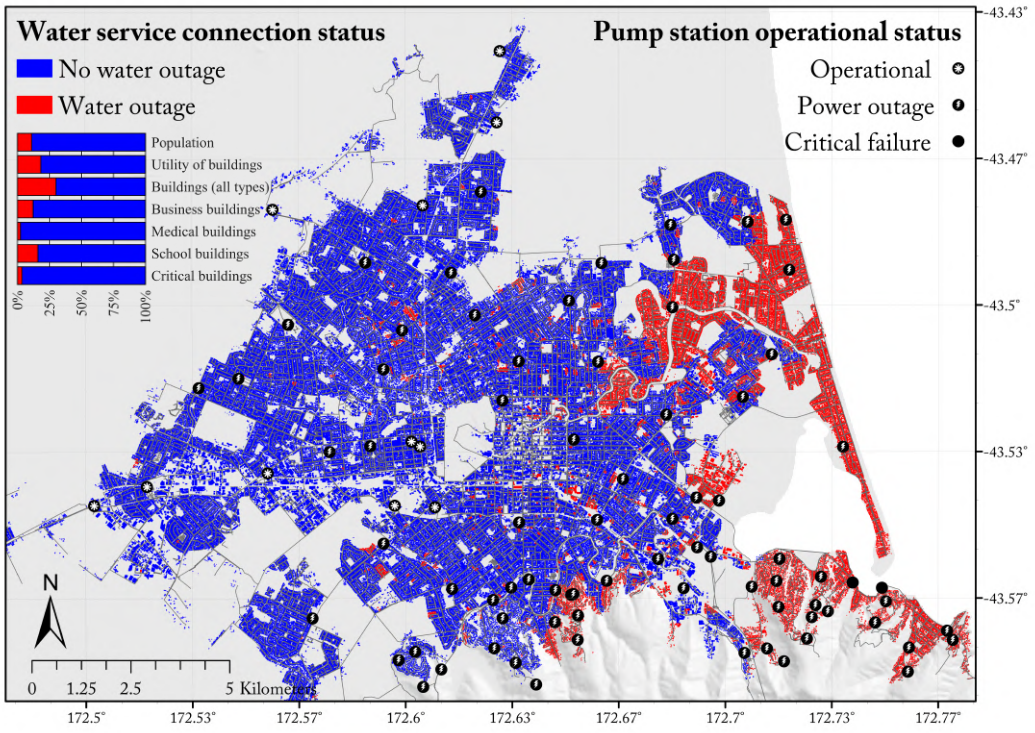

(b)

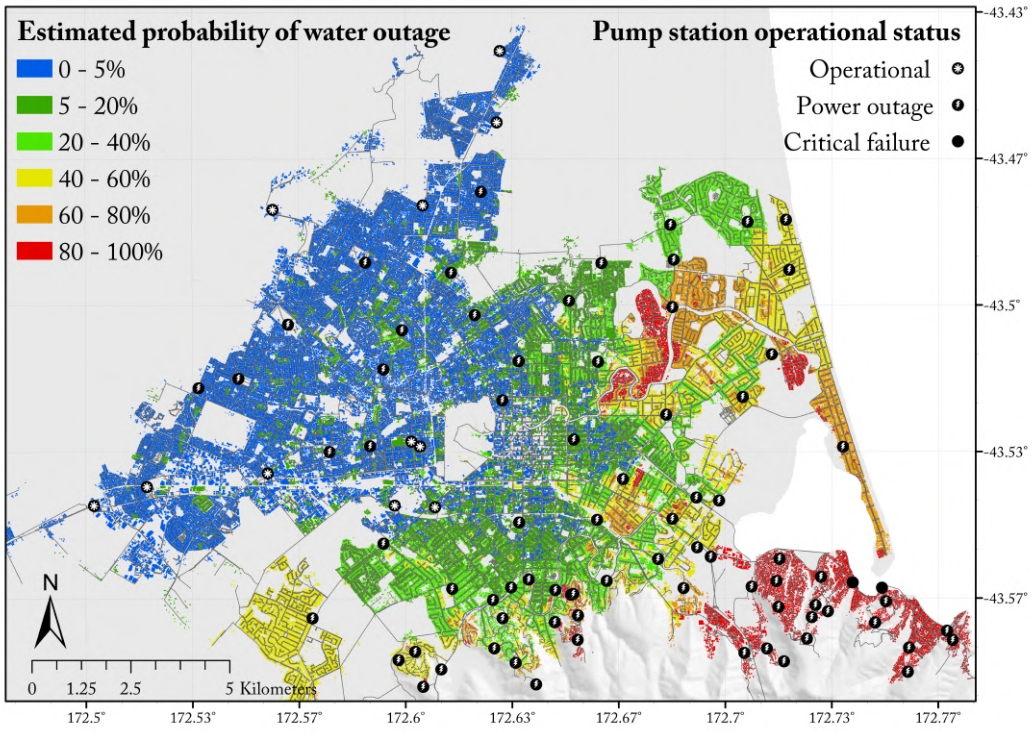

Figure 3.2: Water supply network performance following the 22 February 2011 Mw 6.2 Christchurch earthquake: (a) Map of the inferred co-seismic water outage and histogram indicating the portion of each considered metric suffering from water outages ; (b) Map of predicted initial water outage (probability of water outage)

distribution as shown in Equation 3.2.

$$\text{Delay}_i \sim \mathcal{U}(1, \text{priority}_i) \tag{3.2}$$

where $\sim \mathcal{U}$ denotes that $Delay_i$ is sampled following a uniform distribution and *priorityi* is the assigned priority of pipe failure i. The delays are assumed independent from each other (i.e. no correlation between delays is applied). Figure 3.3 presents the map of the simulated average water outage time. Similarly to the initial performance estimation, because the model does not consider water flow, the outage in the central and eastern suburbs of the city are underestimated by 1 day. It is easy to observe that the most isolated parts of the city (New Brighton, Southshore and Sumner; 3.1) are the latest to recover water access. In these areas, electricity was restored relatively late and therefore pump station functionality could not be restored in a timely manner. The *Red zone* and its neighbourhood also required a long restoration period as the system was heavily damaged due to severe liquefaction and lateral spreading.

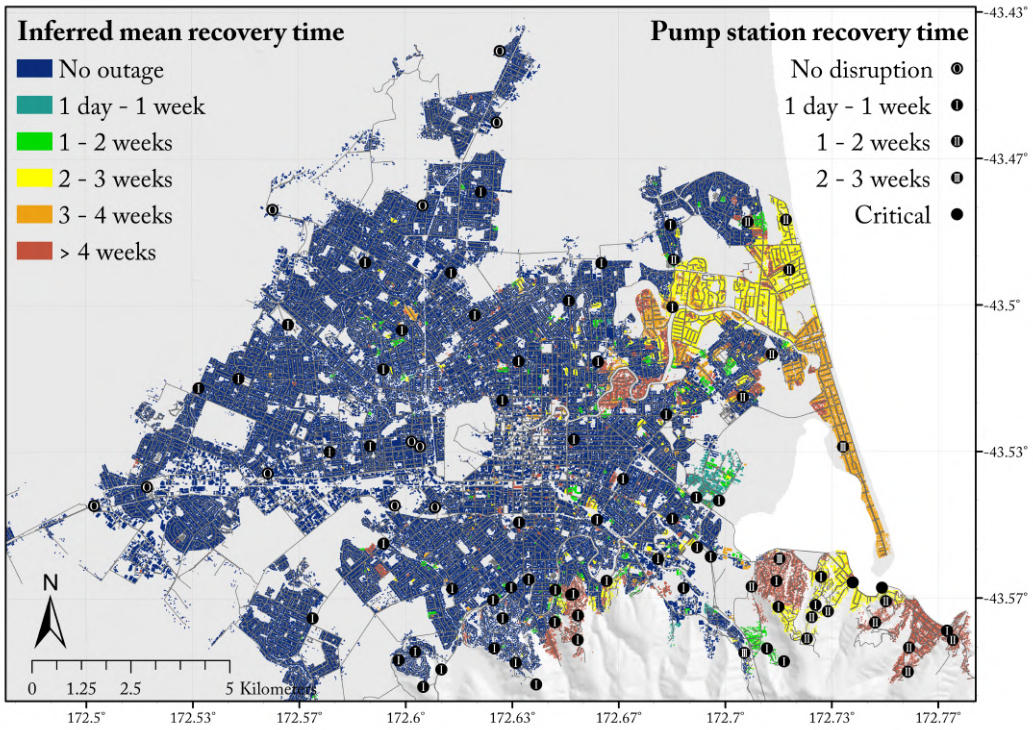

Figure 3.3: Map of mean time for reconnection to water supply network following the historical recovery process inferred from the dates of reported pipe repairs following the 22 February 2011 Mw 6.2 Christchurch earthquake

Figure 3.4 shows the recovery curves over time and resilience of all selected metrics as well as the number of pump stations remaining non-operational. The resilience R is estimated as proposed by Cimellaro et al. (2010, Eq. 1) and reproduced in Equation 3.3.

$$R = \int_{t_{0E}}^{t_{0E}+T_{LC}} Q(t)/T_{LC}\mathrm{d}t \tag{3.3}$$

where t_{0E} is the occurrence time of the event, T_{LC} is the control period of the system set to the entire recovery time and $Q(t)$ is the functionality of the system in percent depending on the time. In the considered case, the control period is therefore set to 63 days (the recovery period), dt is set to one day, and $Q(t)$ is the inferred performance of each selected metrics. Based on the proposed model, it

is worth noting that the pump stations apparently played a second order role in the recovery of the water supply access. However, the reported disruption levels by Giovinazzi et al. (2011) seem to be more strongly correlated with the restoration of the pump stations' operability. This supposes that, as long as a significant portion of the pump stations are non-operational, a connectivity approach might not be sufficient to accurately assess the systemic disruption. Nevertheless, this approach appears to be accurate once the majority of the pump stations are brought back to service (around the 7th day of the recovery). Despite a lower initial estimate, the model seems to corroborate the observations made in previous studies: the 7% disruption (*Buildings (all types)* metric) left after 30 days of recovery is consistent with the 95% of service restoration reported by Giovinazzi et al. (2011), and most of the buildings and population in the simulations had recovered their water access after the 6 weeks proposed by Eidinger and Tang (2012, p. 159) as the end of the post-earthquake repair period. The inflexion point (where the repairs start to have a significant effect on the attenuation of the disruption) occurs around the 15th day, when the northern parts of New Brighton were serviced again (north-eastern yellow areas in Figure 3.3).

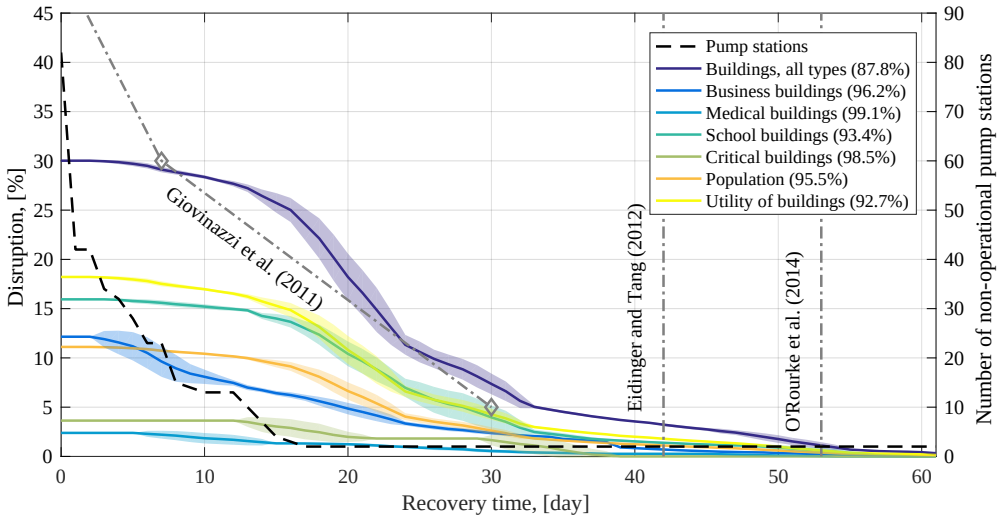

Figure 3.4: Mean water access recovery curves of the selected metrics following the 22 February 2011 Mw 6.2 Christchurch earthquake (shaded areas represent the first standard deviation boundaries of each metric) ; estimated completion of the repair work by Eidinger and Tang (2012) and O'Rourke et al. (2014) ; and interpolation between the levels of disruption (indicated by diamonds) reported by Giovinazzi et al. (2011). Numbers between brackets indicate the resilience of each metric estimated with Cimellaro et al. (2010, eq. 1).

As observable in Figure 3.4, the shape of the presented recovery curves follows a cosine-shape, which is attributed to a "*not well prepared community*" by Cimellaro et al. (2010). This classification should be further interrogated in relation to a number of factors. First, at the beginning of the repair period (about one day), the real recovery curve may be closer to the disruption level interpolation reported by Giovinazzi et al. (2011), which follows an exponential function and can therefore be related to a "*well prepared community*". Second, as the water supply system possesses a strong dependency to the power grid, the water supply system has to "wait" for the restoration of the electric power network, or has to operate on alternative power sources (e.g. diesel-powered backup systems). Third, the damage detection of underground systems requires more resources than systems that are located at the surface, slowing down the actual repair process. Finally, as aforementioned, the potentially positive effects of temporary measures have not been taken into account, reducing the measured resilience of the system.

3.3 Proposed recovery optimization methodology based on a genetic algorithm

In the development of their framework, Bruneau et al. (2003) characterize the seismic resilience of a system with its robustness, redundancy, rapidity and resourcefulness. Therefore, based on the observed system robustness and existing redundancies, the use of its resources and its rapidity to react can be optimized. As observed during the water supply restoration in Christchurch, the detection of the pipe failures can take a non-negligible time, leading to potential changes in the optimal repair priorities. Hence, these repair priorities have to be periodically re-evaluated in order to improve the resilience of the system by maximizing the effect of the repairs on its serviceability. The constraints of the problem are the periodic capacity to inspect and repair pipes (i.e. the maximum inspectable pipe length and the maximum number of executable pipe repairs, respectively). In this section, an inspection priority ranking approach is described, and the proposed GA-optimized repair process explained.

3.3.1 Inspection priority list

Based on predicted damage and serviceability results, an inspection priority list is established. This list ranks the pipes based on the inverse of their probability of survival, and on their probability of connection survival due to their own failure, as proposed in Equation 3.4. The probabilities of pipe disconnection are estimated considering all working or repairable pump stations (i.e. only excluding pump stations suffering from critical failure). Hence, inspections prioritize pipes with high probability of failure and low probability of disconnection (closer to a working or repairable pump station).

$$\text{Score}_i = \frac{1 - P_{Disc,i} + P_{f,i}}{(1 - P_{f,i})^2 + \epsilon} \tag{3.4}$$

where $P_{f,i}$ is the failure probability of pipe i from pipe fragility analysis, and $P_{Disc,i}$ the disconnection probability of pipe i from network connectivity analysis. A small value ϵ (0.00001) is added to the denominator to avoid division by 0. $P_{Disc,i}$ is computed from Equation 3.5.

$$P_{Disc,i} = \min_{1 \le j \le N_i} P_{Disc,i,j} \tag{3.5}$$

$$\text{with} \qquad P_{Disc,i,j} = 1 - \prod_{k=1}^{m_j} (1 - P_{f,k}) \tag{3.6}$$

where N_i is the number of potential routes from any water source to pipe i, and $P_{Disc,i,j}$ is the disconnection probability of route j composed of m_j pipes. The inspection priority list is compiled only once at the beginning and remains unchanged for the entire recovery process for computational reasons. This method is limited by the inability of some of the pump stations to operate at the creation of the list, as they are, for example, not able to access electric power. However, as the first failed pipe on a particular route receives the highest priority, and although it simplifies the inspection process as it has been carried out, the list is believed to optimize it in a relatively realistic fashion.

3.3.2 Formulation of the repair optimization linear program

As mentioned earlier, the recovery process of a spatially-distributed infrastructure system can be expressed as an MILP, whose objective function minimizes the loss of serviceability. Here, the repair optimization takes into account the two parallel processes occurring during the recovery: (1) inspection of the network, and (2) individual pipe repairs. During each repair period, uninspected pipes having the highest inspection score are inspected such that the entire inspection capacity is used. Newly discovered pipe failures are added to the potential repair list at the end of the repair period. In parallel, the serviceability at each repair period is optimized with an MILP that minimizes a weighted combination of the population, the number of buildings and the utility of buildings deprived of water by

prioritizing pipe repairs constrained by the maximum repair capacity. In other words, the objective of the program is the minimization of a linear combination of variables representing the outage impact, decision variables are the detected and unrepaired pipe failures, and the constraint is given in terms of time-dependent repair capacity. Note that the optimal solution of an iteration is agnostic to the optimal solution of the previous one (i.e. the algorithm gives the optimal tactical solution but does not follow a global strategy over time). Equations 3.7 to 3.11 mathematically set the considered MILP.

$$\min \quad \Xi = \sum_{i=1}^{N} \left[Q_i \cdot \min \left(1; \min_{1 \leq j \leq M_i} N_{fail,i,j,t} \left(\Upsilon_{R,t}, \Upsilon_{I,t} \right) \right) \right] \tag{3.7}$$

$$\text{subject to} \quad \| \Upsilon_{R,t} \|_1 \leq C_{R,t} \tag{3.8}$$

$$\| \Upsilon_{I,t} \|_1 \leq C_{I,t} \tag{3.9}$$

$$\text{with} \quad Q_i = \sum_{k=1}^{L=3} w_k q_{i,k} \tag{3.10}$$

$$\text{and} \quad \sum_{k=1}^{3} w_k = 1 \tag{3.11}$$

where N is the number of buildings in the dataset, Q_i is the quantity of the objective metric of building i, M_i is the number of potential routes from any source to building i, $N_{fail,i,j,t}$ is the number of pipe failures on existing route j of building i computed at the end of period t. $N_{fail,i,j,t}$ depends on decision variables $\Upsilon_{R,t}$ and $\Upsilon_{I,t}$, the allocation of the repair and inspection capacities over period t, respectively. Their respective Manhattan norm $\| \Upsilon_{R,t} \|_1$ and $\| \Upsilon_{I,t} \|_1$ represents the utilized repair and inspection resources over period t. $C_{R,t}$ and $C_{I,t}$ are scalars expressing the maximum repair and inspection capacities over period t, respectively. Inspection and repair capacities are given in terms of pipe length and pipe failures, respectively. In a real case, those values will depend on the available human and financial resources and construction material and require careful assessment as discussed in Section 3.4.3. The quantity Q_i is computed as the sum of products between the objective function weights w_k and the three considered quantities $q_{i,k}$. For this work, three different quantities are considered to be optimized: (1) the population; (2) the utility of buildings; and (3) the number of buildings (always equal to 1 for a single building). The weights w_k must be set with respect to the recovery manager's objectives. Weighting based on the maximum number of buildings alone may be appropriate for rural areas where authority-owned buildings may not be able to shelter and provide services for a large number of people. Hence accelerating the service recovery of a large number of buildings (houses and farms) can be seen as critical. The combination of two or more quantities may be more suitable to urban areas, as recovery officers may want to restore services for productive capacities and critical facilities more quickly than in rural areas. The density being generally higher in urban than rural areas, targeting the population and utility would have a greater positive effect on the population and economy than targeting the number of buildings.

3.3.3 Implementation of the genetic algorithm

The periodic allocation of repair resources can be encoded as a binary vector composed of 0 for *do nothing* and 1 for *repair* as proposed by (Fang and Sansavini, 2017, Eq. 10). Following the same reasoning, the allocation of inspection resources at each time period t is encoded as 0 for *do nothing* and the length of pipe occupying a given position in the vector for *inspect*. The length of both the $\Upsilon_{R,t}$ and $\Upsilon I, t$ vectors represents the number of pipes in the system and the number of non-repaired pipe failures for the inspection and repair vectors, respectively. However, as the inspection ranking list is immutable, the allocation of the inspection capacity is predetermined for each period. The dimension of the problem (i.e. the number of decision variables it contains) is then determined by the number of unrepaired pipe failures. The search space of the MILP therefore becomes the set of all potential repair

permutations. The permutation number can be computed as a binomial coefficient with the number of non-repaired pipe failures and the repair capacity as coefficients. As the problem can rapidly become very large and have multiple local minima, brute force approaches or convergence algorithms would be inefficient and lead to suboptimal solutions. Given the encoding of the problem, its size and the potentially non-convex search space, a genetic algorithm (GA) was implemented, which is recognized as an efficient method to solve such problems (Mitchell, 1998, pp.116 –117). GA does not always deliver the optimal solution but yields a '*good*' solution at lesser computational expense than other techniques. However, GA requires a maximization problem. Hence, the objective function presented in Equation 3.7 is transformed into a maximization problem presented in Equation 3.12, whereas the constraints do not change.

$$\Xi = \sum_{i=1}^{N} \left[Q_i \cdot \left(1 - \min \left(1; \min_{1 \leq j \leq M_i} N_{fail,i,j,t} \left(\Upsilon_{R,t}, \Upsilon_{I,t} \right) \right) \right) \right] \tag{3.12}$$

In the GA context, a set of potential solutions of the problem is called a *population*. Individuals of this population are called *chromosomes* and their characteristics, *alleles*. Here, chromosomes are the daily repair solutions that satisfies the constraints (i.e. they are part of the search space) and alleles represent each detected, but unrepaired, pipe failure. An allele encodes a *trait*, the value of the allele (in our case, *repair* or *do nothing*). A *locus* represents the position of a particular allele on a chromosome. Hence a particular locus represents the position of a particular pipe failure in the database. The ability of a chromosome to survive or reproduce is given by its *fitness*, computed as the result of the objective function in Equation 3.12.

To converge toward a fitter population, chromosomes *mate* with each other in pairs over steps called *generations*. The mating process consists of three distinct operations: *selection* (which chromosomes mate), *crossover* (which alleles are exchanged between mating chromosomes) and *mutation* (which alleles are randomly modified). The mating process between two chromosomes creates two *offspring*. More information about GAs and their implementation can be found in Mitchell (1998) and Haupt and Haupt (1998).

In this study, the selection of chromosomes is realized via a binomial tournament and elitism. The former operator randomly picks two chromosomes from the current population and select the fittest ones for reproduction, allowing small fitness chromosomes to mate and slowing down the convergence rate of the algorithm, whereas the latter retains the best N_{elite} chromosomes of each generation for the next one without altering them. Parametrized uniform crossover is chosen as the crossover operator and locus swap as the mutation operator. The parametrized uniform crossover operator assigns the same probability of exchanging traits for all loci from both mating chromosomes. Once the offspring are created, the mutation operator decides if the encoded trait of two randomly chosen loci of the same chromosome are exchanged. Once the new generation is ready, it replaces the old one and the whole process is repeated a determined number of times or until a local optimum has been found (i.e. the standard deviation of the population fitness is equal to 0).

3.4 Case study: Water supply network recovery following the 22 February 2011 Mw 6.2 Christchurch earthquake

To test the efficiency of the proposed GA optimization the Christchurch water supply network recovery following the 22 February 2011 Mw 6.2 earthquake was considered. The number and location of the pipe failures, the operational status and restoration time of pump stations are identical to that presented in Section 3.2. In the paragraphs that follow, first, the assumptions and parameters required to carry out the GA-based process are given. The optimized recovery curves and map are then presented and discussed in relation to the resilience metrics. Finally, the procedure for real-time application of this method is given.

3.4.1 Optimization parameters

In order to account for missing information (e.g. the number of repair teams over the recovery period), several assumptions were made. Justifications for the parameter choices and assumptions are given in the next paragraph. The repair period is fixed to one day (i.e. repair priority assignment and system functionality are evaluated every day). The daily repair capacity is set to 50, the daily inspection capacity is set to 55 kilometres, the objective function weights are set to 0.5, 0.0 and 0.5 for the population, the number of buildings and the utility of buildings, respectively. The genetic algorithm is parametrized with a number of elite chromosomes of 2, a crossover rate of 75% and a mutation rate of 20%. Each generation contains 10 times the number of decision variables or a maximum of 1,000 chromosomes and the maximum number of fitness evaluations (the computational budget) is set to 5,000 per daily solution.

The daily repair and inspection rates represent the average observed repair rate following the Christchurch earthquake, due to the lack of the specific data enabling a time-varying rate to be reasonably assigned. This simple assumption allows all pipe failures to be discovered and repaired over the observed recovery period of 62 days (i.e. that the recovery period following the optimization process is not excessively longer or shorter than the observed one). However, as noted by (Eidinger and Tang, 2012, p. 159), these quantities have largely varied over time during the Christchurch recovery as resources were pulled out of neighbouring regions to participate to the restoration effort. The restoration capacity in a real case is treated in Section 3.4.3. The assigned weights give the same importance to the population and the utility of buildings, excluding de facto non-critical and non-inhabited buildings from the optimization process (e.g. sport and cultural facilities). This choice is consistent with previous observations made on the weighting choice presented in Section 3.3.2. However, given the relatively low population density of Christchurch (most of the buildings are family houses), results are not expected to be significantly different with another weighting. The GA-related parameters are chosen such that a relatively high diversity of chromosomes is held over generations by enforcing most of the genes to be exchanged between mating solutions and frequent mutation. The number of different solutions per optimization problem is set according to the recommendations of Storn (1996) and Mallipeddi and Suganthan (2008) for low dimensionality problems. In addition to the computational burden a large chromosome population imposes, it is seen as an obstacle to convergence in evolutionary algorithms (Mallipeddi and Suganthan, 2008 and Chen et al., 2015). Hence, fixing its upper bound should also improves its convergence. Fixing the computational budget for each periodic solution, the number of generations inversely varies with the population size such that the total number of chromosomes does not exceed 5,000 fitness evaluations (i.e. the minimum number of generation is five). Hence, the algorithm can create up to a maximum of ten generations, when the population size does not exceed 500 chromosomes.

3.4.2 Optimized recovery

Figure 3.5 presents the optimized water service restoration time given the observed pipe failures and aforementioned assumptions. The pump station restoration time is identical to that presented in Figure 3.3. The application of the proposed methodology leads to noteworthy improvements when compared with the inferred recovery in Figure 3.3. First, North New Brighton (location indicated in Figure 3.1) recovers faster than was inferred from historical repairs in Figure 3.3. Moreover, most of the Port Hills region regains access to the water supply system more quickly. However, the *Red Zone*, Bromley, Southshore and the rest of New Brighton suffer from longer water outages. This is explained by the difficulty that the inspection algorithm has in efficiently targeting pipes that have actually failed as subsequently discussed.

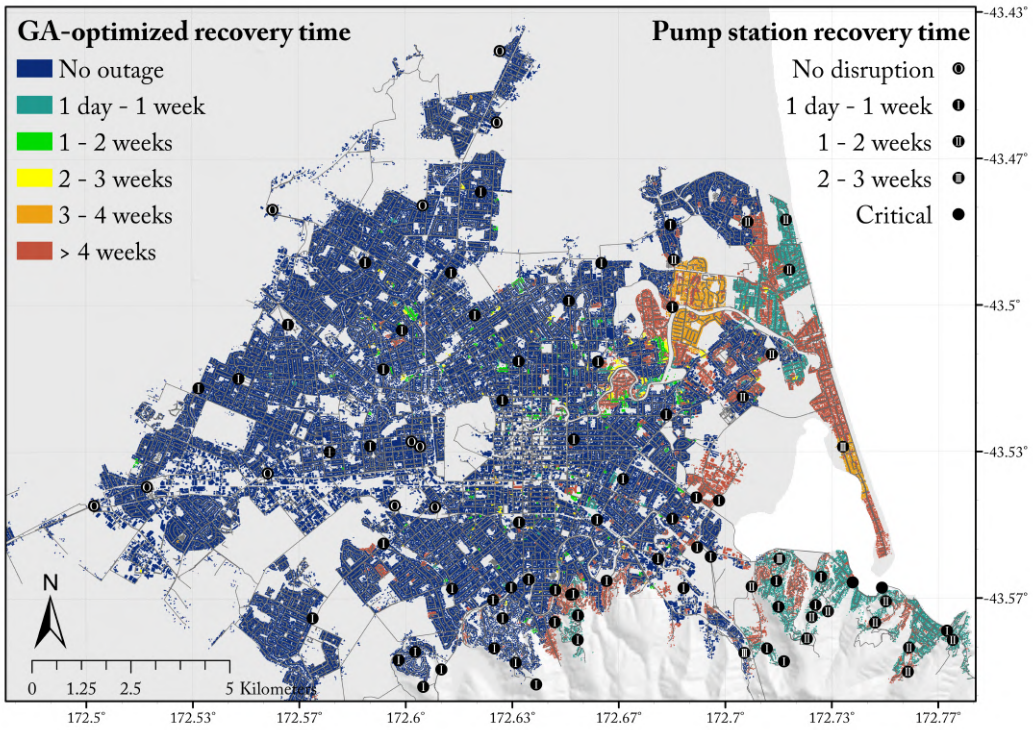

Figure 3.5: Map of time for reconnection to water supply network after the 2011 February Mw 6.2 Christchurch earthquake following the GA-optimized process

Figure 3.6 illustrates the optimized recovery curves and comparison to the inferred recovery curves. Most of the analysed metrics exhibit a steeper slope at the beginning of the recovery. This highlights the significant gains possible by optimization with an emphasis on pipes with high failure probability, low disconnection probability, and those servicing large community areas. A relatively steep slope is also observed after 21 days of recovery and corresponds to the power restoration of the New Brighton pump station and some repairs carried out in the *Red Zone*. However, the rate of improvements tend to be nullified over time. As the failure of individual pipelines is poorly predicted as noted in Figure 3.7 (a), the inspection schedule (the order in which pipes are inspected) fails to efficiently prioritize actually damaged pipes using Equation 3.4. In other words, as pipe inspection becomes less accurate, the number of interesting repair options tends to diminish over time. This issue could be mitigated by assessing the probability of failure with multiple or other fragility functions based on more advanced statistical methods (e.g. Bagriacik et al., 2018).

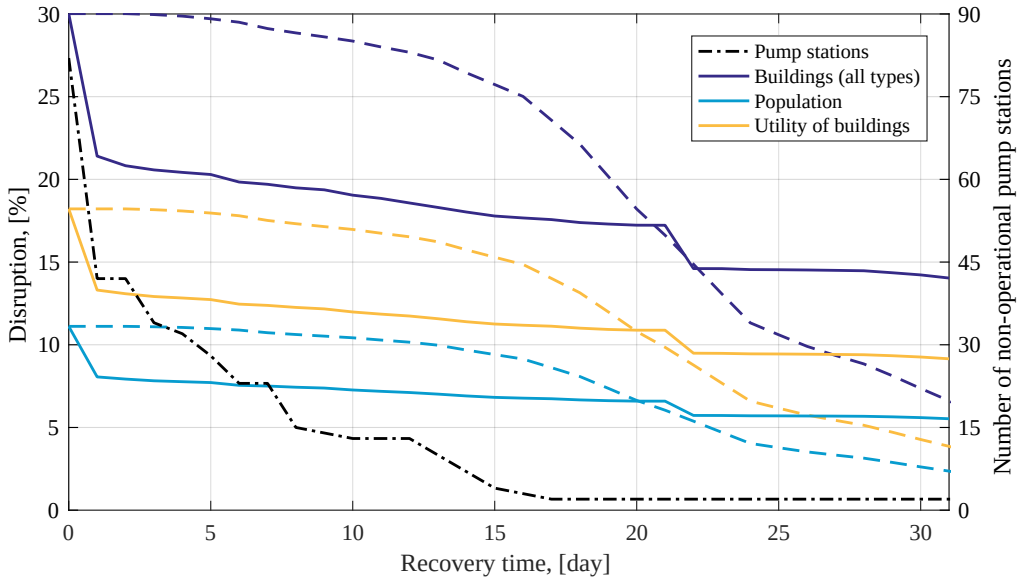

Figure 3.6: Pump station restoration curve and water access recovery curves of the global metrics (Buildings (all types), Population and Utility of Buildings) following the 2011 February Mw 6.2 Christchurch earthquake. Solid lines indicate GA-optimized results, whereas dashed lines show the mean inferred recovery time.

Nevertheless, as the steep slope of the recovery curve on day 1 and 21 suggests, when critical pipe failures are discovered, the optimization algorithm remains highly efficient. Despite this limitation, taking the lower bound of both the inferred and optimized recovery, the water supply network would have significantly gained in resilience. Equations 3.13 to 3.15 quantify the effect of the recovery optimization by looking at the difference of resilience R as described in Equation 3.3 (ΔR), the resilience loss reduction (ΔLR), and the total absolute gain (G), respectively.

$$\Delta R = R_{Inferred} - R_{Optimized} \tag{3.13}$$

$$\Delta LR = \frac{\Delta R}{1 - R_{Inferred}} \tag{3.14}$$

$$G = \Delta R \cdot \text{Quantity}_{Metric} \tag{3.15}$$

where $R_{Inferred}$ and $R_{Optimized}$ are the resilience of a given metric based on the inferred and optimized recoveries, respectively, and Quantity_{Metric} is the total quantity of a given metric as presented in Subsection 3.2.1. Table 3.2 quantitatively presents the benefits of applying the proposed optimization framework.

Table 3.2: Quantitative summary of the recovery optimization gains for the selected metrics

Metrics	**Optimized resilience** $R_{Optimized}$	**Resilience gain** ΔR	**Resilience loss reduction** ΔLR	**Total absolute gain** G
Population	96.4%	0.85%	18.9%	186,000
Utility	94.1%	1.35%	18.5%	186,000
Buildings (all types)	90.4%	2.56%	21.0%	333,000
Business buildings	96.2%	$\ll$0.1%	$\ll$0.1%	288
School buildings	94.8%	1.43%	21.7%	1,980
Medical buildings	99.1%	$\ll$0.1%	$\ll$0.1%	6
Critical buildings	98.9%	0.44%	29.3%	15

It must be noted that results presented in Figures 3.5 and 3.6, and in Table 3.2 only represent the lower-bound improvement possible using the proposed optimization method. By improving the accuracy of the pipe failure prediction, and relaxing the constraints of constant repair and inspection rates, a greater optimization would be possible.

3.4.3 Real-time application

As can be derived from the discussion in the previous section, applying this framework on a real-time recovery would necessitate some adjustments on how the inspection priorities are established, the pipe failure database is managed and the repair capacity is estimated.

The proposed inspection method assesses pipeline integrity based on the score it obtained from Equation 3.4 irrespective of its relative location in respect with other inspections to be carried out. Two problems arise from this. First, inspections are not, and cannot, be carried out this way as inspection teams do not inspect small pipelines individually. Instead, they try to discover pipe failures in one specific area and move to the next one once the network is believed restored at the present location. Hence, the inspection list should be used as an indicator to target areas in which the inspection teams' work will have the highest chances of discovering critical pipe failures. The second problem is the noted poor performance of the individual pipe failure estimation. This can be improved following two different approaches. As already noted, the first option would be the use of improved fragility functions based on more advanced statistical methods. A second option would be to combine post-earthquake LiDAR survey to assess land damage, as it was the case following the major events from the Canterbury Earthquake Sequence (Hughes et al., 2015), with ground strain-based pipeline fragility functions (e.g. O'Rourke et al., 2014; Bouziou and O'Rourke, 2017). This option would remove the intensity measure uncertainty by direct observations, but is unable to assess damage due to transient ground motion. Further research is needed to explore the potential of such ideas. A third option could consist of a periodic Bayesian update of the pipe probability of failure based on observations obtained during the damage inspections throughout the recovery itself. Subsequently, the inspection priority score can be re-evaluated and inspections would be redirected to more critical locations. Note also that some situations (e.g. major medical facility deprived from water) may require more holistic approaches such that the operator will prioritize inspections in potentially less damage areas in order to remedy critical issues.

During the inspection process, some of the discovered pipe failures might not be critical (i.e. they do not hinder the global functioning of the network). Hence, these failures should not be included into the database used by the genetic algorithm to generate solutions, but left for the post-recovery phase as part of a long-term effort to restore or enhance the network quality.

As the inspection capacity was only useful to infer the recovery, the only constraint of the problem becomes the repair capacity. The availability of this resource significantly fluctuates over time and should therefore be carefully and periodically assessed. Two factors can influence the periodic repair capacity. First, the number of repair teams can vary over time as noted by Eidinger and Tang (2012, pp. 159), and second repairing trunk main and main pipelines generally requires more resources and time than repairing submain pipelines as noted by Federal Emergency Management Agency (2003, Table 8.1.c) and Cousins (2013, Table A.4.3). By constantly re-assessing the repair capacity and updating the pipe failure database, this framework could be applied on a daily basis, helping emergency managers to efficiently implement their strategy.

In some instances, the objective of the emergency manager may differ from that proposed by the algorithm. In such cases, the emergency manager can decide to prioritize the repairs differently than the proposed algorithm. The effective changes in the pipe failure database (executed repairs) will be taken into account in the next assessed repair period. In other words, the algorithm adapts its next solution to the previous manger's decision and not to its own solution.

3.5 Conclusion

This paper presented an inferred estimation of the Christchurch water supply recovery following the 22 February 2011 Mw 6.2 Christchurch earthquake and subsequently the development of a genetic algorithm method to optimize the recovery of such systems for potential future events. Based on reported network performance and for a network possessing well-distributed water sources, it was shown that a connectivity analysis is sufficient to estimate the disruption once the majority of the pump stations are operational. As noted in other prior studies, the performance of water supply network is therefore strongly correlated with the power availability to pump stations. However, pipe failures remain a critical factor to restore services, with approximately 30% of buildings remaining without water access after electricity was restored to the majority of the city.

The presented optimization method, as applied to this case study, reduced the proportion disruption after two days by approximately 30% and reduced overall system resilience loss by 20%. However, the restoration of the water services would have taken longer in some areas due to the inefficiency of the adopted pipeline fragility function to accurately determine the probability of individual pipe failure. It must also be noted that no optimization was realized on the restoration of facilities (e.g. pump stations or wells). A global optimization on facilities and pipes could be carried out by iteratively combining the proposed model with a facility restoration model (e.g. Xu et al., 2007). Utilizing this framework, further studies can also determine the optimal number of repair teams deploy following an event. The same methodology could also be applied to other lifelines such as the sewerage system, the gas distribution network or the telecommunication network. Finally, it must be stressed that, combining the best of both the human holistic approach of such a problem and the optimized tactical solutions created by the algorithm would significantly reduce the indirect losses due to lifeline disruption.

3.6 Data and resources

Matthew Hughes (University of Canterbury) provided the building footprint, land usage, meshblock, liquefaction resistance index and ground motion intensity maps as well as the water supply network and pipe failures databases. The power outage map was developed and provided by Roger Paredes and Leonardo Dueñas-Osorio (Rice University). Census information of each meshblock can be found at: `http://www3.stats.govt.nz/meshblock/2013/excel/2013_mb_dataset_Canterbury_Region.zip?_ga=2.241809418.94925561.1523564544-257358082.1516912122`. The authors developed an object-oriented software in C/C++ utilizing the Intel Math Kernal Library (Intel, 2017a) as well as the Intel Message Passing Interface library (Intel, 2017b) for the computation performed. These packages must be installed in order to compile and execute the program. The source code is available in the github repository: `https://github.com/xavierbellagamba/NetworkRecovery`.

3.7 Acknowledgement

The authors thank the three anonymous peer-reviewers, whose comments help to improve the overall quality of this study as well as Irmana Sampedro Garcia and Karn Snyder-Bishop (Christchurch City Council) for sharing their insights on the historical recovery. Matthew Hughes (University of Canterbury) provided several datasets used in the study as well as some insights on the historical recovery. Roger Paredes and Leonardo Dueñas-Osorio (Rice University) shared their power outage dataset. This project was supported by QuakeCoRE, a New Zealand Tertiary Education Commission-funded Centre, Resilience to Nature's Challenges, a Science National Challenge overseen by the New Zealand Ministry of Business, Innovation and Employment, and also the Royal Society of New Zealand Rutherford Discovery Fellowship. This is QuakeCoRE publication number 0297.

3.8 References

Bagriacik, A., Davidson, R., Bradley, B., Hughes, M., and Cubrinovski, M., 2018. Comparison of Statistical and Machine Learning Approaches to Modeling Earthquake Damage to Water Pipelines. *Soil Dynamics and Earthquake Engineering* **112**, 76–88.

Bellagamba, X., Bradley, B., Wotherspoon, L., and Hughes, M., Accepted. Development and validation of fragility functions for buried pipelines based on Canterbury earthquake sequence data. *Earthquake Spectra* .

Bocchini, P., Deodatis, G., and Ellingwood, B., 2013. Computational procedure for the assisted multi-phase resilience-oriented disaster management of transportation systems. *G. Deodatis, BR Ellingwood, & Frangopol (Eds.), Safety, reliability, risk, and life-cycle performance of structures and infrastructures* pp. 581–588.

Borden, F., 1997. *The 1994 Northridge earthquake and the fires that followed*. Building and Fire Research Laboratory, National Institute of Standards and Technology.

Bouziou, D. and O'Rourke, T., 2017. Response of the Christchurch water distribution system to the 22 February 2011 earthquake. *Soil Dynamics and Earthquake Engineering* **97**, 14–24.

Bouziou, D., O'Rourke, T., Cubrinovski, M., and Henderson, D., 2015. Evaluation of ground deformations during the 2010–2011 Canterbury earthquake sequence. In *Proceedings of the 6th International Conference on Earthquake Geotechnical Engineering*. Christchurch, New Zealand.

Bradley, B., 2014. Site-specific and spatially-distributed ground-motion intensity estimation in the 2010–2011 Canterbury earthquakes. *Soil Dynamics and Earthquake Engineering* **61**, 83–91.

Bradley, B. and Cubrinovski, M., 2011. Near-source strong ground motions observed in the 22 February 2011 Christchurch earthquake. *Seismological Research Letters* **82**, 853–865.

Bradley, B., Quigley, M., Van Dissen, R., and Litchfield, N., 2014. Ground motion and seismic source aspects of the Canterbury earthquake sequence. *Earthquake Spectra* **30**, 1–15.

Bruneau, M., Chang, S., Eguchi, R., Lee, G., O'Rourke, T., Reinhorn, A., Shinozuka, M., Tierney, K., Wallace, W., and von Winterfeldt, D., 2003. A framework to quantitatively assess and enhance the seismic resilience of communities. *Earthquake spectra* **19**, 733–752.

Chang, S., Taylor, J., Elwood, K., Seville, E., Brunsdon, D., and Gartner, M., 2014. Urban disaster recovery in Christchurch: the central business district cordon and other critical decisions. *Earthquake Spectra* **30**, 513–532.

Chen, S., Montgomery, J., and Bolufé-Röhler, A., 2015. Measuring the curse of dimensionality and its effects on particle swarm optimization and differential evolution. *Applied Intelligence* **42**, 514–526.

Choi, C. (ed.), 2017. *Global Prospectus*. The Rockfeller Foundation, New York City, NY.

Chung, R., Ballantyne, D., Comeau, E., Holzer, T., Madrzykowski, D., Schiff, A., Stone, W., Wilcoski, J., Borcherdt, R., Cooper, J. et al., 1996. *January 17, 1995 Hyogoken-Nanbu (Kobe) Earthquake: Performance of Structures, Lifelines, and Fire Protection Systems (NIST SP 901). Tech. rep.*, National Institute of Standards and Technology.

Cimellaro, G., Reinhorn, A., and Bruneau, M., 2010. Framework for analytical quantification of disaster resilience. *Engineering Structures* **32**, 3639–3649.

Cousins, J., 2013. *Wellington Without Water - Impact of Large Earthquakes. Tech. rep.*, GNS Science Report, Lower Hutt, New Zealand.

Cubrinovski, M., Bradley, B., Wotherspoon, L., Green, R., Bray, J., Wood, C., Pender, M., Allen, J., Bradshaw, A., Rix, G. et al., 2011. Geotechnical aspects of the 22 February 2011 Christchurch earthquake. *Bulletin of the New Zealand Society for Earthquake Engineering* **44**, 205–226.

Cubrinovski, M., Hughes, M., Bradley, B., Noonan, J., Hopkins, R., McNeill, S., and English, G., 2014. *Performance of horizontal infrastructure in Christchurch city through the 2010-2011 Canterbury earthquake sequence. Tech. rep.*, University of Canterbury. Civil and Natural Resources Engineering, Christchurch, New Zealand.

Dahlhamer, J., Tierney, K., and Webb, G., 1999. *Predicting business financial losses in the 1989 Loma Prieta and 1994 Northridge Earthquakes: Implications for loss estimation research. Tech. rep.*, Disaster Research Center, University of Delaware, Newark, DE.

Davis, C., 2014. Water system service categories, post-earthquake interaction, and restoration strategies. *Earthquake Spectra* **30**, 1487–1509.

Dellow, G., Yetton, M., Massey, C., Archibald, G., Barrell, D., Bell, D., Bruce, Z., Campbell, A., Davies, T., De Pascale, G. et al., 2011. Landslides caused by the 22 February 2011 Christchurch earthquake and management of landslide risk in the immediate aftermath. *Bulletin of the New Zealand Society for Earthquake Engineering* **44**, 227–238.

Eidinger, J. and Tang, A., 2012. *Christchurch, New Zealand Earthquake Sequence of Mw 7.1 September 04, 2010 Mw 6.3 February 22, 2011 Mw 6.0 June 13, 2011: Lifeline Performance. Tech. rep.*, Technical Council on Lifeline Earthquake Engineering, Reston, VA.

Fang, Y. and Sansavini, G., 2017. Emergence of Antifragility by Optimum Postdisruption Restoration Planning of Infrastructure Networks. *Journal of Infrastructure Systems* **23**, 04017024.

Fawcett, T., 2006. An introduction to ROC analysis. *Pattern recognition letters* **27**, 861–874.

Federal Emergency Management Agency, 2003. *HAZUS-MH MR4 Technical Manual. Tech. rep.*, National Institute of Building Sciences, Washington DC.

Feng, C.-M. and Wang, T.-C., 2003. Highway emergency rehabilitation scheduling in post-earthquake 72 hours. *Journal of the Eastern Asia Society for Transportation Studies* **5**, 3276–3285.

Fenwick, T., Hoskin, K., and Brunsdon, D., 2011. *Resilience Lessons: Orion's 2010 and 2011 Earthquake Experience. Tech. rep.*, Kestrel Group, Wellington, New Zealand.

Fraser, I. (ed.), 2017. *Building Urban Resilience in New Zealand: Lessons from our Major Cities*. Centre for Disaster Resilience, Recovery and Reconstruction, University of Auckland, Auckland, New Zealand.

Giovinazzi, S., Stevenson, J., Mitchell, J., and Mason, A., 2012. Temporary housing issues following the 22nd Christchurch Earthquake, NZ. In *Proceedings of the 2012 New Zealand Society for Earthquake Engineering Conference*, pp. 13–15. New Zealand Society for Earthquake Engineering, Ground Floor, 158 The Terrace Wellington 6144 New Zealand, Christchurch, New Zealand.

Giovinazzi, S., Wilson, T., Davis, C., Bristow, D., Gallagher, M., Schofield, A., Villemure, M., Eidinger, J., and Tang, A., 2011. Lifelines performance and management following the 22 February 2011 Christchurch earthquake, New Zealand: highlights of resilience. *Bulletin of the New Zealand Society for Earthquake Engineering* **44**, 402–417.

Hallegatte, S., 2008. An adaptive regional input-output model and its application to the assessment of the economic cost of Katrina. *Risk analysis* **28**, 779–799.

Haupt, R. and Haupt, S., 1998. *Practical genetic algorithms, second edition*. Wiley Interscience.

Hughes, M., Nayyerloo, M., Bellagamba, X., Morris, J., Brabhaharan, P., Rooney, S., Hobbs, E., Wooley, K., and Hutchison, S., 2017. Impacts of the 14th November 2016 Kaikoura Earthquake on the Three Water Systems in Wellington, Marlborough and Kaikoura, New Zealand: Preliminary Observations. *Bulletin of the New Zealand Society for Earthquake Engineering* **50**, 306–317.

Hughes, M., Quigley, M., van Ballegooy, S., Deam, B., Bradley, B., Hart, D. et al., 2015. The sinking city: Earthquakes increase flood hazard in Christchurch, New Zealand. *GSA Today* **25**.

Hynes, W., Purcell, S., Walsh, S., and Ehimen, E., 2016. *IRGC resource guide on resilience, v29-07-2016*, chap. Formalizing Resilience Concepts for Critical Infrastructure. EPFL International Risk Governance Center (IRGC), Lausanne, Switzerland.

Intel, 2017a. Intel Math Kernel Library.

Intel, 2017b. Intel Message Passing Interface.

Jayaram, N. and Baker, J., 2009. Correlation model for spatially distributed ground-motion intensities. *Earthquake Engineering & Structural Dynamics* **38**, 1687–1708.

King, A., Middleton, D., Brown, C., Johnston, D., and Johal, S., 2014. Insurance: Its role in recovery from the 2010-2011 Canterbury earthquake sequence. *Earthquake Spectra* **30**, 475–491.

Klise, K., Bynum, M., Moriarty, D., and Murray, R., 2017. A software framework for assessing the resilience of drinking water systems to disasters with an example earthquake case study. *Environmental Modelling & Software* **95**, 420–431.

Love, T., 2011. *Population movement after natural disasters: a literature review and assessment of Christchurch data. Tech. rep.*, Sapere Research Group, Wellington, New Zealand.

Mallipeddi, R. and Suganthan, P., 2008. Empirical study on the effect of population size on differential evolution algorithm. In *Evolutionary Computation, 2008. CEC 2008.(IEEE World Congress on Computational Intelligence). IEEE Congress on*, pp. 3663–3670. IEEE.

McReynolds, L. and Simmons, R., 1995. LA's rehearsal for the big one. *Journal-American Water Works Association* **87**, 65–70.

Miles, S. and Chang, S., 2006. Modeling community recovery from earthquakes. *Earthquake Spectra* **22**, 439–458.

Mitchell, M., 1998. *An introduction to genetic algorithms*. MIT press.

O'Rourke, T., Jeon, S.-S., Toprak, S., Cubrinovski, M., Hughes, M., van Ballegooy, S., and Bouziou, D., 2014. Earthquake response of underground pipeline networks in Christchurch, NZ. *Earthquake Spectra* **30**, 183–204.

Rose, A., Benavides, J., Chang, S., Szczesniak, P., and Lim, D., 1997. The regional economic impact of an earthquake: Direct and indirect effects of electricity lifeline disruptions. *Journal of Regional Science* **37**, 437–458.

Statistics New Zealand, 2013a. 2013 Census meshblock dataset. http://archive.stats.govt.nz/Census/2013-census/data-tables/meshblock-dataset.aspx.

Statistics New Zealand, 2013b. *The census has been held every five years, with only four exceptions*. `http://archive.stats.govt.nz/Census/2013-census/info-about-the-census/intro-to-nz-census/history/did-you-know/every-five-years.aspx`[Accessed: May 2018].

Stevenson, J., Becker, J., Cradock-Henry, N., Johal, S., Johnston, D., Orchiston, C., and Seville, E., 2017. Economic and social reconnaissance: Kaikōura Earthquake 2016. *Bulletin of the New Zealand Society for Earthquake Engineering* **50**, 346–355.

Stevenson, J., Kachali, H., Whitman, Z., Seville, E., Vargo, J., and Wilson, T., 2011. Preliminary observations of the impacts the 22 February Christchurch Earthquake had on organisations and the economy: A report from the field (22 February-22 March 2011). *Bulletin of the New Zealand Society for Earthquake Engineering* **44**, 65.

Stevenson, J., Vargo, J., Seville, E., Kachali, H., McNaughton, A., and Powell, F., 2012. *The Recovery of Canterbury's Organisations: A comparative analysis of the 4 September 2010, 22 February and 13 June 2011 Earthquake. Tech. rep.*, University of Canterbury. Civil and Natural Resources Engineering, Christchurch, New Zealand.

Storn, R., 1996. On the usage of differential evolution for function optimization. In *Fuzzy Information Processing Society, 1996. NAFIPS., 1996 Biennial Conference of the North American*, pp. 519–523. IEEE.

Tabucchi, T., Davidson, R., and Brink, S., 2010. Simulation of post-earthquake water supply system restoration. *Civil Engineering and Environmental Systems* **27**, 263–279.

Tierney, K., 1997. Business impacts of the Northridge earthquake. *Journal of Contingencies and Crisis Management* **5**, 87–97.

Xu, N., Guikema, S., Davidson, R. A., Nozick, L., Çağnan, Z., and Vaziri, K., 2007. Optimizing scheduling of post-earthquake electric power restoration tasks. *Earthquake engineering & structural dynamics* **36**, 265–284.

Yao, M. and Min, K., 1998. Repair-unit location models for power failures. *IEEE Transactions on Engineering Management* **45**, 57–65.

Zorn, C. and Shamseldin, A., 2016. Quantifying directional dependencies from infrastructure restoration data. *Earthquake Spectra* **32**, 1363–1381.

3.9 Complementary material

3.9.1 Predictive performance of the pipe damage and building connectivity model

This section presents the predictive performance details for both the pipe damage and building connectivity analyses. First, the receiver operation characteristics curves are defined and discussed. Second, differences observed between the inferred and predicted metrics are given and interpreted.

Figure 3.7 provides a summary of the model performance prediction. Figure 3.7 (a) illustrates the cumulative distribution functions (CDF) of the pipes that remained intact (i.e. CDF of the true negatives) and the pipes that failed given the estimated probability of failure of the model (i.e. CDF of the true positives). Figure 3.7 (c) exhibits the buildings that remained historically connected to the water supply network (i.e. CDF of the true negatives) and the buildings that were historically disconnected from the water supply network given the estimated probability of disconnection (i.e. CDF of the true positives). Figures 3.7(b) and (d) show the receiver operating characteristics (ROC) curve for the pipe failure and building disconnection classification, respectively. The area under these curves (AUC) quantifies the model performance (Fawcett, 2006).

In Figures 3.7 (a) and (c), the ideal case (i.e. when the predictions always perfectly match the inferred results) would be vertical CDFs in 0 and 1 for the true negatives and the true positives, respectively. As it can be observed in both Figures 3.7(a) and (c), the true negatives are relatively well predicted as the CDFs tends to be relatively steep towards 0 and flatten out as the probability of

failure or disconnection increases. However, in Figure 3.7 (a), the true positives (observed failed pipes) are poorly predicted. This issue arises from the construction of Poissonian-based fragility functions for horizontal infrastructure, as they are "*less capable of prediction at the individual pipe [...] level*" as noted by Bagriacik et al. (2018). Nevertheless, the global performance remains acceptable with the AUC is equal to 0.7, a value of 1 being perfect. The building disconnection also suffers from a lack of true positive prediction accuracy for several reasons. First, given the high redundancy of the analysed system, the Monte-Carlo simulations of the prediction rarely yields a 100% disconnection probability for a particular building, partially explaining the relatively flat slope below the 95% of disconnection probability. Second, the number of true positives is relatively low compared to the number of the true negatives, inducing less robust results. Nevertheless, the true positive CDF remains below the identity line, indicating a good prediction rate. The goodness of the connection prediction rate is further corroborated by the high AUC (0.92).

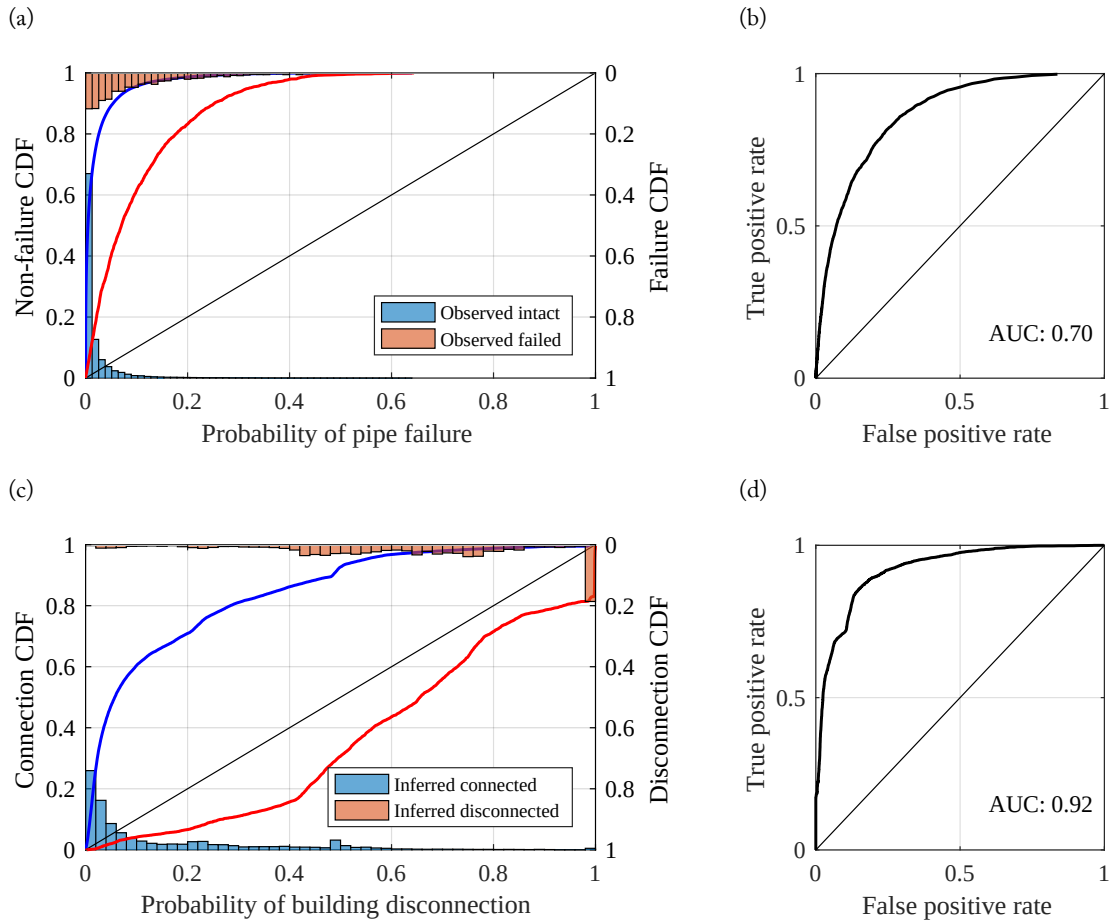

Figure 3.7: Performance of the pipe failure modelling as (a) CDFs and histograms of the true negatives (non-failed pipes) in blue and true positives (failed pipes) in red ; and (b) ROC curve ; and performance of the building connection modelling as (c) CDFs and histograms of the true negatives (connected buildings) in blue and true positives (disconnected buildings) in red ; and (d) ROC curve

Figure 3.8 compares the values from the co-seismic performance inference of the selected metrics with the prediction distribution. Most of the inferred values remain close to the mode of their respective prediction distribution with the notable exception of the medical buildings. In this case, due to the topology of the network and the location of the buildings, less buildings were deprived of water that what was previously inferred. It is worth noting that there are few medical and critical buildings (377 and 55, respectively) comparatively to the total number of buildings (209,442), leading, in the

case of the critical buildings to a non-smooth distribution. The population metric seems to also be slightly overpredicted, whereas the buildings (all types) metric shows the opposite trend. This can indicate that too many residential buildings are predicted to lose their connections to the water supply network and/or that the predicted, impacted areas possess a higher population density than the one simulated from the inferred results. Albeit less pronounced, the same trend can be observed for the utility of buildings.

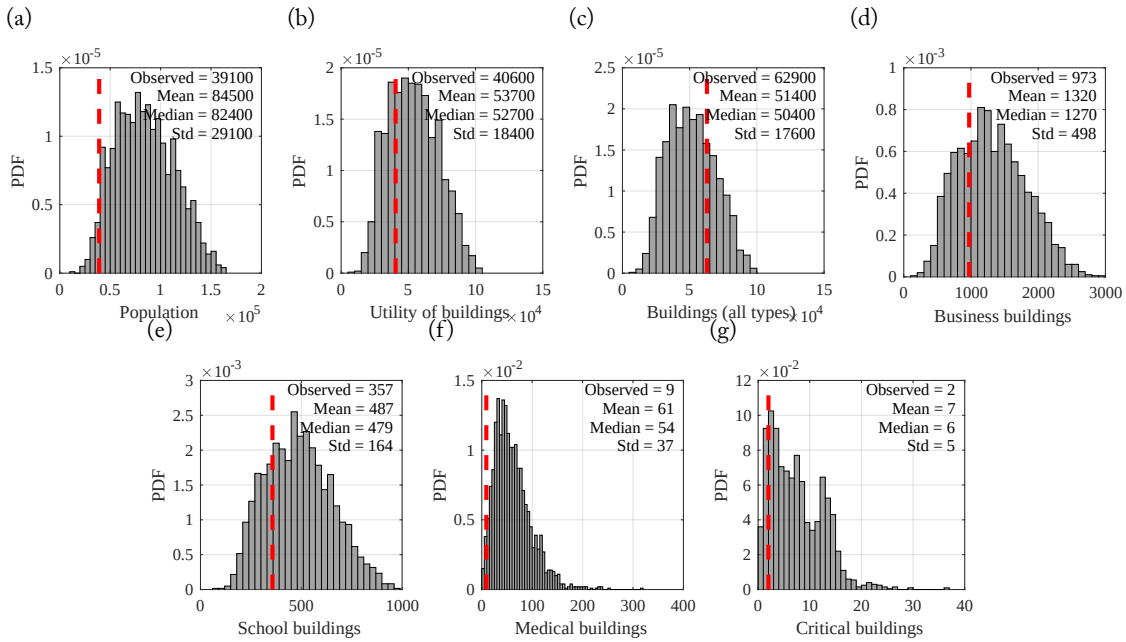

Figure 3.8: Histograms of the prediction distribution for the selected metrics showing deprivation of water supply and comparison with inferred actual results (indicated as a red dashed line)

This page is intentionally left blank

Chapter 4

Real-time source identification and ground motion prediction from major earthquakes using machine learning algorithms trained on simulations

"To become good at anything you have to know how to apply basic principles. To become great at it, you have to know when to violate those principles."

Garry Kasparov, 2017, Deep Thinking

Adapted from: Bellagamba X, Bradley BA, and Vetrova V (in preparation). "Real-time source identification and ground motion prediction from major earthquakes using machine learning algorithms trained on simulations".

This paper presents a machine learning (ML)-based approach for near-real-time earthquake source identification and ground motion intensity prediction. In contrast to conventional methods that employ geophysical inversion for earthquake location and moment tensor properties, and empirical ground motion models; ML is applied to a large dataset of kinematic rupture and physics-based ground motion simulations to develop an *earthquake rupture discriminator* and *ground motion generator*. Based on observed ground motions at instrument locations occurring in real-time the ML algorithm determines the causative fault rupture(s), in a probabilistic sense, and the consequent ground motion intensity (through various intensity measures) over the region of interest. To illustrate the approach we use a New Zealand case study with a dataset of approximately 17,000 rupture and ground motion simulations from 487 different fault geometries, stored at over 20,000 spatial locations, including instrument network locations. We present the development and training of the algorithm, as well as stress-testing through and edge case in which we retrospectively consider near-real-time application for the (extraordinarily complex) 14 November 2016 Kaikōura earthquake, and compare to the results from conventional approaches. Finally, we also reflect on limitations based on the considered training data, and potential going forward with the expected exponential growth in simulation datasets.

4.1 Introduction

Earthquake source identification and ground motion prediction (and subsequent impact estimation (Wald *et al.*, 2008b)) in near-real-time following major earthquakes is critical for emergency response, international aid assessment, and scientific enquiry.

Near-real-time earthquake source identification can be considered hierarchical in its difficulty in that a first-order estimate in the form of a centroid location and moment tensor can be obtained routinely and relatively rapidly (Hayes, 2011), whereas obtaining further information on the finite nature of the causative fault and rupture kinematics and dynamics (often referred to as source inversion (Graves & Wald, 2001; Wald & Graves, 2001; Ide, 2015)) are increasingly more difficult to determine (including non-uniqueness (Hartzell *et al.*, 2007; Ozgun Konca *et al.*, 2013)), and require a greater time period (following the event origin time) to determine - hindering their use in immediate near-real-time assessment. Unfortunately, for large magnitude earthquakes finite fault effects are crucially important to accurately estimate consequent ground motion intensity in the affected region (Allstadt *et al.*, 2018), with point-source estimates systematically underestimating ground motions, while those based on grossly erroneous finite faults are likely equally poor (albeit can be biased high or low).

Empirical ground motion models are most commonly used in near-real-time ground motion estimates because of: (1) their relative insensitivity to uncertainties in source predictor variables (critical for near-real-time assessment given the sentiments above regarding source identification); (2) emerging physics-based ground motion simulation methods are computationally-intensive, thus cannot be performed rapidly for near-real-time applications, and are also highly sensitive to the (uncertain) representation of the earthquake source. The most widely deployed near-real-time ground motion estimation approach is the ShakeMap procedure (Worden *et al.*, 2010), that combines macroseismic intensity observations (*Did You Feel It?*; Atkinson & Wald (2007)), instrumental measurements (Wald *et al.*, 2008), and empirical ground motion models utilizing globally-available topographic (Verdin *et al.*, 2007), soil condition (Allen & Wald, 2009), information to characterise local site effects. Empirical ground motion models are automatically selected based on rupture parameters and regional seismic information (Garcia *et al.*, 2012), and a spatial correlation (e.g. Jayaram & Baker, 2009; Goda & Atkinson, 2010) is applied to the site-specific ground motion estimate following Verros *et al.* (2017). ShakeMap near-real-time ground motion estimates are subsequently used in PAGER (Wald *et al.*, 2008b) to assess economic losses and casualties.

Physics-based ground motion simulation methods - which explicitly incorporate physics associated with earthquake fault rupture, wave propagation, and surfacial site response - have clear conceptual benefits over empirical ground motion models based on worldwide data from historical earthquakes (Bradley *et al.*, 2017b). Recognition of the utility of ground motion simulations has led to continued efforts in their development (Graves, 1993; Graves *et al.*, 1998; Hartzell *et al.*, 1999; Boore, 2003; Graves & Wald, 2004) and validation (Dreger & Jordan, 2014; Bradley *et al.*, 2017a; Razafindrakoto *et al.*, 2018; Lee *et al.*, 2019). In addition to the consideration of future scenario earthquakes (e.g. Graves *et al.*, 2008; Akinci *et al.*, 2017; Smerzini & Pitilakis, 2018), physics-based ground motion simulation methods have also been utilized for probabilistic seismic hazard analysis (e.g. Graves *et al.*, 2011; Tarbali *et al.*, 2018a). As far as the authors are aware, physics-based ground motion simulation methods have not however been applied in near-real-time source identification or ground motion prediction (potentially due to the aforementioned perceived limitations).

In parallel, and despite numerous challenges (e.g. sparse spatio-temporal data, amorphous boundaries and irregular spacing (Karpatne *et al.*, 2018)), machine learning (ML) techniques are seeing increasing application for problems in geoscience. For example, hurricane formation prediction (Racah *et al.*, 2017), volcanic activity monitoring (Titos *et al.*, 2018), and real-time flood risk (Wiesel *et al.*, 2018). In seismology, Ross *et al.* (2018a,b) use ML for seismogram phase picking, Perol *et al.* (2018) for earthquake source location detection, Bellagamba *et al.* (TBD) for ground motion time series quality classification, Kong *et al.* (2016); Li *et al.* (2018) for earthquake early detection, Hulbert *et al.* (2019) for pre-earthquake stress and displacement prediction, and Rouet-Leduc *et al.* (2019) for subduction zone continuous low-amplitude, tremor-like signals. Further examples are given in Kong *et al.* (2018).

In this paper we present a machine learning (ML)-based approach for near-real-time earthquake source identification and ground motion intensity prediction that utilize a dataset of physics-based ground motion simulations. Training a ML algorithm on the simulations allows for the (potential)

benefits of physics-based simulations over empirical ground motion models; yet avoids the need to explicitly undertake the simulations following the earthquake in real-time. In the following sections we present the case study application that we use for the demonstration of the approach, followed by the ML framework and algorithm training. We examine the performance of the algorithm for an edge case in which we retrospectively consider near-real-time application for the (extraordinarily complex) 14 November 2016 Kaikōura earthquake, and compare to the results from conventional approaches. Finally, we also reflect on limitations based on the considered training data, and potential going forward with the expected exponential growth in simulation datasets.

4.2 Earthquake rupture and ground motion simulation dataset

The utilized data is extracted from Cybershake New Zealand v18.6 (Tarbali *et al.*, 2018b). This data is based on 17,000 physics-based ground motion simulations associated with 487 mapped New Zealand faults from the earthquake rupture forecast model of Stirling *et al.* (2012). Time-series are stored at real instrument locations of the GeoNet network (see data source in Section 4.7) as well as a grid of non-uniform spatial density based on the population distribution and soil characteristics (Tarbali *et al.*, 2018b).

Figure 4.1(a) presentes New Zealand faults, and Figure 4.1(b) GeoNet instrument locations. Note that Cybershake New Zealand v18.6 does not include potential subduction zone ruptures, and also excludes offshore shallow crustal faults that produce negligible onshore ground motion amplitudes. The number of simulated rupture realizations per fault (varying the hypocenter location and kinematic slip, rake, rise time distribution) varies from 25 to 50 as a function of the fault magnitude, and ground motions are simulated over a spatial domain that is a function of the rupture (e.g. location and magnitude, Tarbali *et al.*, 2018b). The simulated waveforms are processed to provide engineering-relevant intensity measures such as the peak ground acceleration (PGA), peak ground velocity (PGV), Arias intensity (AI), significant duration (DS_{595}), and the pseudo-spectral acceleration (pSA) at multiple periods.

In this exploratory study, attention is given primarily to major earthquake events, therefore only faults with moment magnitude Mw greater than 6.8 are retained from the original 487 sources (shown in red in Figure 4.1(a)). Hence, 113 faults and 3,857 ground motion simulations were ultimately considered. Each ground motion simulation has three primary attributes as indicated in the example presented in Figure 4.2 and showing an example of a Fjord-to-Kelly segment of the Alpine Fault (AlpineF2K): (1) a name (so-called label) indicating the causative fault and its cluster identification as described subsequently, (2) the associated simulated ground motion intensity at instrument locations, and (3) the simulated ground motion spatial distribution throughout the region of interest. The left-hand side of Figure 4.2 shows all hypocenter locations for the multiple realizations and simulations of the rupture on the AlpineF2K. Colors indicate the respective cluster (subsequently discussed in Section 4.3.2). The central part of the figure gives the different information relative to the name and location of a particular hypocenter. The right-hand side of the figure provides the simulation results at instrument locations (bottom) and over the wider region of interest (top).

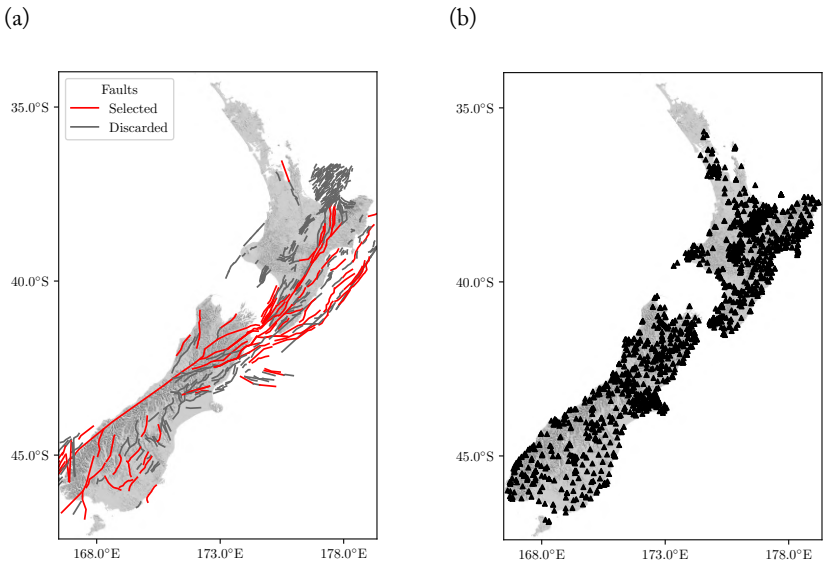

Figure 4.1: (a) Considered faults from the Stirling et al. *(2012) New Zealand earthquake rupture forecast model; and (b) GeoNet instrument locations in New Zealand*

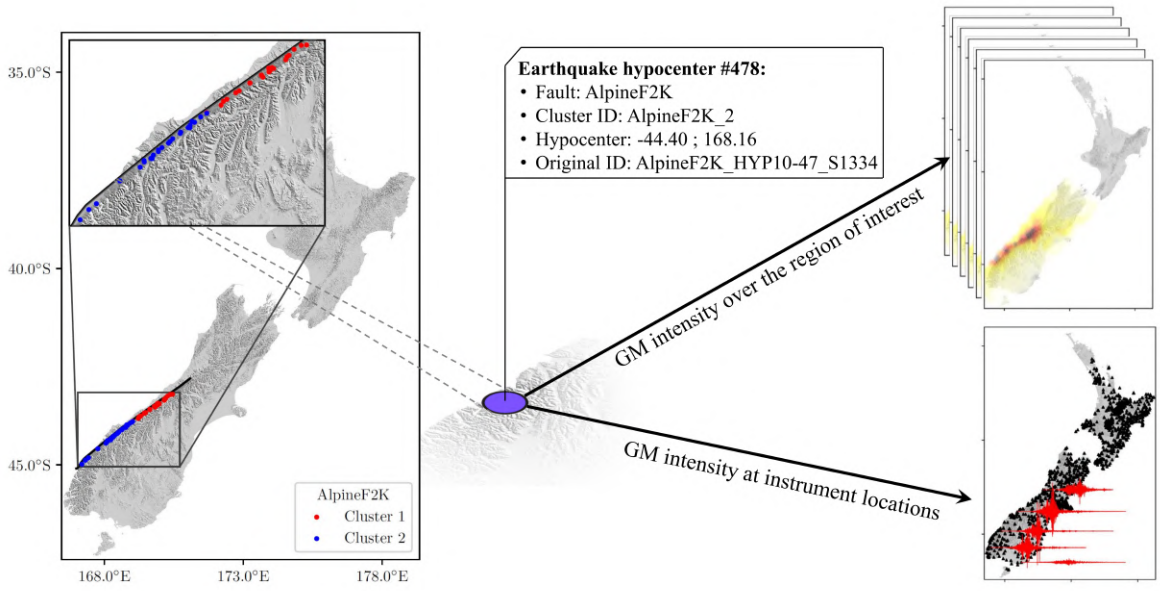

Figure 4.2: Illustration of the data structure for an example AlpineF2K rutpure composed of a label, the associated intensity measures simulated at instrument locations and over the wider region of interest.

4.3 Framework development and algorithm training methodology

As compared to conventional source inversion and regional ground motion estimation, the presented approach is to utilize a comprehensive ensemble of rupture and ground motion simulations to provide a set of potential future earthquakes that may occur in the region of interest (in this case, New Zealand). In the most general sense, a machine learning algorithm (trained on this dataset) can then use observed ground motion characteristics of an earthquake, immediately in real-time, to identify a non-linear

combination of the ruptures from the training dataset that are inferred to have occurred, and similarly, a prediction of the consequent ground motions.

In order to achieve earthquake source identification and estimate the geospatial distribution of ground motion intensities, two different tools are necessary: (1) an earthquake source discriminator, and (2) a ground motion map generator. As machine learning encompasses data-intensive methods that exploit pattern repetitions in training data to correctly predict the class of new data, the grouping of similar ground motion simulations under the same label is also required, as subsequently detailed. The following sections briefly outline the structure of the proposed framework and provide an overview with the aim of providing an intuitive account of the approach and underlying logic of the training method. Comprehensive details about each of the developed methods are given in Sections 4.10.1 and 4.10.2, respectively.

4.3.1 Overview of the training method

The training of the framework occurs in three distinct steps as illustrated in Figure 4.3. First, ruptures from the same considered fault geometry are grouped (clustered) together and re-labelled to form new classes that describe the fault and the ground motion characteristics. Second, the earthquake source discriminator is trained using the ground motion intensity simulated at instrument locations as input and the new rupture cluster labels as target. Third, the ground motion generator is trained by utilizing the earthquake source discriminator output as input, and the simulated ground motion spatial distribution as the target. Once trained, this system uses observed ground motions at instrument locations to provide the probabilities of the potential sources from the training rupture dataset and an estimate of the spatial ground motion intensity.

Figure 4.3 shows the data flows occurring during the training phase and how data propagates through the system in a real application. The entire framework has been implemented in Python 3.6 (see Section 4.7). The rupture clustering algorithm and the earthquake source discriminator have been fitted using the scikit-learn library (Pedregosa *et al.*, 2011), and the ground motion map generator has been developed using Keras (Chollet *et al.*, 2015) with a TensorFlow backend (Abadi *et al.*, 2016).

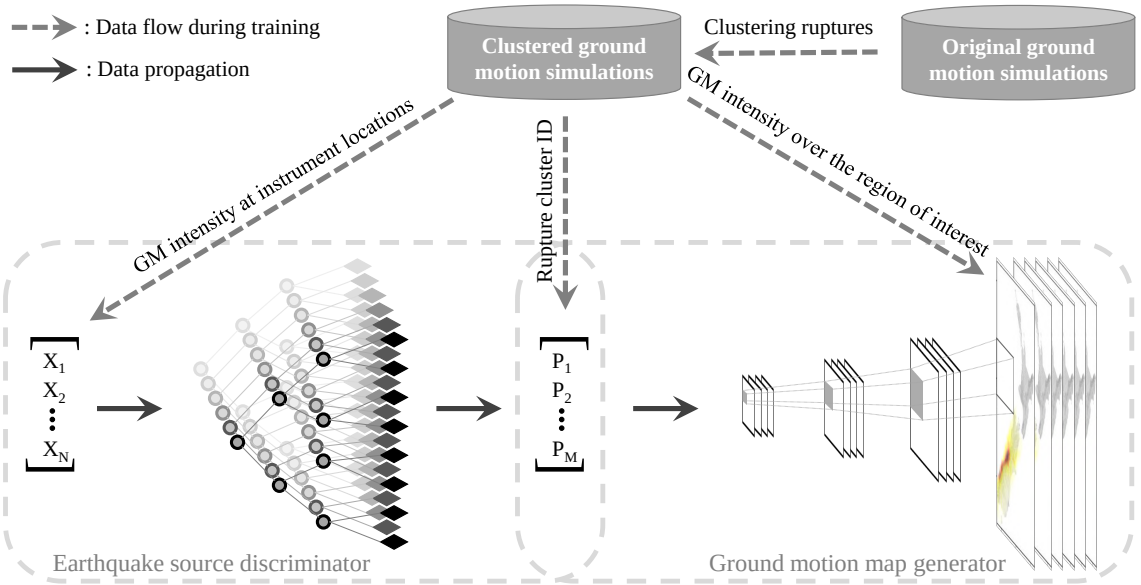

Figure 4.3: Overview of the training and functioning of the proposed framework. $X_1 - X_N$ represent the simulated or recorded ground motion intensity measures at instrument locations, and $P_1 - P_M$ represent the earthquake source discriminator output (the rupture cluster probability of each label).

4.3.2 Earthquake source discriminator

Rupture clustering

Machine learning algorithms exploit repeating patterns and characteristics to classify data. Therefore, it is crucial to group resembling ground motion simulations under the same 'label'. However, earthquakes are by essence unique: influence of source, path and site effects can make recordings vary substantially, even if they originate from the same source idealized geometry. Therefore, it becomes necessary to group similar ruptures from the same fault together. The grouping (or clustering) is generally realized via unsupervised methods, such as K-means clustering, Gaussian mixture or hierarchical clustering (Friedman *et al.*, 2008, pp. 501–520). Unsupervised algorithms use selected intrinsic data characteristics to group similar data points together, such that the variability of salient characteristics within these new groups is minimized.

In the specific application considered hypocenter and kinematic slip, rake, rise time spatial distributions are randomly realized; then these are the characteristics relevant in the clustering. As ruptures from the same fault with different hypocenter locations can generate very different observed ground motion records at a particular instrument location and affect different areas due to directivity effects, simulated ruptures must be grouped such that their hypocenter location can also be identified by the subsequently developed earthquake source discriminator. Kinematic slip, rake, rise time spatial distributions could arguably be of interest as well to accomplish this task, but remains too complex to be integrated within the present exploratory study (discussed in Section 4.6).

As ruptures are characterized with recorded ground motion intensities at instrument locations, these values are used to cluster them. However, the dimensionality of this clustering can be high relative to the number of ruptures to group (maximum number of simulated ruptures per fault geometry is 50). The number of instrument stations greatly exceeds the number of simulations per fault. In order to produce meaningful clusters, this excessively high dimensionality must be reduced. The reduction of dimensions is carried out in two steps. First, instruments are grouped via K-means clustering based on their relative geographic location. Second, rather than having to consider all instruments, a subset is identified. Instruments that show the highest variability of the ground motion intensity of interest within each cluster are selected as their representative. Subsequently, ground motion simulations are grouped via K-means clustering based on the simulated ground motion significant duration (D_{S595}) at selected instruments for a given fault. As significant duration is strongly influenced by the relative hypocentre location to the recording instrument location (Somerville *et al.*, 1997), final clusters from a particular fault separates the data in geographically distinct groups. The minimum number of ruptures within one cluster is set to eight, such that each cluster remains large enough to be split again into subsets as discussed in Section 4.3.2.

Figure 4.4 illustrates the application of clustering for three major faults in terms of hypocenter location realizations: (a) Fjord-to-Kelly segment of the Alpine Fault (AlpineF2K), (b) Offshore Conway segment of the Hope Fault (HopeConwayOS), and (c) Pahaua Fault. The new label of each simulation is therefore composed of its original fault name (e.g. AlpineF2K or Pahaua) and a cluster number of this fault (e.g. 1 or 2). For each fault, the creation of two to five rupture clusters is tested, and the number of selected instruments is set to the currently tested number of rupture clusters plus one. The adequate number of rupture clusters is determined by maximizing the silhouette score of the rupture clustering (Rousseeuw, 1987).

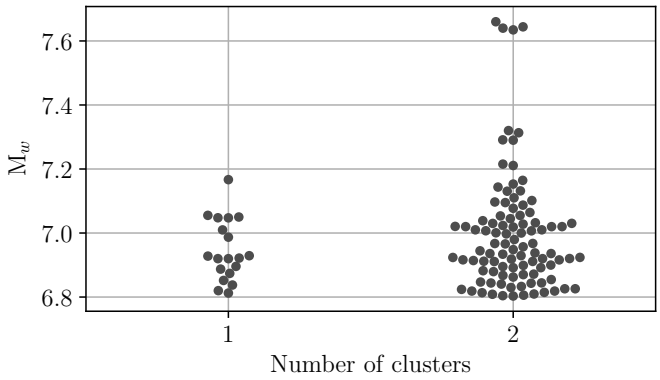

Figure 4.5: Swarm plot showing the relationship between the moment magnitude M_w and the selected number of clusters for the considered faults.

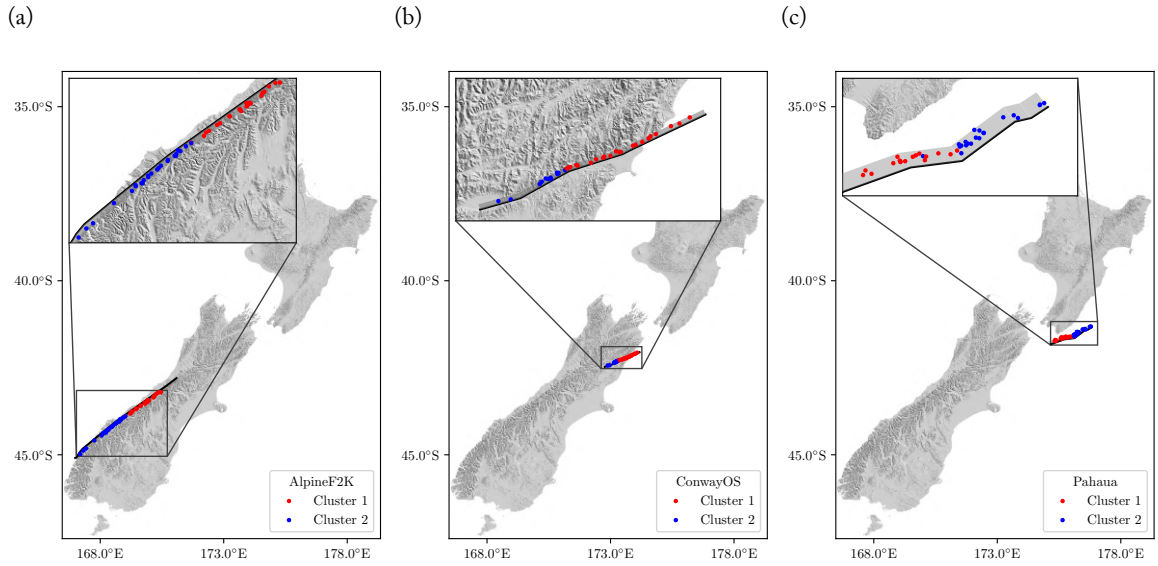

Figure 4.4: Rupture clustering of (a) the AlpineF2K fault; (b) the Hope Conway OS fault; and (c) the Pahaua fault. In all three examples, realizations are clustered in two distinct rupture clusters.

In total, the clustering algorithm creates 213 rupture cluster labels. For the faults shown in Figure 4.4, with the exception of one earthquake realization from the Pahaua fault, the clustering yields hypocenter locations that are largely, geographically distinct. Figure 4.5 gives the number of clusters per fault, indicating that, despite the possibility given to the algorithm to create up to five clusters, and considering the imposed conditions, the optimal number of clusters never exceeds two. The results of this grouping allows the development of subsequent machine learning-based solutions to tackle the two aforementioned problems, namely, source inversion and geospatial ground motion estimation.

Determination of rupture probabilities

Based on the clustered ground motion simulations determined in the previous section, a supervised machine learning algorithm was developed to determine the fault rupture(s) that most likely explain the observed ground motions. Utilizing simulated ground motion intensities at instrument locations as input (Figure 4.3), the proposed algorithm delivers the rupture probability of all labels (identified with a fault name and a cluster number).

Due to the amorphous nature of the problem (i.e. stations are not geospatially uniformly distributed, do not all trigger for a given earthquake, and can even be faulty), tree-based methods are selected as potential earthquake source discriminators, as these methods have previously proven useful to deal with missing inputs (Friedman *et al.*, 2008, Table 10.1). Two different algorithms are tested: (1) random forest (RF) (Friedman *et al.*, 2008, pp. 587–601 and James *et al.*, 2013, pp. 319–321), and (2) gradient boosting machines (GBM) (Friedman *et al.*, 2008, pp. 337–379 and James *et al.*, 2013, pp. 321–323). Both methods yield results in form of a vector of probabilities, which sum to 1.0. Each vector element represents a particular rupture cluster label. The input is a single intensity measure simulated at instrument locations, and the algorithms learn to discriminate between earthquake sources using the rupture labels obtained from the clustering process. Therefore, the input is a one dimensional vector, whose elements represent one intensity measure at all instrument locations. Each instrument has a unique position in the input vector. Several intensity measures were tested for the discriminator: PGA, PGV, AI, pSA(0.5s), pSA(1.0s), and pSA(3.0s).

The relabelled dataset is split in a training (80%) and a testing (20%) datasets. Selection of the data composing the two subsets is performed at random with the only constraint being that all labels are present in the training dataset. To maximize the efficiency of the earthquake source discriminator, several algorithm architectures are tested via grid search combined with a 5-fold cross-validation scheme (Friedman *et al.*, 2008, pp. 241–249 and Bergstra & Bengio, 2012). Further technical details about the RF and GBM implementation and validation are given in Section 4.10.1. In particular, Table 4.2 summarizes the tested hyper-parameters and their associated values, and Figures 4.16 and 4.17 show the 5-fold cross-validation error of the model architectures that were evaluated for both methods. The best models from both methods use the AI as intensity measure, and approximately return 90% accuracy on their respective validation and test datasets.

In order to choose between RF and GBM, their resistance to 'input dropout' is also tested. This test is realized by dropping out a certain percentage of instruments present in the ground motion simulation domain (to reflect instruments that do not immediately return recordings), reducing the amount of available information to solve the source inversion problem. Figure 4.6 shows the input dropout resistance of both models at two levels of granularity: (1) rupture cluster (fine granularity), and (2) fault (coarse granularity). The fault level is simply the aggregation of its composing rupture clusters (i.e. the fault probability is the sum of the rupture cluster probabilities for a given fault). For both methods, the probability of predicting the correct rupture cluster presented in Figures 4.6 (a and c) remains high despite important input dropout. The assigned probabilities at rupture cluster level tend to be more dispersed with RF than GBM. At the rupture cluster level, GBM yields higher probabilities for the correct label, and it appears to have a higher resistance to input dropout than the RF-based algorithm. However, this difference of performance is less pronounced at the fault level (Figures 4.6(b and d)), where both RF and GBM return an accuracy near 100%. It should be noted that most of the misclassification occurrences at rupture cluster level are between cluster labels of the same fault as misclassification of faults remains extremely rare (i.e. almost 100% accuracy with no input dropout and even over 90% for an extreme dropout of 12.5%). In other words, in a case in which 12.5% of the recording instruments that would trigger have a fault or unable to transmit their recording, the earthquake source discriminator would still assign a high rupture probability to the correct rupture cluster label. Based on these results, the GBM is selected as earthquake source inversion algorithm.

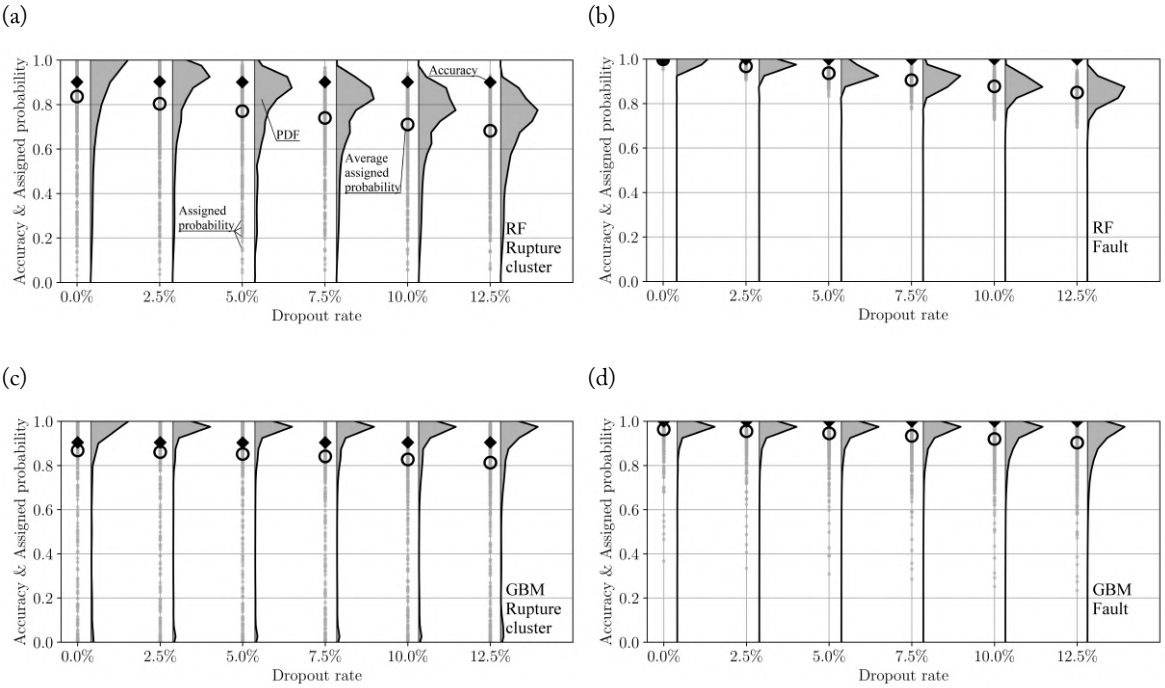

Figure 4.6: Input dropout resistance plots at (a) and (c) rupture cluster; and (b) and (d) fault levels. Results are given for the test dataset only. RF results are at the top (a and b), whereas GBM results are at the bottom (c and d). For each tested dropout rate, black diamonds and empty circles indicate the accuracy of the algorithm and the assigned average probability to the true label, respectively. Grey dots show the probability of the correct labels (either a rupture or a fault), and the shaded areas represent their probability density function (PDF).

4.3.3 Ground motion map generator

The vector of rupture cluster probabilities yielded by the earthquake source discriminator can be perceived as an 'encoded signal' of the regional ground motion. In other words, a unique set of rupture cluster probabilities can be used to re-estimate the geospatial intensity of ground motion from the (unknown) causative rupture. The entire method (earthquake source discriminator and ground motion map generator) can be assimilated to autoencoders that are generally used in generative adversarial neural networks (Goodfellow *et al.*, 2014). In addition to the development of the ground motion map generator, this section also presents an approach for dealing with multi-segment ruptures that are more complex than the training data (which in this study comprises single segment rupture). This is an important attribute to address, reality always being more complex than the most detailed physics-based ground motion modelling.

Development of the algorithm

The ground motion map generator utilizes the rupture probability vector from the earthquake source discriminator as input (Figure 4.3), and its associated simulated ground motion spatial distribution as a target. A predictive generative network (Chalasani & Principe, 2013) is designed to model the ground motion map generator, whose purpose is to predict effects from causes, or in this case, from the probability of causes (i.e. $P_i - P_M$ in Figure 4.3). This algorithm is based on a deep deconvolutional neural network that sequentially adds dimensions to, and transforms, the originally encoded signal to estimate the spatially-distributed ground motion intensity. To facilitate the transformation of the input probability vector into ground motion maps, the model concatenates ten regional submodels identical in size that are responsible to evaluate the spatial distribution of ground motion intensity. Creating submodels reduces the number of training variables needed to obtain a similar accuracy if no

submodel was created. Figure 4.7 illustrates how the model integrates the different submodels to produce ground motion maps. The model evaluates six intensity measures simultaneously: PGA, PGV, AI, pSA(0.5s), pSA(1.0s), and pSA(3.0s). The correlation between the different intensity measures are not explicitly modelled, but implicitly learned from the training dataset by the ground motion map generator.

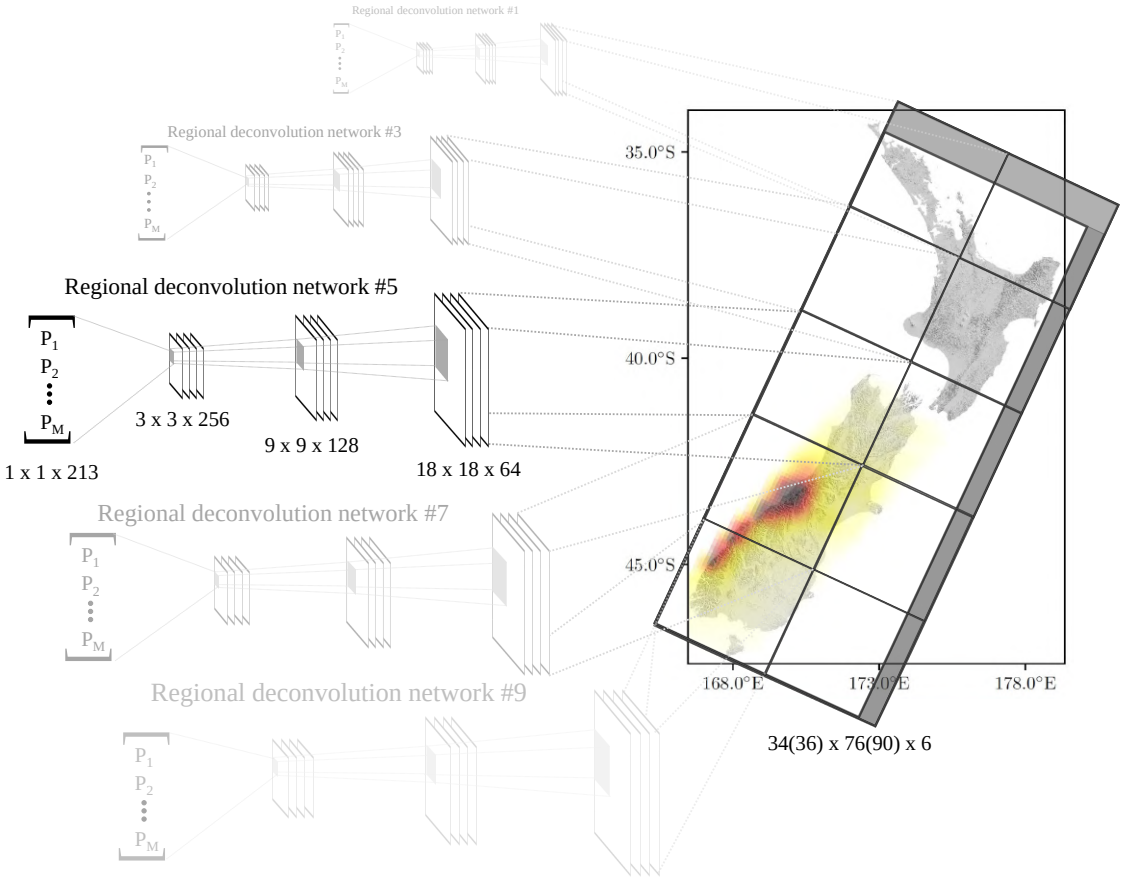

Figure 4.7: Structure of the predictive generative network comprised of ten regional submodels. Only the structure of the western regional submodels are shown. The size of the layers are indicated for the output layer and regional submodel 5, where the last number represents layer depth. The shaded area of the output layer is the cropped zone of the concatenated model. Numbers between brackets indicate the size of the final layer before the cropping.

The training of the predictive generative network is identical to that of a standard neural network. Two operations are repeated iteratively (each iteration being called an *epoch*): (1) stochastic gradient descent, and (2) back-propagation (Goodfellow *et al.*, 2016, pp. 203–224). Stochastic gradient descent is responsible for estimating the gradient of the model misfit (also called *loss*). Back-propagation updates the weights used in the (de)convolution operations by the learning rate-corrected stochastic gradient descent result following the chain rule of calculus.

The predictive generative network is trained on the logarithmic ground motion spatial distributions, and the loss is evaluated as a mean squared error. The final architecture was selected via manual search (the exploration of the entire hyper-parameter search space being too computationally demanding). The training is optimized with the Adadelta method (Zeiler, 2012) that adjusts the learning rate during the training process, and early stopping is applied to avoid overfitting (Prechelt, 1998). More technical details about the architecture and training of the network can be found in Section 4.10.2. In particular, Figure 4.19 shows the training history with a GBM and RF encoding, and Figure 4.18 shows the precise architecture of the designed algorithm.

Figures 4.8 and 4.9 illustrate example results for the Fjord-to-Kelly segment of the Alpine Fault

(AlpineF2K), and Northeast-to-Vernon segment of the Awatere Fault (AwatNEVer), respectively. Each figure provides a comparison of results for PGA and PGV intensity measures of the ground motion simulation (from the testing dataset), the predictive generative network (from the model), and the ratio of the two. In both cases, and for these intensity measures, the model delivers a relatively good estimate of the geospatial distribution of the ground motion intensity. To allow a quantifiable comparison, residual distributions are provided within each figure showing the difference between the physics-based modelling and the ML-generated ground motion (Figures 4.8 (c) and 4.9 (c)). Residuals are evaluated only at locations experiencing a PGV greater than 2.5 cm/s in the physics-based ground motion simulations. Other intensity measures are provided in Figures 4.20 and 4.21 in Section 4.10.2.

Once the earthquake source discriminator and the ground motion map generator trained, the model (Figure 4.3) can be used in predictive cases based on observed time series at network instrument locations. Because the computational evaluation of the model is relatively lightweight, an estimate of the causative earthquake sources (i.e. source inversion) and consequent ground motion (i.e. ground motion prediction) can be obtained near instantaneously. Specifically, results for individual earthquake events can be obtained in tens of seconds from processed signals recorded at instrument locations. For example, results presented in Figures 4.8 and 4.9 have been computed using a standard laptop (Intel(R) Core(TM) i7 5600 with 8GB of RAM) in about two minutes and hence larger computational resources that are common place can reduce this time by more than an order of magnitude. Details about the architecture and training of the predictive generative network are also given in Section 4.10.2.

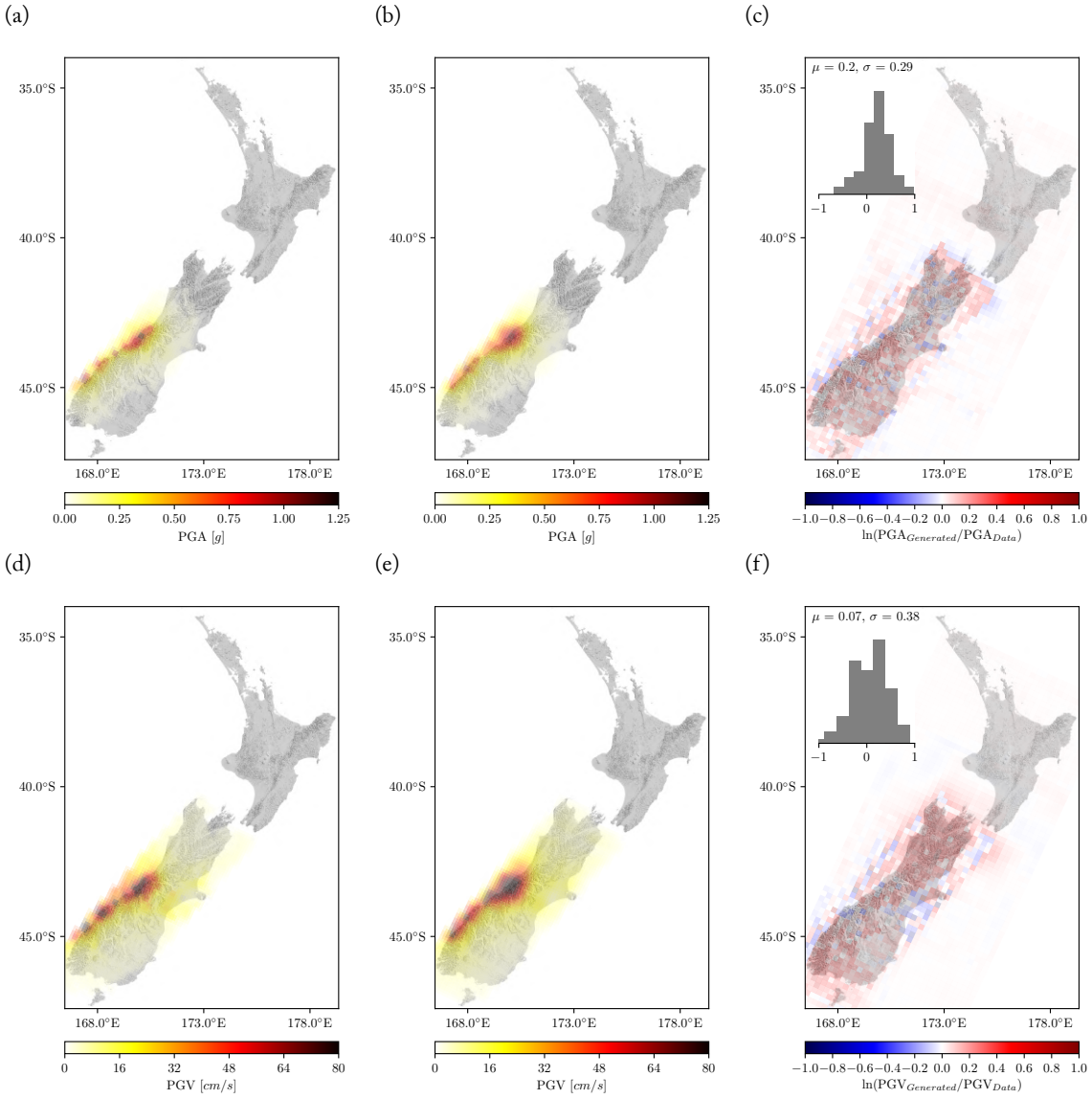

Figure 4.8: Result comparison for a rupture from the Fjord-to-Kelly segment of the Alpine Fault from the test dataset. (a) and (d): physics-based simulated ground motion results (testing dataset); (b) and (e): ground motion map generator results (model) based on the GBM encoding; and (c) and (f): logarithmic residuals between the two. (a-c): PGA; (d-f): PGV.

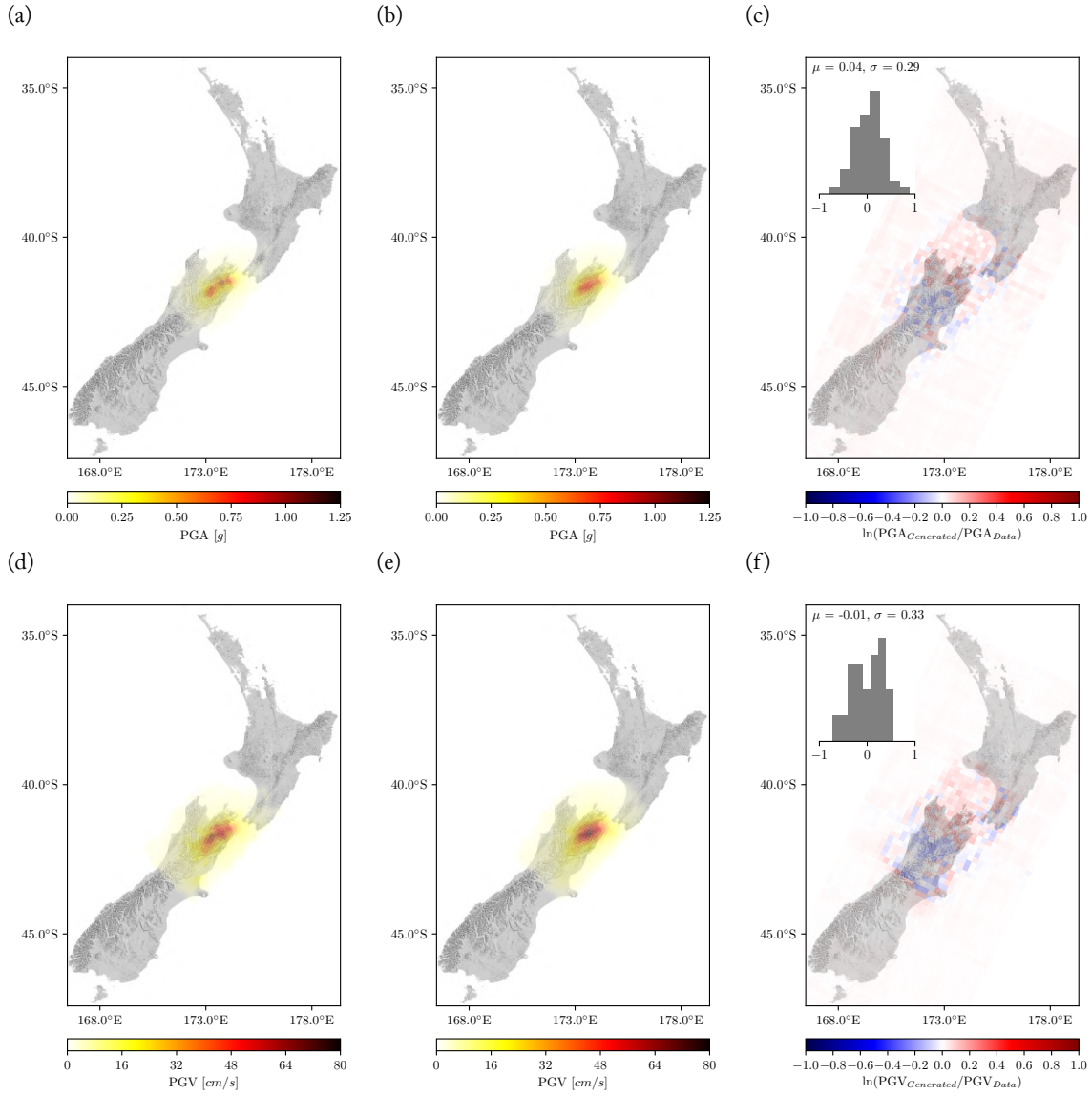

Figure 4.9: Result comparison for a rupture from the Northeast-to-Vernon segment of the Awatere Fault from the test dataset. (a) and (d): physics-based simulated ground motion results (testing dataset); (b) and (e): ground motion map generator results (model) based on the GBM encoding; and (c) and (f): logarithmic residuals between the two. (a-c): PGA; (d-f): PGV.

Ground motion map generation of complex, multi-segment fault ruptures

The utilized dataset in this study is composed solely of single segment ruptures as defined in Stirling *et al.* (2012) and Tarbali *et al.* (2018b). Hence, the earthquake source discriminator and subsequently the ground motion map generator are not explicitly trained, and therefore will have a relative poorer performance in assessing complex multi-segment fault ruptures. It is however possible to obtain satisfactory results by slightly altering the pre- and post-processing of the ground motion map generator. This is important to allow this approach to handle complex ruptures, which are frequent for large magnitude earthquakes.

When applied to a complex rupture, the earthquake source discriminator results in a vector of rupture probabilities, it is expected that most likely ruptured faults and rupture clusters would naturally emerge, though with lower rupture probabilities than observed for single segment ruptures. Therefore, this part of the framework does not need any modification, but will provide the necessary condition

to modify the ground motion map generator usage.

The modification of the ground motion map generator follows a three steps procedure.

1. Starting from the rupture cluster with the highest assigned probability, incrementally add rupture clusters with smaller rupture probability to the list of considered sources until a first evident geographic outlier is found (e.g. 50 km away from already considered sources).

2. Compute the ground motion map for each of the identified rupture cluster separately with a probability of 1.0 (i.e. all other rupture cluster probabilities are set to 0.0). In the case of too low probabilities, the predictive generative network would yield insignificant ground motion intensities (the algorithm training is realized with input vector containing at one probability greater than 50%).

3. At any given geographic location of interest, select the maximum ground motion intensity generated in the previous step. The most probable cause of the observed ground motion intensity being the closest identified source, the use of the maximum appears reasonable.

Switching from a simple to a complex rupture analysis is appropriate when the highest predicted rupture probability is lower than 50%. As it can be observed in Figures 4.6 (c and d), when the correct rupture cluster is poorly predicted, its associated fault is not, meaning that another rupture cluster from the same fault has a been assigned a high rupture probability (i.e. greater than 50%).

4.4 Application to the 21 July 2013 Seddon Mw 6.5 earthquake

For future earthquakes originating from known sources with simple geometries (e.g. single ruptured faults), the proposed framework is expected to deliver results that are comparable to those obtained from test data (i.e. high rupture probability for a single label and relatively well-predicted ground motion spatial distribution as presented above). To test the presented model on a relatively simple real case, it is applied to the 21 July 2013 Seddon Mw 6.5 earthquake, the main event of the Cook Strait earthquake sequence described by Holden *et al.* (2013). The hypocenter is located between two known faults present in the training set: the Awatere Needles-Vernon fault, and the Kekerengu-Needles fault. Ground motion records are extracted from the GeoNet file transfer protocol (url given in the Data and Resources section). The best available estimation of the ground shaking was estimated by Shakemap (Worden *et al.*, 2010) and assumed a point source (url given in the Data and Resources section). The moment magnitude being smaller than the one selected to train the model (Mw 6.8), discrepancies are expected between what was originally inferred and the model predictions, especially when it comes to the ground motion intensity estimation.

4.4.1 Earthquake source discriminator results

Fed with the ground motion records from the activated stations, the GBM predicts a complex rupture (the highest rupture probability is less than 50%). Despite the low complexity of this rupture, this prediction is not very surprising as such small magnitude earthquakes were not part of the training dataset, hence difficult to identified by the discriminator. The first rupture probability is given to the Marlborough Slope 04 fault (0.96%). The second highest rupture (NMFZM, 0.88%) being relatively far away from the first one given the magnitude and according to the process described in Section 4.3.3, only the first source is considered. Figure 4.10 shows the epicentre location of the point source (in blue) as defined in Holden *et al.* (2013), the identified most likely causative source (in red), and the closest known faults from the assumed point source (in green) from the selected finite fault set. The difference between this inference (in red) and the closest known faults (in green) is likely due to the way information is processed within the GBM. There the intensity observed at each station is utilized to select the most probable source. A rupture from the closest finite faults would have led to

drastically different recordings at some of the activated stations. In particular, recorded intensity north of the South Island would have been much higher. A second explanation for this inaccuracy is the magnitude of the observed earthquake: being less than the Stirling *et al.* (2012) model assumes (Mw 7.7 and 7.4 for the Awatere Needles-Vernon fault and the Kekerengu-Needles fault, respectively), the GBM predicts a source from larger magnitude that is further away from the stations but remains constrained by the available ground motion records. It is expected that this effect would be far less present for cases where the constraints (the stations) would geographically surround the rupture (i.e. with an offshore rupture, constraints are only present in inland areas as no offshore recording stations were present in the training set).

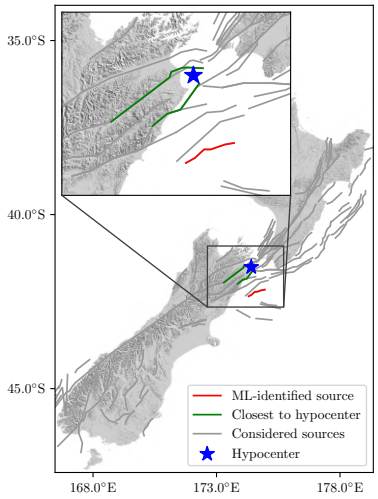

Figure 4.10: Map showing the hypocenter location used to estimate the ground motion intensity in Shakemap (blue star), the most likely earthquake source identified by the GBM (red line), the two closest known faults to the hypocenter present in the training set (green lines), and the faults present in the training set (grey lines).

4.4.2 Ground motion map generator results

Figures 4.11 (a) and (c) presents the Shakemap results for PGA and PGV, respectively, while Figures 4.11 (b) and (d) show these intensity measures from the predictive generative network. Here the developed model tends to largely overestimate the ground motion intensity at the predicted rupture location. However, it can be observed that the inland ground motion intensities resemble the one given by Shakemap, both in terms of amplitude and geospatial distribution. This overestimation is due to the smallest minimal magnitude considered to train this framework and to the absence of offshore stations to constrain the choice of the causative source.

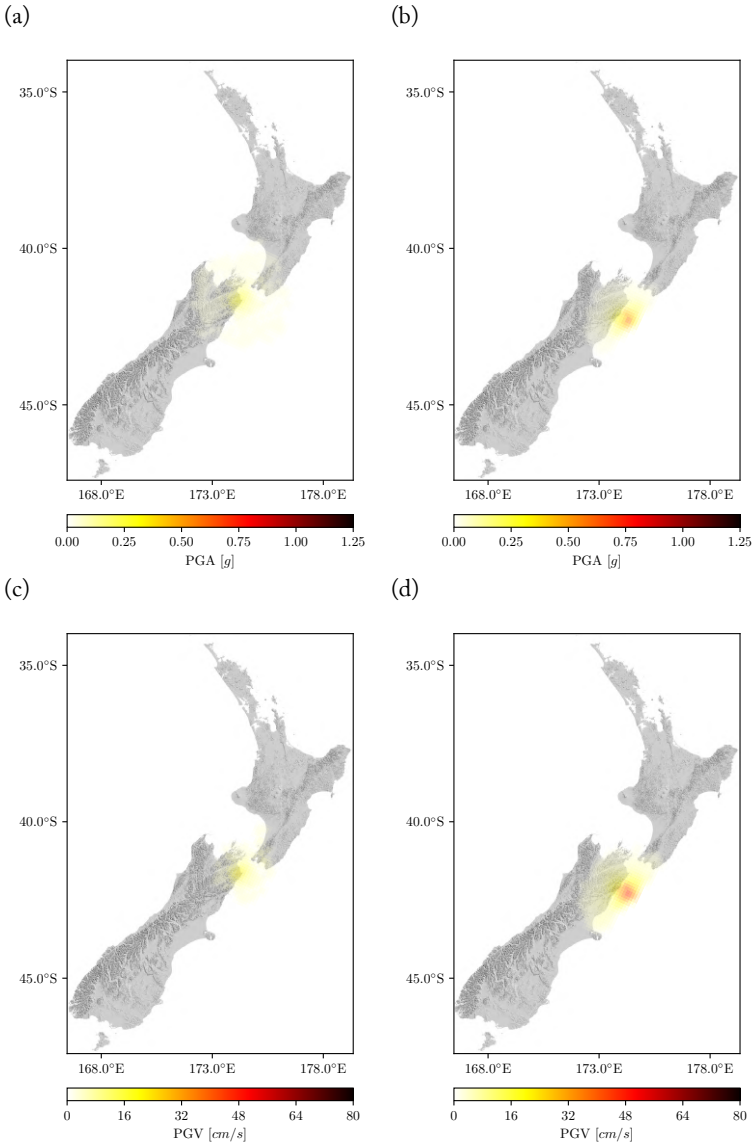

Figure 4.11: Result comparison for the 21 July 2013 Seddon Mw 6.5 earthquake. (a) and (c): Shakemap estimate of the ground motion intensity; (b) and (d): ground motion map generator results based on the GBM encoding.

Despite the noted discrepancies between observations and predictions, the framework operates with a relatively good accuracy given that this case clearly lies outside its realm of applicability. These inaccuracies lead to the conclusion that, for small to moderately large magnitude earthquakes, the point source assumption yields good enough immediate results, and does not necessitate such complex methods. Discussing a much more complex case, the next section will show the benefits of applying this method to larger magnitude earthquakes.

4.5 Application to the 14 November 2016 Kaikōura Mw 7.8 earthquake

To stress-test its validity of real complex cases, the proposed framework is applied to the 14 November 2016 Kaikōura Mw 7.8 earthquake and compared against the ground motion estimate published on PAGER (Wald *et al.*, 2010) two hours after the event and presented in Allstadt *et al.* (2018), and against the physics-based ground motion estimate by Bradley *et al.* (2017a) based on a modified version of the Hamling *et al.* (2017) rupture geometry.

In terms of the 'input' data - the recorded ground motions - , the four closest instruments to the rupture (marked as red triangles in Figure 4.12 (c)) could not immediately transmit their recordings and three of them recorded the highest amplitudes from this earthquake (PGA greater than $1g$) (Bradley *et al.*, 2017a; Allstadt *et al.*, 2018), providing a real illustration of input dropout as well. Therefore, two cases are analyzed and presented in parallel: (1) the initially-available recordings, and (2) the entire set of recordings. First, source identification results using the GBM are given and discussed. And second, the spatial distribution of ground motion estimate from Bradley *et al.* (2017a) is compared with the generated ground motion maps.

4.5.1 Earthquake source discriminator results

For the two analyzed cases, Arias Intensity computed from GeoNet instrument signals are fed to the earthquake source discriminator. Table 4.1 provides the probability of rupture for all faults that have been selected using the complex rupture procedure proposed in Section 4.3.3. Figures 4.12 (a) and (b) present faults that have been identified by the earthquake source discriminator for the two analyzed cases. For the sake of comparison, sources inferred by Bradley *et al.* (2017c) from the Hamling *et al.* (2017) rupture geometry and ML-considered earthquake sources are presented in Figure 4.12 (c).

Owing to the complexity of the rupture (Litchfield *et al.*, 2016) and the resulting ground motions, rupture probabilities remain relatively small ($P_{max} = 10.3\%$), but approximately designate faults that have indeed ruptured. It can be observed that, given the sources present in the training dataset, onshore sources are relatively well predicted. Note that as discussed by Bradley *et al.* (2017c) and Allstadt *et al.* (2018), the *Awatere* fault was included in first earthquake source inferences, but eventually removed.

In contrast to these results, the earthquake source discriminator also inferred the rupture of offshore faults, namely *NMFZB0*, *NMFZB2*, *NMFZK1*, and *NMFZKM*, that have not ruptured. Moreover, two of them obtained the highest assigned rupture probabilities. It is believed that the selection of these offshore faults is due to the absence of instruments in their surroundings (the closest instruments are only located on their west because of the coastal nature of the earthquake event). In the proposed tree-based algorithm, instruments act as constraints that add potential discrimination possibilities (i.e. help confirm or reject a particular earthquake source from other stations' recorded signal). Potential solutions to overcome this limitations are discussed in Section 4.6. Nevertheless, due to the way the ground motion intensities are estimated in the case of a complex rupture, poor offshore constraints do not significantly influence results required to assess inland ground motion intensities. It may however be problematic to assess the co-seismic tsunami risk.

Table 4.1: List of rupture clusters selected using the complex rupture procedure developed in Section 4.3.3. Probabilities indicate the assigned rupture probability of the rupture cluster based on the initially available recordings and on all the recordings. Numbers between bracket indicate rupture clusters that have not been selected in one of the developed analyses. Numbers following the underscore in the cluster name indicate the ID of the fault. Note that MS04 has only 1 cluster.

Cluster name	Rupture probability, initially available recordings	Rupture probability, full recordings
NMFZB0_0	7.08%	7.03%
NMFZB2_0	5.52%	5.67%
NMFZB0_1	3.19%	3.14%
NMFZB2_1	2.29%	2.21%
HopeConway_1	0.91%	1.16%
HopeConway_0	0.79%	1.05%
HopeConwayOS_0	0.78%	0.84%
MS04	0.67%	0.81%
NMFZK1_0	0.75%	0.80%
NMFZM_1	0.63%	0.75%
JorKekNeed_1	(0.50%)	0.74%
AwatereNE_0	0.68%	0.72%
HopeTeRapa1n2_1	(0.59)%	0.70%
NMFZK1_0	(0.60%)	0.70%
NMFZM_1	(0.54%)	0.66%
HopeConwayOS_1	(0.62%)	0.64%

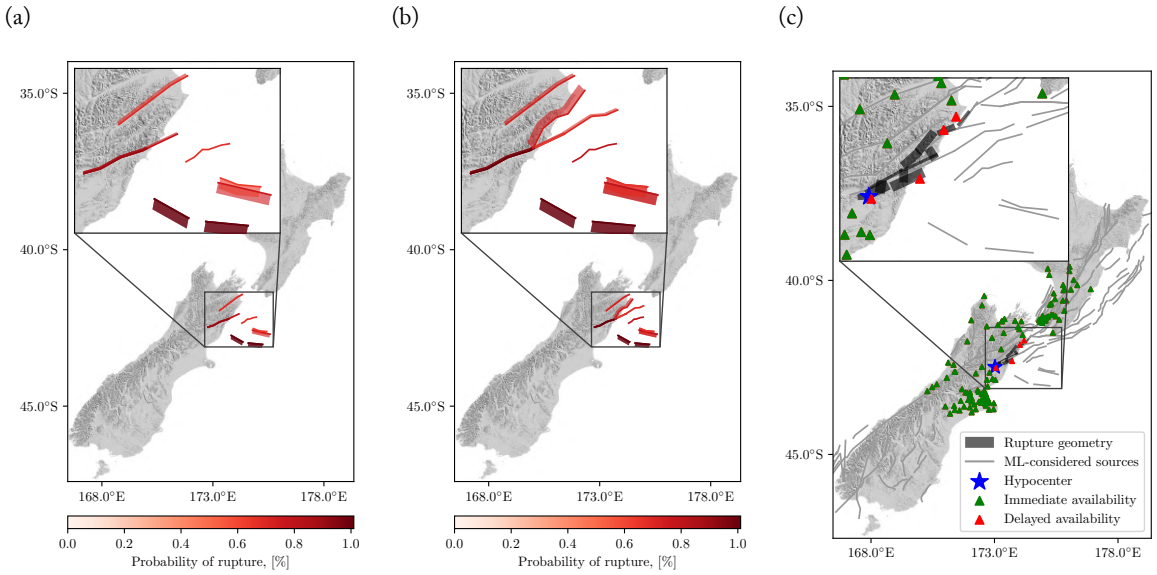

Figure 4.12: Maps of (a) the discriminator-selected earthquake sources from the originally available recordings; and (b) the discriminator-selected earthquake sources from all recordings; and (c) the physics-based earthquake sources inferred by Bradley et al. *(2017c) from the Hamling* et al. *(2017) rupture geometry. Colours of the planes in (a) and (b) indicate the assigned probability of rupture, green and red triangles in (c) the instruments with immediate and delayed availability, grey segments in (c) the ML-considered faults from Stirling* et al. *(2012), and the blue star in (c) the location of the hypocenter. Note that colours in (a) and (b) discriminate results up to 2% of rupture probability for representation purposes.*

4.5.2 Ground motion map generator results

To provide context to contemporary approaches used here for comparison, the first near-real-time point-source-based estimate of the ground motion spatial distribution for this earthquake was released 19 minutes after the event, and was followed two hours later by a site-effects-corrected version (Allstadt *et al.*, 2018). The first ground motion estimate based on a finite fault was released after five hours. The physics-based ground motion estimate, submitted 21 days after the event by Bradley *et al.* (2017c), is based on a modified rupture geometry by Hamling *et al.* (2017). Utilizing a New Zealand-specific empirical ground motion model (Bradley, 2013), the same rupture geometry has been used to develop the 16$^{\text{th}}$ version and final Shakemap ground motion estimate available after three months. Figure 4.13 presents (a) the point-source-based, ground condition-corrected and (b) final ShakeMap versions, as well as (c) the physics-based estimate of the ground motion spatial distribution. It can be seen that the maximum amplitude and geospatial extent of ground motion are largely underestimated in the early point source-based version, when compared to the other estimates.

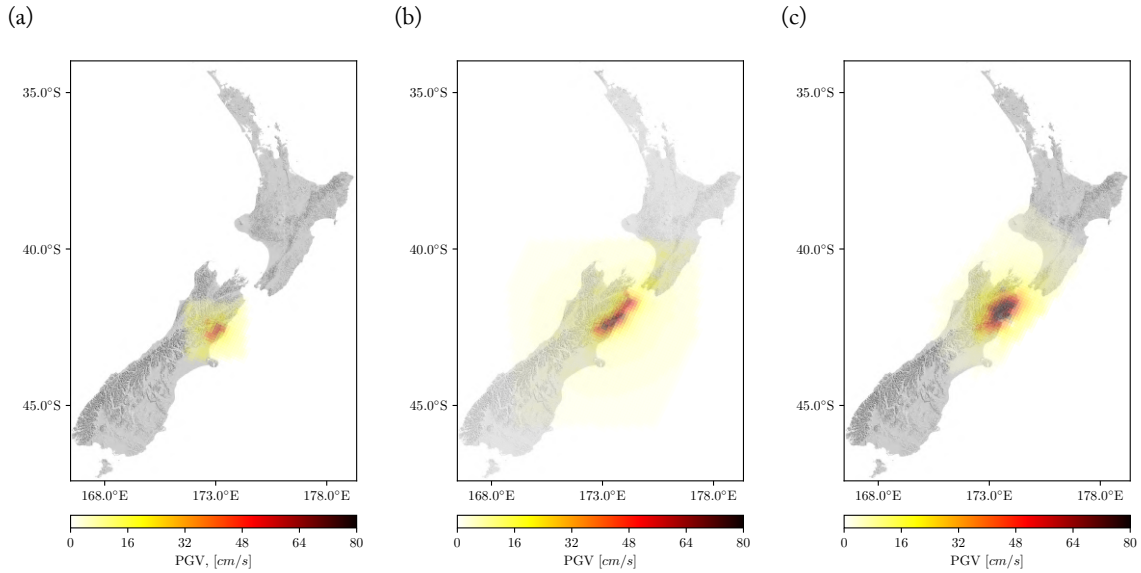

Figure 4.13: (a) 2nd ShakeMap version (available after $t + 19$ minutes) accounting for site effects and based on a point source; (b) 16th and final ShakeMap version (available after $t + 3$ months); and (c) physics-based ground motion estimate from Bradley et al. *(2017a) of the 14 November 2016 Kaikōura Mw 7.8 earthquake (submitted after $t + 21$ days).*

As the highest rupture probability for a fault (aggregated rupture cluster) is below 50%, the GBM-encoded results are not directly usable by the ground motion generator. Instead, the procedure described in Section 4.3.3 is applied. Figures 4.14 and 4.15 present the PGA and PGV results for the initially available and full recordings, respectively. Results for the additionally generated intensity measures are given in Figures 4.22 and 4.23, respectively. In both cases, it can be observed that, despite a strong overestimation of the ground motion intensity in the offshore region due to the selected offshore faults, the proposed method offers a substantial improvement of immediate ground motion estimate in terms of ground motion intensity and spatial extent.

To quantify the misfit between the physics-based and ML-generated ground motion maps, summary statistics (mean μ and standard deviation σ) and histograms of the residuals are also provided in Figure 4.14 (c and f) and 4.15 (c and f). As presented in Section 4.3.3, residuals are considered only at locations where the physics-based simulated PGV is greater than 2.5 cm/s. In addition, as no construction nor societal activities are located in the overestimated offshore regions, only onshore locations are used to the develop the aforementioned statistics and histograms (statistics developed on

the onshore and offshore regions are given in the captions of Figure 4.14 and 4.15). When compared to the residuals between the physics-based ground motion simulation and the 2nd Shakemap version for PGV ($\mu = -1.86$, $\sigma = 1.51$), the proposed method yields much more accurate results. Due to the mutliple considered sources, the residuals in Figures 4.14 (c and f) and 4.15 (c and f) show a greater dispersion than the one observed in the two simple rupture example presented in Section 4.3.3. A small uncertainty reduction can be observed in the case, where all instruments are being used to identify the sources.

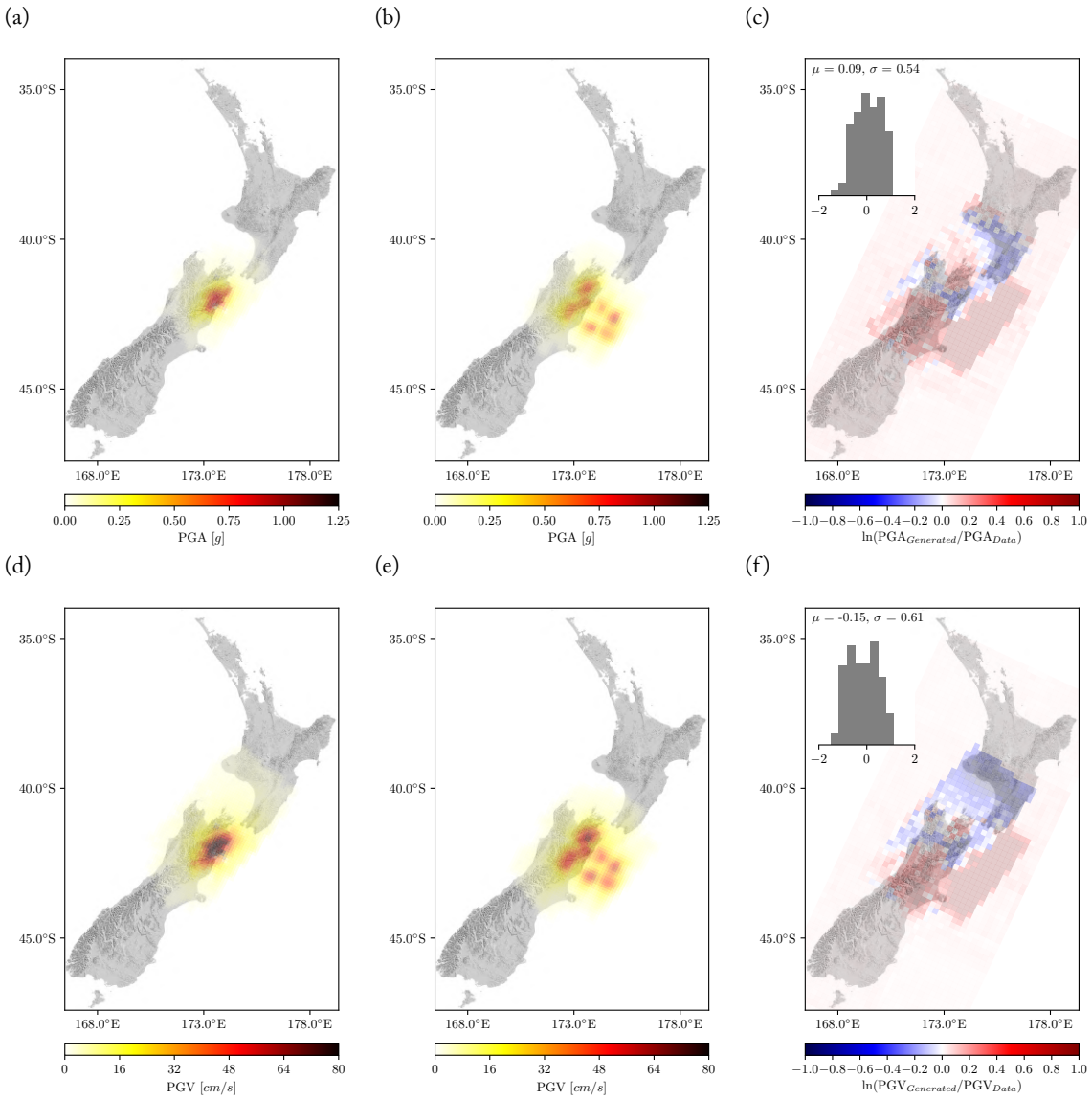

Figure 4.14: Result comparison for the 14 November 2016 Kaikōura Mw 7.8 earthquake using the initially available recordings. (a) and (d): physics-based simulated best estimate ground motion results; (b) and (e): ground motion map generator results based on the GBM encoding; and (c) and (f): residuals between the two. (a-c): PGA; (d-f): PGV. Statistics and histograms in (c) and (f) are based on the residuals computed from onshore locations only.

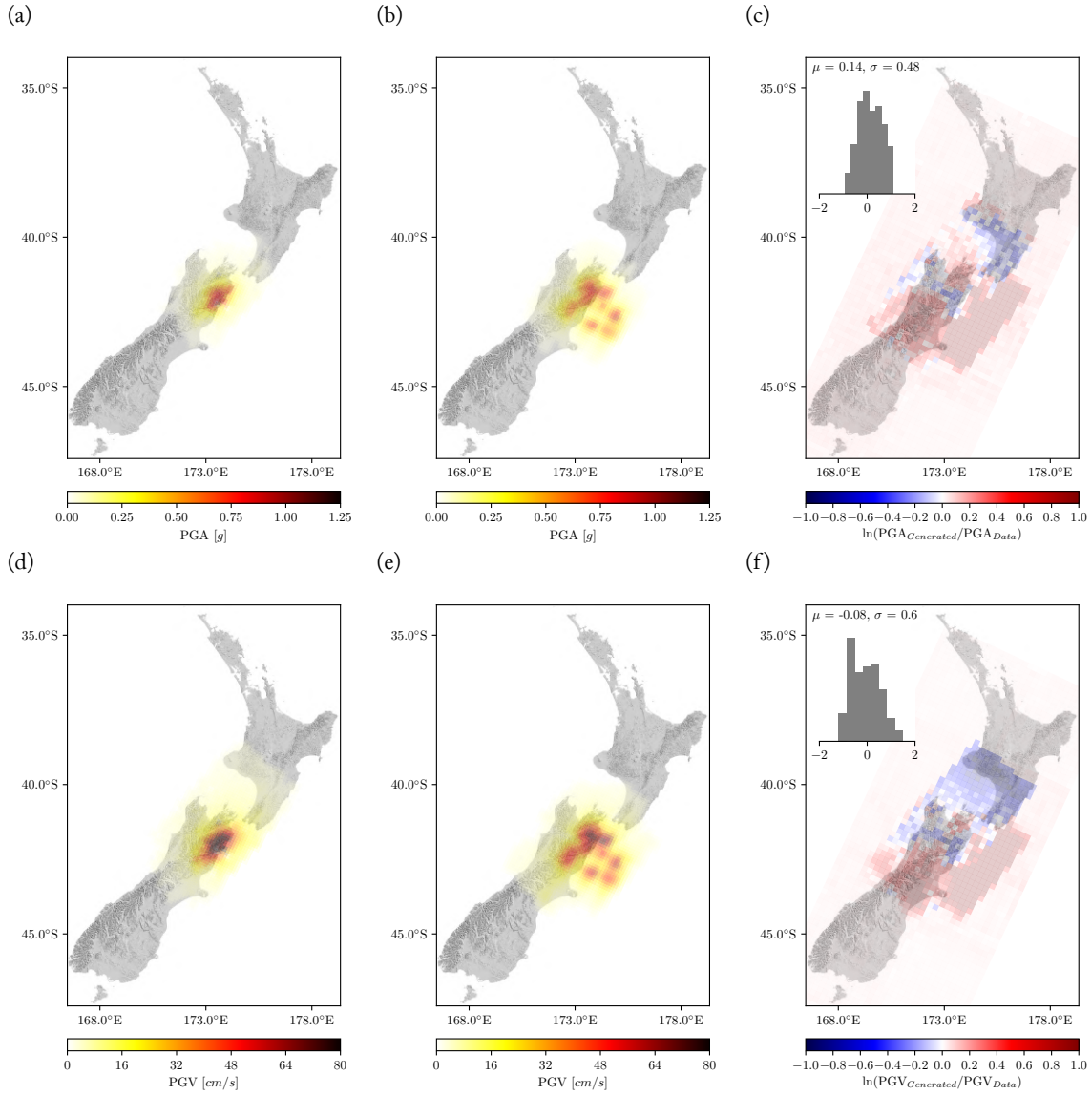

Figure 4.15: Result comparison for the 14 November 2016 Kaikōura Mw 7.8 earthquake using all the recordings. (a) and (d): physics-based simulated best estimate ground motion results; (b) and (e): ground motion map generator results based on the GBM encoding; and (c) and (f): residuals between the two. (a-c): PGA; (d-f): PGV. Statistics and histograms in (c) and (f) are based on the residuals computed from onshore locations only.

4.6 Conclusion and future directions

This paper presented a machine learning (ML)-based method for near-real-time earthquake sources identification and ground motion prediction based on training data from physics-based ground motion simulations. The approach utilized tree-based methods (random forest (RF) and gradient boosting machine (GBM)) as an *earthquake source discriminator* to infer causative fault rupture(s) and a predictive generative network to generate ground motion intensities over the region of interest. The training dataset comprised approximately 3,857 simulations from 113 fault geometries recorded at network instrument locations and approximately 20,000 other locations in the region of interest (New Zealand). Algorithm training and validation illustrated that the earthquake source discrimination and spatial ground motion estimation on data from the test set show very good results. Retrospective near-real-time application for the (extraordinarily complex) 14 November 2016 Mw 7.8 Kaikōura earthquake

was examined, and compared to the results from conventional approaches.

The specific implementation of the ML algorithm and associated underlying training data presented for the purposes of illustration result in several limitations that warrant discussion, as well as providing an opportunity to discuss forward-looking improvements. The sheer size and quality of training data are instrumental in the determination of the quality of a ML-approach to solve a problem. In the context of this paper, the presented example utilized approximately 4,000 physics-based ground motion simulations from 113 fault geometries as a subset from the earthquake rupture forecast (ERF) of Stirling *et al.* (2012). Increasing the number of simulations through a combination of a larger number of rupture realizations per fault, as well as a larger number of faults would increase the volume of training data. Furthermore, the Stirling *et al.* (2012) does not consider multisegment ruptures, nor non-characteristic earthquakes, hence increasing the diversity of potential ruptures would greatly benefit the ML training. Consideration of only major (mapped) faults, and not distributed seismicity sources, limits the use of the method for significant earthquakes. While it is possible to utilize comparable simulations of smaller magnitude earthquakes, near-real-time modelling of such events is neither complex (point source assumption is adequate) nor critical (impacts are generally smaller). Because the ML method uses physics-based simulations as a surrogate for real (empirical) observations, then the validity of simulations is also a critical factor in the performance of the ML approach, and consistently-observed validation improvements (Bradley *et al.*, 2017b) will thus advance the utility of this approach.

There are several improvements in the adopted ML algorithms that can also advance the overall concept proposed in this work (which were limited here principally because of the nature of the training data). Within the current modelling paradigm for the earthquake source discriminator (i.e. tree-based RF or GBM methods), a greatly increased number of simulations would enable a larger number of rupture clusters to be considered, and also the use of more than a single discriminating intensity measure. Furthermore, the clustering can also be expanded such that it captures more subtle variations between ground motion prediction from the same rupture geometry (e.g. slip amplitude, rise time, rake distribution; rather than just principally via hypocenter location). With greatly increased training dataset size, a more significant change in methodology could enable to switch from a finite-fault to a cell-based representation of ruptures (a single finite fault being represented as a contiguous series of cells), which would seamlessly enable the combination of multiple faults to address complex ruptures and other edge cases. With a significant advancement in ground motion simulation method accuracy and precision, simulated waveforms (and not simply intensity measures as 'summary statistics') could be directly utilized, allowing the exploration of other machine learning methods. For example, tree-based methods for the earthquake source discriminator could be replaced with recurrent neural networks that analyze the raw signal instead of its derived intensity measures. Because the consideration of time series greatly increases the dimensionality of the problem, then such approaches also would require a significant increase in training data.

The quantitative results presented for the examples examined; the speed at which the method is able to obtain outputs (two minutes on a conventional laptop); and the exponential advancements that are expected in the performance of ground motion simulation methods and size of simulation datasets offer insight into the potential for the approach to be used in conjunction with, and (we believe) eventually replace, conventional methods.

4.7 Resources

Information on the GeoNet instrument network can be found at `ftp://ftp.geonet.org.nz/` (last access on the 22 January 2019). Python codes are stored in the following github repository: `https://github.com/xavierbellagamba/EQSourceIdentificationGMGeneration.git`. Models are stored in the following dropbox repository `https://www.dropbox.com/s/1o2tdve6ve3r2q6/BellagambaEtAl_2019_Models.zip?dl=0`. Information regarding the Cybershake data can be found in `https:`

//wiki.canterbury.ac.nz/display/QuakeCore/Cybershake+NZ (last access on the 22 January 2019).

4.8 Acknowledgement

This project was supported by QuakeCoRE, a New Zealand Tertiary Education Commission-funded Centre. This is QuakeCoRE publication number 0376. Training of the predictive generative network was carried out using a NVIDIA Quadro P6000 obtained via the NVIDIA Academic Grant.

4.9 References

Abadi, M, Barham, P, Chen, J, Chen, Z, Davis, A, Dean, J, Devin, M, Ghemawat, S, Irving, G, Isard, M, *et al.* 2016. Tensorflow: a system for large-scale machine learning. *Pages 265–283 of:* 12^{th} *USENIX Symposium on Operating Systems Design and Implementation*, vol. 16.

Akinci, A, Aochi, H, Herrero, A, Pischiutta, M, & Karanikas, D. 2017. Physics-Based Broadband Ground-Motion Simulations for Probable Mw≥ 7.0 Earthquakes in the Marmara Sea Region (Turkey) Physics-Based Broadband Ground-Motion Simulations for Probable Mw≥ 7.0 Earthquakes. *Bulletin of the Seismological Society of America*, **107**(3), 1307–1323.

Allen, TI, & Wald, DJ. 2009. *Evaluation of ground-motion modeling techniques for Use in Global ShakeMap-A critique of instrumental ground-motion prediction equations, peak ground motion to macroseismic intensity conversions, and macroseismic intensity predictions in different tectonic settings*. Tech. rept. Open File Report 2009–1047. US Geological Survey, Reston, VA, USA.

Allstadt, KE, Jibson, RW, Thompson, EM, Massey, CI, Wald, DJ, Godt, JW, & Rengers, FK. 2018. Improving near-real-time coseismic landslide models: Lessons learned from the 2016 Kaikōura, New Zealand, earthquake. *Bulletin of the Seismological Society of America*, **108**(3B), 1649–1664.

Atkinson, GM, & Wald, DJ. 2007. "Did You Feel It?" intensity data: A surprisingly good measure of earthquake ground motion. *Seismological Research Letters*, **78**(3), 362–368.

Bellagamba, X, Lee, R, & Bradley, BA. TBD. A neural network for automated quality screening of ground motion records from small magnitude earthquakes. *Earthquake Spectra*.

Bergstra, J, & Bengio, Y. 2012. Random search for hyper-parameter optimization. *Journal of Machine Learning Research*, **13**(Feb), 281–305.

Boore, DM. 2003. Simulation of ground motion using the stochastic method. *Pure and applied geophysics*, **160**(3-4), 635–676.

Bradley, BA. 2013. A New Zealand-specific pseudospectral acceleration ground-motion prediction equation for active shallow crustal earthquakes based on foreign models. *Bulletin of the Seismological Society of America*, **103**(3), 1801–1822.

Bradley, BA, Razafindrakoto, HNT, & Polak, V. 2017a. Ground-Motion Observations from the 14 November 2016 M w 7.8 Kaikoura, New Zealand, Earthquake and Insights from Broadband Simulations. *Seismological Research Letters*, **88**(3), 740–756.

Bradley, BA, Bae, SE, Polak, V, Lee, RL, Thomson, EM, & Tarbali, K. 2017b. Ground motion simulations of great earthquakes on the Alpine Fault: effect of hypocentre location and comparison with empirical modelling. *New Zealand Journal of Geology and Geophysics*, **60**(3), 188–198.

Bradley, BA, Razafindrakoto, HNT, & Nazer, MA. 2017c. Strong ground motion observations of engineering interest from the 14 November 2016 Mw7.8 Kaikoura, New Zealand earthquake. *Bulletin of the New Zealand Society for Earthquake Engineering*, **50**(2), 85–93.

Chalasani, R, & Principe, JC. 2013. Deep predictive coding networks. *arXiv preprint arXiv:1301.3541*.

Chollet, F, *et al.* 2015. *Keras*. `https://keras.io`.

Dreger, DS, & Jordan, TH. 2014. Introduction to the Focus Section on validation of the SCEC broadband platform V14. 3 simulation methods. *Seismological Research Letters*, **86**(1), 15–16.

Friedman, J, Hastie, T, & Tibshirani, R. 2008. *The elements of statistical learning*. Vol. 1. Springer series in statistics Springer, Berlin.

Garcia, Daniel, Wald, David J, & Hearne, MG. 2012. A global earthquake discrimination scheme to optimize ground-motion prediction equation selection. *Bulletin of the Seismological Society of America*, **102**(1), 185–203.

Goda, Katsuichiro, & Atkinson, Gail M. 2010. Intraevent spatial correlation of ground-motion parameters using SK-net data. *Bulletin of the Seismological Society of America*, **100**(6), 3055–3067.

Goodfellow, I, Pouget-Abadie, J, Mirza, M, Xu, B, Warde-Farley, D, Ozair, S, Courville, A, & Bengio, Y. 2014. Generative adversarial nets. *Pages 2672–2680 of: Advances in Neural Information Processing Systems*.

Goodfellow, I, Bengio, Y, & A, Courville. 2016. *Deep Learning*. Cambridge, MA, USA: MIT Press. `http://www.deeplearningbook.org`.

Graves, R, Jordan, TH, Callaghan, S, Deelman, E, Field, E, Juve, G, Kesselman, C, Maechling, P, Mehta, G, Milner, K, *et al.* 2011. CyberShake: A physics-based seismic hazard model for southern California. *Pure and Applied Geophysics*, **168**(3-4), 367–381.

Graves, RW. 1993. Modeling three-dimensional site response effects in the Marina District Basin, San Francisco, California. *Bulletin of the Seismological Society of America*, **83**(4), 1042–1063.

Graves, RW, & Wald, DJ. 2001. Resolution analysis of finite fault source inversion using one-and three-dimensional Green's functions: 1. Strong motions. *Journal of Geophysical Research: Solid Earth*, **106**(B5), 8745–8766.

Graves, RW, & Wald, DJ. 2004. Observed and simulated ground motions in the San Bernardino basin region for the Hector Mine, California, earthquake. *Bulletin of the Seismological Society of America*, **94**(1), 131–146.

Graves, RW, Pitarka, A, & Somerville, PG. 1998. Ground-motion amplification in the Santa Monica area: Effects of shallow basin-edge structure. *Bulletin of the Seismological Society of America*, **88**(5), 1224–1242.

Graves, RW, Aagaard, BT, Hudnut, KW, Star, LM, Stewart, JP, & Jordan, TH. 2008. Broadband simulations for Mw 7.8 southern San Andreas earthquakes: Ground motion sensitivity to rupture speed. *Geophysical Research Letters*, **35**(22), L22302.

Hamling, IJ, Hreinsdóttir, S, Clark, K, Elliott, J, Liang, C, Fielding, E, Litchfield, N, Villamor, P, Wallace, L, Wright, TJ, *et al.* 2017. Complex multifault rupture during the 2016 M w 7.8 Kaikōura earthquake, New Zealand. *Science*, **356**(154), eaam7194.

Hartzell, S, Harmsen, S, Frankel, A, & Larsen, S. 1999. Calculation of broadband time histories of ground motion: Comparison of methods and validation using strong-ground motion from the 1994 Northridge earthquake. *Bulletin of the Seismological Society of America*, **89**(6), 1484–1504.

Hartzell, S, Liu, P, Mendoza, C, Ji, C, & Larson, KM. 2007. Stability and uncertainty of finite-fault slip inversions: Application to the 2004 Parkfield, California, earthquake. *Bulletin of the Seismological Society of America*, **97**(6), 1911–1934.

Hayes, GP. 2011. Rapid source characterization of the 2011 M w 9.0 off the Pacific coast of Tohoku earthquake. *Earth, planets and space*, **63**(7), 4.

Holden, C, Kaiser, AE, Van Dissen, RJ, & Jury, R. 2013. Sources, ground motion and structural response characteristics in Wellington of the 2013 Cook Strait earthquakes. *Bulletin of the New Zealand Society of Earthquake Engineering*, **46**(4), 188–195.

Hulbert, C, Rouet-Leduc, B, Johnson, PA, Ren, CX, Rivière, J, Bolton, DC, & Marone, C. 2019. Similarity of fast and slow earthquakes illuminated by machine learning. *Nature Geoscience*, **12**, 69–74.

Ide, S. 2015. Slip inversion. *Chap. 9 of: Earthquake Seismology*. Treatise on Geophysics, second edition, vol. 4. Amsterdam, The Netherlands: Elsevier.

James, G, Witten, D, Hastie, T, & Tibshirani, R. 2013. *An introduction to statistical learning*. Vol. 112. Springer.

Jayaram, N, & Baker, JW. 2009. Correlation model for spatially distributed ground-motion intensities. *Earthquake Engineering & Structural Dynamics*, **38**(15), 1687–1708.

Karpatne, A, Ebert-Uphoff, I, Ravela, S, Babaie, HA, & Kumar, V. 2018. Machine Learning for the Geosciences: Challenges and Opportunities. *IEEE Transactions on Knowledge and Data Engineering*.

Kong, Q, Allen, RM, Schreier, L, & Kwon, Y-W. 2016. MyShake: A smartphone seismic network for earthquake early warning and beyond. *Science advances*, **2**(2), e1501055.

Kong, Q, Trugman, DT, Ross, ZE, Bianco, MJ, Meade, BJ, & Gerstoft, P. 2018. Machine Learning in Seismology: Turning Data into Insights. *Seismological Research Letters*.

Lee, RL, Bradley, BA, Stafford, P, Graves, RW, & Rodriguez-Marek, A. 2019. Hybrid broadband ground motion simulation validation of Canterbury, New Zealand. *TBD*, **TBD**(TBD), TBD.

Li, Zefeng, Meier, Men-Andrin, Hauksson, Egill, Zhan, Zhongwen, & Andrews, Jennifer. 2018. Machine Learning Seismic Wave Discrimination: Application to Earthquake Early Warning. *Geophysical Research Letters*.

Litchfield, NJ, Benson, A, Bischoff, A, Hatem, A, Barrier, A, Nicol, A, Wandres, A, Lukovic, B, Hall, B, Gasston, C, *et al.* 2016. 14th November 2016 Mw 7.8 Kaikoura earthquake. Preliminary surface fault displacement measurements, Version 2. *GNS Science*.

Maas, AL, Hannun, AY, & Ng, AY. 2013. Rectifier nonlinearities improve neural network acoustic models. *In: 30th International Conference on Machine Learning*.

Ozgun Konca, A, Kaneko, Y, Lapusta, N, & Avouac, J-P. 2013. Kinematic inversion of physically plausible earthquake source models obtained from dynamic rupture simulations. *Bulletin of the Seismological Society of America*, **103**(5), 2621–2644.

Pedregosa, F, Varoquaux, G, Gramfort, A, Michel, V, Thirion, B, Grisel, O, Blondel, M, Prettenhofer, P, Weiss, R, Dubourg, V, Vanderplas, J, Passos, A, Cournapeau, D, Brucher, M, Perrot, M, & Duchesnay, E. 2011. Scikit-learn: Machine Learning in Python. *Journal of Machine Learning Research*, **12**, 2825–2830.

Perol, T, Gharbi, M, & Denolle, M. 2018. Convolutional neural network for earthquake detection and location. *Science Advances*, **4**(2), e1700578.

Prechelt, L. 1998. Early stopping-but when? *Pages 55–69 of: Neural Networks: Tricks of the trade*. Springer.

Racah, E, Beckham, C, Maharaj, T, Ebrahimi K, S, Prabhat, M, & Pal, C. 2017. ExtremeWeather: A large-scale climate dataset for semi-supervised detection, localization, and understanding of extreme weather events. *Pages 3402–3413 of:* Guyon, I., Luxburg, U. V., Bengio, S., Wallach, H., Fergus, R., Vishwanathan, S., & Garnett, R. (eds), *Advances in Neural Information Processing Systems 30*. Curran Associates, Inc.

Razafindrakoto, HNT, Bradley, BA, & Graves, RW. 2018. Broadband Ground-Motion Simulation of the 2011 M w 6.2 Christchurch, New Zealand, Earthquake. *Bulletin of the Seismological Society of America*, **108**(4), 2130–2147.

Ross, ZE, Meier, M-A, Hauksson, E, & Heaton, TH. 2018a. Generalized Seismic Phase Detection with Deep Learning. *arXiv preprint arXiv:1805.01075*.

Ross, ZE, Yue, Y, Meier, MA, Hauksson, E, & Heaton, TH. 2018b. PhaseLink: A Deep Learning Approach to Seismic Phase Association. *arXiv preprint arXiv:1809.02880*.

Rouet-Leduc, B, Hulbert, C, & Johnson, PA. 2019. Continuous chatter of the Cascadia subduction zone revealed by machine learning. *Nature Geoscience*, **12**, 75–79.

Rousseeuw, Peter J. 1987. Silhouettes: a graphical aid to the interpretation and validation of cluster analysis. *Journal of computational and applied mathematics*, **20**, 53–65.

Smerzini, C, & Pitilakis, K. 2018. Seismic risk assessment at urban scale from 3D physics-based numerical modeling: the case of Thessaloniki. *Bulletin of Earthquake Engineering*, **16**(7), 2609–2631.

Somerville, PG, Smith, NF, Graves, RW, & Abrahamson, NA. 1997. Modification of empirical strong ground motion attenuation relations to include the amplitude and duration effects of rupture directivity. *Seismological Research Letters*, **68**(1), 199–222.

Stirling, M, McVerry, G, Gerstenberger, M, Litchfield, N, Van Dissen, R, Berryman, K, Barnes, P, Wallace, L, Villamor, P, Langridge, R, *et al.* 2012. National seismic hazard model for New Zealand: 2010 update. *Bulletin of the Seismological Society of America*, **102**(4), 1514–1542.

Tarbali, K, Bradley, BA, Huang, J, Lagrava, D, Motha, J, Bae, S, & Polak, V. 2018a. Cybershake NZ v17.9: New Zealand simulation-based probabilistic seismic hazard analysis. *In: 16th European Conference on Earthquake Engineering*.

Tarbali, K, Bradley, BA, Lee, R, Huang, J, Lagrava, D, Polak, V, Motha, J, Bae, S, & Zhu, M. 2018b. Cybershake NZ v18. 6: New Zealand simulation-based probabilistic seismic hazard analysis. *In: SCEC Annual Meeting*.

Titos, M, Bueno, A, García, L, & Benítez, C. 2018. A Deep Neural Networks Approach to Automatic Recognition Systems for Volcano-Seismic Events. *IEEE Journal of Selected Topics in Applied Earth Observations and Remote Sensing*, **11**(5), 1533–1544.

Verdin, KL, Godt, J, Funk, C, Pedreos, D, & Worstell, B. 2007. *Development of a global slope dataset for estimation of landslide occurrence resulting from earthquakes*. Tech. rept. Open File Report 2007–1188. US Geological Survey, Reston, VA, USA.

Verros, Sarah A, Wald, David J, Worden, C Bruce, Hearne, Mike, & Ganesh, Mahadevan. 2017. Computing spatial correlation of ground motion intensities for ShakeMap. *Computers & Geosciences*, **99**, 145–154.

Wald, DJ, & Graves, RW. 2001. Resolution analysis of finite fault source inversion using one-and three-dimensional Green's functions: 2. Combining seismic and geodetic data. *Journal of Geophysical Research: Solid Earth*, **106**(B5), 8767–8788.

Wald, DJ, Earle, PS, Allen, TI, Jaiswal, K, Porter, K, & Hearne, M. 2008a. Development of the US Geological Survey's PAGER system (prompt assessment of global earthquakes for response). *In: Proceedings of the 14th world conference on earthquake engineering*.

Wald, DJ, Lin, K-W, & Quitoriano, V. 2008b. *Quantifying and Qualifying USGS ShakeMap Uncertainty*. Tech. rept. Open File Report 2008–1238. US Geological Survey, Reston, VA, USA.

Wald, DJ, Jaiswal, K, Marano, KD, Bausch, D, & Hearne, M. 2010. *PAGER–Rapid assessment of an earthquake? s impact*. Tech. rept. Fact Sheet 2010–3036. US Geological Survey, Reston, VA, USA.

Wiesel, A, Hassidim, A, Elidan, G, Shalev, G, Schlesinger, M, Zlydenko, O, El-Yaniv, R, Nevo, S, Matias, Y, Gigi, Y, *et al.* 2018. Ml for flood forecasting at scale. *In: 32nd Conference on Neural Information Processing Systems)*.

Worden, CB, Wald, DJ, Allen, TI, Lin, K-W, Garcia, D, & Cua, G. 2010. A revised ground-motion and intensity interpolation scheme for ShakeMap. *Bulletin of the Seismological Society of America*, **100**(6), 3083–3096.

Zeiler, MD. 2012. ADADELTA: an adaptive learning rate method. *arXiv preprint arXiv:1212.5701*.

4.10 Complementary material

4.10.1 Earthquake source discriminator development and training

This section presents the details of the earthquake source discriminator training. To optimize the architecture of both algorithms (RF and GBM), multiple hyper-parameter combinations are tested via grid search (Bergstra & Bengio, 2012) and 5-fold cross-validated (Friedman *et al.*, 2008, pp. 241–248). As the number of simulations (N_{Sim}) remain relatively small with respect to the number of instrument stations (N_{Inst}), only one intensity measure is utilized to discriminate earthquake sources (which can be extended in future applications when $N_{Sim} \gg N_{Inst}$). Hence, in addition to the above described potential hyper-parameters (e.g. tree size or learning rate), the following intensity measures were tested as the input vector: PGA, PGV, AI, pSA(0.5s), pSA(1.0s), and pSA(3.0s). For RF, decision trees are allowed to grow until all terminal nodes represent only one rupture cluster. For GBM, the maximum depth of each decision tree has been fixed to four and the subsampling rate to 50% as recommended in Friedman *et al.* (2008, p. 363 and p. 365). The specific tested hyper-parameters are summarized in Table 4.2, and the ultimately selected models are indicated by a black diamond in Figures 4.16 and 4.17.

Table 4.2: Tested hyper-parameters during the 5-fold cross-validation of the earthquake source discriminator.

Algorithm	**Hyper-parameters**	**Tested values**
Random forest	Number of trees, B	[50, 100, ..., 2000]
	Intensity measure, IM	PGA, PGV, AI, pSA(0.5s), pSA(1.0s), pSA(3.0s)
Gradient boosting machine	Shrinkage coeff., η	$[5 \cdot 10^{-1}, 10^{-2}, 5 \cdot 10^{-3}, 10^{-3}, 5 \cdot 10^{-4}, 10^{-4}]$
	Intensity measure, IM	PGA, PGV, AI, pSA(0.5s), pSA(1.0s), pSA(3.0s)

Figures 4.16 and 4.17 present the training results for RF and GBM, respectively. In both cases, the best intensity measure is AI, followed by PGV. pSA(3.0s) seems only slightly better than PGA and shorter period pSA to discriminate between labels. It can be observed in Figure 4.16 that the number of trees in the RF rapidly loses its influence on the validation error. However, overfitting does not occur. Overfitting refers to a degradation of the validation error (as opposed to training error) that appears when models become too complex for the training data and start memorizing it instead of learning from it (i.e. generalization is lost). Therefore, the selected model is designed with 1000 trees, such that tree diversity allows the random forest to resist input dropout (discussed in Section 4.3.2).

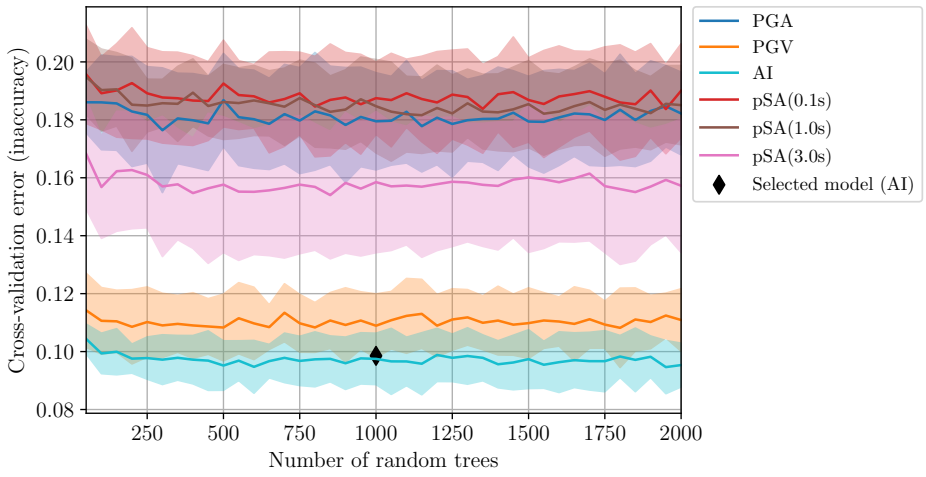

Figure 4.16: RF 5-fold cross validation results. Each color is associated to one intensity measure, and shaded areas indicate the standard deviation of the cross-validated error. The black diamond represents the error of the selected model on the test dataset.

As shown in Figure 4.17(a), the cross-validation results of the GBM shows that reducing the shrinkage coefficient beyond 0.001 only has marginal effects on the algorithm performance. Overfitting is avoided by monitoring the loss on a small portion of the training data (10%) and apply early stopping (Prechelt, 1998) with a 'patience' of five iterations (i.e. if no improvement is observed during five iterations, the training stops).

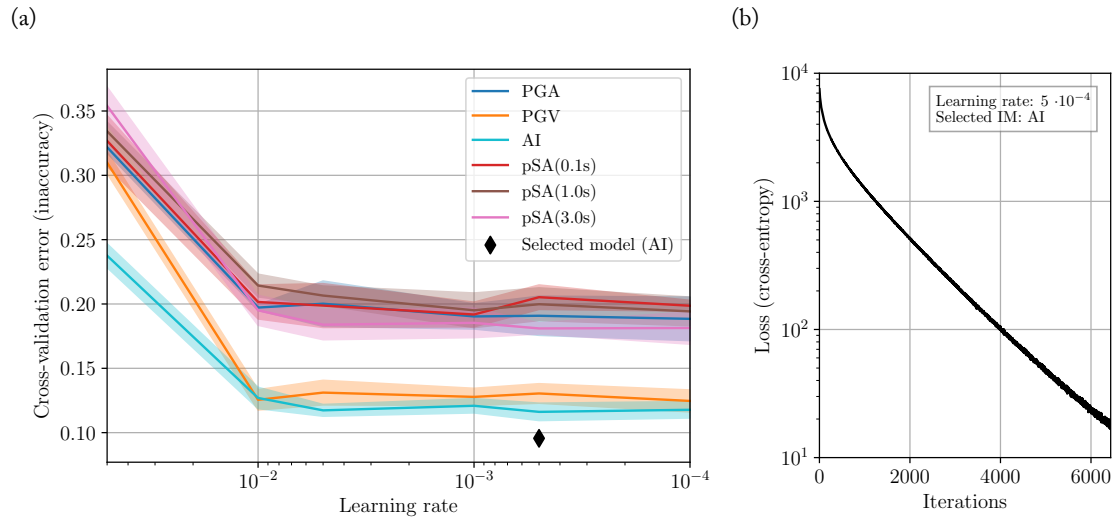

Figure 4.17: (a) GBM 5-fold cross validation results. Each color is associated to one intensity measure, and shaded areas indicate the standard deviation of the cross-validated error. The black diamond represents the error of the selected model on the test dataset. (b) Selected GBM using AI as intensity measure architecture training.

4.10.2 Ground motion generator development and training

As described in Section 4.3.3, the predictive generative network is composed of ten similar regional submodels that receive input data (the rupture cluster probability vector), to which Gaussian noise is added to (1) regularize the network by making it less sensitive to small input variations; and (2) virtually augment the size of the training dataset (Goodfellow *et al.*, 2016, pp. 240–243). All submodels have the same architecture that consists of three deconvolutional layers (see Figure 4.7). Deconvolutional layers are composed of three operations. First, the layer input is upsampled (its dimensions are multiplied). Second, N different convolutions are applied to the upsampled data, where N represents the depth of the layer. The convolutions are carried out with a size of three and a stride of one in both directions (i.e. each convolution kernel is a 3x3 matrix that is shifted by one element until it covers the entire region). Third, results from the convolution are activated with 'leaky' rectified linear units (Maas *et al.*, 2013). Before the convolution, the first upsampling produces a 3x3x213 matrix, where the first two dimensions are a coarse geospatial representation of the final ground motion map. In other words, as the submodels are square and of equal size, their 3x3 dimensions represent a 144x144km portion of New Zealand, where each cell of the 3x3 matrix represents a 48x48km portion of New Zealand. The last dimension (213) is the augmented (i.e. with Gaussian noise) rupture cluster probability vector. For each submodel, the output of the first convolutional layer is a 3x3x256 matrix, where the last number (256) represents the number of different convolutions that were applied to the input. This dimension is also called the layer depth. The second upsampling produces a three-times-finer geospatial representation of the final ground motion map (9x9x128), and the third upsampling a two-times-finer representation (18x18x64). Final submodels represent a 144 by 144 km area of New Zealand (each of its cell representing an eight-by-eight km cell) and are composed of 64 layers. Once all regional submodels are built (not trained), they are concatenated together to provide a New Zealand-wide coverage. In order to save computational effort, the final layers are cropped such that the amount of area covering the Pacific Ocean is minimized (i.e. the grey shaded area in Figure 4.7). A final convolution of kernel size 1x1x6 with a stride of one is applied to the concatenated submodels' results to predict the six ground motion intensities over the whole country. Figure 4.18 presents the entire development of the predictive neural network.

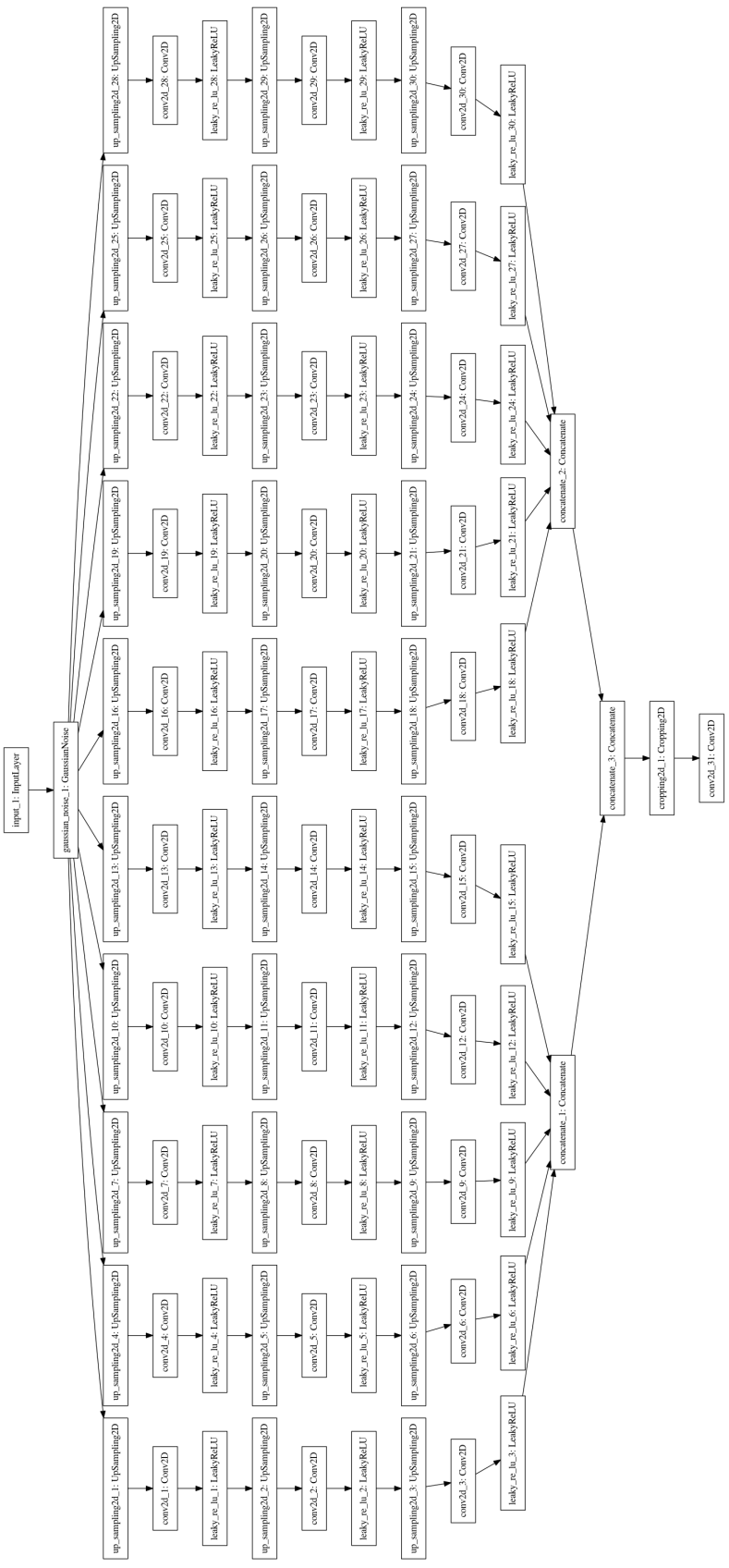

Figure 4.18: Architeture of the deconvolutional neural network. Graph plotted using the embedded function in Keras (Chollet et al., *2015).*

The training of the network is optimized with Adadelta (Zeiler, 2012) and early-stopping (Prechelt, 1998). The loss of the model is evaluated with the mean squared error (MSE). The size of the network, in particular, the depth of its layers, was determined via manual search as the exploration of the potential hyper-parameter space would have been too computationally demanding. Multiple mini-batch sizes were also tested, and a size of four identified as producing the best results. To ensure that no encoding is superior to another (between RF and GBM), both are tested on the same architectures. Figure 4.19 shows the validation loss for both encodings. No clear advantage emerges from using a particular encoding over the other. Hence, the GBM encoding is retained as it also shows better performance in earthquake source identification (see Section 4.3.2).

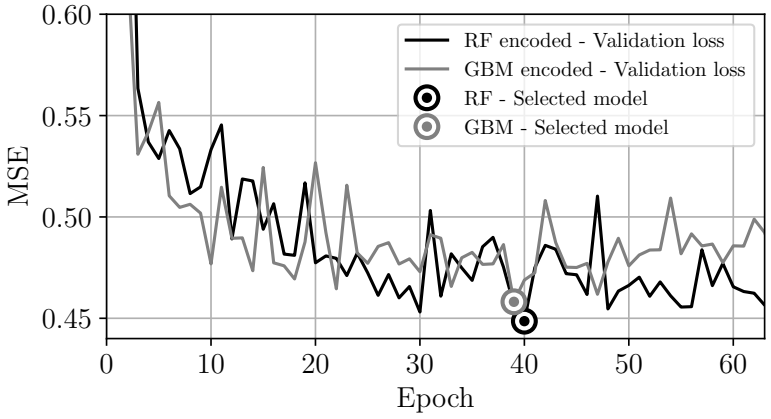

Figure 4.19: Validation loss of the ground motion generator with RF and GBM encoding over the training epochs.

Figures 4.20 and 4.21 present all intensity measures predicted by the predictive generative network from the two analyzed test cases presented in Section 4.3.3.

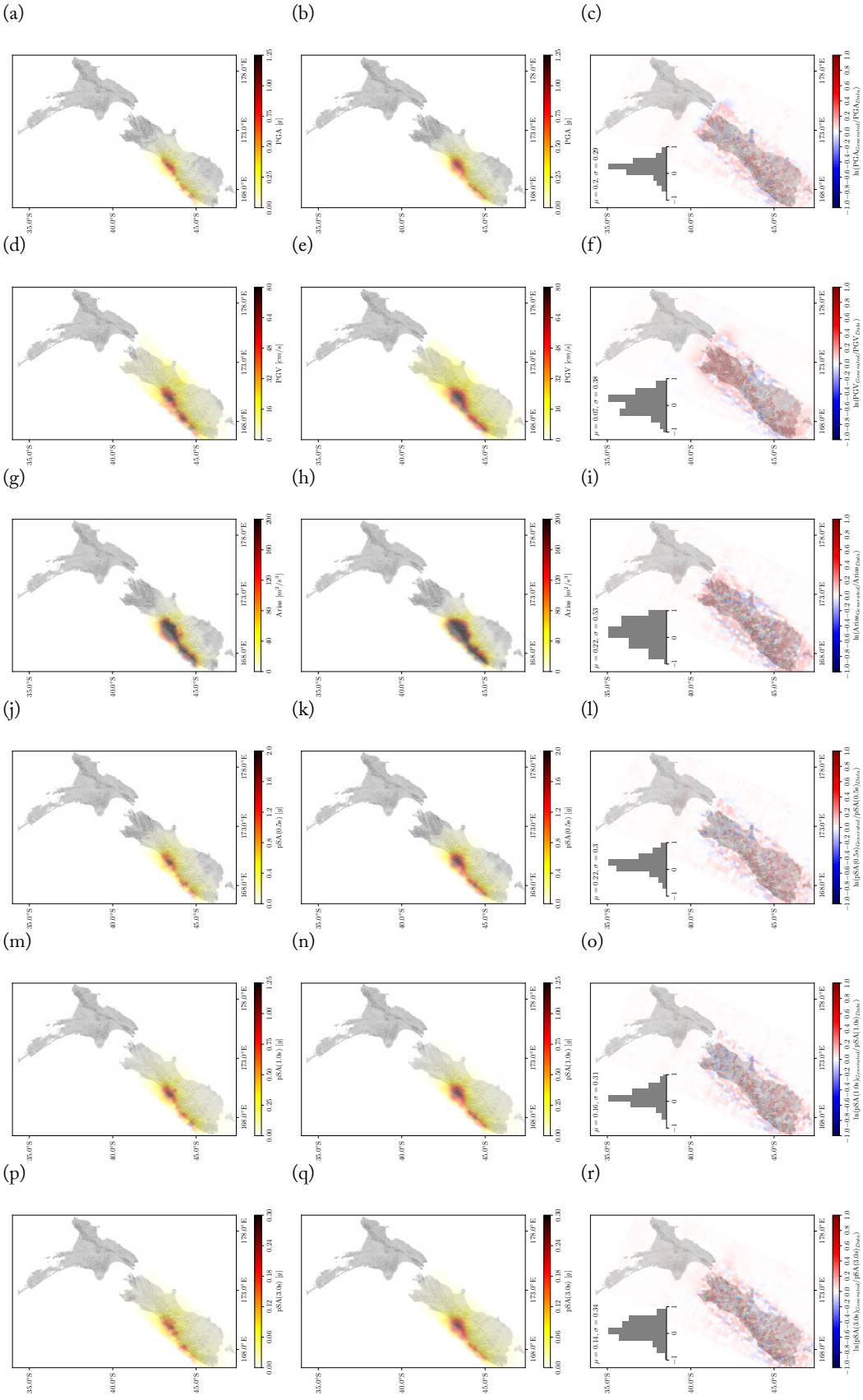

Figure 4.20: Result comparison for an AlpineF2K rupture from the test dataset. (a, d, g, j, m, p): physics-based simulated ground motion results; (b, e, h, k, n, q): ground motion map generator results based on the GBM encoding; and (c, f, i, l, o, r): residuals between the two. (a-c): PGA; (d-f): PGV; (g-i): AI; (j-l): pSA(0.5s); (m-o): pSA(1.0s); and (p-r): pSA(3.0s).

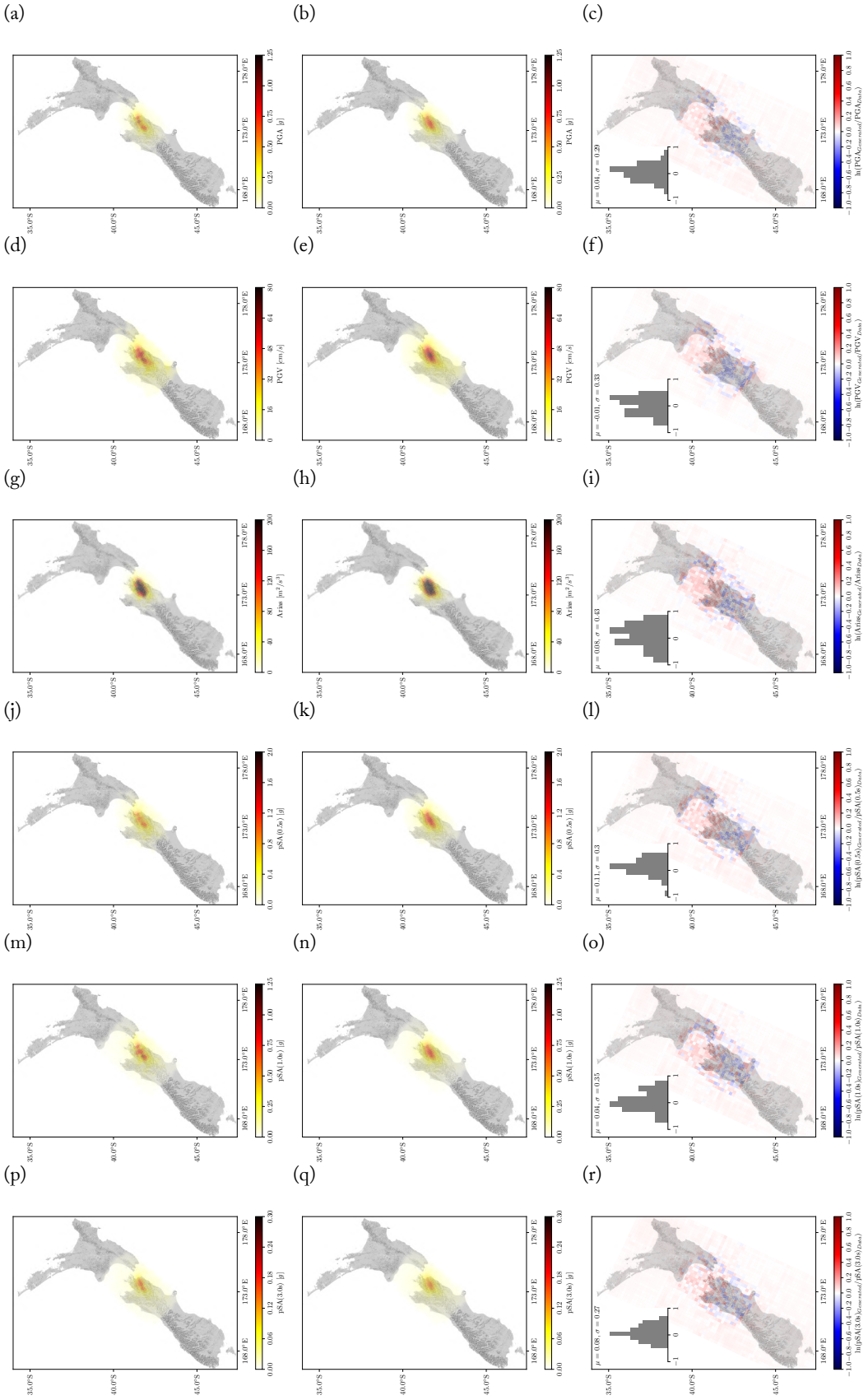

Figure 4.21: Result comparison for an AwatNEVer rupture from the test dataset. (a, d, g, j, m, p): physics-based simulated ground motion results; (b, e, h, k, n, q): ground motion map generator results based on the GBM encoding; and (c, f, i, l, o, r): residuals between the two. (a-c): PGA; (d-f): PGV; (g-i): AI; (j-l): pSA(0.5s); (m-o): pSA(1.0s); and (p-r): pSA(3.0s).

4.10.3 Ground motion map generator results of the 14 November 2016 Kaikōura Mw 7.8 earthquake

This section provides results that complements the analysis of the 14 November 2016 Mw 7.8 earthquake presented in Section 4.5. In particular, Figures 4.22 and 4.23 give the additional intensity measures for the initially available instrument recordings and the entire set of instrument recordings, respectively.

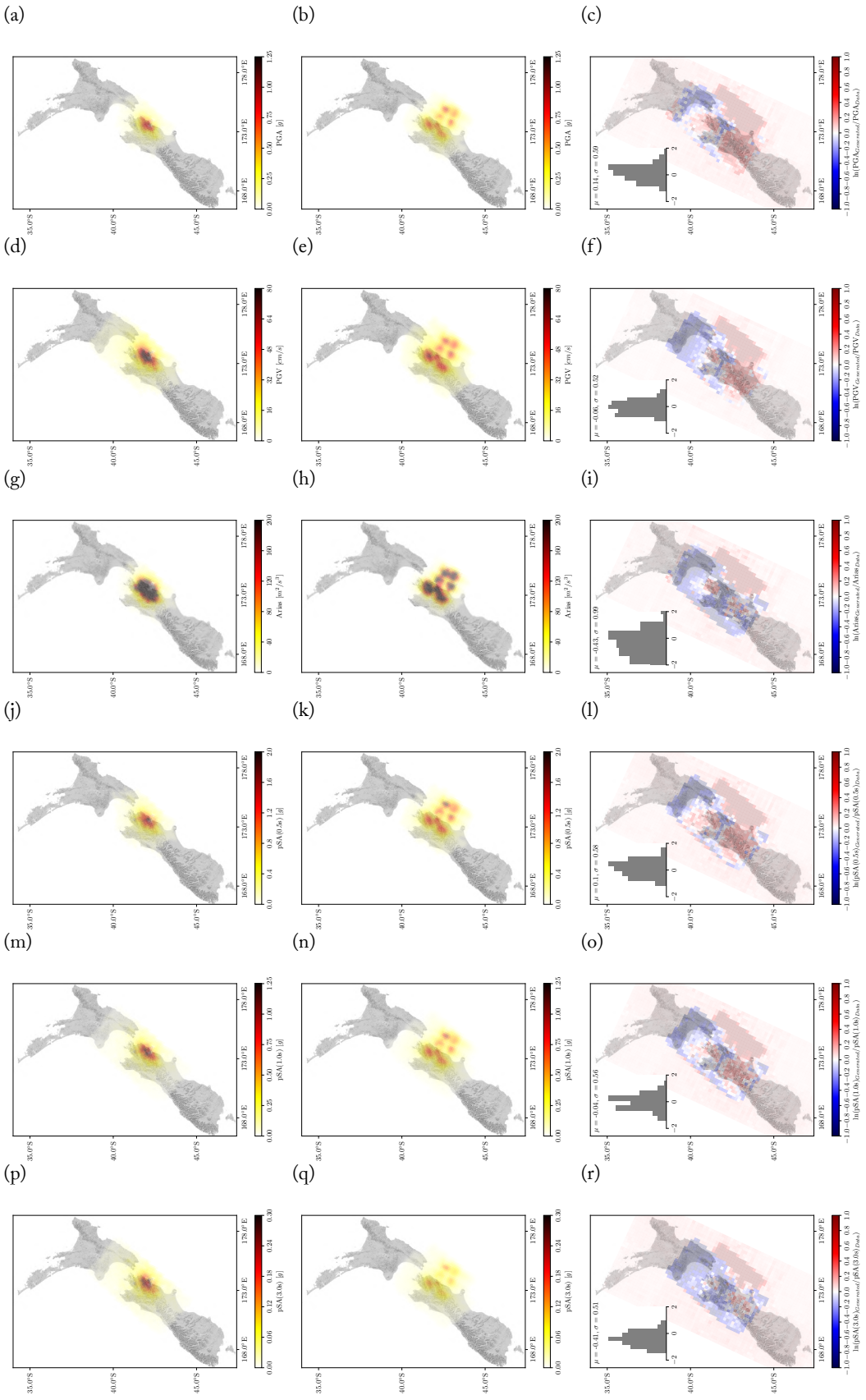

Figure 4.22: Result comparison for the 14 November 2016 Kaikōura Mw 7.8 earthquake using the initially available recordings. (a, d, g, j, m, p): physics-based simulated ground motion results; (b, e, h, k, n, q): ground motion map generator results based on the GBM encoding; and (c, f, i, l, o, r): residuals between the two. (a–c): PGA; (d–f): PGV; (g–i): AI; (j–l): pSA(0.5s); (m–o): pSA(1.0s); and (p–r): pSA(3.0s).

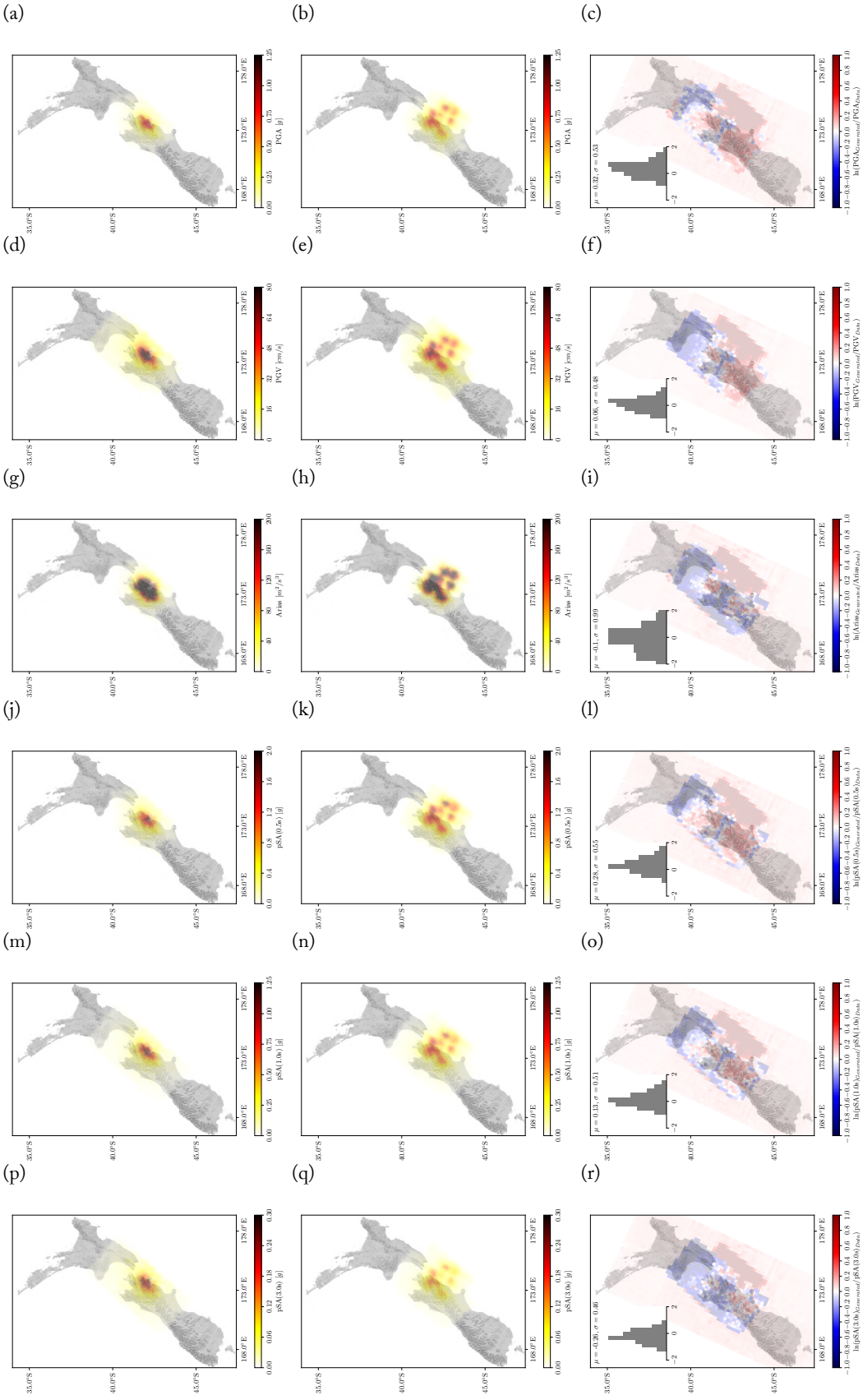

Figure 4.23: Result comparison for the 14 November 2016 Kaikōura Mw 7.8 earthquake using all the recordings. (a, d, g, j, m, p): physics-based simulated ground motion results; (b, e, h, k, n, q): ground motion map generator results based on the GBM encoding; and (c, f, i, l, o, r): residuals between the two. (a–c): PGA; (d–f): PGV; (g–i): AI; (j–l): pSA(0.5s); (m–o): pSA(1.0s); and (p–r): pSA(3.0s).

Chapter 5

A neural network for automated quality screening of ground motion records from small magnitude earthquakes

"If a machine is expected to be infallible, it cannot also be intelligent."

Alan Mathison Turing, 1946, Technical prospectus

Adapted from: Bellagamba X, Lee RL, and Bradley BA (in press). "A neural network for automated quality screening of ground motion records from small magnitude earthquakes". *Earthquake Spectra*. DOI:10.1193/122118EQS292M

The ambitious scopes of recent earthquake ground motion studies are generating a need for more quality ground motion records. As the number of deployed sensors is rapidly growing through improved accessibility and cost (e.g. ground motion stations, low cost accelerometers, smart phones), an exponentially increasing amount of data is being generated. Previously, quality-assured ground motion datasets for engineering applications were generated using both manual and automated quality screening methodologies. More recently, new techniques have emerged that potentially offer both improved classification accuracy, and computational expediency. This work presents a machine learning-oriented method to facilitate and accelerate the quality classification of ground motion records from small magnitude earthquakes. Feedforward neural networks are selected for their ability to efficiently recognize patterns and are trained on two New Zealand datasets. An application to physics-based ground motion simulation validation indicates that the proposed approach delivers results that are comparable to manual quality selection. Robust automatic ground motion quality screening allows a significant increase in dataset size for development, calibration and validation of ground motion models.

5.1 Introduction

The quality of earthquake-induced recorded ground motions has been a topic of discussion for decades, previously with respect to analog instruments, but more recently with digital instruments (Hudson, 1979; Douglas, 2003; Boore & Bommer, 2005; Douglas & Boore, 2011). Here, quality refers to how well the instrument recording (comprising signal and noise) represents the actual ground shaking (signal) at a particular location. In this context, the content of the ground motion record attributed to the shaking caused by the earthquake (the desired information) is considered the signal and any error or undesired disturbance is considered noise. As the quantity of operational strong ground motion

recording stations are continuously increasing and providing better spatial coverage, the need for automated determination of ground motion quality becomes a necessity. This is further accentuated by the developing technology for low cost recording instruments, which could realistically lead to a big data explosion (Anthony *et al.*, 2018).

Ground motions are inherently complex as a result of the underlying nature of earthquake rupture, wave propagation and local site effects. Each of these effects can influence the amplitude, frequency content and duration of ground motions. Small amplitude shaking from small magnitude earthquakes (e.g. $M_w \leq 5.0$), in particular, are more likely to have their quality compromised due to noise that may have comparable amplitudes and can contaminate the record. At low frequencies (below 1Hz), seismic noise is predominantly due to natural causes, such as ocean waves, variations in atmospheric pressure and wind. At high frequencies (above 1Hz), seismic noise is caused by human activities, such as motor vehicles, industrial work and machinery, and electrical currents, as well as natural sources, such as rivers (Okada & Suto, 2003). While conventional signal processing techniques, such as baseline correction and filtering, are able to correct records for some types of noise, often ground motions are affected in a way that no amount of processing can reliably recover the signal. These low quality recordings are detrimental for ground motion studies and are generally discarded to maintain robust inferences.

The most commonly used metric for determining ground motion quality is the signal-to-noise ratio (SNR) (Ancheta *et al.*, 2014; Dawood *et al.*, 2016; Kishida *et al.*, 2017; Rennolet *et al.*, 2018). Fundamentally, SNR is a measure of the strength of a signal relative to background noise. This requires identification of the signal and the noise which can be difficult to isolate. To simplify the calculation, it is common to take the noise as the pre-event duration of the ground motion record or use a generic white noise corresponding with expected amplitudes and frequency content (e.g. Cauzzi & Clinton (2013)). The signal can also be isolated, but is often taken as the entire ground motion record for simplicity (Boore & Bommer, 2005; Dawood *et al.*, 2016). There are several mathematical definitions for SNR. The most simple definition is to take the peak ground acceleration (PGA) and divide it by the peak absolute acceleration of the noise. A more complex definition, from an energy perspective, compares the Arias intensity of the signal with that of the noise. Boore & Bommer (2005) also suggests other means to check the quality of ground motions including examining the shape of the Fourier amplitude spectra (FAS), and integrated velocities and displacements, to see if they are realistic. Additionally, Dawood *et al.* (2016) also enforced limits on final displacements and velocities. However, many of these tests are inherently manual and hence time consuming when conducted for a large number of ground motions.

In recent years, there have been large ground motion datasets created using various methods of quality screening and processing (Ancheta *et al.*, 2014; Cauzzi *et al.*, 2016; Dawood *et al.*, 2016; Van Houte *et al.*, 2016). While the ground motion processing steps are broadly similar, comprising baseline corrections, instrument corrections (if necessary), and filtering at low and high frequencies, the tests for whether a ground motion is of acceptable quality varied. The PEER record processing methodology (Ancheta *et al.*, 2013), for example, employed in the development of the NGA-West2 database (Ancheta *et al.*, 2014) is one of the most commonly adopted methodologies. However, a significant drawback of this methodology is the need for manual, user-determined high-pass and low-pass filter frequencies, subsequent visual inspection of corrected displacements, and review of Fourier spectra, which can be excessively time-consuming. Dawood *et al.* (2016) developed a step-by-step automated protocol to systematically process ground motion records, which alleviated the need for manual intervention, by iterating on processing parameters (e.g. high-pass corner frequency) until the record met some predefined criteria, or was discarded otherwise.

Despite numerous challenges (non-uniform geospatial and temporal recordings, amorphous boundaries of studied objects or highly multidimensional problems), machine learning applications in geosciences are gaining momentum (Karpatne *et al.*, 2018). Such methods are now used to detect hurricanes (e.g. Racah *et al.*, 2017) or monitor volcanic activity (e.g. Titos *et al.*, 2018). In seismology,

machine learning techniques are applied to a relatively broad range of problems such as early-detection (e.g. Kong *et al.*, 2016; Li *et al.*, 2018), phase picking (e.g. Ross *et al.*, 2018a,b) or earthquake location detection (e.g. Perol *et al.*, 2018). More examples of applications are given in Kong *et al.* (2018). However, to the knowledge of the authors, little effort has so far been dedicated to optimize the expediency of ground motion record quality screening.

This work presents a machine-learning-based method that automatically classifies ground motion records based on their underlying characteristics. The training dataset comprises both pre-existing and newly classified data. The former has been previously used to validate physics-based ground motion modelling in the Canterbury, New Zealand, region, whereas the latter comes from the Wellington, New Zealand, region and has been classified to increase the dataset diversity. The proposed classifier is based on a feedforward neural network (described in Section 5.3), based on its recognized ability to efficiently detect, extract and recombine patterns hidden in the data (Friedman *et al.*, 2008, p. 352). This paper presents the details of the utilized dataset, the assumptions and methodology to build the neural network classifier, its validation and effects on the distribution of the selected ground motion records from both an intensity measure and a geospatial perspective, and finally its application to physics-based ground motion model validation.

5.2 Ground motion dataset

5.2.1 Dataset characteristics

To develop a neural network for ground motion quality classification, a large dataset is required for model training and validation purposes. This study considers ground motion recordings from small magnitude earthquakes ($3.5 \leq M_w \leq 5.0$) which have occurred in the Canterbury and Wellington regions of New Zealand between 2003–2018, as shown in Figure 5.1. The two regions are geographically separated by approximately 300km, resulting in diverse source, path and site characteristics. Earthquakes considered generally occur on active shallow crustal faults (i.e. centroid depth less than 20km) and shallow site conditions vary from softer sedimentary basin deposits (gravel and marine fines) to harder rock (Begg *et al.*, 2000; Forsyth *et al.*, 2008).

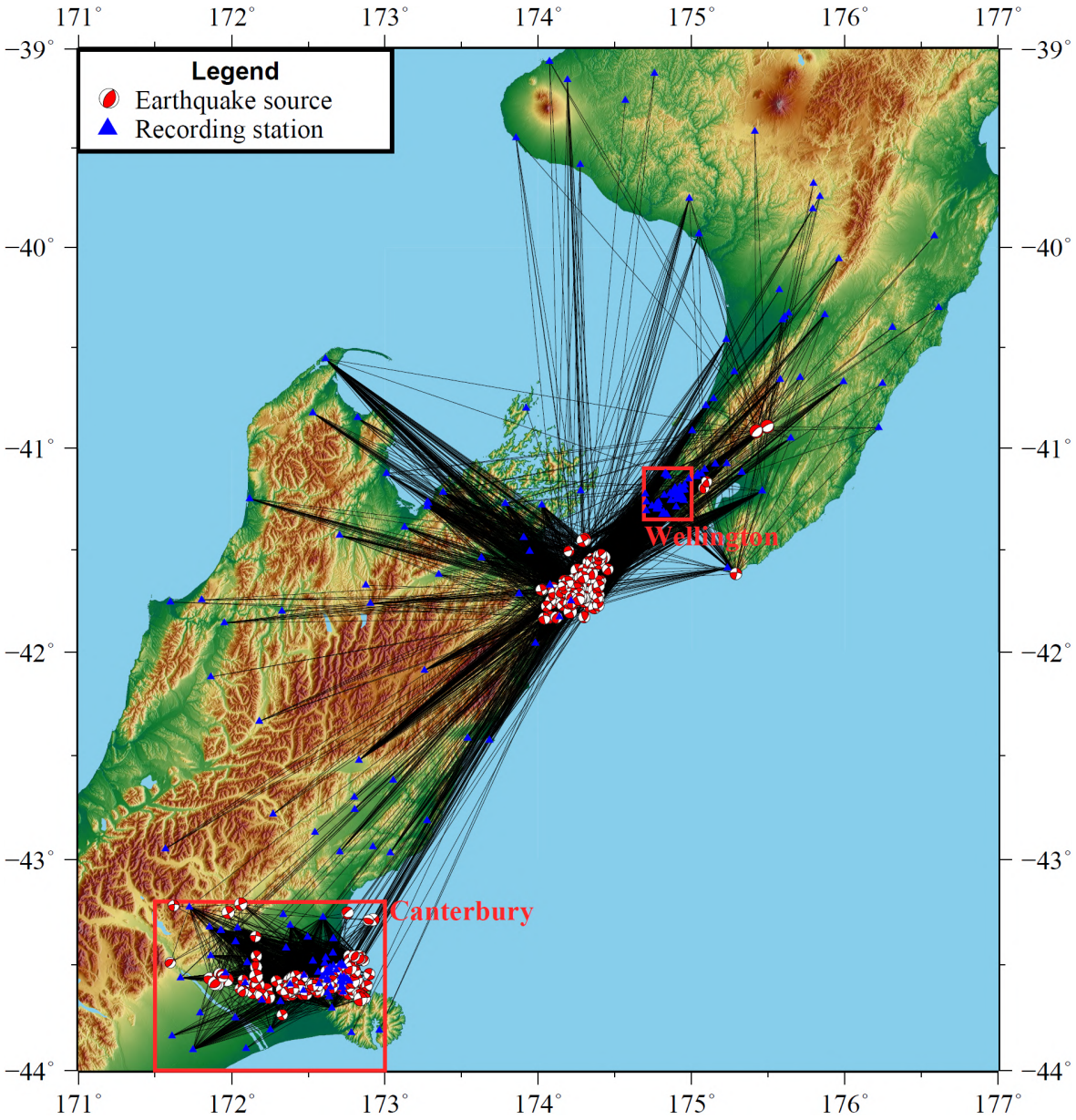

Figure 5.1: 327 earthquake sources with 8467 ground motions recorded across 195 stations are considered in this study. Schematic ray paths of observed ground motions are also shown as black lines. The Canterbury and Wellington regions are explicitly highlighted.

The Canterbury dataset is based on the ground motions considered in a hybrid broadband ground motion simulation validation study conducted by Lee *et al.* (2019), with 3989 records from 148 earthquakes across 43 stations. This subset of data has been geographically limited for the application which it was initially inteded for and is used as-is (this limitation can be alleviated in the future as more data can be assimilated into the model developed in this study). Source-to-site distances do not exceed 100km as a result of this geographic limitation. The Wellington dataset has been specifically developed for this study, with 4478 records from 179 earthquakes across 142 stations. This subset of data has no enforced geographic limitation. Collectively, this amounts to a dataset of 8467 ground motion records. Instruments used to record the ground motions generally have flat response between roughly 0.1Hz to 50Hz or 200Hz (Patterson *et al.*, 2007; Van Houte *et al.*, 2016). Sample rates of instruments at broadband stations are mostly 50Hz while instruments at strong motion stations are usually 200Hz.

5.2.2 Manual ground motion quality screening

In determining the quality score of a ground motion record, several key pieces of information are considered from both raw and processed records. Here, raw records refer to version 1 unprocessed records obtained from the GeoNet file transfer protocol (link to the ftp provided in Section 5.7). Two variations of processed records are considered to investigate the ground motions at different frequencies. Both variants are baseline corrected (by removing the mean of the record and the remaining linear trend) but are bandpass filtered at different frequencies (with 4th order butterworth filters). One set of processed motions are filtered with a high-pass frequency of 0.08Hz (to retain Fourier amplitudes at 0.1Hz) and a low-pass frequency of 20Hz or 50Hz, for records with sample rates of 50Hz or 200Hz, respectively, and is referred to as broadband-processed. The other set of processed motions are filtered with high-pass and low-pass frequencies of 0.08Hz and 1Hz, respectively, and is referred to as low frequency-processed.

The quality of the ground motions were manually determined primarily by visual examination of time series and FAS plots of the raw and processed records. The raw records were examined to determine how the time series and FAS looked as they were recorded (allowing for determination of SNR), the broadband-processed motions provided insight on how the records appear in engineering applications, and the low frequency-processed motions emphasized the characteristics of the low frequency motion (which are small amplitude relative to higher frequencies). Several criteria were considered when visually examining the ground motion time series. A compact summary is presented here while a comprehensive guideline is included in Section 5.10.1.

1. Comparison of the acceleration amplitudes of the pre-event noise with that of the earthquake ground motion signal.
2. Inspection of the acceleration amplitudes at the end of the record to determine if the ground motion has adequately finished or terminated early in the coda.
3. Comparison of record FAS with noise FAS, effectively measuring frequency-dependent SNR.
4. Inspection of the shape of the record FAS, with emphasis on the sloped/decaying low frequency branch.
5. Inspection of the velocity time series obtained via integration of the filtered acceleration.

Based on the adopted criteria, each three component set of ground motions for one source-site pair (two horizontal components and one vertical component) are scored with discrete values of either 0, 0.25, 0.5, 0.75 or 1 where 0 represents the lowest quality and 1 represents the highest quality. Scores of 0, 0.25 and 0.5 are considered low quality and scores of 0.75 and 1 are considered high quality. Records which have distinguished multiple wave trains corresponding to multiple earthquakes, electronic malfunctions, or were triggered late such that the P-wave arrival was not recorded were manually removed if encountered. It is important to note that the manual classification performed here has an engineering-oriented application mindset, so ground motion features which are considered important may differ for other applications.

Table 5.1 provides the results of the manual quality classification for the Canterbury and Wellington regions. The dataset across both regions are relatively balanced between high quality ground motions and low quality ground motions. The Wellington dataset also has a larger proportion of 0.25–0.75 scores as the ground motions were more difficult to definitively classify as high or low quality. Figure 5.2 presents the distribution of high and low quality ground motions, showing relatively wide coverage across all magnitudes and source-to-site distance. The histograms (which are partially transparent with high and low quality bars overlapping) show that there is a higher proportion of high quality ground motions occurring from relatively larger magnitude earthquakes and at shorter source-to-site distances, and vice versa for low quality ground motions. As it can be expected, this indicates that, for the same magnitude, signal quality tends to deteriorate with distance to the site.

Table 5.1: Distributions of manually determined quality scores for the Canterbury, Wellington, and combined datasets.

Quality score	Canterbury	Wellington	Combined
1	1729	1313	3042
0.75	431	916	1347
0.5	11	88	99
0.25	67	365	432
0	1751	1796	3547

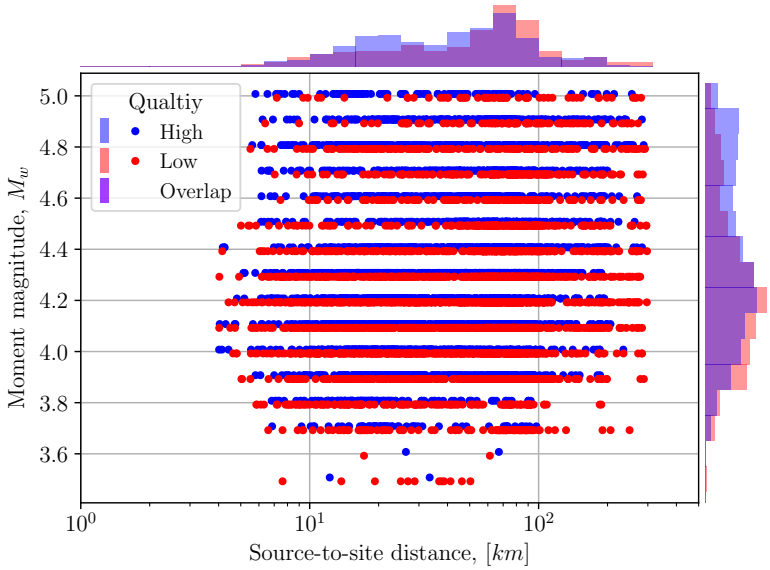

Figure 5.2: Earthquake ground motion magnitude and source-to-site distance distributions for manually classified high and low quality ground motions.

Table 5.2: Ground motion quality metrics used to quantitatively characterise ground motion records and their associated broader categories. Further details are provided in Sections 5.10.1 and 5.10.2.

Category	Detailed metric
Time domain acceleration amplitude ratios	A: Peak noise to PGA ratio
	B: Average tail ratio
	C: Maximum tail ratio
	D: Average tail noise ratio
	E: Maximum tail noise ratio
	F: Average head ratio
Ground motion durations and duration ratios	G: 10%–20% bracketed duration ratio
	H: 5-75% significant duration
	I: 5-95% significant duration
Fourier amplitude ratios	J: Low frequency (below 0.1Hz) pre-event FAS to maximum signal FAS ratio
	K: Low frequency (below 0.1Hz) entire signal FAS to maximum signal FAS ratio
	L: Fourier amplitude ratio
Signal-to-noise ratios	M: Minimum SNR
	N: Maximum SNR
	O: Average SNR
	P: Average SNR between 0.1-0.5Hz
	Q: Average SNR between 0.5-1.0Hz
	R: Average SNR between 1.0-2.0Hz
	S: Average SNR between 2.0-5.0Hz
	T: Average SNR between 5.0-10.0Hz

5.2.3 Ground motion quality metrics

To develop a neural network for ground motion quality classification, 20 ground motion quality metrics were defined and calculated, related to the amplitude, frequency content, and duration, to separate high and low quality ground motions. The considered metrics are presented in Table 5.2 with comprehensive details regarding the calculation of the metrics detailed in Section 5.10.2. The values for each metric are geometric means of the two horizontal components of the raw (unprocessed) records. The interaction of the metrics are not trivial and assigning a pass or fail value for each parameter is subjective. Therefore this problem lends itself well to a machine learning solution.

To highlight the difference between a high and low quality ground motion record which would be scored 1 and 0, respectively, an example of each are provided in Figure 5.3. Figure 5.3(a) and (b) present the raw acceleration time series of one horizontal component of a high and low quality record, respectively. Annotated on the plots are the maximum absolute acceleration amplitudes of the noise/pre-event trace (PN), entire record (PGA), and tail end (PT), and the dashed line denotes the P-wave arrival. Based on this comparison, it is evident that the PN and PT are small relative to the PGA for the high quality record compared to the low quality record. Large PN/PGA values suggest that the noise is significant relative to the earthquake signal while large PT/PGA values suggest that the ground motion records may have been terminated early in the coda. Figures 5.3(c) and (d) present Husid plots corresponding to Figures 5.3(a) and (b), respectively. Prior to the arrival of seismic waves, the high quality record has practically zero build-up in normalized cumulative Arias intensity (AI) compared to the low quality record which has roughly 3% at the P-wave arrival. Figures 5.3(e) and (f) present the FAS of the pre-event trace and entire record with corresponding smoothed spectra. The FAS of the high quality signal has a shape which is broadly consistent with seismic theory, with

slopes at low and high frequencies that are linear in log space and a plateau at moderate frequencies, while the low quality signal has an irregular shape. Figures 5.3(g) and (h) present the SNR of the records, where the high quality record has large SNR at frequencies of interest (0.1-20Hz) while the low quality record has low SNR (<1) at low frequencies.

5.3 Feedforward neural network for quality screening

The quality screening of ground motion records is a multivariate and subjective classification problem. Furthermore, the potentially large dataset size makes it an ideal target for machine-learning-based approaches. As discussed subsequently, selected quality metrics show non-linear interactions that complicates the record classification. The idea is therefore to train an algorithm that searches for specific patterns in the data that qualify high quality ground motion records. Neural networks have been proven particularly efficient in pattern recognition (Friedman *et al.*, 2008, p. 352). They also have better predictive capabilities than most other classification techniques with the notable exception of support-vector machines (Friedman *et al.*, 2008, Table 10.1), which fitting can be excessively computationally expensive (Abdiansah & Wardoyo, 2015). However, neural networks remain less interpretable than other machine learning algorithms like tree-based methods (Benítez *et al.*, 1997, Friedman *et al.*, 2008, p. 352 and Table 10.1, Heinert, 2008). Weights between the input and the first hidden layer can nevertheless provide some intuitive insights on the importance of each utilized metrics. Despite this last caveat, and given the problem at hand, neural networks are selected to assess the quality of ground motion records. This section briefly introduces neural networks, details the composition of the training and testing datasets, provides and justifies the pre-processing of the data, and describes the key elements of the neural network training.

5.3.1 Introduction to feedforward neural networks

A feedforward neural network is a supervised classification technique using repeated, activated, weighted linear combinations of a given input to predict its class (in the present case, low or high quiality ground motion records). A very simple feedforward neural network architecture is provided in Figure 5.4. More details about neural network architecture, training methodologies and validation techniques than the herein introduction can be found in Haykin (1994); Friedman *et al.* (2008); Goodfellow *et al.* (2016). In the machine learning context, supervised means that the algorithm learns to recognize, or fit, labelled training data (i.e. being provided the correct result of each data point). Feedforward denotes the type of neural network being used in this study. Feedforward neural networks do not perform any convolution on the input data, and do not possess any feedback loops as, for example, recurrent neural networks. A feedforward neural network is a stack of multiple layers composed of neurons. A neuron is a series of two operations. The first operation is the weighted sum of the neuron input and its internal bias, and the second one is the activation of this weighted sum by a non-linear function like the hyperbolic tangent, the sigmoid or the rectifier functions. Figure 5.4 (b) shows the anatomy of a neuron.

A typical feedforward neural network, like the one proposed in Figure 5.4(a), is composed of three main parts: (1) an input layer, (2) N hidden layers, and (3) an output layer. The input layer represents the vector of input variables for the problem, in this case, the ground motion record quality metrics. Hidden layers create the non-linear hyperplane that separates the data into different classes by recombining and activating the output from previous layers. The output layer delivers the model prediction, which is further used to estimate its loss (or residual). A neural network is trained using stochastic gradient descent (SGD) coupled with the so-called back-propagation method, the former being responsible for randomly picking the training data and evaluating the learning rate-weighted loss gradient, and the latter for updating the model parameters following the chain rule of calculus. By repeating SGD and back-propagation iteratively (each iteration referred to as an *epoch*), the neural network weights and biases are updated and it *learns* to correctly classify the data.

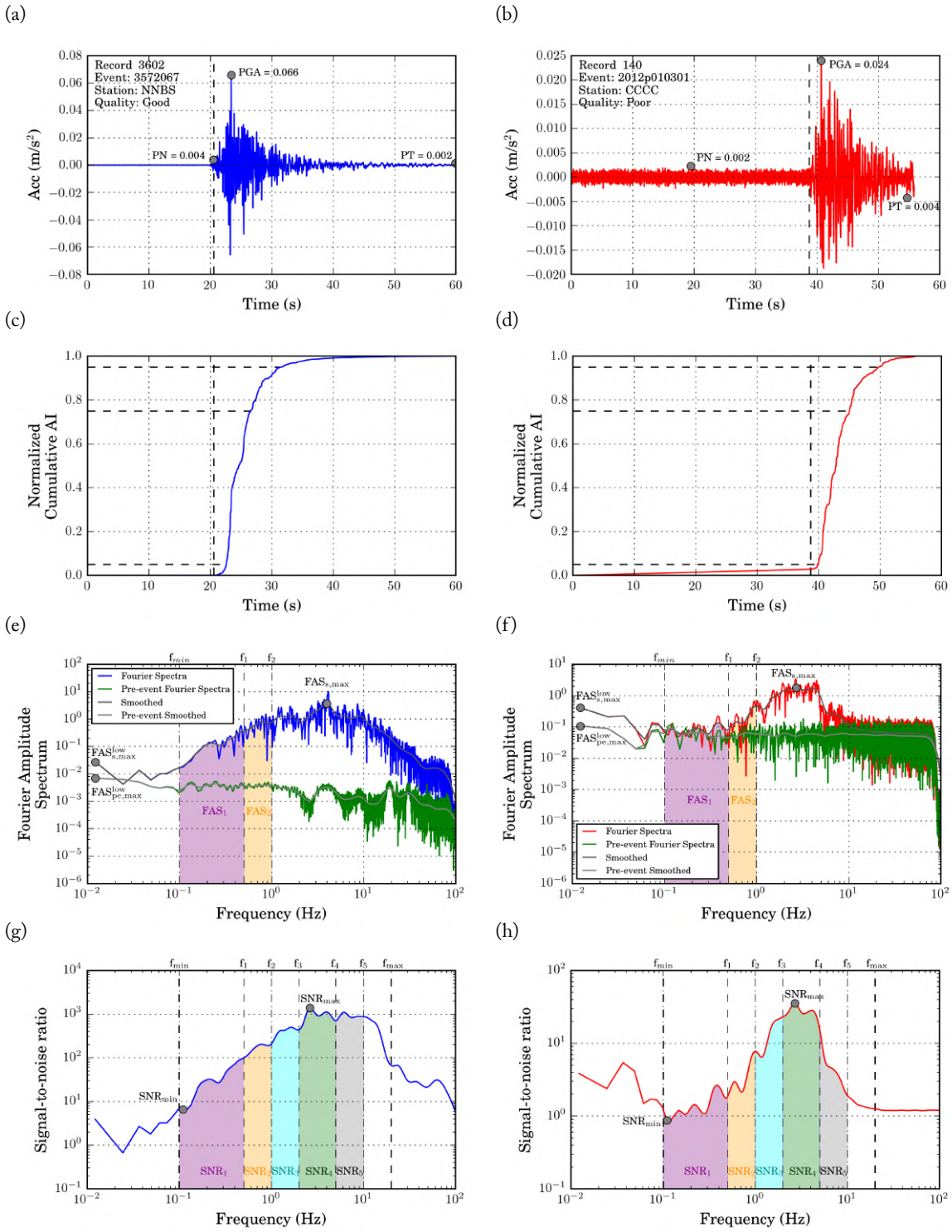

Figure 5.3: Comparison between a high (left) and low (right) quality ground motion record. (a) and (b): raw ground motion time series; (c) and (d): Husid plots; (e) and (f): FAS; and (g) and (h): SNR.

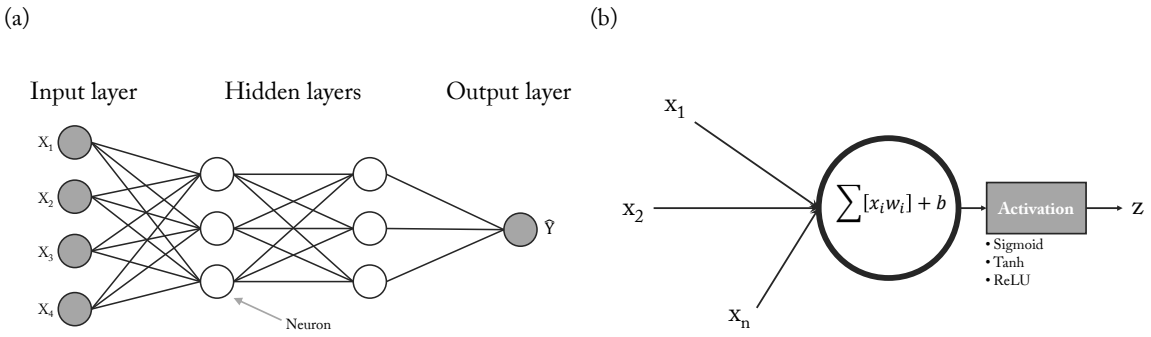

Figure 5.4: (a) Layout of a two-hidden-layer feedforward neural network; and (b) anatomy of a single neuron

Table 5.3: Composition of the training and validation datasets used to train both the single region and the mixed regions neural networks. The composition of each subset is given by quality score. As described in Section 5.3.3, numbers between brackets are not utilized.

Training configuration	Quality score	Training set	Test set
A: Canterbury only	1.0	1729	1313
	0.75	(431)	916
	0.5	(11)	88
	0.25	(67)	365
	0.0	1751	1796
B: Canterbury and Wellington	1.0	1525	1517
	0.75	(691)	656
	0.5	(41)	58
	0.25	(208)	224
	0.0	1796	1751

In machine learning, it is usual to keep a portion of the data undisclosed to the algorithm during its training phase. This data is referred to as the test dataset and is used to evaluate the predictive capabilities of the developed model. To avoid overfitting, a portion of the training dataset, called the validation dataset, is used to monitor the loss during the training phase.

5.3.2 Ground motion record training and testing datasets

Given the different origins of the considered datasets (Canterbury and Wellington regions), two different neural networks are trained against different data mixes. The first model is trained exclusively using the Canterbury dataset and tested against the entire Wellington dataset. The second model is trained against a mix of the Wellington and Canterbury datasets and tested against the remainder of the data. The partitioning of the data are summarized in Table 5.3. This approach allows a direct comparison of the effect of ground motion record origin diversity within the training set.

5.3.3 Hypothesis on ground motion quality and data pre-processing

To assess ground motion record quality, the assumption is made that ground motion records of high and low quality do not share the same quality metric distribution. The pre-processing of the data used on the neural network input data will show that this assumption cannot be rejected.

As noted by da Silva & Adeodato (2011), neural networks tend to exhibit better performance on decorrelated and amplitude-like data. Hence, the data pre-processing consists of a deskewing

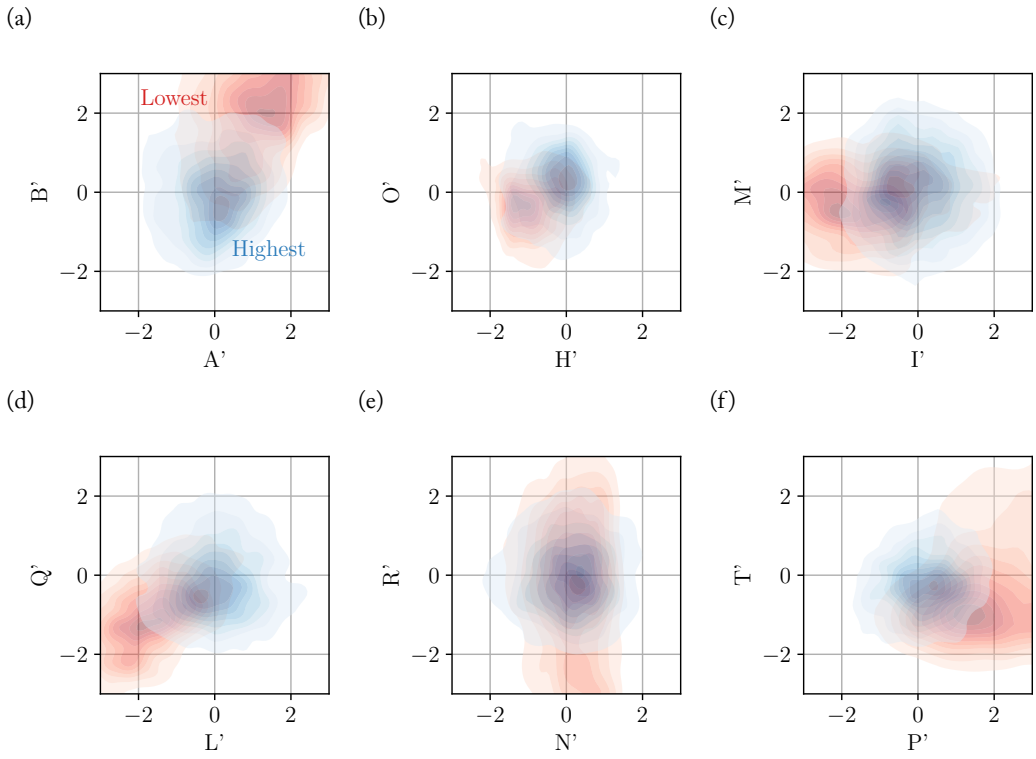

Figure 5.5: Joint plots of some transformed variable pairs of lowest (in red) and highest (in blue) quality ground motion records.

operation based on a Tukey's ladder of powers (Helsel & Hirsch, 2002), and a standardizing and decorrelating procedure using a ZCA whitening transform (Kessy *et al.*, 2018). The transformed input variables are therefore decorrelated and follow the standard Gaussian distribution ($\mathcal{N}(0.0, 1.0)$). Due to the mathematical transform, these new variables lose their physical meaning (e.g. B' does not represent the transformed average tail ratio). Note that all the transformed variables from the ZCA are kept in order to preserve the full variability of the dataset. Details on the original quality metric distributions (cumulative density functions in Figure 5.11 and correlation matrix 5.12) can be found in Section 5.10.3.

The pre-processing operations are fitted on the ground motions of highest quality only, such that the distribution of ground motion records of lower quality would be different if the initial assumption is proven to be true. Neural networks trained on data split A and B presented in Table 5.3 have their own pre-processing operation series (i.e. both pre-processings are fitted on their respective training dataset). Results of the pre-processing are available in Section 5.10.4 and show that all transformed variables follow the Gaussian distribution in Figures 5.13 and 5.14 for the Canterbury and Canterbury-Wellington pre-processings, respectively.

Figure 5.5 (a-f) present the joint plots of six pairs of transformed variables. It can be observed in Figure 5.5(e) that some important overlaps could exist between variables. Nevertheless, even such extreme cases of transformed variable pairs allow partial separation of low and high quality ground motion records. In the other presented pairs, the separation of data is more evident. However, there are no observed cases where the data is linearly separable (i.e. minor overlaps exist between all pairs). P-values developed from Kolmogorov-Smirnov (KS) tests (Benjamin & Cornell, 1975, pp. 466–471) indicate that the distributions of lowest and highest quality ground motion records show appreciable differences. Details about the KS tests and their results are available in Section 5.10.4 and Figure 5.15, respectively.

Table 5.4: Neural network parameters and their respective values used in the grid search

Varying neural network hyper-parameter	Tested values
Number of neurons in the first hidden layer, n_1	10; 15; 20
Number of neurons in the second hidden layer, n_2	0, 10; 15; 20
Mini-batch size, m	4, 8, 16

5.3.4 Neural network architecture selection and training method

Bergstra & Bengio (2012) have shown that the performance of a neural network is linked to its architecture and parametrization (e.g. number of hidden layers, number of neurons, learning rate, etc.). While the exploration of the entire parameter search space is practically impossible (Bergstra & Bengio, 2012; Bengio, 2012), combinations of only a few parameters given in Table 5.4 are tested via grid search (Bengio, 2012 and Goodfellow *et al.*, 2016, pp. 434–436). In this approach, the number of layers (1 or 2), the number of neurons, and the size of the mini-batches are tested. As oversized and overtrained neural networks tend to overfit (Baum & Haussler, 1989; Geman *et al.*, 1992; Lawrence *et al.*, 1998), the size of the developed neural network remains small in order to retain good generalization capabilities and the so-called early-stopping method is used to stop training if validation loss has not improved for ten epochs (Prechelt, 1998). When mini-batches are used (mini-batch size $m > 1$), the back-propagation algorithm combines the results from m SGD before updating the weights and biases of the neural network. The Nadam optimization technique (Dozat, 2016) is utilized to enhance the stochastic gradient descent algorithm. It automatically adapts the learning rate at each epoch during training based on the previously evaluated gradient loss. For this binary classification problem, the trained neural networks deliver two outputs: a score for its resemblance to a highest quality ground motion records, and a score for its resemblance to a lowest quality ground motion records. The output activation function is the sigmoid function and the loss is characterized by the binary cross-entropy (Friedman *et al.*, 2008, Eq. 2.36). The result of each combination is validated using a 5-fold cross-validation scheme as proposed by Friedman *et al.* (2008, pp. 241–249). This framework has been implemented in Keras (Chollet *et al.*, 2015) with a TensorFlow back-end (Abadi *et al.*, 2016).

5.4 Training results and model assessment

The performance of the proposed model is critical for ground motion studies, such as validation of physics-based ground motion models. Hence, in addition to the performance of the neural network, the distribution of the selected ground motion records both from an intensity measure and a geospatial viewpoint are also important. This section briefly summarizes the results of the 5-fold cross-validation, provides the training history of the retained models, discusses the predictive performance on the test datasets, analyzes the potential introduction of biases from an intensity measure and a geospatial point of view for both neural network configurations.

5.4.1 Cross-validation results and training history

Table 5.5 presents the selected parameter combination as well as the mean and standard deviation of the 5-fold cross-validation error for the two models trained on the different subsets of data presented in Table 5.3.

Final models are then trained against a newly drawn subset representing 80% of the training sets, validated against the remaining 20% to avoid overfitting, and their architectures are based on the aforementioned parameters. According to the observed validation errors, both models are expected to exhibit similar predictive performances. In Section 5.10.5, Figure 5.16 presents the training of both final models.

Table 5.5: Selected neural network parameter values (see Table 5.4 for definitions) and their respective 5-fold validation mean and standard deviation loss

Training set	Parameter combination	Mean loss	Standard deviation loss
A: Canterbury	$n_1 = 15$ $n_2 = 20$ $m = 16$	0.0859	0.0108
B: Canterbury & Wellington	$n_1 = 15$ $n_2 = 15$ $m = 8$	0.0725	0.0081

5.4.2 Model performance assessment

The predictive performance of the neural networks is studied against their respective test dataset. As the objective is to retain a relatively high number of high quality ground motion records, while discarding as many low quality ground motion records as possible, several acceptance threshold values are tested on the high quality ground motion record score: 0.5, 0.6, 0.7, 0.8, 0.9, and 0.95. The acceptance threshold value is used to determine whether an analyzed record is of low or high quality. For example, if the acceptance threshold is fixed to 0.7 and a record has a score of 0.82, it will be flagged as a high quality record and will therefore be retained. Conversely, if the acceptance threshold is now fixed to 0.9, the same record will be flagged as a low quality record and will be discarded. Traditionally, performance of binary predictors are given in terms of accuracy and represented by receiver operation characteristics (ROC) curves (Fawcett, 2006) and confusion matrices. However, in the present case, not only is the classifier's accuracy of interest but also its relative performance to each class (i.e. lowest, low, average, high and highest quality). Therefore, the performance results are presented as bar plots in Figure 5.6 in terms of absolute number and portion of selected ground motion records for each class. Note that confusion matrices and ROC curves are available in Figures 5.17 and 5.18, respectively. Results presented in Figure 5.6 show that, as expected, both models perform very similarly for acceptance thresholds up to 0.8. Above this particular value, the model trained exclusively on the Canterbury data tends to discard more high quality ground motion records than the model trained on the Canterbury and Wellington data. However, the Canterbury-only trained model also seems to marginally reduce the proportion of average to lowest quality ground motion records compared to the Canterbury-Wellington model. Note that the reduction of this value can be observed for both models with an increasing acceptance threshold.

Tables 5.1 and 5.1 in Section 5.10.6 summarize results for manually removed records and records from two large earthquake magnitudes, respectively. In both cases, the proposed model tends to accurately predict the quality of these recorded ground motions. In addition, Section 5.10.7 provides implementation strategies to apply the proposed model in a near-real-time fashion, giving workarounds to alleviate potential signal clipping-related problems and the possible absence of a pre-event noise window.

5.4.3 Intensity measure comparison between manually and automatically selected ground motion records

Figure 5.7 shows the distribution of the discarded high quality records for the peak ground acceleration (PGA), the peak ground velocity (PGV), the spectral acceleration at 3.0s (SA(3.0s)), the 5%-95% significant duration (Ds_{595}), and the Aria's intensity (AI). For conciseness, only results using an acceptance threshold of 0.5 are shown here, but the same analysis is carried out for all other acceptance threshold values and presented in Figures 5.3 to 5.7. It can be observed that, with the exception of

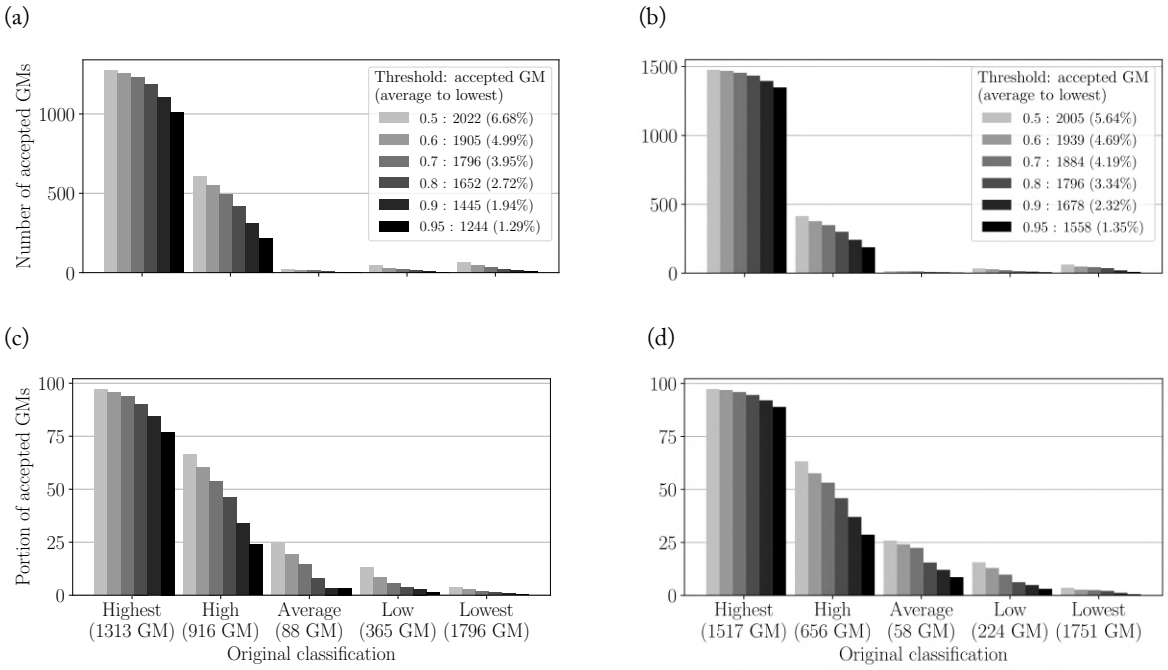

Figure 5.6: Effect on the number and proportion of selected ground motion records given their quality by applying different acceptance thresholds on the high quality predicting score for the Canterbury-trained and Canterbury-Wellington-trained neural networks in (a) and (c), and (b) and (d), respectively. The number of ground motions in each category from both test datasets is given in brackets under the X-axis of (c) and (d) for the Canterbury-trained and Canterbury-Wellington-trained models, respectively. For each tested threshold, the total number of selected ground motions and the proportion of average to lowest quality ground motion records (between brackets) is given in the legends of (a) and (b) for the Canterbury-trained and Canterbury-Wellington-trained models, respectively.

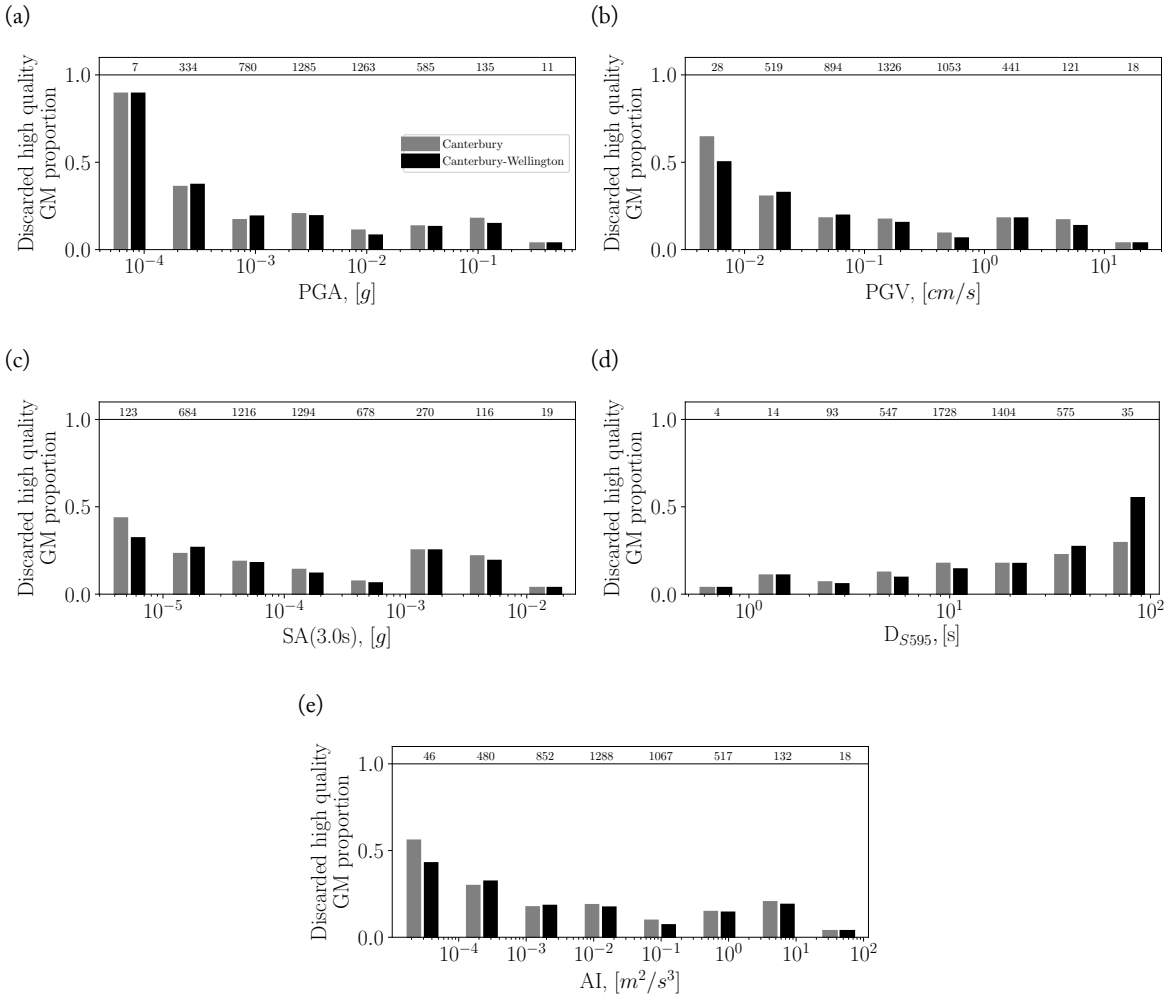

Figure 5.7: Proportion of discarded high quality ground motions from the Canterbury-trained (in grey) and Canterbury-Wellington-trained (in black) neural networks on the entire dataset for (a) PGA ; (b) PGV ; (c) SA(3.0s) ; (d) $DS_{5\text{-}95}$; and (e) Aria's intensity using the 0.5 acceptance threshold. Number of manually selected ground motion records are given at the top of each bar pair.

Ds_{595}, the smaller the intensity measure value, the more likely the record would be discarded. This can be explained by the different signal-to-noise ratio metrics used to predict the quality of the records: the smaller the signal, the lower the signal-to-noise ratio. As ground motion duration is highly correlated with the distance to the source, the distribution of Ds_{595} also implies that the farther away from the source the recording is occurring, the more likely it is to be rejected. However, there is no statistically significant case where an entire subset is removed by the algorithm, meaning that the same range of intensities will remain present, regardless of the selection method (manual or automated). To statistically show that the distributions from manual and automated selection are not significantly different, KS test are performed and shown in Figure 5.8 of Section 5.10.8. Results indicate that for an acceptance threshold below 0.7, intensity measure distributions of the manually and automatically selected ground motion records are similar. This similarity tends to diminish with higher acceptance thresholds.

5.4.4 Geospatial assessment of automatic ground motion record selection

By investigating the percentage of false predictions occurring at each recording station, it is possible to determine if there is any spatial bias being introduced by automatic screening of ground motions. In other words, are a significant percentage of ground motions being wrongly discarded or included at a site as a result of false predictions. This exercise is carried out using the Canterbury and Wellington neural network with an acceptance threshold of 0.5 and is focussed on the Canterbury and Wellington areas.

Figures 5.8(a) and (b) present maps which detail the false negative prediction (manually classified as high quality, but predicted to be low quality) percentage at recording stations in the Canterbury and Wellington areas, respectively. Triangles represent the recording stations and are sized based on how many recordings are observed at that station, and coloured based on what percentage of these recorded ground motions are false negatives. This means that lighter shaded triangles imply good model performance while darker shaded triangles imply poor model performance. However, if the number of records are small, then the result is less substantial (i.e. when there is only one record at a station, 100% false prediction does not provide a strong statement of poor model performance). Therefore the only real significant issue is where there is a darker shaded large triangle. There are no stations which match these criteria but a few which are darker shaded and smaller (e.g. SMTC and ROLC in Canterbury, and PIPS and INSS in Wellington). Upon inspection of the records at these stations, it was found that most records were manually scored 0.25–0.75, and were therefore already fringe cases. Additionally, the list of ground motion quality metrics considered don't completely represent the quality of the ground motion which may contribute to the number of false predictions too. In terms of applications, discarding high quality ground motions is generally less detrimental than including low quality ground motions for strong motion studies.

Figures 5.9(a) and (b) present maps which detail the false positive prediction (manually classified as low quality but predicted to be high quality) percentage at recording stations in Canterbury and Wellington, respectively. In both Canterbury and Wellington, there appears to be less false positive predictions than false negative predictions. None of the stations have both large quantity of records and high percentage of false positive predictions. Compared to the false negative predictions, there appears to be less false predictions, which is advantageous as including low quality ground motions in strong motion studies can lead to incorrect inferences. Overall, there does not appear to be any significant geospatial bias being introduced with the Canterbury and Wellington screening model with a 0.5 acceptance threshold.

5.5 Application to physics-based ground motion model validation

To test the developed neural networks, they are used in an example of physics-based ground motion simulation validation. Ground motion simulation validation involves the comparison between simu-

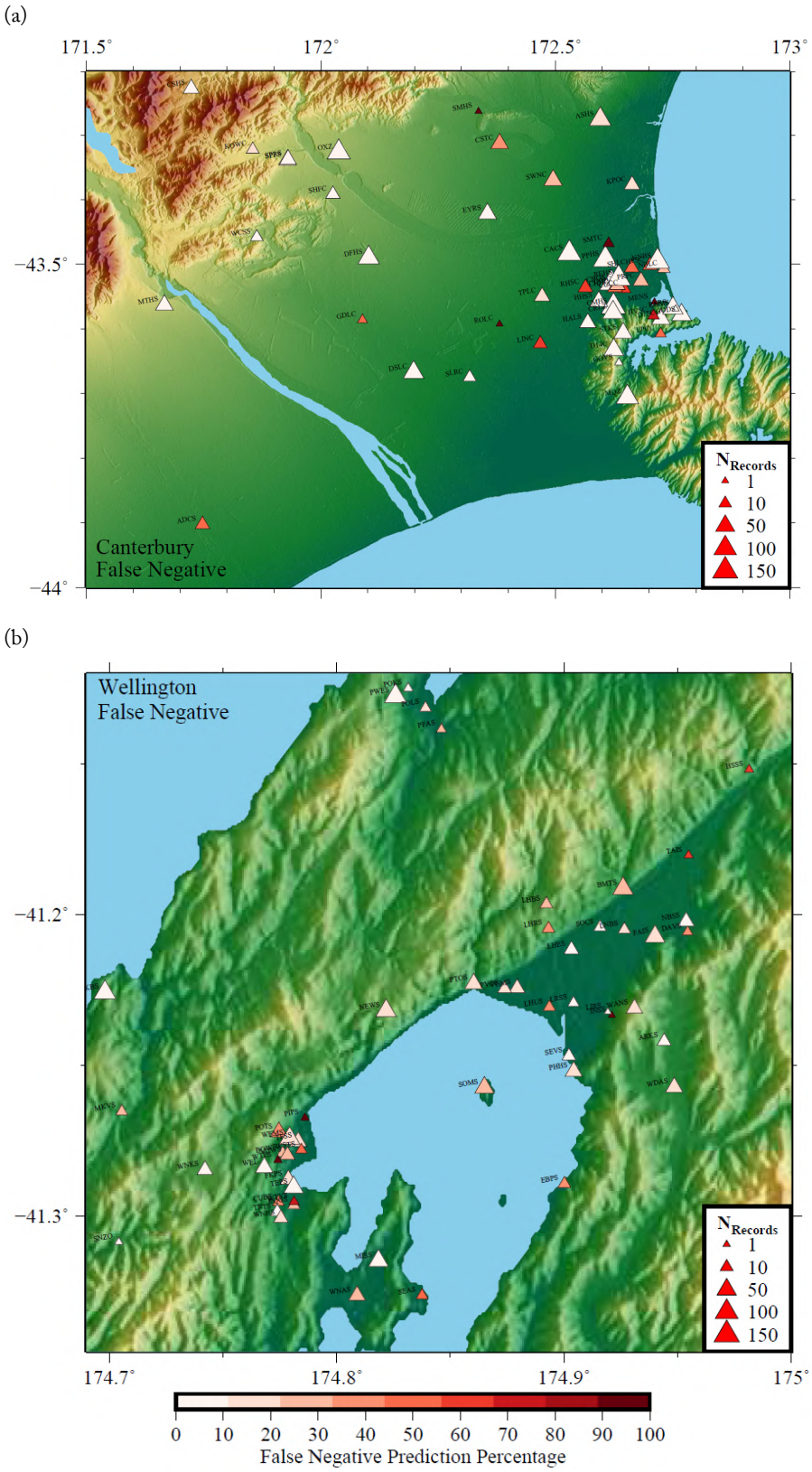

Figure 5.8: False negative prediction (manual high quality, predicted low quality) percentage of ground motion recording stations in (a) Canterbury ; and (b) Wellington (locations shown in Figure 5.1).

lated and observed ground motions, and hence quantification of the predictive capability of the simulation methodology. For this example, the adopted broadband simulation methodology is the Graves & Pitarka (2010, 2015) hybrid approach. Rather than carry out a comprehensive validation (which is beyond the scope of this paper), an assessment of the model prediction bias and total standard deviation, and their sensitivity to the different neural networks and acceptance thresholds, is the focus of the discussion below.

A previous study by Lee *et al.* (2019) carried out ground motion simulation validation in the Canterbury region using the subset of Canterbury ground motions in this study (148 earthquake sources with 3989 ground motion records across 43 strong motion stations). The analysis compared a suite of ground motion intensity measures from simulated and observed ground motions and partitioned the residuals, using mixed-effects regression, into various components of ground motion variability to infer systematic biases inherent in the simulations. In terms of model prediction bias, the ground motion simulations were found to overpredict peak acceleration metrics (e.g. PGA and SA) but underpredict significant durations (e.g. D_{s575} and D_{s595}). This example follows the framework used by Lee *et al.* (2019) to identify the model bias and associated total standard deviation.

For this application, the 327 earthquake sources used in developing the Canterbury and Wellington neural network model are simulated, with the 8467 prospective ground motions across 195 stations. As ground motion simulations have finite spatial domains, chosen to balance scope and computational demands, not all observed ground motions will have corresponding simulated ground motions produced in the simulations. It is important to note that while Lee *et al.* (2019) sought to validate the suitability of ground motion simulations in Canterbury for use in seismic hazard analysis and engineering application, the purpose of this example is to simply test the sensitivity of the validation metrics to the various neural networks and acceptance thresholds. Therefore the relative change in the results are of interest, as opposed to the absolute values of the model prediction biases and total standard deviations, which depend on a multitude of other factors.

The Canterbury-only (Cant) and Canterbury and Wellington (CantWell) neural network models are considered with various acceptance thresholds, Y = [0.5, 0.6, 0.7, 0.8, 0.9, 0.95]. A control case with no quality screening is also included along with a case which utilises the manual screening scores. Figure 5.9 presents the model bias and total standard deviation for the intensity measures considered, as well as the number of high quality ground motions included in the analysis, for a few selected scenarios. The scenarios shown capture the extreme cases of screening with acceptance thresholds of Y = 0.5 and Y = 0.95 for each model. Table 5.2 provides additional details regarding numerical values of bias and standard deviation for all cases considered. The bias values for duration are not shown in the plot, as they are too big, but are included in Figure 5.2. For both Canterbury and Canterbury-Wellington models, an increase in the acceptance threshold expectedly reduces the number of ground motions included in the analysis as more ground motions fail to meet the criteria. Comparing the two neural networks, the Canterbury and Wellington model includes marginally more ground motions than the Canterbury-only model for a given acceptance threshold.

Comparing bias and standard deviation values for the various screening scenarios, there appears to be only small differences between neural network models and acceptance thresholds. The largest difference in bias between screened scenarios for all intensity measures is on the order of 0.1 natural log units which corresponds to roughly 10% difference. Comparing between the different scenarios, the acceptance threshold appears to be more influential than the choice between the two neural network models. When compared against the control case with no quality screening, the short period SA are similar but the long period SA (e.g. T$\geq$3.0s) bias becomes significantly more positive, suggesting that the neural networks remove these observed ground motions which have disproportionately large low frequency acceleration amplitudes. Standard deviations are also mostly similar between all cases with the exception of the no screening case at long period SA which has signficantly larger standard deviations, further reinforcing that the screening is removing low quality ground motions. Overall, using either neural network with any of the considered thresholds appears to improve the observed

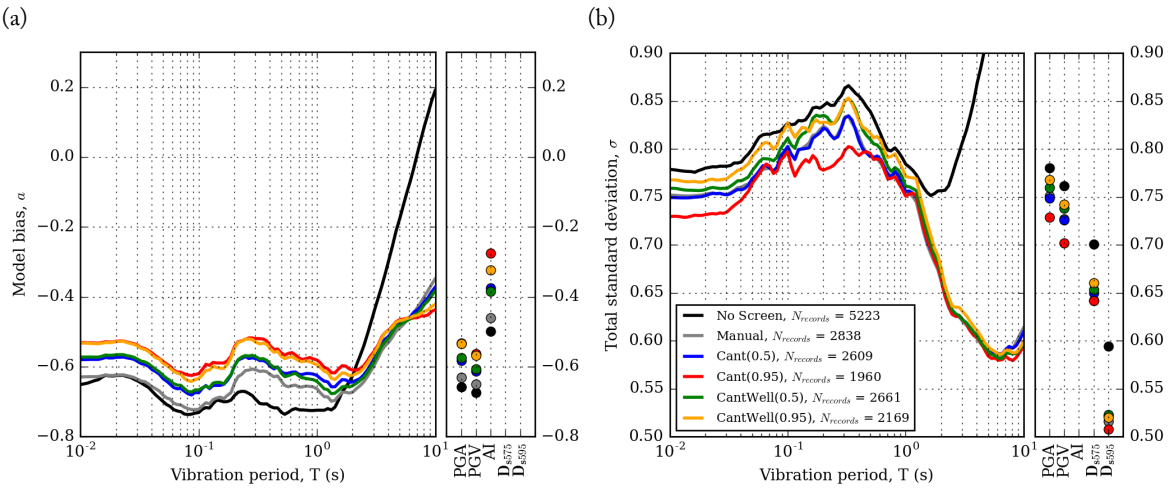

Figure 5.9: Model prediction (a) bias ; and (b) total standard deviation from ground motion simulation validation of 327 earthquakes for various intensity measures. Positive bias values indicate underprediction and negative bias values indicate overprediction.

ground motion dataset's quality relative to no screening. As the manual screening also has error, deviations from this case should not be strictly considered as being less correct. However, there is a tradeoff of quantity of ground motions with increasing acceptance threshold. To retain a satisfactory number of observed ground motions, an acceptance threshold of 0.5 or 0.6 seems most appropriate.

5.6 Conclusion

This paper presented a machine-learning-based tool that classifies ground motion recordings from small earthquakes based on quantifiable characteristics. The pre-processing of the available data has shown that high and low quality ground motion records do not share the same quality metric distributions. Using the natural acceptance threshold on the Wellington-Canterbury model yields greater than 95% of correct classification for both lowest and highest quality ground motion records.

Despite the demonstrated accuracy of the fitted classifier, some limitations remain. First, it has been shown that increasing the acceptance threshold (i.e. the minimum score to classify a ground motion records as high quality) increases the statistical differences between the manually and automatically selected distributions of intensity measures without removing all low quality ground motion records. Hence trying to eliminate almost all low quality records using the proposed method is detrimental as it drastically reduces the number of available ground motion records and changes their associated intensity measure distributions. Second, the model has so far been tested in two regions only, namely the Canterbury and Wellington, New Zealand regions. Higher rejection and acceptance rates for high and low quality ground motions, respectively, from other regions cannot be excluded. Third, further investigation is required to assess high rejection rates for high quality ground motion records at particular stations. In some cases, peculiar geological and topographical effects may not be adequately captured by the developed algorithm.

However, as shown in Sections 5.4 and 5.5, the global effect of automatic quality screening on the ground motion simulation validation process remains beneficial. First, by using an appropriate acceptance threshold, it has been shown in Section 5.4.3 that the intensity measure distributions from manually and automatically selected ground motion records are not statistically different. Second, the manual time required to scrutinize the observational data has now been reduced to a fraction of what would be required if a manual approach was undertaken.

Further applications may be imagined for the proposed algorithm. By comparing classified datasets

from other locations with the results yielded by the algorithm, particular geological and topographical effects can be easily detected as outliers. In other words, if most of the ground motion records considered of high quality are rejected by the algorithm, some particular site effects may distort the signal. Once evaluated and, if needed, recalibrated to other regions, this method can also be used to monitor instruments' average recording quality, helping to maintain a high quality sensor network.

In the future, more data from other regions should be utilized to further validate or re-train the developed classifier. Furthermore, alternatives to the proposed method may be explored to classify ground motion records. For example, a recurrent neural network, coupled with a performant phase picking algorithm such as Ross *et al.* (2018a), may be designed to assess the ground motion record quality as full time series as opposed to utilizing summary quality metrics.

5.7 Resources

The implementation of the entire framework has been made in Python 3.6, using Obspy (Krischer *et al.*, 2015) to process ground motions (particularly the 'ar_pick' tool for picking P-wave arrivals), Keras (Chollet *et al.*, 2015) to create the neural network architecture and TensorFlow (Abadi *et al.*, 2016) to train them. Observed ground motions were originally obtained from the GeoNet file transfer protocol (`ftp://ftp.geonet.org.nz/strong/processed/Raw`). The ground motion record dataset and the final classifiers (Canterbury and Canterbury-Wellington trained models) are available in the following github repository: `https://github.com/xavierbellagamba/GroundMotionRecordClassifier`.

5.8 Acknowledgement

This project was supported by QuakeCoRE, a New Zealand Tertiary Education Commission-funded Centre. This is QuakeCoRE publication number 0368.

5.9 References

Abadi, M, Barham, P, Chen, J, Chen, Z, Davis, A, Dean, J, Devin, M, Ghemawat, S, Irving, G, Isard, M, *et al.* 2016. Tensorflow: a system for large-scale machine learning. *Pages 265–283 of:* 12^{th} *USENIX Symposium on Operating Systems Design and Implementation*, vol. 16.

Abdiansah, A, & Wardoyo, R. 2015. Time complexity analysis of support vector machines (SVM) in LibSVM. *International Journal Computer and Application*, **128**(3), 28–34.

Ancheta, TD, Darragh, RB, Stewart, JP, Seyhan, E, Silva, WJ, Chiou, BS-J, Wooddell, KE, Graves, RW, Kottke, AR, Boore, DM, Kishida, T, & Donahue, J. 2013. *PEER NGA-West2 database*. Tech. rept. Pacific Earthquake Engineering Research Center, University of California, Berkeley, CA.

Ancheta, TD, Darragh, RB, Stewart, JP, Seyhan, E, Silva, WJ, Chiou, BS-J, Wooddell, KE, Graves, RW, Kottke, AR, Boore, DM, Kishida, T, & Donahue, J. 2014. NGA-West2 database. *Earthquake Spectra*, **30**(3), 989–1005.

Anthony, RE, Ringler, AT, Wilson, DC, & Wolin, E. 2018. Do Low-Cost Seismographs Perform Well Enough for Your Network? An Overview of Laboratory Tests and Field Observations of the OSOP Raspberry Shake 4D. *Seismological Research Letters*.

Baum, EB, & Haussler, D. 1989. What size net gives valid generalization? *Pages 81–90 of: Advances in neural information processing systems*.

Begg, JG, Johnston, MR, & McSaveney, E. 2000. *Geology of the Wellington area*.

Bengio, Y. 2012. Practical recommendations for gradient-based training of deep architectures. *Pages 437–478 of: Neural networks: Tricks of the trade*. Springer.

Benítez, JM, Castro, JL, & Requena, I. 1997. Are artificial neural networks black boxes? *IEEE Transactions on neural networks*, **8**(5), 1156–1164.

Benjamin, JR, & Cornell, CA. 1975. *Probability, statistics, and decision for civil engineers. 1970*.

Bergstra, J, & Bengio, Y. 2012. Random search for hyper-parameter optimization. *Journal of Machine Learning Research*, **13**(Feb), 281–305.

Boore, DM, & Bommer, JJ. 2005. Processing of strong-motion accelerograms: needs, options and consequences. *Soil Dynamics and Earthquake Engineering*, **25**(2), 93–115.

Cauzzi, C, & Clinton, J. 2013. A high-and low-noise model for high-quality strong-motion accelerometer stations. *Earthquake Spectra*, **29**(1), 85–102.

Cauzzi, C, Sleeman, R, Clinton, J, Ballesta, JD, Galanis, O, & Kästli, P. 2016. Introducing the European rapid raw strong-motion database. *Seismological Research Letters*, **87**(4), 977–986.

Chollet, F, *et al.* 2015. *Keras*. `https://keras.io`.

da Silva, IBV, & Adeodato, PJL. 2011. PCA and Gaussian noise in MLP neural network training improve generalization in problems with small and unbalanced data sets. *Pages 2664–2669 of: Proceedings of the* 11^{th} *International Joint Conference on Neural Networks*. IEEE, San Jose, CA, USA.

Dawood, HM, Rodriguez-Marek, A, Bayless, J, Goulet, C, & Thompson, E. 2016. A flatfile for the KiK-net database processed using an automated protocol. *Earthquake Spectra*, **32**(2), 1281–1302.

Douglas, J. 2003. What is a poor quality strong-motion record? *Bulletin of Earthquake Engineering*, **1**(1), 141–156.

Douglas, J, & Boore, DM. 2011. High-frequency filtering of strong-motion records. *Bulletin of Earthquake Engineering*, **9**(2), 395–409.

Dozat, T. 2016. Incorporating nesterov momentum into adam. *In:* 4^{th} *International Conference on Learning Representations*.

Fawcett, T. 2006. An introduction to ROC analysis. *Pattern recognition letters*, **27**(8), 861–874.

Forsyth, PJ, Barrell, DJA, & Jongens, R. 2008. *Geology of the Christchurch Area. Institute of Geological and Nuclear Sciences 1: 250,000 geological map 16, 1 sheet*.

Friedman, J, Hastie, T, & Tibshirani, R. 2008. *The elements of statistical learning*. Vol. 1. Springer series in statistics Springer, Berlin.

Geman, S, Bienenstock, E, & Doursat, R. 1992. Neural networks and the bias/variance dilemma. *Neural computation*, **4**(1), 1–58.

Goodfellow, I, Bengio, Y, & A, Courville. 2016. *Deep Learning*. Cambridge, MA, USA: MIT Press. `http://www.deeplearningbook.org`.

Graves, R, & Pitarka, A. 2015. Refinements to the Graves and Pitarka (2010) broadband ground-motion simulation method. *Seismological Research Letters*, **86**(1), 75–80.

Graves, RW, & Pitarka, A. 2010. Broadband ground-motion simulation using a hybrid approach. *Bulletin of the Seismological Society of America*, **100**(5A), 2095–2123.

Haykin, S. 1994. *Neural networks: a comprehensive foundation*. Upper Saddle River, NJ, USA: Prentice Hall PTR.

Heinert, M. 2008. Artificial neural networks–how to open the black boxes? *Application of Artificial Intelligence in Engineering Geodesy (AIEG 2008), S*, 42–62.

Helsel, DR, & Hirsch, RM. 2002. *Statistical methods in water resources*. Vol. 323. US Geological Survey, Reston, VA.

Hudson, DE. 1979. *Reading and interpreting strong motion accelerograms*. Vol. 1. Earthquake Engineering Research Institute.

Karpatne, A, Ebert-Uphoff, I, Ravela, S, Babaie, HA, & Kumar, V. 2018. Machine Learning for the Geosciences: Challenges and Opportunities. *IEEE Transactions on Knowledge and Data Engineering*.

Kessy, A, Lewin, A, & Strimmer, K. 2018. Optimal whitening and decorrelation. *The American Statistician*, 1–6.

Kishida, T, Di Giacinto, D, & Iaccarino, G. 2017. Comparison of Manual and Automated Ground Motion Processing for Small-to-Moderate-Magnitude Earthquakes in Japan. *Earthquake Spectra*, **33**(3), 875–894.

Kong, Q, Allen, RM, Schreier, L, & Kwon, Y-W. 2016. MyShake: A smartphone seismic network for earthquake early warning and beyond. *Science advances*, **2**(2), e1501055.

Kong, Q, Trugman, DT, Ross, ZE, Bianco, MJ, Meade, BJ, & Gerstoft, P. 2018. Machine Learning in Seismology: Turning Data into Insights. *Seismological Research Letters*.

Krischer, L, Megies, T, Barsch, R, Beyreuther, M, Lecocq, T, Caudron, C, & Wassermann, J. 2015. ObsPy: A bridge for seismology into the scientific Python ecosystem. *Computational Science & Discovery*, **8**(1), 014003.

Lawrence, S, Giles, CL, & Tsoi, AC. 1998. *What size neural network gives optimal generalization? Convergence properties of backpropagation*. Tech. rept. University of Maryland, College Park, MD 20742, USA.

Lee, R, Bradley, BA, Stafford, P, Graves, R, & Rodriguez-Marek, A. 2019. Hybrid broadband ground motion simulation validation of Canterbury, New Zealand. *TBD*, **TBD**(TBD), TBD.

Li, Zefeng, Meier, Men-Andrin, Hauksson, Egill, Zhan, Zhongwen, & Andrews, Jennifer. 2018. Machine Learning Seismic Wave Discrimination: Application to Earthquake Early Warning. *Geophysical Research Letters*.

Okada, H, & Suto, K. 2003. *The microtremor survey method*. Society of Exploration Geophysicists.

Patterson, N, Gledhill, K, & Chadwick, M. 2007. *New Zealand National Seismograph Network Report for the Federation of Digital Seismograph Networks Meeting, 2007*. Tech. rept. GNS Science, Wellington, New Zealand.

Perol, T, Gharbi, M, & Denolle, M. 2018. Convolutional neural network for earthquake detection and location. *Science Advances*, **4**(2), e1700578.

Prechelt, L. 1998. Early stopping-but when? *Pages 55–69 of: Neural Networks: Tricks of the trade*. Springer.

Racah, E, Beckham, C, Maharaj, T, Ebrahimi K, S, Prabhat, M, & Pal, C. 2017. ExtremeWeather: A large-scale climate dataset for semi-supervised detection, localization, and understanding of extreme weather events. *Pages 3402–3413 of:* Guyon, I., Luxburg, U. V., Bengio, S., Wallach, H., Fergus, R., Vishwanathan, S., & Garnett, R. (eds), *Advances in Neural Information Processing Systems 30*. Curran Associates, Inc.

Rennolet, SB, Moschetti, MP, Thompson, EM, & Yeck, WL. 2018. A flatfile of ground motion intensity measurements from induced earthquakes in Oklahoma and Kansas. *Earthquake Spectra*, **34**(1), 1–20.

Ross, ZE, Meier, M-A, Hauksson, E, & Heaton, TH. 2018a. Generalized Seismic Phase Detection with Deep Learning. *arXiv preprint arXiv:1805.01075*.

Ross, ZE, Yue, Y, Meier, MA, Hauksson, E, & Heaton, TH. 2018b. PhaseLink: A Deep Learning Approach to Seismic Phase Association. *arXiv preprint arXiv:1809.02880*.

Titos, M, Bueno, A, García, L, & Benítez, C. 2018. A Deep Neural Networks Approach to Automatic Recognition Systems for Volcano-Seismic Events. *IEEE Journal of Selected Topics in Applied Earth Observations and Remote Sensing*, **11**(5), 1533–1544.

Van Houte, C, Bannister, S, Holden, C, Bourguignon, S, & McVerry, G. 2016. The New Zealand Strong Motion Database. *Bulletin of the New Zealand Society for Earthquake Engineering*, **50**(1).

Yang, Wenzheng, & Ben-Zion, Yehuda. 2010. An algorithm for detecting clipped waveforms and suggested correction procedures. *Seismological Research Letters*, **81**(1), 53–62.

Zhang, Jinhai, Hao, Jinlai, Zhao, Xu, Wang, Shuqin, Zhao, Lianfeng, Wang, Weimin, & Yao, Zhenxing. 2016. Restoration of clipped seismic waveforms using projection onto convex sets method. *Scientific reports*, **6**, 39056.

5.10 Complementary material

5.10.1 Manual quality screening guidelines

This section provides comprehensive details on the manual quality screening guidelines used to develop the dataset to train and validate the neural networks, and a concise comparison against other ground motion quality procedures.

1. Comparison of the acceleration amplitudes of the pre-event noise with that of the earthquake ground motion signal, effectively measuring SNR. Lower noise amplitudes relative to signal amplitudes are favourable. Records with peak noise values greater than 10% of the PGA were generally discarded.

2. Inspection of the acceleration amplitudes at the end of the record to determine if the ground motion has adequately finished or terminated early in the coda, where the latter is unfavourable. Records were generally discarded if the average absolute acceleration near the end of the record was greater than roughly 8% of the PGA.

3. Comparison of record FAS with noise FAS, effectively measuring frequency-dependent SNR. This is considered across frequencies of engineering interest, 0.1Hz to 20Hz. Lower noise amplitudes relative to signal amplitudes are favourable. A target frequency-dependent SNR of 2.0 was utilized as ground motions from small earthquakes were being considered.

4. Inspection of the shape of the record FAS, with emphasis on the sloped/decaying low frequency branch, which should theoretically be linear in log space with a slope of 2. An acceptable range of values was not enforced, rather, consistency of Fourier amplitude characteristics along the slope was emphasised.

5. Inspection of the velocity time series obtained via integration of the filtered acceleration. Poor records will often have non-physical quantities, not appear to originate from the earthquake source, or have significant amplitudes before the P-wave arrival.

The adopted criteria have some similarities and differences to established ground motion quality screening methodologies and guidelines. Similar to this study, Boore & Bommer (2005) suggests that a target value for frequency-dependent SNR of 3.0 is often considered, that the low frequency slope of the FAS should be 2 (but does not give a suggested range of acceptable values), and that the integrated velocity and displacements from the corrected accelerations should not be unphysical (although this is subject to the judgement of the person manually classifying the ground motions). The screening component of the PEER record processing methodology focusses on whether the integrated displacement from the corrected acceleration is acceptable (i.e. physically feasible) with filter frequencies determined via visual inspection. This study did not place a large emphasis on the displacement, as low frequncy acceleration amplitudes are known to be modest for small magnitude earthquakes. Lastly, Dawood *et al.* (2016) placed a strong emphasis on residual displacements but also required that the slope of a best fit line fitted to the final 10% of the velocity and displacement time series be less than 0.001cm/s and 0.001cm/s^2, respectively. In agreement with Boore & Bommer (2005), Dawood *et al.* (2016) requires the smoothed low frequency FAS slope to be between 1–3 (as the theoretical value is 2) and for the minimum frequency-dependent SNR to be 3.0. These two criteria were also considered in this study but with less strict enforcement.

5.10.2 Ground motion quality metric calculation

This section provides a comprehensive description on how to calculate the ground motion quality metrics utilised in the neural networks developed in Section 5.2.3. 20 metrics were defined which characterise the amplitude, duration and frequency content of the ground motion records. Figure 5.10, which presents examples of a high and low quality ground motion, was included in the main article but is presented here again for completeness.

A significant part of the quality classification methodology developed depends on identifying and isolating the pre-event trace of the record as noise. In this study, this was considered to be the section of the record before the P-wave arrival. This study utilised the 'ar_pick' tool from the ObsPy python library (Krischer *et al.*, 2015) which determines the time of the P-wave arrival based on long term average to short term average ratios, STA/LTA.

The following, with reference to Figure 5.10, provides the explicit details on the calculation of each quality metric, and a brief explanation on the reasoning behind it's inclusion. The subsequent descriptions are only for a single component of ground motion. The final metric used with the neural network should be the geometric mean of two orthogonal horizontal components.

A: Peak noise to peak ground acceleration ratio, PN/PGA:

This metric is the ratio of the peak noise to peak ground acceleration (PGA) which is a time domain signal-to-noise ratio. Peak noise is taken as the maximum absolute acceleration amplitude of the noise (pre-event trace) and PGA is taken as the maximum absolute acceleration amplitude of the entire record. These are highlighted as PN and PGA in Figure 5.10(a) and (b).

$$\frac{\mathrm{PN}}{\mathrm{PGA}} = \frac{\max\left(|\mathrm{acc}(\mathrm{t} < \mathrm{t_{p-arrival}})|\right)}{\max|\mathrm{acc}(\mathrm{t})|} \tag{5.1}$$

B: Average tail ratio, TRave:

This metric is the mean of the absolute acceleration of the tail duration of the record divided by the PGA. The tail duration is the lesser of 5.0s or 10% of the record duration. This is a measure of the relative amplitude at the end of the record to help identify if the record has adequately finished or terminated early in the coda.

$$\mathrm{TR_{ave}} = \frac{\mathrm{mean}(|\mathrm{acc}(\mathrm{t} \geq \mathrm{t_{tail}})|)}{PGA} \tag{5.2}$$

where $t_{tail} = \min(5.0s, 0.1t_{max})$.

C: Maximum tail ratio, TRmax:

This metric is the maximum of the absolute acceleration of the tail duration of the record divided by the PGA. The tail duration is the lesser of 2.0s or 10% of the record duration. Note that the considered tail duration for this metric is different than that for the average tail ratio. This is because the maximum absolute accelerations for longer tail durations were found to be too large and not representative of whether the record had adequately finished or not. The maximum of the absolute absolute acceleration of the tail duration is highlighted in Figure 5.10(a) and (b) as PT.

$$\mathrm{TR_{max}} = \frac{\max(|\mathrm{acc}(\mathrm{t} \geq \mathrm{t_{tail}})|)}{PGA} \tag{5.3}$$

where $t_{tail} = \min(2.0s, 0.1t_{max})$.

D: Average tail noise ratio, TNRave:

This metric is the average tail ratio normalised by the mean of the absolute acceleration of the noise. This metric highlights the interaction between average acceleration amplitudes at the beginning and end of the records with the PGA.

$$\mathrm{TNR_{ave}} = \frac{\mathrm{TR_{ave}}}{\mathrm{mean}(|\mathrm{acc}(\mathrm{t} < \mathrm{t_{p-arrival}})|)} \tag{5.4}$$

E: Maximum tail noise ratio, TNRmax:

This metric is the maximum tail ratio normalised by the peak noise. This metric highlights the interaction between the peak accleration amplitudes at the beginning and end of the records with the PGA.

$$\mathrm{TNR_{max}} = \frac{\mathrm{TR_{max}}}{\mathrm{PN}} \tag{5.5}$$

F: Maximum head ratio, HRmax:

This metric is the ratio between the maximum absolute acceleration of first 1.0s of the record divided by the PGA. This identifies cases where the noise may be too large relative to the PGA or P-wave arrivals which occur before 1.0s.

$$\mathrm{HR_{max}} = \frac{\max(|\mathrm{acc}(\mathrm{t} \leq \mathrm{t_{head}})|)}{PGA} \tag{5.6}$$

where $t_{head} = 1.0s$.

G: 10%-20% bracketed duration ratio, $\mathrm{Db_{,10\%\text{-}20\%}}$:

Ratio of 10% of PGA bracketed duration to 20% of PGA bracketed duration. Note that the bracketed durations used in this metric are based on amplitudes that are a percentage of the PGA while the conventional definition uses an absolute acceleration amplitude threshold. Hence, for example, the 10% of PGA bracketed duration would be the difference between the first and last time at which the amplitude exceeds 10% of the PGA. This measures the relative rate of energy being recorded.

H: 5-75% significant duration, $\mathrm{Ds_{595}}$:

5-75% significant duration based on Arias intensity. This is the duration between which the 5% and 75% of Arias intensity occurs. This metrics helps to identify ground motions which are too long for a small magnitude rupture as a result of source-to-site distance being too large, or other reasons, from the perspective of body waves.

I: 5-95% significant duration, Ds_{595}:

5-95% significant duration based on Arias intensity. This is the duration between which the 5% and 95% of Arias intensity occurs. This metrics helps to identify ground motions which are too long for a small magnitude rupture as a result of source-to-site distance being too large, or other reasons, from the perspective of surface waves.

J: Low frequency pre-event FAS to maximum signal FAS ratio, $FASpe_{(LF)}/s$:

This metric is the ratio between the maximum Fourier amplitude of the pre-event trace at frequencies below 0.1Hz and the maximum Fourier amplitude of the whole record across all frequencies. This provides a relative sense of how significant the low frequency noise amplitudes are compared to the strongest signal amplitudes. The components are identified in Figures 5.10(e) and (f) as $\mathrm{FAS}^{\mathrm{low}}_{\mathrm{pe,max}}$ and $\mathrm{FAS}_{\mathrm{s,max}}$.

$$\mathrm{FAS}_{\mathrm{pe(LF)/s}} = \frac{\max(\mathrm{FAS}_{\mathrm{pe}}(f \leq 0.1Hz))}{\max(\mathrm{FAS}_{\mathrm{s}}(f))} = \frac{\mathrm{FAS}^{\mathrm{low}}_{\mathrm{pe,max}}}{\mathrm{FAS}_{\mathrm{s,max}}} \tag{5.7}$$

K: Low frequency signal FAS to maximum signal FAS ratio, $FASs_{(LF)}/s$:

This metric is the ratio between the maximum Fourier amplitude of the pre-event trace at frequencies below 0.1Hz and the maximum Fourier amplitude of the whole record across all frequencies. This provides a relative sense of how significant the low frequency records amplitudes are compared to its strongest amplitudes. The components are identified in Figures 5.10(e) and (f) as $\mathrm{FAS}^{\mathrm{low}}_{\mathrm{s,max}}$ and $\mathrm{FAS}_{\mathrm{s,max}}$.

$$\mathrm{FAS}_{\mathrm{s(LF)/s}} = \frac{\max(\mathrm{FAS}_{\mathrm{s}}(f \leq 0.1Hz))}{\max(\mathrm{FAS}_{\mathrm{s}}(f))} = \frac{\mathrm{FAS}^{\mathrm{low}}_{\mathrm{s,max}}}{\mathrm{FAS}_{\mathrm{s,max}}} \tag{5.8}$$

L: Fourier amplitude ratio, FASratio:

Ratio between average FAS between 0.1-0.5Hz and 0.5-1.0Hz. The average of the FAS between 0.1–0.5Hz is calculated by taking the integral of the FAS between the 0.1–0.5Hz and then dividing by the difference in the frequencies. The average of the FAS between 0.5–1.0Hz is calculated by taking the integral of the FAS between the 0.5–1.0Hz and then dividing by the difference in the frequencies. This metric provides a relative sense of how the Fourier amplitudes change along the sloping low frequency branch. The two components correspond to the segments in Figure 5.10(e) and (f) that are labelled FAS_1 and FAS_2.

$$\mathrm{FAS}_{ratio} = \frac{\frac{\int_{f_{min}}^{f_1} \mathrm{FAS}(f)\ df}{f_1 - f_{min}}}{\frac{\int_{f_1}^{f_2} \mathrm{FAS}(f)\ df}{f_2 - f_1}} = \frac{\frac{\int_{0.1}^{0.5} \mathrm{FAS}(f)\ df}{0.5 - 0.1}}{\frac{\int_{0.5}^{1.0} \mathrm{FAS}(f)\ df}{1.0 - 0.5}} \tag{5.9}$$

M: Minimum SNR, SNRmin:

Minimum signal-to-noise ratio between frequencies $f_{min} = 0.1$Hz and $f_{max} = 20$Hz. This metric corresponds to SNRmin identified in Figures 5.10(g) and (h).

$$\mathrm{SNR}_{min} = \min(\mathrm{SNR}(f)) \qquad f_{min} \leq f \leq f_{max} \tag{5.10}$$

N: Maximum SNR, SNRmax:

Maximum signal-to-noise ratio between frequencies $f_{min} = 0.1$Hz and $f_{max} = 20$Hz. This metric corresponds to SNRmax identified in Figures 5.10(g) and (h).

$$\mathrm{SNR}_{max} = \max(\mathrm{SNR}(f)) \qquad f_{min} \leq f \leq f_{max} \tag{5.11}$$

O: Average SNR, SNRave:

Average signal-to-noise ratio between frequencies $f_{min} = 0.1$Hz and $f_{max} = 20$Hz, calculated by taking the integration of the SNR between 0.1-20Hz and then dividing by the frequencies spanned.

$$\mathrm{SNR}_{ave} = \frac{\int_{f_{min}}^{f_{max}} \mathrm{SNR}(f)\ df}{f_{max} - f_{min}} = \frac{\int_{0.1}^{20.0} \mathrm{SNR}(f)\ df}{20.0 - 0.1} \tag{5.12}$$

P: Average SNR between 0.1-0.5Hz, SNR_1:

Average signal-to-noise ratio between frequencies 0.1–0.5Hz calculated by taking the integration of the SNR between 0.1–0.5Hz and then dividing by the frequencies spanned. This metric corresponds to the segment of Figures 5.10(g) and (h) labelled SNR_1.

$$\mathrm{SNR}_1 = \frac{\int_{f_{min}}^{f_1} \mathrm{SNR}(f)\ df}{f_1 - f_{min}} = \frac{\int_{0.1}^{0.5} \mathrm{SNR}(f)\ df}{0.5 - 0.1} \tag{5.13}$$

Q: Average SNR between 0.5-1.0Hz, SNR_2:

Average signal-to-noise ratio between frequencies 0.5–1.0Hz calculated by taking the integration of the SNR between 0.1–20Hz and then dividing by the frequencies spanned. This metric corresponds to the segment of Figures 5.10(g) and (h) labelled SNR_2.

$$\mathrm{SNR}_2 = \frac{\int_{f_1}^{f_2} \mathrm{SNR}(f)\ df}{f_2 - f_1} = \frac{\int_{0.5}^{1.0} \mathrm{SNR}(f)\ df}{1.0 - 0.5} \tag{5.14}$$

R: Average SNR between 1.0-2.0Hz, SNR_3:

Average signal-to-noise ratio between frequencies 1.0–2.0Hz calculated by taking the integration of the SNR between 1.0–2.0Hz and then dividing by the frequencies spanned. This metric corresponds to the segment of Figures 5.10(g) and (h) labelled SNR_3.

$$\mathrm{SNR}_3 = \frac{\int_{f_2}^{f_3} \mathrm{SNR}(f)\ df}{f_3 - f_2} = \frac{\int_{1.0}^{2.0} \mathrm{SNR}(f)\ df}{2.0 - 1.0} \tag{5.15}$$

S: Average SNR between 2.0-5.0Hz, SNR_4:

Average signal-to-noise ratio between frequencies 2.0–5.0Hz calculated by taking the integration of the SNR between 2.0–5.0Hz and then dividing by the frequencies spanned. This metric corresponds to the segment of Figures 5.10(g) and (h) labelled SNR_4.

$$\mathrm{SNR}_4 = \frac{\int_{f_3}^{f_4} \mathrm{SNR}(f)\ df}{f_4 - f_3} = \frac{\int_{2.0}^{5.0} \mathrm{SNR}(f)\ df}{5.0 - 2.0} \tag{5.16}$$

T: Average SNR between 5.0-10.0Hz, SNR_5:

Average signal-to-noise ratio between frequencies 5.0–10.0Hz calculated by taking the integration of the SNR between 5.0–10.0Hz and then dividing by the frequencies spanned. This metric corresponds to the segment of Figures 5.10(g) and (h) labelled SNR_5.

$$\mathrm{SNR}_5 = \frac{\int_{f_4}^{f_5} \mathrm{SNR}(f)\ df}{f_5 - f_4} = \frac{\int_{5.0}^{10.0} \mathrm{SNR}(f)\ df}{10.0 - 5.0} \tag{5.17}$$

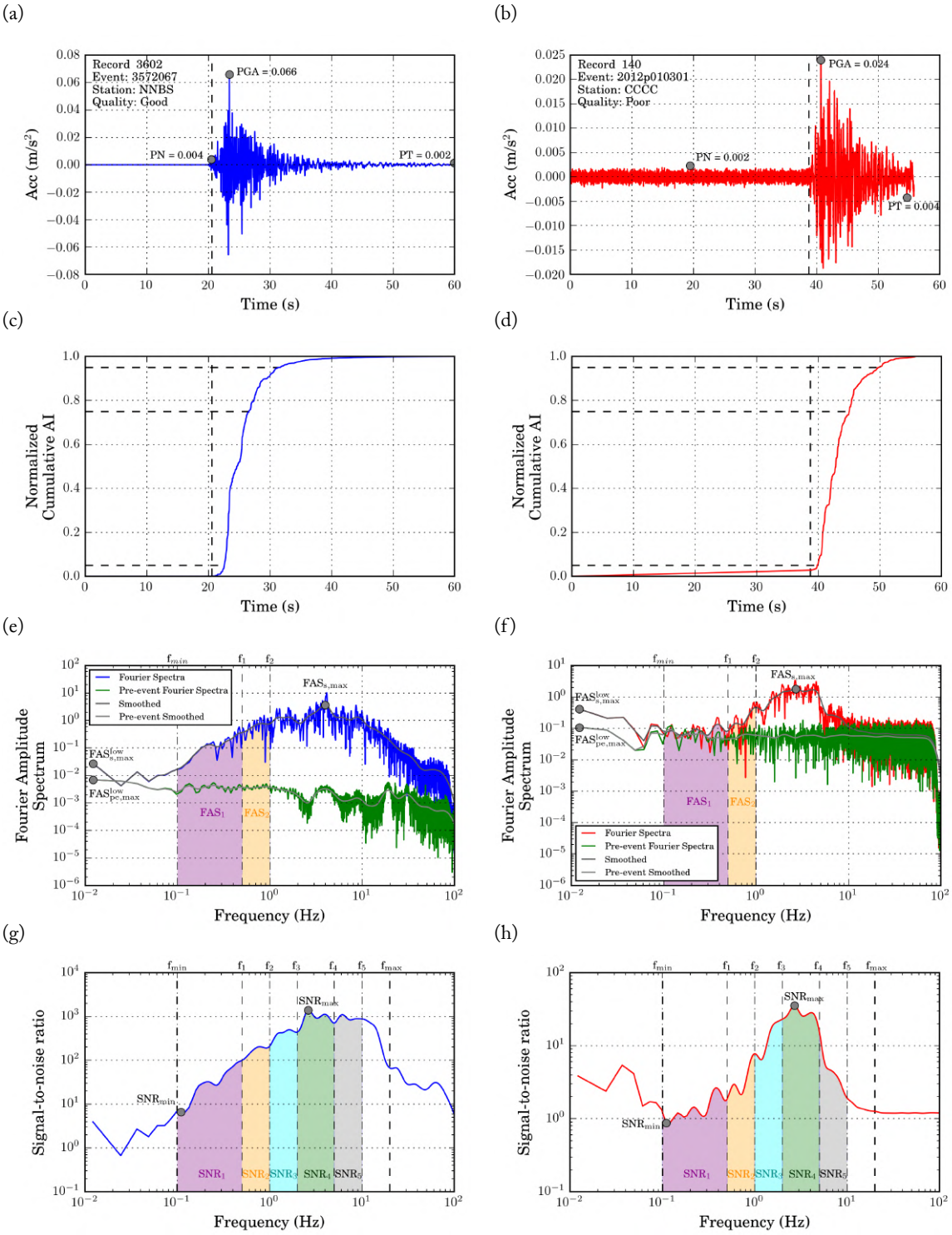

Figure 5.10: Comparison between a high (on the left) and low (on the right) quality ground motion record. (a) and (b): raw ground motion time series; (c) and (d): Husid plots; (e) and (f): FAS; and (g) and (h): SNR.

5.10.3 Quality metric distribution

This section presents the original distribution, in the form of cumulative distribution functions (CDF) in Figure 5.11 and the correlation matrix in Figure 5.12, of the utilized quality metrics described in Table 5.2. For each quality metric, five CDFs corresponding to the five potential qualities (lowest,

low, average, high, and highest described in 5.2.2) are given. The correlation matrix only shows the relationship between ground motion records of highest quality as explained in Section 5.3.3.

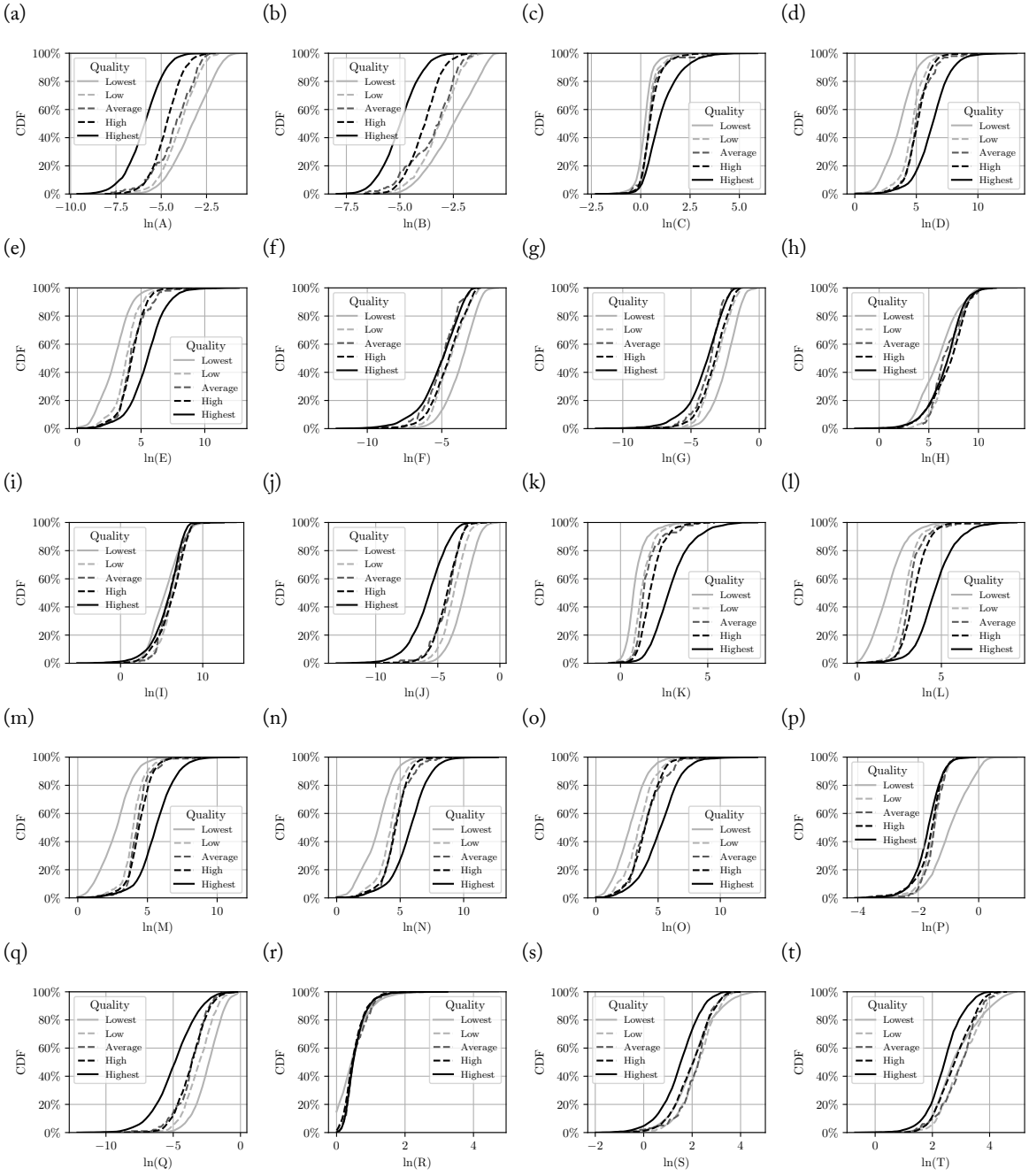

Figure 5.11: Cumulative density function of the quality metric distribution given the manually assigned quality. A: Maximum of low frequency (below 0.1Hz) pre-event Fourier amplitude divided by maximum record Fourier Amplitude; B: Maximum of low frequency (below 0.1Hz) signal Fourier amplitude divided by maximum record Fourier Amplitude; C: Minimum SNR; D: Maximum SNR; E: Average SNR; F: Average tail ratio; G: Maximum tail ratio; H: Average tail noise ratio; I: Maximum tail noise ratio; J: Average head ratio; K: Average SNR between 0.1-0.5Hz; L: Average SNR between 0.5-1.0Hz; M: Average SNR between 1.0-2.0Hz; N: Average SNR between 2.0-5.0Hz; O: Average SNR between 5.0-10.0Hz; P: Fourier amplitude ratio; Q: Peak noise to PGA ratio; R: Bracketed duration ratio; S: Ds575; and T: Ds595.

It can be observed in Figure 5.12 that the correlation coefficients between some pairs of the con-

sidered variables are significant. Interestingly, SNR metrics (M-T) seems to be strongly correlated with each other but not with other metrics. With the exceptions of average tail noise ratio (D), maximum tail noise ratio (E) and 10%–20% bracketed duration ratio (G), the rest of the metrics seems to be relatively well correlated.

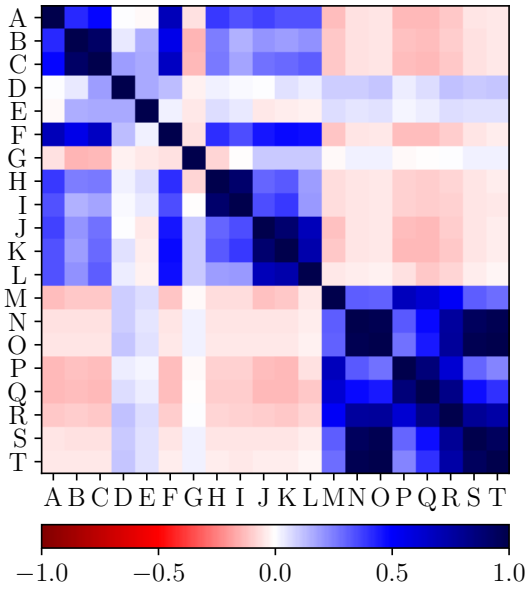

Figure 5.12: Correlation matrix between the selected ground motion record metrics. Letters indicate the ground motion quality metrics as presented in Table 5.2

5.10.4 Pre-processing results

This section presents the pre-processing results for both neural networks developed. The results are presented as Q-Q plots of each transformed variable. Q-Q plots are a statistical tool that enables visual inspection of an empirical distribution against a reference distribution. In the present case, the reference distribution is the Gaussian distribution $\mathcal{N}(0.0, 1.0)$ and the empirical distributions are derived from the ZCA-transformed highest quality ground motion records as presented in Section 5.3.3. Figure 5.13 shows the pre-processing results of the Canterbury training dataset, whereas Figure 5.14 shows the equivalent of the Canterbury-Wellington training dataset as defined in Table 5.3.

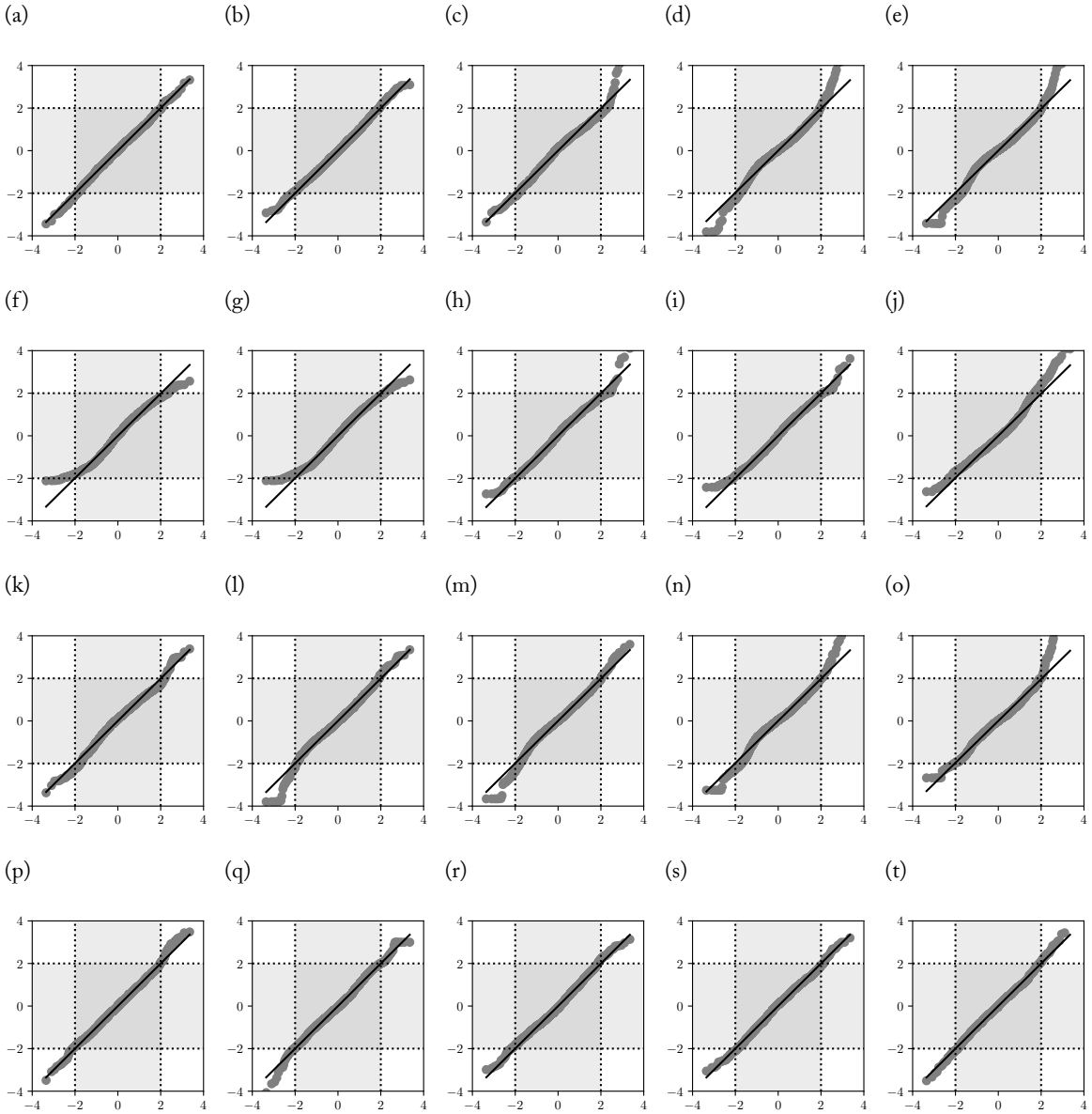

Figure 5.13: QQ-plots of the highest quality ground motion records' transformed variables A' to T' against the Gaussian distribution $\mathcal{N}(0,1)$ of the Canterbury model

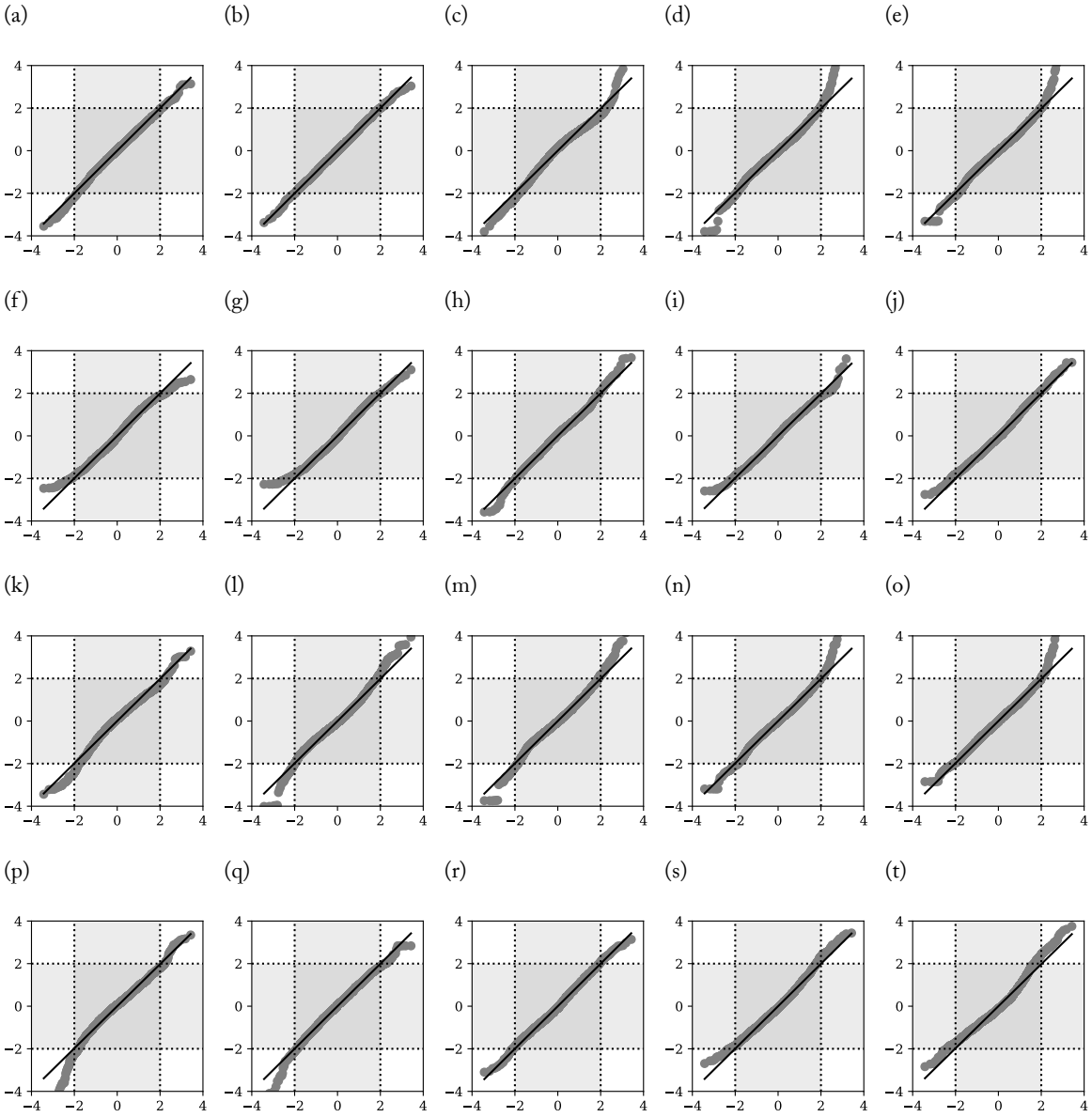

Figure 5.14: QQ-plots of the highest quality ground motion records' transformed variables A' to T' against the Gaussian distribution $\mathcal{N}(0,1)$ of the Canterbury-Wellington model

To test if the distributions of the considered transformed variables are different, the distributions of highest quality ground motion records are compared to bootstrapped samples from the distributions of lowest quality ground motion records with a two-sided Kolmogorov-Smirnov test (KS test). KS test is a non-parametric method that tests the alternative hypothesis against the null hypothesis by comparing the p-values to the level of significance α (Benjamin & Cornell, 1975, pp. 466–471). In this study, α is set to 0.05. P-values smaller than the selected level of significance indicate that the null hypothesis may be rejected (i.e. that the highest quality ground motion records may not share the same distribution as the lowest quality ground motion records). As multiple comparisons are carried out for each variable, the higher the number of samples being assigned a low p-value, the more likely is the alternative hypothesis for the analyzed variables. Note that this exercise is only executed for the Canterbury-Wellington pre-processing.

P-value histograms shown in Figure 5.15(g) indicate that the distributions of lowest and highest quality ground motion records show appreciable differences as the majority of the KS tests yield values

significantly below the selected α. Notable exceptions are D', N', and S'.

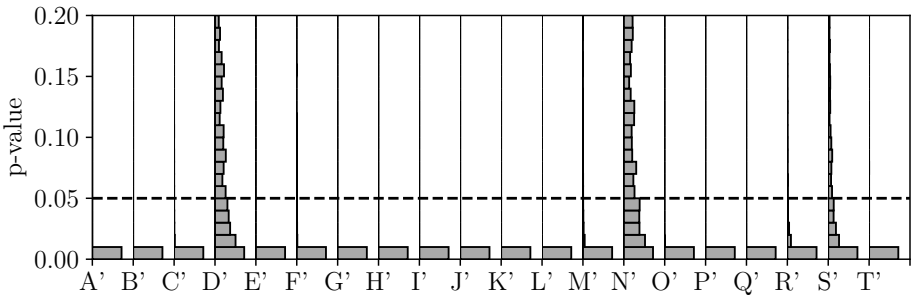

Figure 5.15: P-value histograms comparing the lowest and highest quality ground motion records distributions of the transformed variables A' to T'. The dashed lines indicate the selected level of significance α.

5.10.5 Model training and performance

This section presents the model training and performance in terms of training curves and confusion matrices and receiver operation characteristics (ROC) curves, respectively. Figure 5.16 shwos the training history of both the Canterbury and Wellington-Canterbury trained models. Based on these curves, both models are expected to yield similar results.

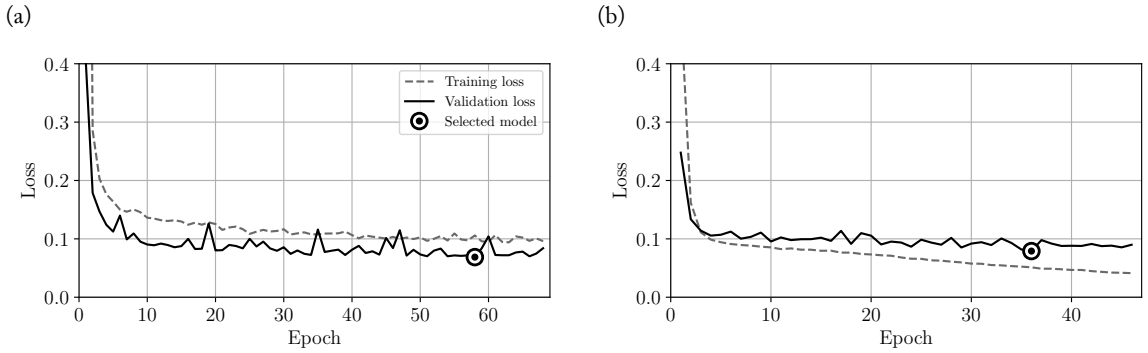

Figure 5.16: Loss on the training and validation datasets during the neural network training using (a) the Canterbury dataset; and (b) the Canterbury and Wellington datasets as presented in Table 5.5. Circles indicate the epoch and validation loss at which the models have been saved.

Confusion matrices are a graphical method that summarizes the performance of statistical classifiers. The matrix is square and each of its row and columns correspond to the list of classes in the same order. The rows correspond to the original labels (in this case the manually assigned quality of ground motion records), and the columns to the predicted labels (the automated classification results).

The ROC curves are another way to represent the performance of binary classifiers. As described by Fawcett (2006), it is based on the percentages of false and true positive and negative rates of the model. A weak classifier ROC curve would remain close to identity function (1:1), whereas a strong classifier would yield a vertical line at *False positive rate = 0*. To quantify ROC results, the area under the ROC curve (AUC) is evaluated. A perfect model would have a AUC of 1.0. For both final models presented in Section 5.4.1, the six acceptance thresholds given in Section 5.4.2 are analyzed using these two methods in Figures 5.17 and 5.18, respectively. Note that two labels considered here are: (1) high quality (enclosing both high and highest quality ground motion records), and (2) low quality (enclosing average, low and lowest quality ground motion records).

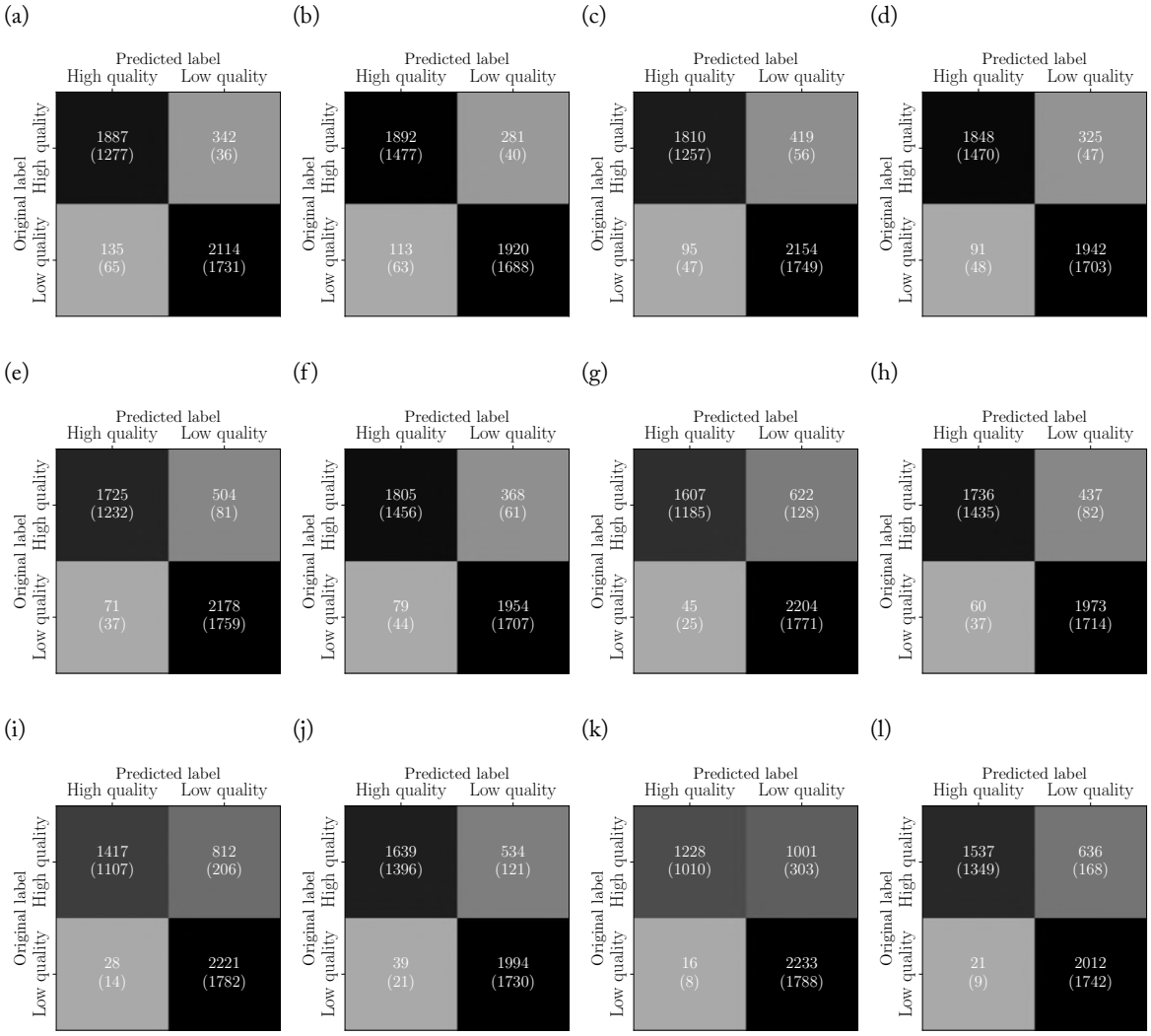

Figure 5.17: Threshold-dependent confusion matrices of the Canterbury-trained (a, c, e, g, i, k), and the Canterbury-Wellington-trained (b, d, f, h, j, l) models. Threshold of 0.5: (a)-(b) ; 0.6: (c)-(d) ; 0.7: (e)-(f) ; 0.8: (g)-(h) ; 0.9: (i)-(j) ; and 0.95: (k)-(l). Color intensities indicate the portion of correct classification for each category. Numbers in each cell give the quantity of high (score $>$ 0.5) or low (score $\leq$ 0.5) quality ground motion records and numbers in brackets give the quantity of highest and lowest quality ground motion records within the confusion matrix cells, respectively.

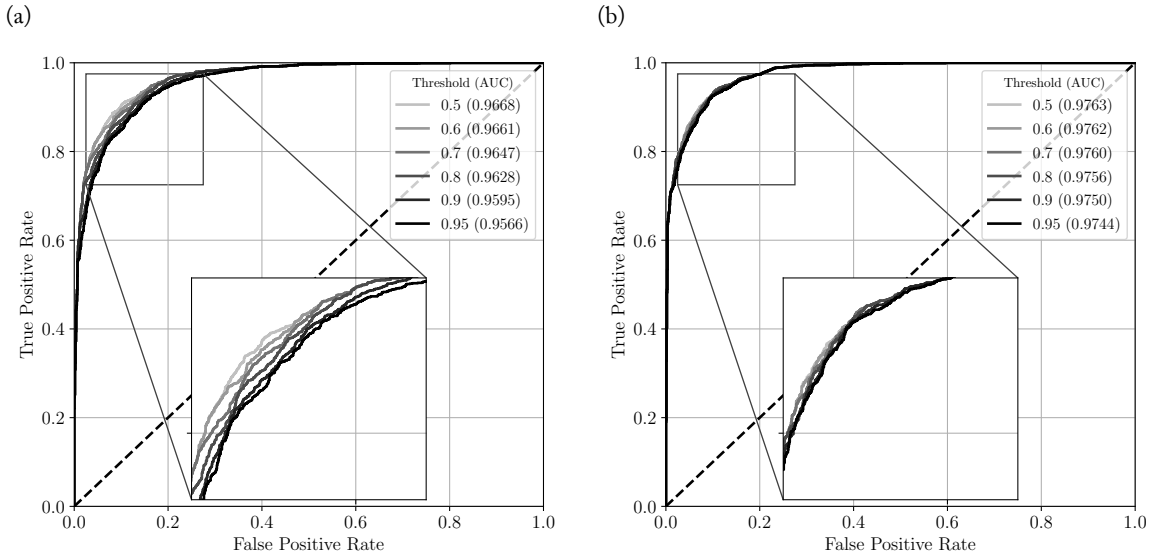

Figure 5.18: Threshold-dependent receiver operational characteristics (ROC) of (a) the Canterbury-trained model; and (b) the Canterbury-Wellington-trained model evaluated on their respective test dataset. Threshold-dependent area under the curves (AUC) of each model are given in brackets in the legends.

5.10.6 Test on the manually removed ground motion records

This section presents Table 5.1 which briefly summarizes the classification results on the manually removed ground motion records (see Section 5.10.2) using the Canterbury-Wellington neural network model. In total, 334 ground motions records were manually removed (across 74 different earthquakes).

Table 5.1: Results from application of Canterbury-Wellington model neural network to ground motions which were manually removed from the dataset.

Neural network prediction	Number of records
High-quality	179
Low-quality	155

Although the neural network does not appear to accurately flag the records as poor quality, interrogation of the records and identification of the reason they were manually removed provides a basis for this behaviour.

1. **HQ prediction**: The records which were predicted as HQ were often removed as they had (i) incorrect metadata or were records corresponding to the wrong earthquake event, (ii) anomalous waveform shape, or (iii) significant pre-arrival velocities. Having the wrong metadata or being associated with the wrong event has no implication on the quality of the record hence a HQ prediction could be expected if the records are high quality. Anomalous waveform shape and significant pre-arrival velocities were not specifically or exhaustively targeted with the quality metrics, hence it is possible for such records to be classified as HQ by the neural network.

2. **LQ prediction**: The records which were predicted as LQ were often removed as they appeared to have (i) apparent instrument or electronic malfunction, (ii) evidently excessive and disproportionate low frequency amplitudes or noise, (iii) large amplitudes at the start of record, or (iv) were affected by lower limit clipping. The factors listed here directly or indirectly affect the quality metrics considered, hence it is reasonable for the records to be classified as LQ by the neural network.

3. **Both HQ and LQ prediction**: Characteristic features frequent in both HQ and LQ predicted records were the presence of multiple wave trains in a record (i.e. multiple earthquakes were recorded in a single file) and concealed or unclear P-wave arrival. Both of the factors identified are related to determining the P-wave arrival and subsequently the noise window. Whether the record is classified as HQ or LQ is heavily dependent on what the adopted automated P-wave picker selects.

While it is outside of the scope of this work, it should be possible to develop automated pre-screening tests which can automatically remove records which are inherently problematic, or apply some additional signal pre-processing which can alleviate some of the problems (e.g. splitting/truncating multiple earthquake records to have only the ground motion of interest).

5.10.7 Stability of the method for near-real time applications and ground motion records from large magnitude events

In systems estimating the regional ground motion intensity in the immediate aftermath of large magnitude earthquakes such as ShakeMap (Worden *et al.*, 2010), the quality of the recorded ground motion can also be of interest (E. Thompson, pers. comm.). However, two shortcomings hinder the application of the developed algorithm. Firstly, and independently of the earthquake magnitude, the pre-event noise used to evaluate some of the quality metrics presented in Table 5.2 may not be available, and secondly, the developed algorithm was trained on ground motion records from small magnitude events (Mw $\leq$ 5.0). This section proposes a way to evaluate the quality metrics without any recorded pre-event noise, and tests the stability of the Canterbury-Wellington model against ground motion records from the 22 February 2011 Mw 6.2 Christchurch earthquake and 21 July 2013 Mw 6.5 Seddon earthquake (located at the top of the South Island, approximately 70km south of Wellington).

In case the pre-event noise is not available, two options can be implemented to evaluate the required quality metrics and apply the proposed framework.

1. **Pre-recorded noise**: for each station of interest, a time-dependent noise can be recorded and used as a substitute for the missing noise window. The time dependency is necessary due to the nature of noise sources as discussed in Section 5.1 (e.g. tides and human activity Okada & Suto, 2003), which can be highly correlated with time.

2. **Replacement with foreign noise**: in case the noise has not been previously recorded at a particular station, it can be replaced with noise from another station with similar recording conditions (e.g. proximity to a river, an ocean, and human activity, ground conditions, and topographical effects). The selection of an appropriate station can be done using unsupervised algorithms such as k-nearest neighbour (k-NN). To achieve this task, stations with recorded noise are the classes, the distance to potential noise sources, the instrument's characteristics, and the soil characteristics are the classification dimensions, and the number of nearest neighbours k is set to 1). As this is outside the scope of this study, this implementation details of this method are not presented here.

To test the model performance on large magnitude earthquakes, 124 ground motion records from the 22 February 2011 Mw 6.2 Christchurch earthquake and 106 ground motion records from the 21 July 2013 Mw 6.5 Seddon earthquake were considered. The records were manually classified as high or low quality (HQ and LQ, respectively) and then compared against the corresponding neural network classification. Table 5.1 presents the classification results of these ground motion records using the Canterbury-Wellington model.

Table 5.1: Results from application of Canterbury–Wellington model neural network to two large Mw earthquakes, Christchurch and Seddon earthquakes. Correct prediction indicates the neural network matches the manual classification, and vice versa for incorrect prediction. Numbers between brackets represent the portion of classified records for each analyzed earthquake.

	Manual Classification			**Neural network classification**					
				True prediction			**False prediction**		
Earthquake	**Total**	**HQ**	**LQ**	**HQ**	**LQ**	**Total**	**HQ**	**LQ**	**Total**
Christchurch	124	57	67	54	61	115 (92.7%)	3	6	9 (7.3%)
Seddon	106	81	25	76	22	98 (92.5%)	5	3	8 (7.5%)

Results indicate that, despite being trained on small magnitude earthquakes, the model delivers relatively accurate results for large magnitude earthquakes. In particular, the neural network has correctly predicted 213 out of 230 records (92.6% accuracy). Of the 17 records which were incorrectly predicted, 12 were manually scored between 0.25–0.75 which suggests they were already disputable. However, it should be noted that two quality metrics, low frequency pre-event FAS to maximum signal FAS ratio ($FASpe_{(}LF_{)}/s$) and low frequency signal FAS to maximum signal FAS ratio, ($FASs_{(}LF_{)}/s$) assumes that large Fourier amplitudes for $f < 0.1$Hz are caused by factors unrelated to the earthquake-induced ground motion. Therefore the algorithm could yield incorrect results if the lower corner frequency of the ground motion is near $f = 0.1$Hz. To circumvent this issue, it may be possible to train a neural network without the these two quality metrics.

If the neural network is applied for ground motion records from large magnitude earthquakes, then the possibility of upper limit clipping should be addressed (this should not be an issue for small magnitude earthquakes which have weaker shaking though). In this scenario, the presence of clipping would need to be flagged as inappropriate, and corrected if desired.

To be flagged as inappropriate, a pre-screening test can be implemented to determine if clipping has affected the record. In order to identify the presence of clipping, the amplitude at which clipping occurs for the particular record (a function of the instrumentation setup) needs to be known. Subsequently an algorithm such as Yang & Ben-Zion (2010) can be used to determine if clipping occurred. The algorithm is developed for Back-to-Zero type clipping (clipped points take values of zero) instead of Flat-Top type clipping (clipped points take the upper limit value) so modifications will need to be made to the algorithm in the case of Flat-Top type clipping. The general steps would be to determine if the point is clipped based on it's value (either zero or the upper limit value), relative location along the record (ensuring it is within the duration of earthquake-induced ground motion), and the characteristics of the surrounding values (they should be relatively large and their signs, positive or negative, should be the same either side). If correction is desired, there are many existing algorithms of varying complexity which can be employed. For example, Yang & Ben-Zion (2010) proposed two algorithms, one via Kriging interpolation and another using similar waveforms, and Zhang *et al.* (2016) proposed an algorithm which "interpolates" based on convexity of the peaks and troughs in the waveforms.

5.10.8 Effects of the automated selection of the IM distributions

This section presents the IM-related model performance in three ways. First, Figures 5.1 and 5.2 gives the CDFs of selected ground motion records' IMs for both models and each analyzed acceptance threshold. Second, Figures 5.3 to 5.7 provide results presented in Figure 5.7 for the other acceptance thresholds. Expectedly, it can be observed that the higher the acceptance threshold, the more the distributions seem to diverge from the original distribution derived from manually selected ground motion records. Finally, to statistically show that the distributions from manual and automated selection cannot be called different, histograms of p-values are created in Figure 5.8 from bootstrapped KS tests performed by comparing the manually selected ground motion records with randomly drawn data from the automatic selection. These histograms indicate that the proportion of cases where an

alternative hypothesis has to be considered is relatively small for acceptance threshold between 0.5 and 0.7 (i.e. the histograms have a relatively small tail around 0). However, it can be observed that greater acceptance thresholds lead to greater distribution differences and may therefore be detrimental to the preservation of the natural shape of the distributions.

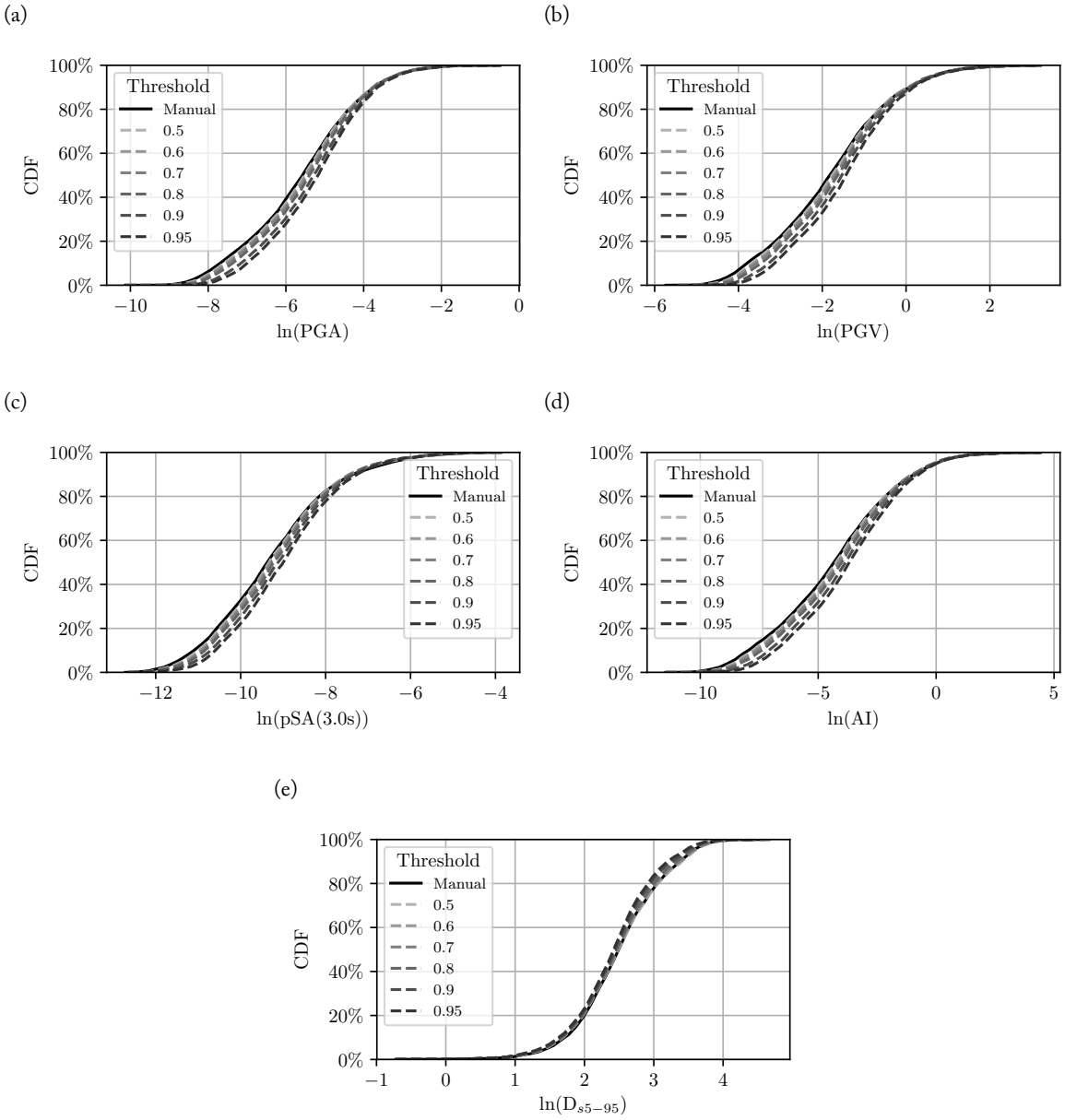

Figure 5.1: Cumulative density function given acceptance threshold and manual selection of (a) PGA ; (b) PGV ; (c) SA(3.0s) ; (d) DS$_{5\text{-}95}$; and (e) Aria's intensity for the Canterbury model.

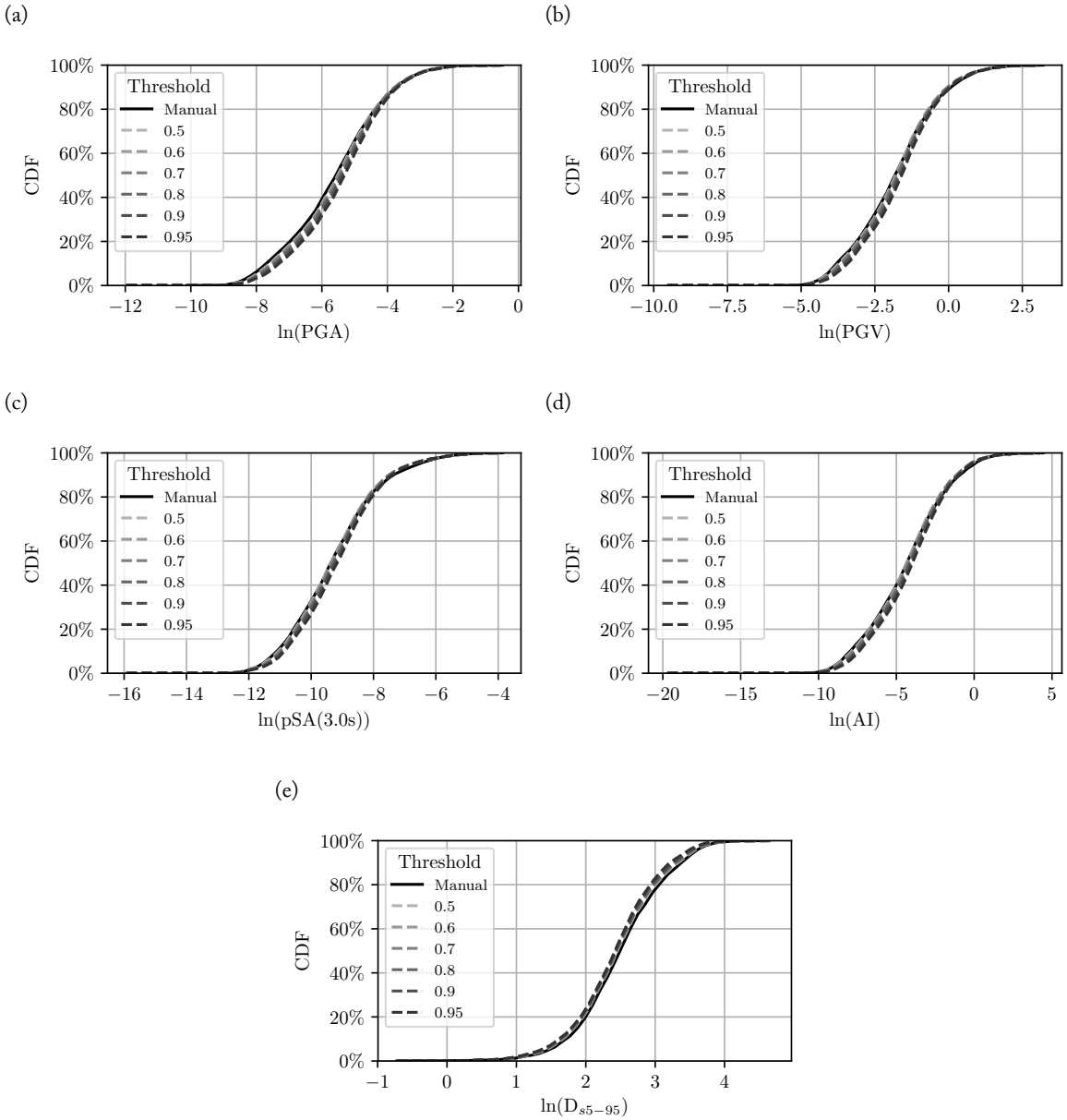

Figure 5.2: Cumulative density function given acceptance threshold and manual selection of (a) PGA ; (b) PGV ; (c) SA(3.0s) ; (d) $DS_{5\text{-}95}$; and (e) Aria's intensity for the Canterbury–Wellington model.

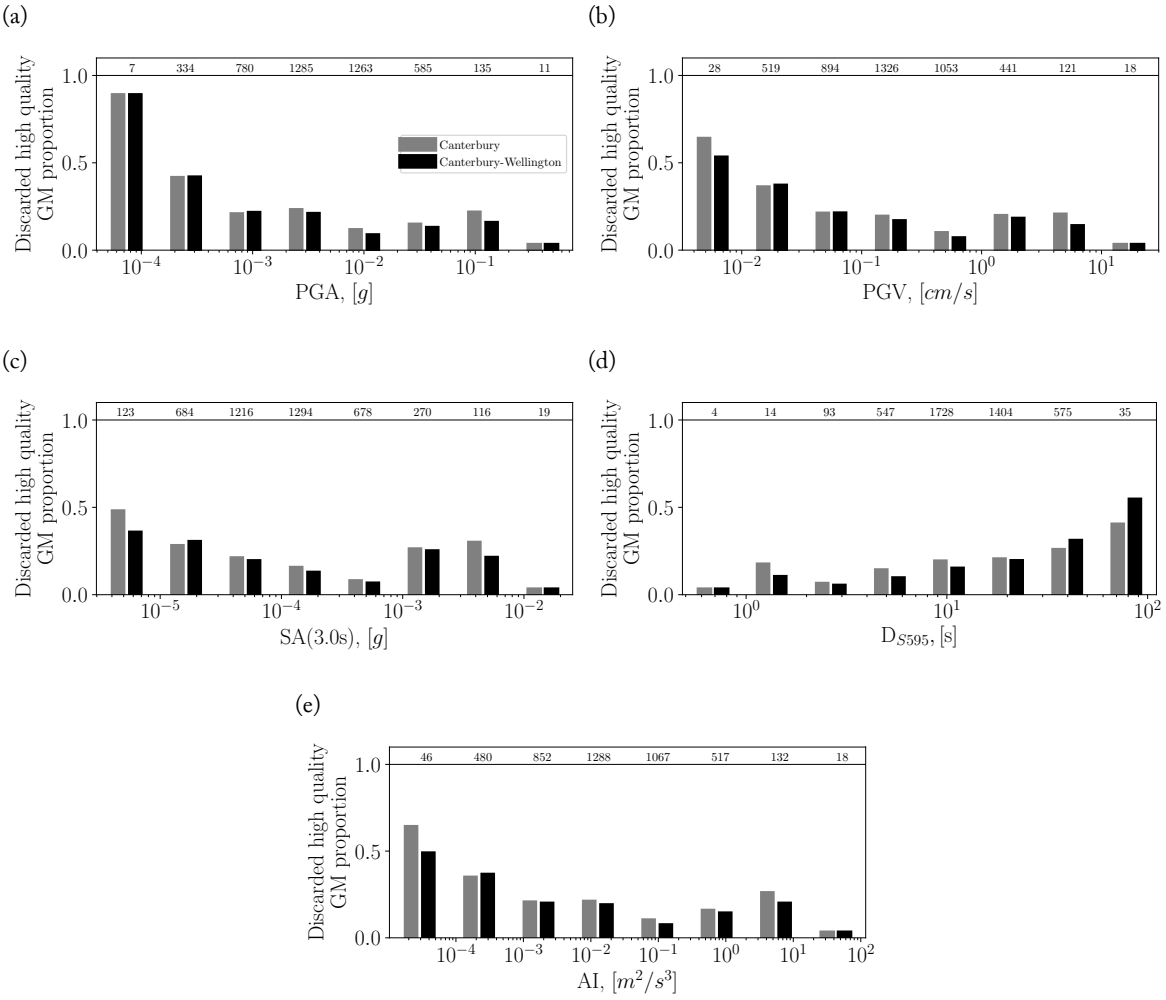

Figure 5.3: Portion of discarded high quality ground motions from the Canterbury-trained (in grey) and Canterbury-Wellington-trained (in black) neural networks on the entire dataset for (a) PGA ; (b) PGV ; (c) SA(3.0s) ; (d) $DS_{5\text{-}95}$; and (e) Aria's intensity using the 0.6 threshold. Number of manually selected ground motion records are given at the top of each bar.

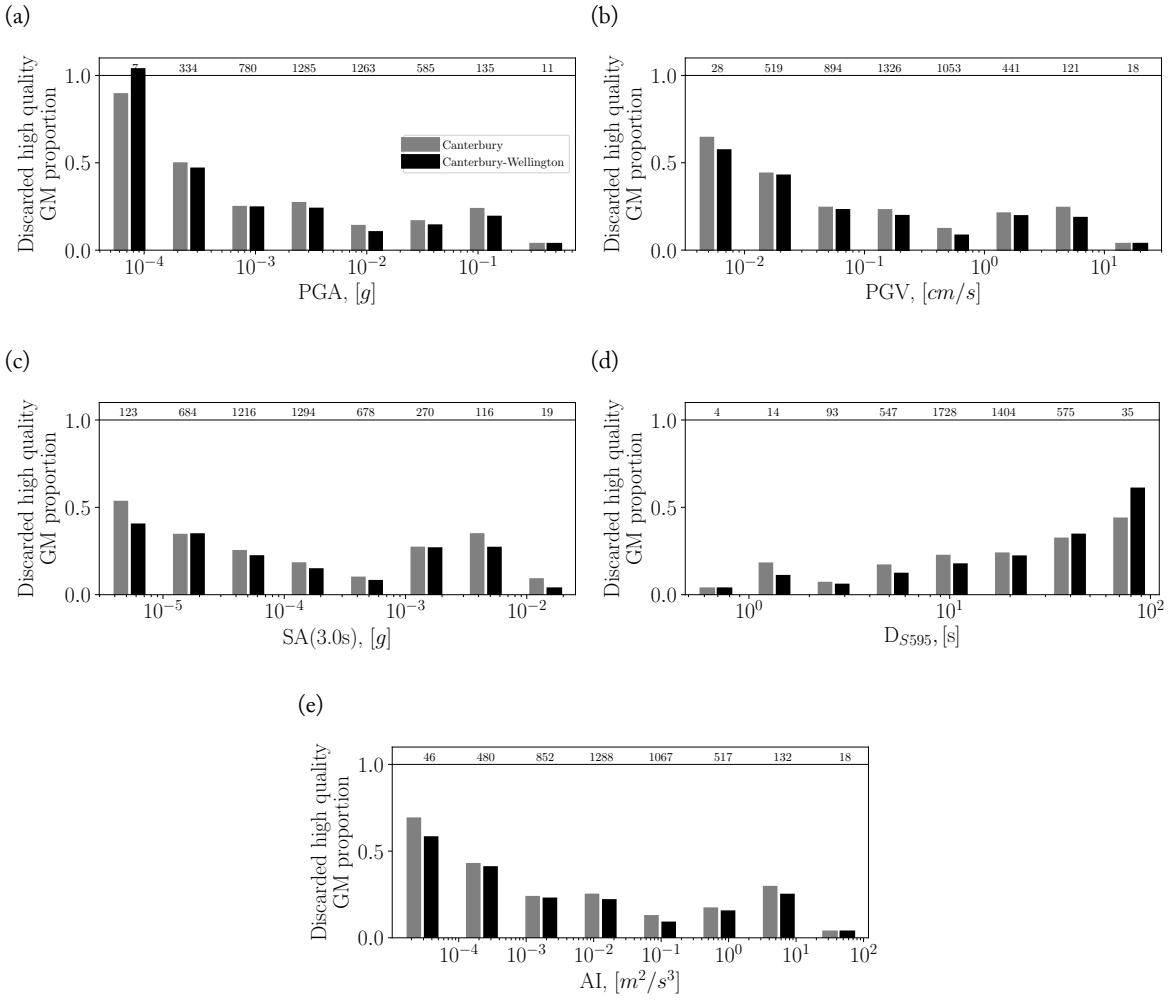

Figure 5.4: Portion of discarded high quality ground motions from the Canterbury-trained (in grey) and Canterbury-Wellington-trained (in black) neural networks on the entire dataset for (a) PGA ; (b) PGV ; (c) SA(3.0s) ; (d) $DS_{5\text{-}95}$; and (e) Aria's intensity using the 0.7 threshold. Number of manually selected ground motion records are given at the top of each bar.

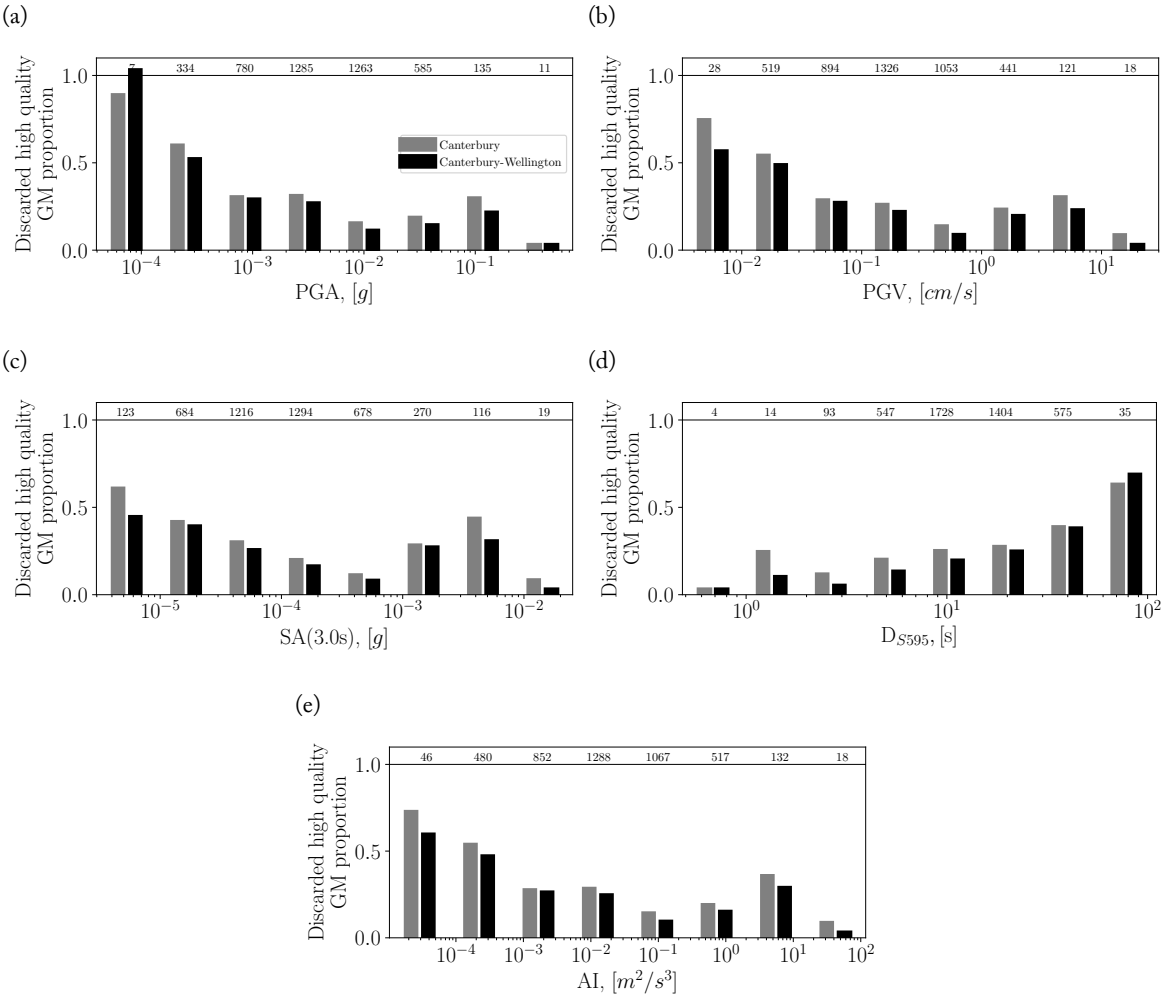

Figure 5.5: Portion of discarded high quality ground motions from the Canterbury-trained (in grey) and Canterbury-Wellington-trained (in black) neural networks on the entire dataset for (a) PGA ; (b) PGV ; (c) SA(3.0s) ; (d) $DS_{5\text{-}95}$; and (e) Aria's intensity using the 0.8 threshold. Number of manually selected ground motion records are given at the top of each bar.

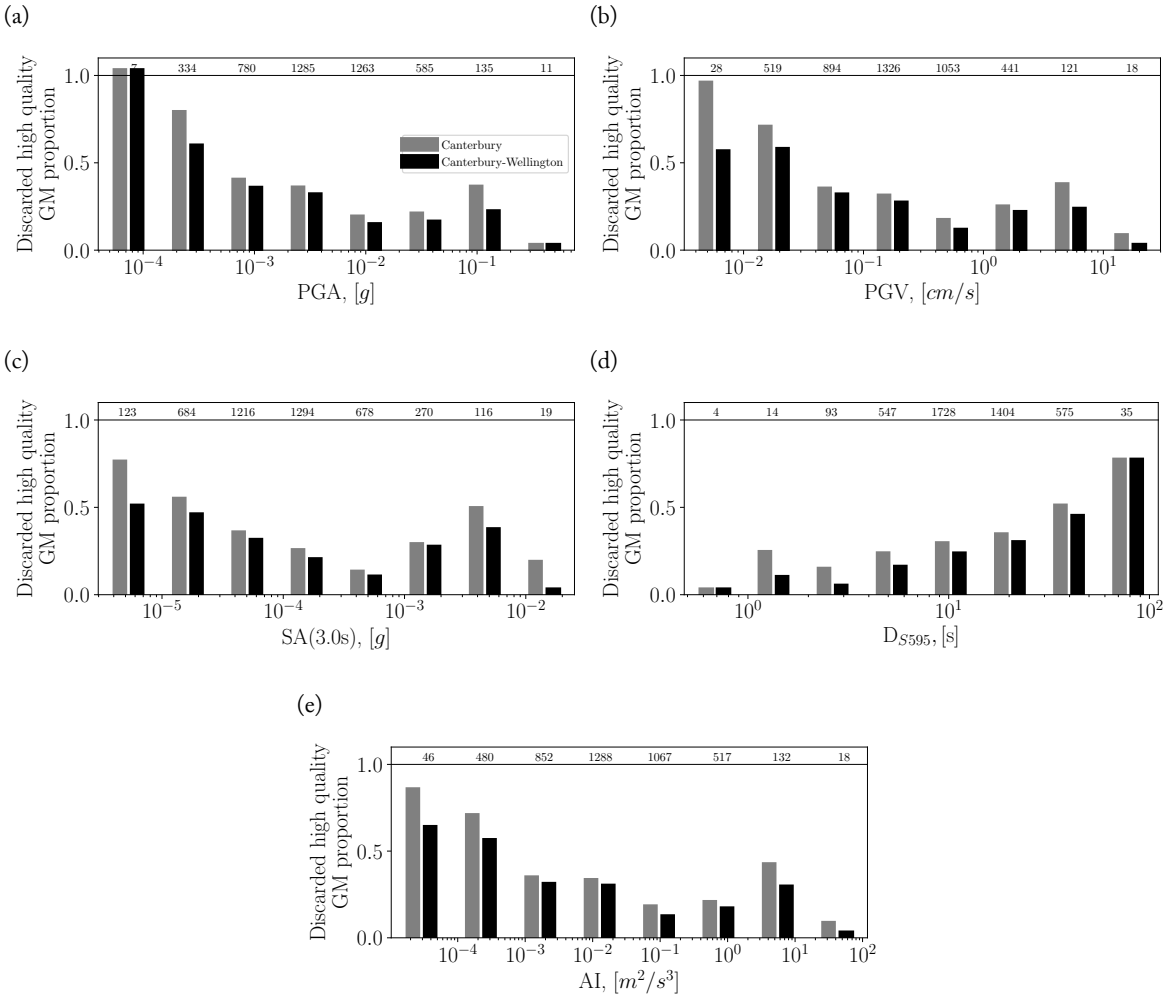

Figure 5.6: Portion of discarded high quality ground motions from the Canterbury-trained (in grey) and Canterbury-Wellington-trained (in black) neural networks on the entire dataset for (a) PGA ; (b) PGV ; (c) SA(3.0s) ; (d) $DS_{5\text{-}95}$; and (e) Aria's intensity using the 0.9 threshold. Number of manually selected ground motion records are given at the top of each bar.

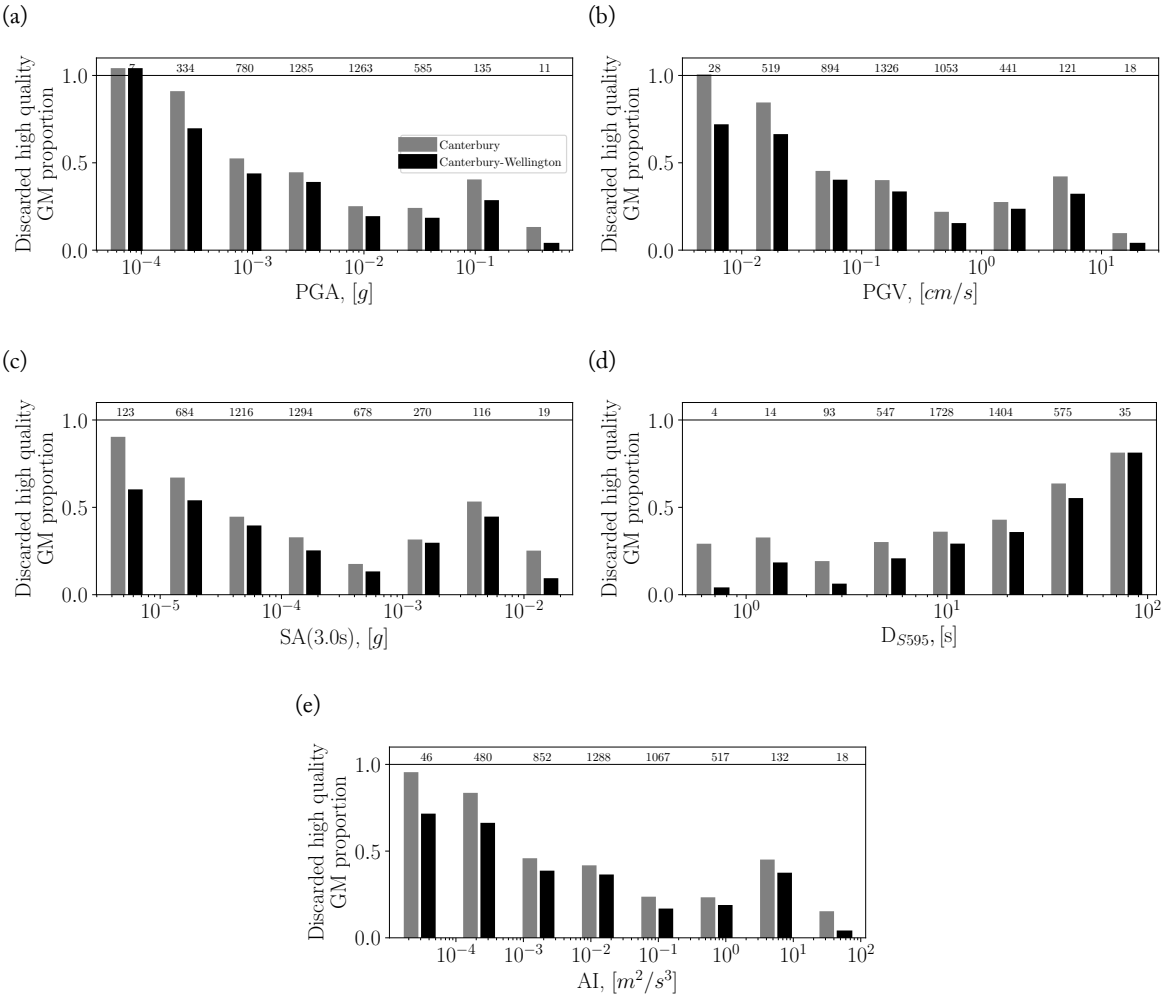

Figure 5.7: Portion of discarded high quality ground motions from the Canterbury-trained (in grey) and Canterbury-Wellington-trained (in black) neural networks on the entire dataset for (a) PGA ; (b) PGV ; (c) SA(3.0s) ; (d) $DS_{5\text{-}95}$; and (e) Aria's intensity using the 0.95 threshold. Number of manually selected ground motion records are given at the top of each bar.

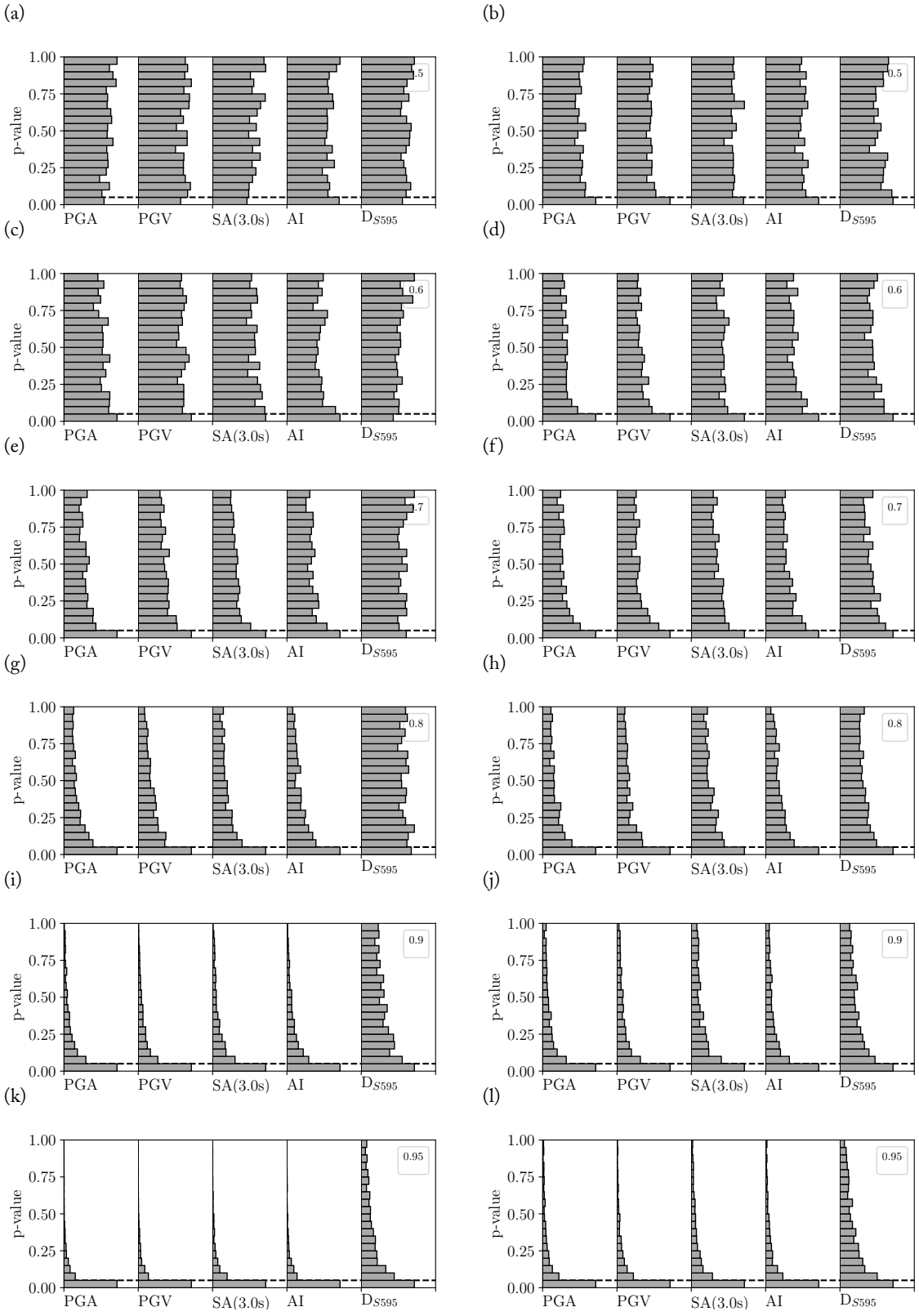

Figure 5.8: P-value histograms comparing the automatically selected with the manually selected distributions of PGA, PGV, SA(3.0s), AI and DS_{595}, given different acceptance threshold (indicated at the top right corner of each plot). Results from the Canterbury model are presented on the left-hand side, whereas results from the Canterbury-Wellington model are presented on the right-hand side.

5.10.9 False positive prediction maps for geospatial assessment

This section presents Figure 5.9 which provides a map that identifies the false positive prediction percentage at recordings in stations in Canterbury and Wellington. This figure was omitted from the main article as it practically presents a uniform trend of low false positive prediction percentage everywhere shown.

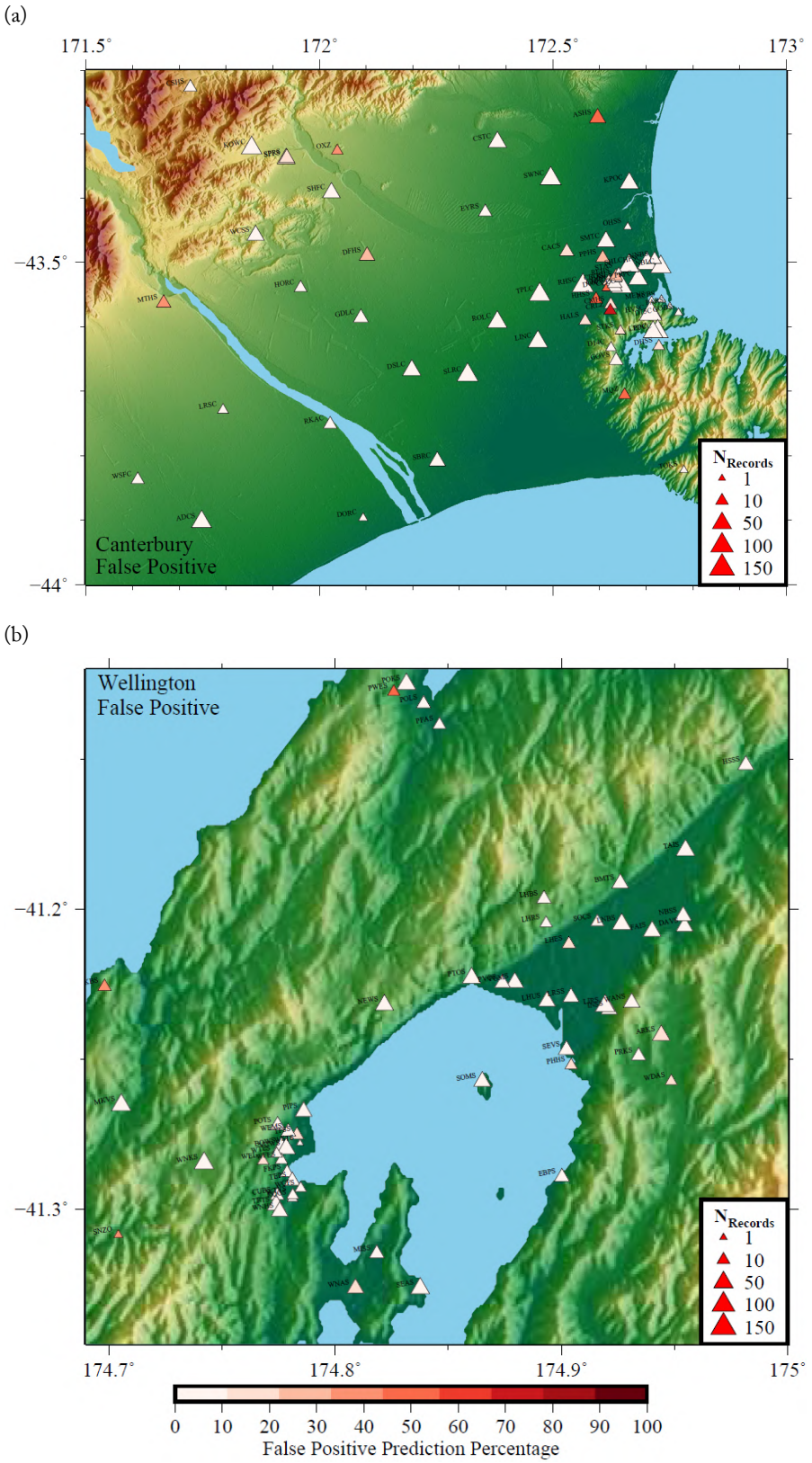

Figure 5.9: False positive prediction (manual low quality, predicted high quality) percentage of ground motion recording stations in (a) Canterbury ; and (b) Wellington (locations shown in Figure 5.1).

5.10.10 Ground motion simulation validation bias and standard deviations

This section presents Table 5.2 which provides the numerical values of bias and standard deviation of the ground motion simulation validation example in Section 5.5 associated with the various ground motion screening scenarios.

Table 5.2: Bias values from the ground motion simulation validation results for various ground motion quality screening scenarios. Five intensity measures are presented. Standard deviations are in parentheses.

Method	$\mathbf{N}_{GM}$	**PGA**	**PGV**	**AI**	$\mathbf{D}_{s595}$	**SA(3.0)**
No Screen	5223	-0.66 (0.78)	-0.67 (0.76)	-0.5 (1.35)	2.11 (0.59)	-0.45 (0.81)
Manual	2838	-0.63 (0.75)	-0.65 (0.73)	-0.46 (1.29)	2.01 (0.52)	-0.6 (0.62)
Cant(0.5)	2609	-0.58 (0.75)	-0.61 (0.73)	-0.38 (1.28)	2.01 (0.52)	-0.58 (0.62)
Cant(0.6)	2515	-0.58 (0.75)	-0.61 (0.73)	-0.37 (1.29)	2.01 (0.52)	-0.59 (0.63)
Cant(0.7)	2428	-0.58 (0.75)	-0.61 (0.73)	-0.38 (1.29)	2.01 (0.52)	-0.59 (0.63)
Cant(0.8)	2302	-0.57 (0.75)	-0.6 (0.72)	-0.35 (1.29)	2.0 (0.51)	-0.58 (0.63)
Cant(0.9)	2134	-0.56 (0.73)	-0.58 (0.7)	-0.32 (1.26)	1.99 (0.51)	-0.57 (0.62)
Cant(0.95)	1960	-0.53 (0.73)	-0.56 (0.7)	-0.28 (1.26)	1.99 (0.51)	-0.56 (0.62)
CantWell(0.5)	2661	-0.57 (0.76)	-0.61 (0.74)	-0.38 (1.31)	1.98 (0.52)	-0.59 (0.62)
CantWell(0.6)	2599	-0.58 (0.76)	-0.61 (0.74)	-0.39 (1.32)	1.98 (0.52)	-0.59 (0.63)
CantWell(0.7)	2529	-0.57 (0.76)	-0.6 (0.74)	-0.37 (1.32)	1.98 (0.52)	-0.59 (0.63)
CantWell(0.8)	2445	-0.57 (0.76)	-0.61 (0.74)	-0.37 (1.32)	1.98 (0.53)	-0.59 (0.62)
CantWell(0.9)	2308	-0.55 (0.77)	-0.58 (0.74)	-0.35 (1.32)	1.97 (0.52)	-0.57 (0.63)
CantWell(0.95)	2169	-0.53 (0.77)	-0.57 (0.74)	-0.32 (1.33)	1.97 (0.52)	-0.56 (0.63)

Chapter 6

Conclusion and future work

This chapter briefly summarizes the practical implication and limitations of each objective and discusses direction for future research.

6.1 Practical implications

6.1.1 Simplification of pipeline fragility assessment in liquefaction-prone regions

Chapter 2 introduced new empirical pipeline fragility functions based on Canterbury, New Zealand earthquake sequence data, that simplifies pipeline fragility assessment in liquefaction-prone regions by bypassing the liquefaction severity estimation process. This is achieved by integrating a soil liquefaction susceptibility quantifiable metric (the cyclic resistance ratio) as a fragility model parameter. The positive by-product of this model lies in the alleviation of the relatively regional validity from previous models accounting for liquefaction (due to the qualitative description of the soil, e.g. Isoyama *et al.*, 2000), and allows more confident applications to foreign infrastructure networks. Furthermore, constructed as an additive parametric model, whose uncertainty grows with the number of unknown parameters, the developed functions can be applied on assets that are not perfectly characterized or identical (e.g. material and/or diameter unknown).

These functions can be used in two different ways. As deformation-based pipeline fragility functions are expected to be more accurate than the proposed model, it can serve as a first post-earthquake damage estimate for buried pipe networks before soil deformation information become available via LiDAR or satellite imagery, and inform emergency managers on the expected number and locations of repairs. These functions can also be used in probabilistic loss assessments in regions, where the soil liquefaction susceptibility is sufficiently characterized without the need for statistically estimating liquefaction severity.

6.1.2 Training and post-earthquake optimization for recoveries of water supply systems

In Chapter 3, the inferred water supply system recovery following the 22 Februry 2011 Mw 6.2 Christchurch earthquake and a method to recover services for future event have been presented. In this study, the historical recovery is inferred from the pipe repair dataset combined with other information sources, and results are presented from temporal and geospatial perspectives. Furthermore, a mixed integer linear program is proposed to optimize potential future recoveries. Its solution is approached using a genetic-algorithm.

In addition to the lessons this historical analysis brings, the optimization method can be utilized in future recoveries to inform network operators on their options. In particular, priorities can be suggested to emergency managers to find and repair pipe failures. Furthermore, it can be used in preparation projects such as the AF8 (Orchiston *et al.*, 2018) or the HayWired (Detweiler & Wein, 2018) projects to benchmark large scale exercise results.

6.1.3 Accuracy improvement of immediate post-earthquake loss assessment

As pointed out by Allstadt *et al.* (2018), loss assessment based on the first ground motion estimates that do not account for the spatial nature of the earthquake source leads to dramatic underestimation of the losses. Chapter 4 presented a method to optimize the immediate ground motion intensity estimation at regional scale for major earthquakes. Despite its pioneering nature, this method can already be applied in New Zealand following a major earthquake with a limited degree of confidence. It can deliver first insights on the more likely faults to have ruptured and provide decision-makers with an immediate regional ground motion estimate superior to the one delivered using the current point-source assumption.

Combined with fragility functions able to produce reliable results using little information (e.g. the pipeline fragility functions presented in Chapter 2) and with infrastructure network engines such as the one presented in Chapter 3, the accuracy of immediate service loss estimation could be significantly improved. These combined research elements could constitute the next generation of PAGER (Wald *et al.*, 2008), providing more granular information to decision-makers.

6.1.4 Demonstrated benefits of integrating machine learning techniques in earthquake engineering

Research in earthquake engineering and seismology is based on data-intensive, computationally expensive analyses. This dissertation promoted the adoption and use of machine learning techniques as casual research tools in these fields. Chapter 3, 4 and 5 presented research elements that utilize machine learning to tackle problems that would have been too complex and too long to solve, or would have led to poor results if conventional methods were applied. Specifically, the linear program designed in Chapter 3 to optimize network service recoveries is solved via a genetic algorithm that explores an almost infinite search space as the number of permutations for pipe repairs is dramatically high. The source identification and ground motion map generation algorithms presented in Chapter 4 yield faster and superior first estimates that currently employed methods. The ground motion record classifier developed in Chapter 5 achieves human-comparable results within a fraction of the time needed by a human analyst for the same task. In all these cases, limited effort was dedicated to the acquisition of new data as most utilized datasets already existed.

6.2 Main limitations and future work

This section discusses the main limitations of each of the presented research elements and identifies potential, future research avenues.

6.2.1 Pipeline fragility functions

The pipeline fragility functions presented in Chapter 2 have three main limitations. First, not all possible pipe types have been analyzed due to data scarcity or absence. Second, as it has been observed in the development of the post-earthquake network recovery framework (see Chapter 3), assessment of individual pipes remains relatively uncertain. Third, the individual pipe level of service has not been estimated (i.e. the results from the fragility analysis is binary).

To remedy these limitations, multiple datasets could be joined together to fill potential data gaps. Bagriacik *et al.* (2018) provide a first potential solution toward the individual pipe failure assessment by applying machine learning technique to evaluate the asset fragility. Future data collection should try to capture the approximate level of service of each repaired asset such that fragility function can provide the residual functionality of each asset.

6.2.2 Water supply network recovery

The proposed inferred recovery and its subsequent optimization have two main limitations. First, the network engine is based on a connectivity algorithm and does not consider water flow explicitly. As detailed in Chapter 3, this assumption tends to be sufficient when water sources across the considered network are spatially well-distributed and operational. This may not be the case for networks operating with only a couple of major sources. The integration of a fast flow engine could alleviate this issue.

Second, the residual functionality of each network element (pipes and sources) is binary (working or not). As results from the historical recovery tend to show, this has little influence on the functionality evaluation of the system (i.e. the proposed inference is close to the reported observations). However, to fully realize the potential of recovery optimization, a finer description of each element functionality should be estimated as described in the above section.

6.2.3 Source identification and regional ground motion estimation

The framework presented in Chapter 4 is mainly limited by the size of its training dataset. Currently, only a quarter of known New Zealand faults are integrated into the framework and multi-segmented and partial ruptures are not part of the training dataset. As the number of ground motion simulations and their complexity (e.g. multi-segmented ruptures, partial fault ruptures) will increase, these elements will be incorporated. Furthermore, as physics-based ground motion are being refined and validated, the use of waveforms to identify earthquake sources will become possible.

6.2.4 Ground motion records classification

The algorithm presented in Chapter 5 shows great performance on test data. However, it remains limited by the relatively narrow origin of its training data. It is possible that ground motions recorded in locations of particular ground conditions or topography may not be selected by the proposed neural network, despite its apparent validity for a human analyst.

To ensure the validity of such an approach, future research should validate this model on datasets from other origins. Alternatively, the use of recurrent neural networks that assess the raw signal instead of summarizing metrics may be tested.

6.3 Concluding remarks

This dissertation presented four different research elements that improve, directly or indirectly, the current understanding and optimization of buried infrastructure network resilience. Promotion of machine learning techniques within the earthquake engineering and seismological communities is also achieved by demonstrating the positive impacts they have on the expediency and accuracy of some demanding processes. In the future, incorporating these methods to solve complex problems such as liquefaction severity assessment should have a substantial positive impact on the work earthquake scientists and engineers are conducting. Ultimately, the proposed work provides a foundation based on modern data-oriented techniques for communities that are in the pursuit of earthquake resilience.

6.4 References

Allstadt, KE, Jibson, RW, Thompson, EM, Massey, CI, Wald, DJ, Godt, JW, & Rengers, FK. 2018. Improving near-real-time coseismic landslide models: Lessons learned from the 2016 Kaikōura, New Zealand, earthquake. *Bulletin of the Seismological Society of America*, **108**(3B), 1649–1664.

Bagriacik, A, Davidson, RA, Bradley, BA, Hughes, MW, & Cubrinovski, M. 2018. Comparison of Statistical and Machine Learning Approaches to Modeling Earthquake Damage to Water Pipelines. *Soil Dynamics and Earthquake Engineering*, **112**, 76–88.

Detweiler, ST, & Wein, AM. 2018. *The HayWired Earthquake Scenario — Engineering Implications*. Reston, VA, USA: U.S. Geological Survey and U.S. Department of the Interior. Chap. Chapter N: A New Model of Water-Network Resilience, with Application to the HayWired Scenario by Porter KA.

Isoyama, R, Ishida, E, Yune, K, & Shirozu, T. 2000. Seismic damage estimation procedure for water supply pipelines. *In: 12th World Conference Of Earthquake Engineering, New Zealand*.

Orchiston, C, Mitchell, J, Wilson, T, Langridge, R, Davies, T, Bradley, BA, Johnston, D, Davies, A, Becker, J, & McKay, A. 2018. Project AF8: developing a coordinated, multi-agency response plan for a future great Alpine Fault earthquake. *New Zealand Journal of Geology and Geophysics*, 1–14.

Wald, DJ, Earle, PS, Allen, TI, Jaiswal, K, Porter, K, & Hearne, M. 2008. Development of the US Geological Survey's PAGER system (prompt assessment of global earthquakes for response). *In: Proceedings of the 14th world conference on earthquake engineering*.